The turbulent boundary layer:

spanwise structure,

evolution of low-velocity regions

and response to artificial disturbances

Arnold Joost Brand

The turbulent boundary layer:

spanwise structure,

evolution of low-velocity regions

and response to artificial disturbances

Proefschrift

ter verkrijging van de graad van doctor
aan de Technische Universiteit Delft,
op gezag van de Rector Magnificus,
prof. drs. P.A. Schenck,
in het openbaar te verdedigen
ten overstaan van een commissie
aangewezen door het College van Dekanen
op 11 mei 1992 om 14.00 uur
door

Arnold Joost Brand,

geboren te Sliedrecht,
natuurkundig ingenieur

Dit proefschrift is goedgekeurd

door de promotor:

prof. dr. ir. F.T.M. Nieuwstadt

aan Janny

Keywords

<u>fluid dynamics</u>
    coherent structures
    flow visualization
    fluid injection
    stability analysis
    turbulent boundary layer
<u>digital image processing</u>
    image analysis
    logical operations
    morphological operations

Contents

Introduction

The flow in a turbulent boundary layer is characterized by flow events and fluid motions which are collectively known as coherent structures. This view on near-wall turbulence is different from the classic one which states that turbulent boundary layer flow is random, and can only be characterized by a statistical description. One of the challenging features of the modern structural description is that it considers near-wall turbulence to contain regions of flow which are highly deterministical, i.e. flow regions whose behaviour can be predicted.

Since the coherent structures are supposed to dominate the production of both Reynolds stress and turbulent energy, it is likely that they play a role in turbulent transport processes. A better understanding of the dynamics of coherent structures may consequently lead to applications in the domains of turbulent momentum, energy and heat transport; especially if it proves to be possible to manipulate coherent structures. Technological benefits may spin off when the concept of coherent structures is incorporated in the physics of entrainment, mixing, heat transport, combustion, drag reduction or chemical reactions. However, to date no engineering application of the concept of coherent near-wall turbulence exists, and the study of coherent structures in the turbulent boundary layer still is pure fundamental scientific research.

In this thesis we contribute to a better understanding of near-wall turbulence by developing methods to measure, predict and manipulate specific coherent structures. But first we briefly introduce the basic knowledge on (turbulent) boundary layer flow, its statistical and structural description, and the aims and organization of this thesis.

In a boundary layer the fluid velocity increases from 0 at the wall to the free-stream velocity U_∞. If the free-stream velocity is sufficiently large, the flow in the boundary layer becomes turbulent. Compared to the laminar boundary layer, the turbulent boundary layer has a larger thickness and a larger wall shear-stress. The momentum thickness θ is a measure of the loss of momentum in the boundary layer, as compared to the approaching flow. Generally, the Reynolds number $R_\theta = U_\infty \theta / \nu$ (where ν is the kinematic viscosity of the fluid) is used to characterize a boundary layer.

The boundary layer over a flat plate was first studied by Burgers (1924). It is laminar near the leading edge, and becomes turbulent further downstream (figure 1). The point x_t of transition from laminar to turbulent flow is determined by the critical Reynolds number $R_{x_t} = U_\infty x_t / \nu$. Transition takes place for $R_{x_t} > 3\ 10^5$, and can be forced to occur at a lower critical Reynolds number by attaching a so-called 'tripping' wire to the wall and perpendicular to the flow direction. The approximate minimum value for turbulent flow is $R_\theta = 425$.

As was shown by Reynolds (1883) in his famous flow-visualization experiment, in a turbulent flow an irregular fluctuation is superimposed on the main flow. Turbulent flow is therefore considerably different from laminar flow: it can not be represented by fluid layers which are sliding over each other.

A useful tool in analysing a turbulent flow is the decomposition of the instantaneous
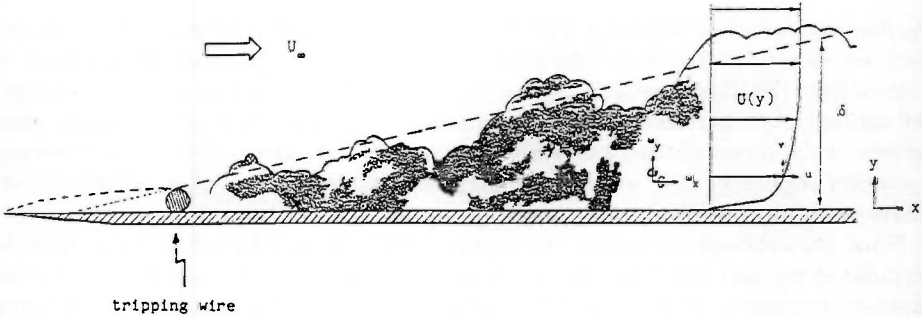
Figure 1: The boundary layer over a flat plate grows laminar until the flow reaches the tripping wire, and becomes turbulent further downstream. Indicated are the coordinate axes in streamwise direction and normal to the wall (x and y), the free-stream velocity (U_∞), the boundary layer thickness (δ), the mean velocity profile ($U(y)$), the fluctuation in the velocity components in x and z direction (u' and v'), and the instantaneous vorticity in x and y direction (ω_x and ω_y). (After Tennekes and Lumley, 1972)

flow into a mean and a fluctuating component. Using this decomposition (which is appropriately called the Reynolds decomposition), it can be shown that in a turbulent flow kinetic energy is continuously transported from the mean flow to the fluctuations. In the prevailing interpretation of this process (which is due to Richardson, 1920), the mean flow feeds its energy into a hierarchy of eddies, with large scale eddies on top and small scale eddies at the bottom. Eventually, the kinetic energy is dissipated by viscous diffusion at the smallest scales.

The Reynolds decomposition is the basis of two measures of a turbulent flow: the turbulent (kinetic) energy and the Reynolds (shear) stress. Therefore, consider the decomposition of the components u_i of the instantaneous fluid velocity vector according to $u_i = U_i + u'_i$ (where $i = 1, 2, 3$ is a direction of the coordinate system, and U and u' denote the mean and the fluctuating part of the velocity, respectively). Then the instantaneous turbulent (kinetic) energy is $u'_i u'_j$ with $i = j$, and the instantaneous Reynolds (shear) stress is $u'_i u'_j$ with $i \neq j$.

The statistical description of the turbulent boundary layer employs time-averaged flow quantities, such as the mean velocity and the velocity variance. By analysing the processes relevant to the turbulent boundary layer, it can be shown that, in the time-averaged sense, a turbulent boundary layer is characterized by two sets of variables: the inner and the outer flow-variables. The inner flow-variables are the friction velocity u_* (which follows from the Reynolds stress at the wall) and the kinematic viscosity ν of the
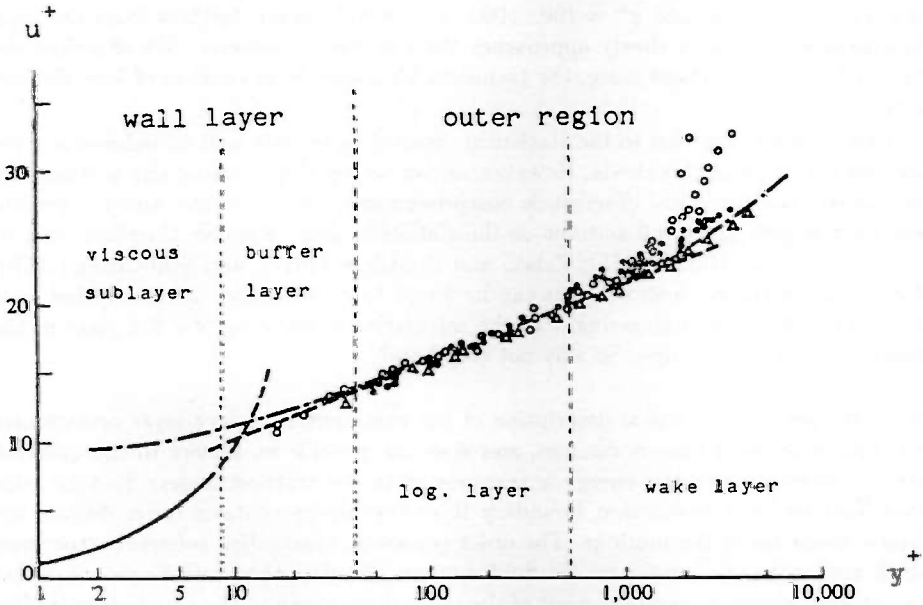
Figure 2: The non-dimensional mean streamwise velocity U^+ in a turbulent boundary layer as a function of the non-dimensional distance y^+ to the wall. Four distinct layers are present: the viscous sublayer, the buffer layer, the logarithmic layer and the wake layer. (The profile is adopted from Hinze, 1975).

fluid. These variables define the viscous scales, which are the viscous velocity u_*, the viscous length $l_* = \nu/u_*$ and the viscous time $t_* = \nu/u_*^2$. A variable non-dimensionized with a viscous scale is indicated with a 'sup +'; e.g. $u^+ = u/u_*$. The outer flow-variables, on the other hand, are the free-stream velocity U_∞ and the boundary layer thickness δ. These variables define the outer time scale δ/U_∞.

With the two types of scaling two main regions can be identified: the wall layer and the outer region (figure 2). In the wall layer, which is the region nearest to the wall, the roughness of the wall and the viscosity of the fluid play a major role. The lower wall layer is dominated by viscous forces, and is called the viscous sublayer. It has a linear non-dimensional streamwise velocity profile. Above it the buffer layer can be found. Generally, the buffer layer extends from $y^+ = 7...10$ to $y^+ = 30...40$, where y^+ is the dimensionless distance to the wall. The outer region consists of the logarithmic layer and the wake layer. In this region the velocity profile depends only on the friction velocity and the geometry of the flow. In the logarithmic layer the flow

is dominated by inertial forces, and this layer is characterized by a logarithmic non-dimensional streamwise velocity profile. The logarithmic layer generally can be found between $y^+ = 30...40$ and $y^+ = 100...1000$. In the wake layer, farthest from the wall, the streamwise velocity slowly approaches the free-stream velocity. We therefore see that, in the time-averaged sense, the turbulent boundary layer consists of four distinct layers.

This brief introduction to the statistical description of near-wall turbulence is sufficient for the scope of this thesis. However, as can be found by reading any textbook on the subject, the statistical description comprises more than the scales and the profiles described before. For a full account on the statistical description we therefore refer to the literature, e.g. Hinze (1975), Cebeci and Bradshaw (1977), and Schlichting (1979). More importantly, in these works it can be found that the statistical description suits many applications in engineering, e.g. the calculation of the drag of a flat plate or the transport of mass in a pipe. So why not stop here?

By its nature, the statistical description of the turbulent boundary layer presupposes that near-wall turbulence is random, and does not provide an answer to the question how the mean flow kinetic energy is transported to the smallest scales. To this point investigations have shown that boundary layer turbulence contains order despite the chaotic character of the motions. The order is present in so-called coherent structures, which are large-scale quasi-periodic fluid motions. To date the prevailing view is that the coherent motions transport most of the mean flow energy to the smallest scales (see e.g. Robinson, 1991).

Although it had been recognized that the flow near the wall of a turbulent boundary layer is neither laminar nor fully turbulent (e.g. Theodorsen, 1955; Einstein and Li, 1956; Hanratty, 1956), near-wall turbulence research started with a series of flow visualization experiments. For example, by introducing hydrogen bubbles or dye near the wall, it was found that in the viscous sublayer markers concentrate in streaks at a regular transversal distance (figure 3)(Kline and Runstadler, 1959; Kline e.a., 1967). This phenomenon was attributed to the presence of elongated regions with a lower-than-average fluid velocity: the low-speed streaks. Also, by injecting dye in the buffer layer, it was found that after some oscillations the dye streaks break up in a violent motion which was called burst (Kline e.a., 1967). Later it was found that 70% of the production of turbulent kinetic energy occurs during bursts (Kim e.a., 1971). Other flow-visualization experiments revealed two types of motion which are related to the burst: the ejection (i.e. the flow of low-momentum fluid away from the wall) and the sweep (i.e. the movement of high-momentum fluid towards the wall) (Corino and Brodkey, 1969). It was found that these types of motion contribute most to the production of Reynolds stress.

The discovery of the coherent motions initiated the development of techniques to detect the visually identified flow patterns in measured velocity traces. All of the detection schemes are conditional sampling schemes, i.e. schemes that sample a velocity signal when a specified condition is met. Unfortunately, these schemes involve parameters and/or algorithms which are not prescribed by the physics. Clearly, this gives

**Original
line of dye**

**Flow
direction**
←
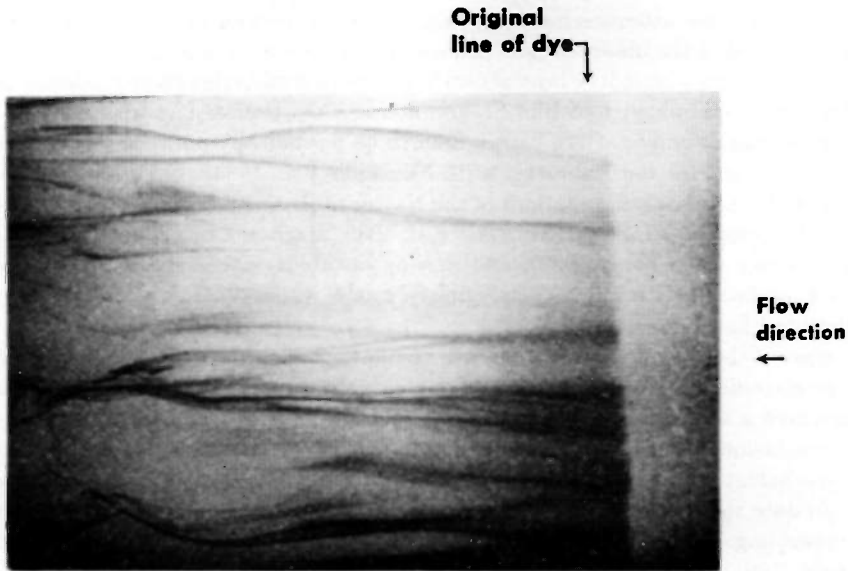
Figure 3: When dye is injected in the near-wall region of a turbulent boundary layer, it concentrates in streaks at a regular transversal distance. (Kline and Runstadler, 1959)

the interpretation of the data a subjective character. Of the many detection techniques VITA (Gupta e.a., 1971; Blackwelder and Kaplan, 1972 and 1976) and Quadrant (Wallace e.a., 1972; Willmarth and Lu, 1972) are the most popular, and the grouping of second-quadrant events seems to be the most reliable method to detect bursts (Bogard and Tiederman, 1986). However, in general it is difficult to relate probe-detected flow events to visually identified fluid motions (Offen and Kline, 1973).

Both visualization and conditional sampling studies revealed new coherent motions. These include horseshoe vortices (Head and Bandyopadhyay, 1981), typical eddies (Falco, 1977), pockets (Falco, 1978), counter-rotating streamwise vortices (Blackwelder and Eckelmann, 1979), and near-wall shear layers (Johansson e.a., 1987).

Since the early investigations on the structure of near-wall turbulence, attempts have been made to capture in a conceptual model an idealized account of the physics involved in the observed flow behaviour. A popular theme is to attribute the coherent structure of the turbulent boundary layer to the presence of horseshoe-shape vortex tubes. This concept goes back to Theodorsen (1955), and led, for example, to a cyclic model which describes the relation of a hairpin vortex to low-speed streaks, streamwise vortices, ejections and sweeps (Smith, 1984; Acarlar and Smith, 1984). Other conceptual models explain near-wall turbulence as the result of instabilities in a near-wall vortex sheet (Sreenivasan, 1988), and the flow due to a system of counter-rotating streamwise vortex pairs (e.g. Blackwelder and Swearingen, 1989).

In the meantime, attention had been paid to the development of deterministic models in order to predict the observed flow behaviour. Numerical studies of the behaviour of vortex filaments in a boundary layer show that a transversal vortex filament deforms and lifts up under the influence of Biot-Savart interactions (Doligalski and Walker, 1984), and that a regular eddy pattern causes fluid to be periodically pumped away from the wall (Hatziavramides and Hanratty, 1979; Nikolaides e.a., 1983). Other computational themes are (non)linear perturbations of the Navier-Stokes equation (e.g. Landahl, 1977 and 1990; Zhang and Lilley, 1982; Jang e.a., 1986; Haritonides, 1989), a forest of Λ-vortices (Perry and Chong, 1982), and moving instability zones (Beljaars e.a., 1981). However, to date there exists no deterministic model which predicts all of the observed and detected flow behaviour.

A class-of-their-own are the numerical simulations of a turbulent channel flow. In fact, these studies have been used to verify data on the structure of near-wall turbulence, and are even a source of new information (see e.g. Robinson e.a., 1989).

In conclusion, the discovery of coherent motions has led to the structural description of the turbulent boundary layer, which is to supplement the classic statistical description. To date there exists an extensive amount of literature, amongst which a number of reviews (e.g. Laufer, 1975; Willmarth, 1975; Cantwell, 1981; Blackwelder, 1988; Robinson, 1991).

The coherent motions detected via flow visualization or conditional sampling are second order concepts, which means that they are statements on both the flow under consideration and the measuring technique that is used. Moreover, the evaluation of flow-structure data necessarily involves a subjective factor: the interpretation of the data by the investigator. It is therefore no surprise that 30 years of research has led to numerous controversies and schools of thought, and that to date there are attempts to find a community-wide consensus on what is known about coherent structures (Kline and Robinson, 1989). In any case, a point of considerable interest in the evaluation of the knowledge should be the question whether a particular motion is a fact (i.e. an event in the flow) or an artefact (i.e. a feature of the investigative technique). At the moment it is too early to decide on the significance of the concept of coherent motion in the turbulent boundary layer. In this thesis it is therefore assumed that the knowledge on the structure of the turbulent boundary layer is reliable and significant.

May this be as it is, it is evident that near-wall turbulent flow is quasi periodical, and, in fact, a lot is known about the quasi-periodic fluid motions. However, their origin is not yet understood. There are a number of factors which have contributed to this situation. In our view the most important are:

1. The inability of the traditional measurement techniques to identify both the temporal and the spatial characteristics of the coherent motions,

2. The lack of a deterministic model for (elements of) near-wall turbulent flow,

3. The quasi-periodic occurrence of the coherent motions in a specific position.

In this thesis we address these factors in the following way. First, we develop a technique to measure spanwise profiles of the streamwise fluid velocity, and use it to study the structure of these profiles. Second, we determine the evolution in time of the flow in the near-wall low-velocity regions, and use this information to develop a simple model for this kind of flow. Third, we develop a mechanism by which non-random fluid motion can be generated artificially. With this strategy it might be possible to measure, predict and manipulate coherent motions, and, consequently, come to a better understanding of near-wall turbulence.

The main body of this thesis consists of four chapters.

Chapter 1 presents a review and evaluation of the developments in the structural description of the turbulent boundary layer. Rather than familiarizing the reader with the subject by a description of coherent motions and conceptual models, we represent the key flow visualization and conditional sampling studies, two and a half conceptual model, and two studies aimed at changing the structure of the turbulent boundary layer (section 1.2). Furthermore, we give our own biased view and the objectives of this study (section 1.3).

Chapter 2 deals with the spanwise structure of a turbulent boundary layer as it is revealed by a quantitative analysis of horizontal hydrogen-bubble time-lines. Presented are a review of the hydrogen-bubble technique (section 2.2), and an account of the effect that the wake of the wire and the velocity gradient in the flow have on the motion of the fluid markers (section 2.3). Experimental results are reported on the velocity mean and variance (section 2.4), and the structure of spanwise profiles of the streamwise velocity (section 2.5). We also evaluate the quantitative use of hydrogen-bubble time-lines (section 2.6).

Chapter 3 concerns the evolution in time of the flow in the low-velocity regions (i.e. the streaks) of near-wall turbulence. The material in this chapter is organized into three parts: measurements on the evolution of the flow in the low-velocity regions (section 3.2), an analysis of the stability of a two-dimensional velocity gradient (section 3.3), and an evaluation of the measurements and the stability analysis (section 3.4).

Chapter 4 deals with the response of a turbulent boundary layer to artificially generated disturbances. Presented are an overview of the experimental procedure (section 4.2), the results of the measurements on the response (section 4.3), and an evaluation of the results (section 4.4).

In Conclusion we recapitulate the major findings of our experiments and analyses, and present the points which are open for further research.

Chapter 1

Investigations on the structure of the turbulent boundary layer

In the classic view, turbulent boundary layer flow is random, and can only be characterized by moments of flow quantities. However, experiments have shown that this flow has a quasi-periodic character. In the modern view, near-wall turbulence is coherent on specific scales, and is characterized by flow events and fluid motions such as 'bursts' and low-speed streaks.

Even so, an evaluation of the knowledge on near-wall turbulence structure shows that data might not be correct, inferences might not be appropriate and opposite views may exist. It is therefore too early to decide on the significance of the concept of coherent near-wall flow, and necessary to assume that this knowledge is reliable and significant.

To this situation have contributed: 1) the inability to detect the joint temporal-spatial characteristics of the coherent motions, 2) the lack of a deterministic model for (elements of) near-wall turbulent flow, and 3) the quasi-periodic occurrence of the coherent motions. Therefore, the understanding of near-wall turbulence will benefit from 1) 'measuring' spanwise velocity profiles, and evaluating their structure, 2) determining the time evolution of the low-velocity regions, and developing a simple model for this kind of flow, and 3) developing a method by which non-random fluid motion can be generated artificially.

1.1 Prologue

According to the classic view, the flow in the turbulent boundary layer is random. As quasi-periodic fluid motions were observed via flow visualization, gradually came the view that turbulent boundary layer flow is not entirely random. In this chapter we present the developments in the structural description of the turbulent boundary layer.

Regarding the extensive literature in the field, this review is limited to the non-numerical flat-plate turbulent boundary layer. This means that, with a few exceptions, turbulent channel and pipe flow is left out of focus, notwithstanding the fact that these flow types are statistically and structurally similar to the turbulent boundary layer. Also, the large-eddy and direct numerical simulations are not represented, notwithstanding the fact that these simulations provide three-dimensional velocity, vorticity and pressure fields with a structure that at least qualitatively resembles the structure found experimentally. Furthermore, turbulent drag reduction by means of micro grooves or polymer addition is not treated, although it is hypothesized that these phenomena are related to changes in the coherent motion in the near-wall region.

In section 1.2 we represent those studies that made an important contribution to the view that turbulent boundary layer flow is non-random. Since it is essential to

distinguish between fact (i.e. the result of an experiment) and inference (i.e. the interpretation of the experimental result), we will do so by closely following the statements in the original publications. First, we treat in four separate subsections the key flow-visualization and conditional-sampling studies. The reader will then be familiarized with the subject by a description of coherent motions, but will also be confused by the multitude of results and interpretations. In the fifth subsection we try to get the picture clear by representing the two conceptual models that seem to be the most complete in explaining the observed flow behaviour, and a suggestion for the mechanism of streak instability. Next, we represent a number of studies on the spatial flow-structure. Finally, we address the field of boundary-layer manipulation, but we limit our treatment to the manipulations aimed at the generation of burst-like events.

In section 1.3 we present our own biased view on the structure of turbulent boundary layer flow, and the objectives of the present study.

1.2 Review of studies on the structure of near-wall turbulence

1.2.1 The discovery on non-random near-wall fluid motion

Although it had been recognized by some (e.g. Theodorsen, 1955; Einstein and Li, 1956; and Hanratty, 1956) that near-wall fluid motion in a turbulent boundary layer is neither laminar nor fully turbulent, F.R. Hama probably was the first investigator who visualized the flow in the near-wall region (see Corrsin, 1957). When dye was injected through a transversal slot, Hama observed that elongated regions of dye concentration developed. Since the dye at the wall initially marked the low-momentum fluid, these concentrations became known as *low-speed streaks*. In subsequent studies (Kline and Runstadler, 1959; Runstadler e.a., 1963; and Kline e.a., 1967), investigators visualized the wall layer of the turbulent boundary layer in a water channel with both dye and hydrogen bubbles. They concluded that the wall layer consists of a relatively regular spanwise arrangement of low and high-speed streaks (figure 1.1), the latter being regions of relatively high-momentum fluid in between the low-speed streaks. Visual counting schemes and the spanwise correlation of the streamwise velocity fluctuation yielded an average streak-spacing of about $\lambda_z^+ = 100$, and a standard deviation of 30...40% of the mean.

The investigations of Runstadler e.a. (1963) and Kline e.a. (1967) also revealed a second feature of the flow in the wall layer ($550 < R_\theta < 1400$) in the form of the motion of a dye streak. They described the *burst* (of a dye streak) as the following sequence of events (figure 1.2): 1) The streak moves slowly away from the wall while the complete structure *migrates* downstream, 2) The streak *lifts up* until it penetrates the buffer layer, 3) After reaching $y^+ = 8...12$ the lifted streak *oscillates* for a few cycles, and 4) At a height of $y^+ = 10...30$ the streak *breaks up* into smaller scales, which develop a chaotic motion. The experimental results suggested that a clear break-up rate exists. It was conjectured that the wall-layer streak break-up dominates the transfer processes between the inner and the outer region.
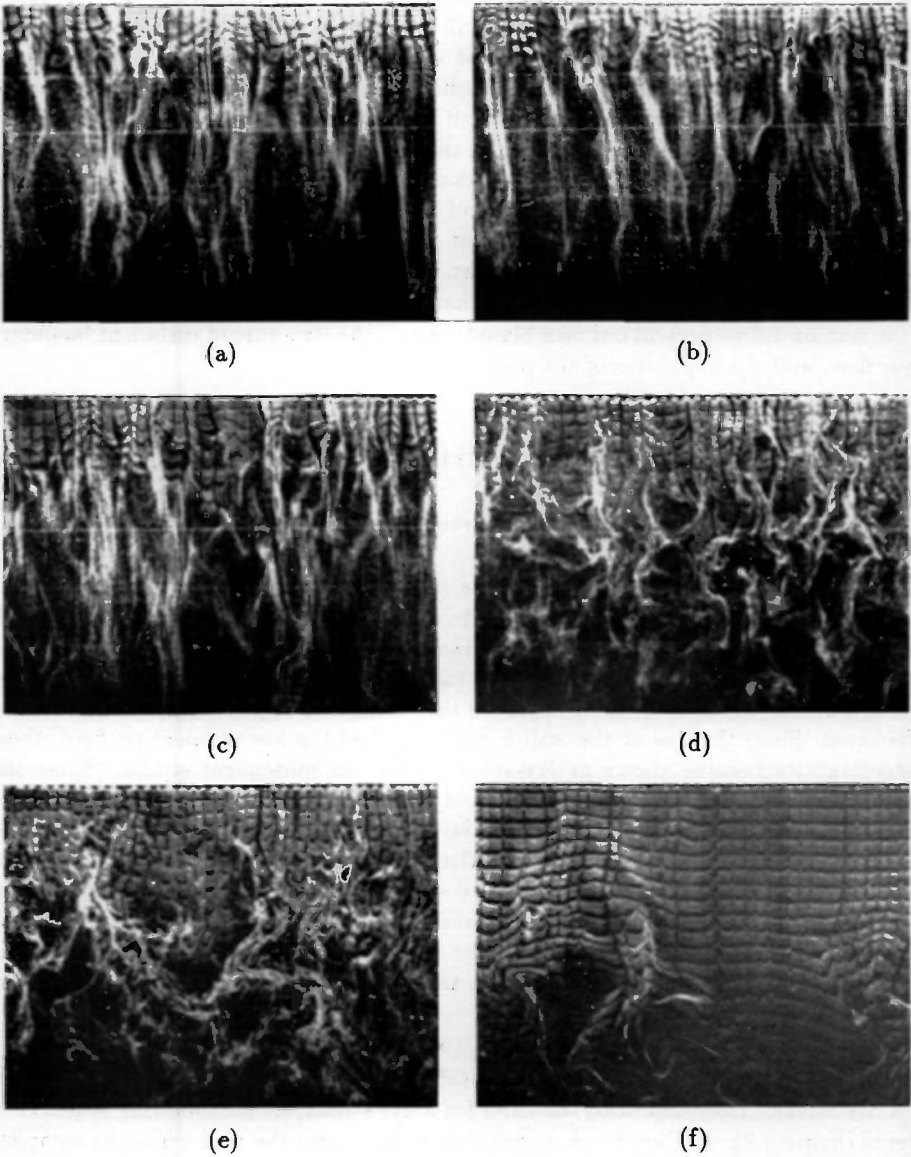
Figure 1.1: Visualization of the structure of the turbulent boundary layer over a flat plate using a horizontal bubble wire at (a) $y^+ = 2.7$, (b) $y^+ = 4.5$, (c) $y^+ = 9.6$, (d) $y^+ = 38$, (e) $y^+ = 82$, and (f) $y^+ = 407$; the flow is from top to bottom. In the near-wall region *low-speed streaks* are present. (Kline e.a., 1967)
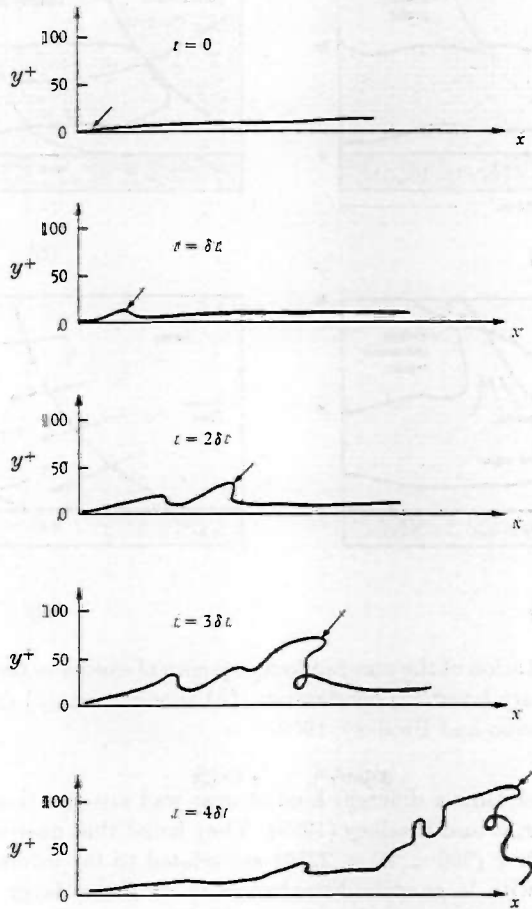
Figure 1.2: Representation of the *bursting* of a dye streak in a turbulent boundary layer. The dye streak *migrates* downstream, *lifts up* until it reaches the buffer layer, *oscillates* for a few cycles, and finally *breaks up* into smaller scales. (Kline e.a., 1967)
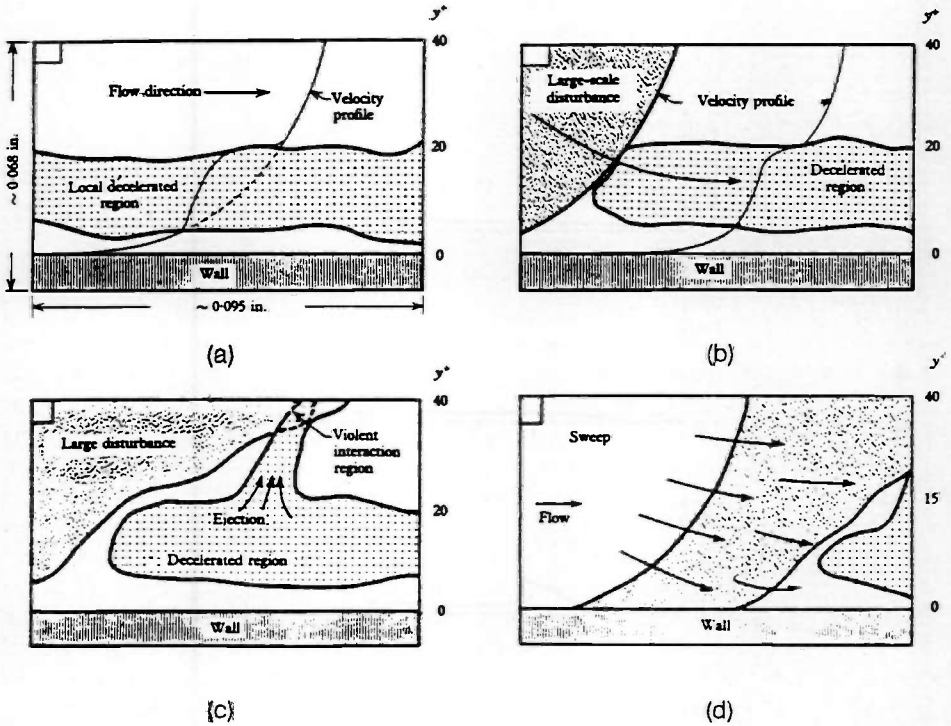
Figure 1.3: Representation of the non-random sequence of events in the near-wall region in a turbulent boundary layer: (a) deceleration, (b) acceleration, (c) *ejection* event, and (d) *sweep* event. (Corino and Brodkey, 1969)

At about the same time a different kind of near-wall visualization was carried out independently by Corino and Brodkey (1969). They found that near-wall fluid motions in a turbulent pipe flow ($900 < R_\theta < 2250$) are related to the interaction of a region of decelerated fluid with large-scale disturbances in the outer layer. Using neutrally buoyant particles for visualization, they observed in the near-wall region ($0 < y^+ < 30$) a sequence of events that repeated randomly in space and time (figure 1.3): 1) The streamwise fluid velocity decelerates to 50% of the local mean velocity, 2) The fluid is accelerated towards the wall and interacts with the fluid in the decelerated region, 3) Low-momentum fluid is *ejected* from the decelerated region ($5 < y^+ < 15$), and 4) The ejection phase ends when high-speed fluid from upstream enters the observed region and *sweeps* the field of the retarded flow.

Although there are apparent differences in the sequences of events described by Kline e.a. (1967) and Corino and Brodkey (1969) because of the differences in the visualization techniques, both groups of authors concluded that the general picture drawn by the two studies is consistent: in the near-wall region a characteristic pattern is present in the

fluid motion. Unfortunately, both sequences of events became known as the *bursting process*, and, moreover, in attempts to find more quantitative descriptions of these events, different definitions of 'bursting' have been introduced by other investigators. To date several meanings are ascribed to 'bursting', without agreement as to the proper one (see Robinson, 1991).

1.2.2 The first quantitative data on the observed flow structure

The evolution in the meaning of the term 'bursting' was set in motion by Kim e.a. (1971), who concentrated on the 'bursting' process in the wall layer of a water channel flow ($R_\theta = 666$ and 1100). They employed two measurement methods: the combined use of two perpendicular bubble-wires employing the time-streak marker method, and hot-wire measurements in combination with dye injection at the wall (figure 1.4). The qualitative data obtained with the first method confirmed that the 'bursting' process consists of three stages, which correspond to the stages 2, 3 and 4 of the description by Kline e.a. (1967). (Here we see the shift in nomenclature). After the break-up stage a quiescent flow returns, which marks the end of the 'bursting' cycle and sets the conditions for a new cycle. In the second method Kim e.a. related a visually detected 'burst' to a velocity trace when an outward moving low-speed streak passes the hot-wire probe. The quantitative data obtained with this method showed that almost all of the production of turbulent energy occurs during the 'burst'. By comparing the 'burst' rate determined from the breakup of dye streaks, they found that the mean time-interval between 'bursts' can be estimated from the second maximum in the auto-correlation coefficient of the streamwise velocity. This time interval scales with the outer flow-variables and leads to the dimensionless 'burst' period $T_b U_\infty / \delta \approx 5$.

The main goal of Gupta e.a. (1971) was to see whether or not it would be possible to obtain a more quantitative picture of the flow in the viscous sublayer. In their preliminary investigations it became clear that the use of a conventional long-time averaging process did not reveal any structure in velocity traces. Since Gupta e.a. believed that a sublayer flow-event has a relatively short life-time, they applied a *variable-interval time-averaging* (VITA) technique in order to detect these events. Two-point cross-correlations of the VITA-processed streamwise velocity in different spanwise locations in the sublayer of a wind-tunnel flow ($2200 < R_\theta < 6500$) showed that a spanwise periodicity is present with a wavelength of about $100 l_*$. Gupta e.a. concluded that this result is consistent with Kline e.a. (1967).

Laufer and Badri Narayan (1971) used the auto-correlation of the streamwise velocity component, obtained with a hot-wire mounted flush with the wall of a windtunnel, to measure the average time-interval T_b between 'bursts' in the viscous sublayer. They found that the non-dimensional period $U_\infty T_b / \delta$ and not $u_*^2 T_b / \nu$ is independent of the Reynolds number R_θ, and concluded that the near-wall 'bursting'-process scales with outer flow-variables: $U_\infty T_b / \delta = 5$.

Rao e.a. (1971) studied 'bursts' with a hot wire in a turbulent boundary layer in air ($R_\theta = 620$). They considered a band-pass filtered velocity-signal. Bursts were identified as the alternate periods of activity in the velocity signal. According to Rao e.a., the

(a)
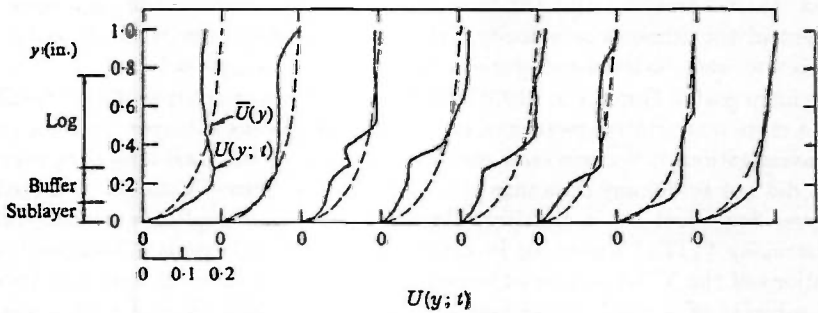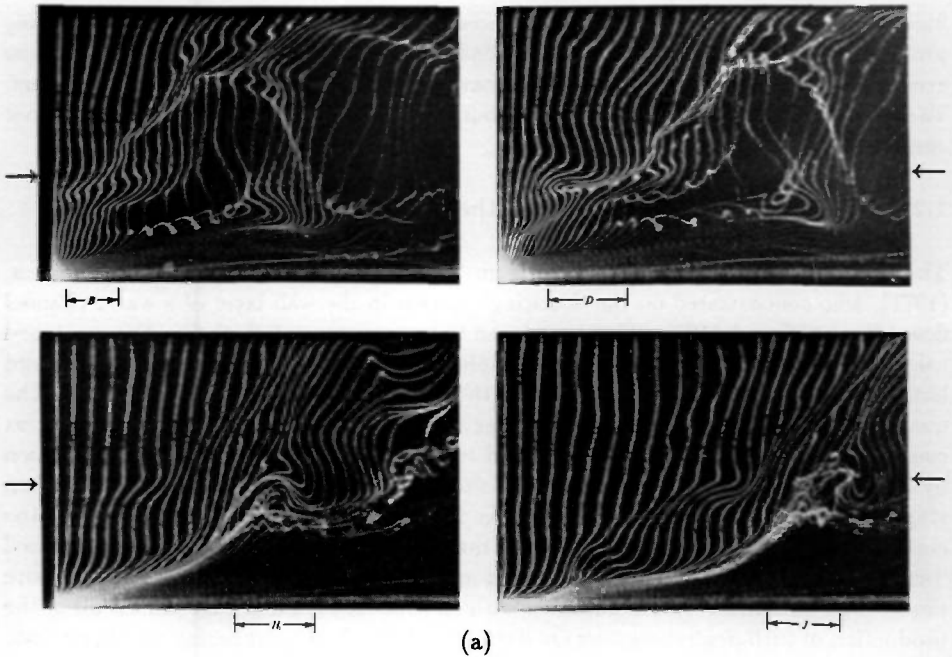
(b)

Figure 1.4: 'Bursting' visualized with vertical hydrogen-bubble time-lines. (a) The hypothesized creation and the break-up of a transversal vortex during the 'bursting' process. At first an inflection point (intersection of arrow and zone B) and later on a shear zone (arrow and zone D) appears in the time lines. The vortex develops, travels downstream (arrow and zone H) and finally breaks up (arrow and zone J). (b) Comparison of the instantaneous and the mean velocity profile during a 'bursting' cycle. (Kim e.a., 1971)

Bursting phenomenon: $H=0$

Ejection-like event $RS_2 = -\overline{uv} > 0$ at $\begin{cases} u<0 \\ v>0 \end{cases}$	Interaction (outward) event $RS_1 = -\overline{uv} < 0$ at $\begin{cases} u>0 \\ v>0 \end{cases}$
Interaction (inward) event $RS_3 = -\overline{uv} < 0$ at $\begin{cases} u<0 \\ v<0 \end{cases}$	Sweep-like event $RS_4 = -uv > 0$ at $\begin{cases} u>0 \\ v<0 \end{cases}$
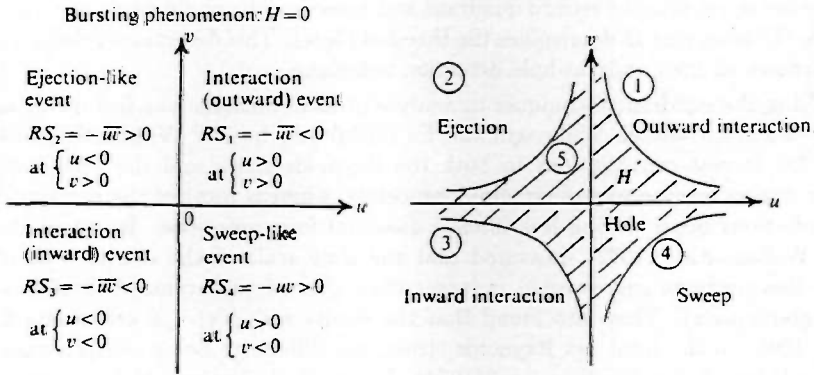
Figure 1.5: The classification of the near-wall events according to the quadrant splitting analysis-technique. (Nakagawa and Nezu, 1977)

'bursting' frequency could be counted without much difficulty when proper settings for the amplitude discriminator and the filter frequency were used. The mean 'burst'-period was found to be consistent with the one measured by Kline e.a. (1967). Rao e.a. also found that the 'bursting' frequency does not vary greatly with distance from the wall, and that the time interval between two 'bursts' is distributed according to a lognormal law.

To make quantitative measurements of the flow near the wall, Willmarth and Lu (1972) introduced the *u-level* detection technique. This technique detects a 'burst' when the amplitude of the lowpass-filtered streamwise velocity is less than a threshold level: $u < -Lu'$, with L the threshold level and u' the deviation of the instantaneous velocity from the mean. This idea is based on the observation of Kline e.a. (1967) and Corino and Brodkey e.a. (1969) that during 'bursting' the fluid velocity is lower than the mean. Using a X hot-wire probe and decomposing its velocity signals into an u and a v component, Willmarth and Lu found that 60% of the contribution to $\overline{u'v'}$ is produced when the sublayer velocity is lower than the mean.

In subsequent investigations, Willmarth and Lu (1972) introduced the *quadrant splitting* analysis of the velocity signals obtained with a X hot-wire probe. They used the products of the instantaneous values of u' and v' to define four events (figure 1.5): 1) outward interaction ($u' > 0$ and $v' > 0$), 2) ejection ($u' < 0$ and $v' > 0$), 3) inward interaction ($u' < 0$ and $v' < 0$), and 4) sweep ($u' > 0$ and $v' < 0$). (These events became also known as the *first-quadrant, second-quadrant, third-quadrant* and *fourth-quadrant event*, respectively.) On basis of the observation of Corino and Brodkey (1969) that the instantaneous value of the Reynolds stress $u'v'$ can be very large during

an ejection, Willmarth and Lu (and independently Wallace e.a., 1972) developed the quadrant detection-technique. This technique detects a 'burst' when the instantaneous Reynolds-stress is in the second quadrant and exceeds a threshold level: $(u'v')_2 > H\overline{u'v'}$, where the holes size H determines the threshold level. This detection technique became also known as the quadrant-hole detection technique.

Using the quadrant techniques to analyse measurements in the turbulent boundary layer of a wind tunnel, Willmarth and Lu (1972) and Lu and Willmarth (1973) found that the largest contributions to both the Reynolds stress and the turbulent energy occur during intense second-quadrant processes, whereas most of the remainder of the contributions occur during less intense quadrant-four processes. In a turbulent pipe flow Wallace e.a. (1972) measured that the time scale of the events with $u'v' < 0$ (i.e. the ejections and sweeps) is larger than that of the events with $u'v' > 0$ (i.e. the interactions). They also found that the events with $u'v' < 0$ contribute for more than 100% to the total net Reynolds stress; the difference being compensated by the interactions. Later Brodkey e.a. (1974) showed that ejections and sweeps are more intense than the interactions, and that the ejections are more intense than the sweeps. The four events occur with about the same frequency.

In their studies of the near-wall structure, Blackwelder and Kaplan (1972 and 1976) introduced the *VITA detection-technique*. This technique detects a 'burst' when $var > ku_{rms}$, with var the short time-interval variance of u', and u_{rms} the long time-interval variance of u' (figure 1.6). This condition characterizes intense fluctuations of u over the short time-interval T. Blackwelder and Kaplan found that the number of detected 'bursts' depends on k and T, and that VITA is equivalent to low-pass filtering. They performed experiments in a turbulent boundary layer in air ($R_\theta = 2550$), and used a single hot wire at $y^+ = 15$ to detect events with $T = 10t_*$, and a rake with hot-wires mounted downstream of the detector probe to examine the detected flow structures. Conditional averaging the velocity traces obtained with the rake gave the velocity pattern which characterizes the detected event (figure 1.7). Although the detection and the analysis took place in different locations, Blackwelder and Kaplan concluded that the detected sequence of events is the same as that reported by Kline e.a. (1967) and Corino and Brodkey (1969).

Mainly to seek the existence of relationships between 'bursts' and the other fluid motions known by that time, Offen and Kline (1973 and 1974) combined the use of a vertical hydrogen-bubble wire with dye injection (figure 1.8). They observed that simultaneous with (or shortly after) the first oscillation in a near-wall dye-streak, the time lines show small zones of high shear. The streamwise extent of such a zone corresponds to the length of the oscillating dye streak. The shear zones in the time lines are all located along the same curve. As an explanation of this behaviour, Offen and Kline conjectured that along this curve either a longitudinal or a transversal vortex is present. Most lift-ups of wall dye were observed some time after the appearance of the shear zones, and seemed to be initiated by disturbances in the logarithmic layer which are characterized by a wallward motion. They believed that these disturbances are generated by the interaction of an older 'burst' and the flow in the logarithmic layer. Since individual 'bursts' vary greatly, Offen and Kline hypothesized that 'bursts' are
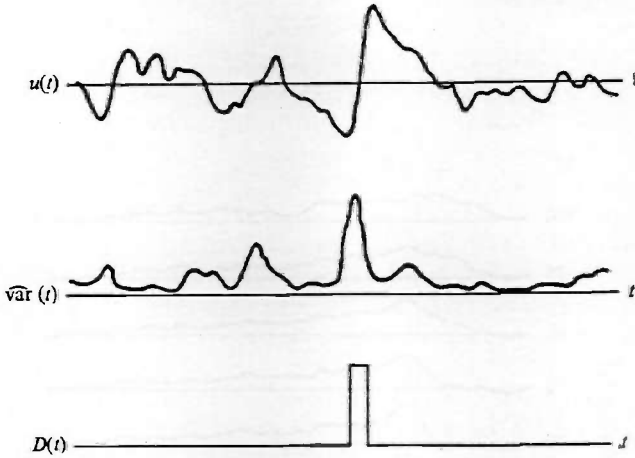
Figure 1.6: Representation of the VITA detection-technique. A 'burst' is detected when the short-time variance of the streamwise velocity is k times as large as the rms velocity. The signature of a 'burst' is: 1) a (slowly) decreasing velocity, 2) a rapid increasing velocity and 3) a (slowly) decreasing velocity. (Blackwelder and Kaplan, 1976)

due to the temporary existence of a spatially *coherent flow pattern*.

The quantitative detection techniques were introduced in order to indicate the occurrence of a 'burst' without having to rely on visual data. However, all of these techniques contain a great deal of subjectivity because of the role played by the parameters of the techniques. Therefore, one might question the reliability of these techniques in detecting the visually observed flow events. In section 1.2.4 we represent various studies on the relation between flow events detected with different techniques. The hypothesis of coherent flow in near-wall turbulence stimulated many to develop conceptual models that give an idealized description of the observed flow-behaviour. In section 1.2.5 we represent three of the many proposed models. However, before turning to these topics we represent some new observations on the flow structure.
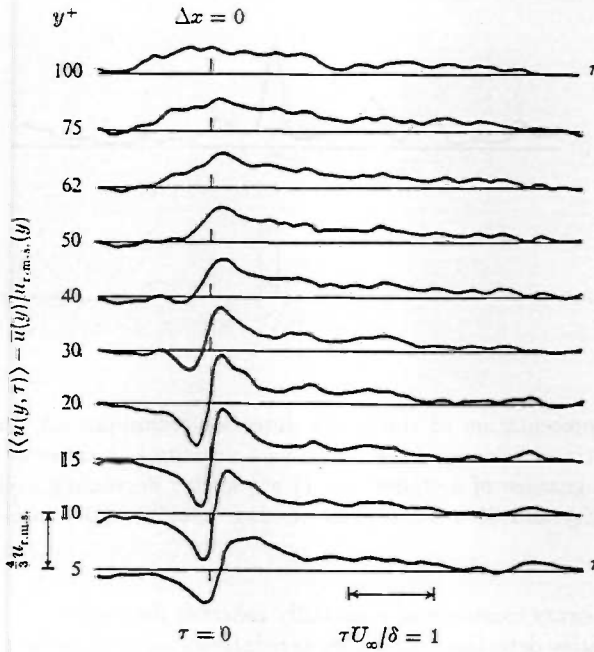
Figure 1.7: Characteristic velocity patterns in ten different positions in a turbulent boundary layer after a 'burst' was detected at $y^+ = 15$. (Blackwelder and Kaplan, 1976)
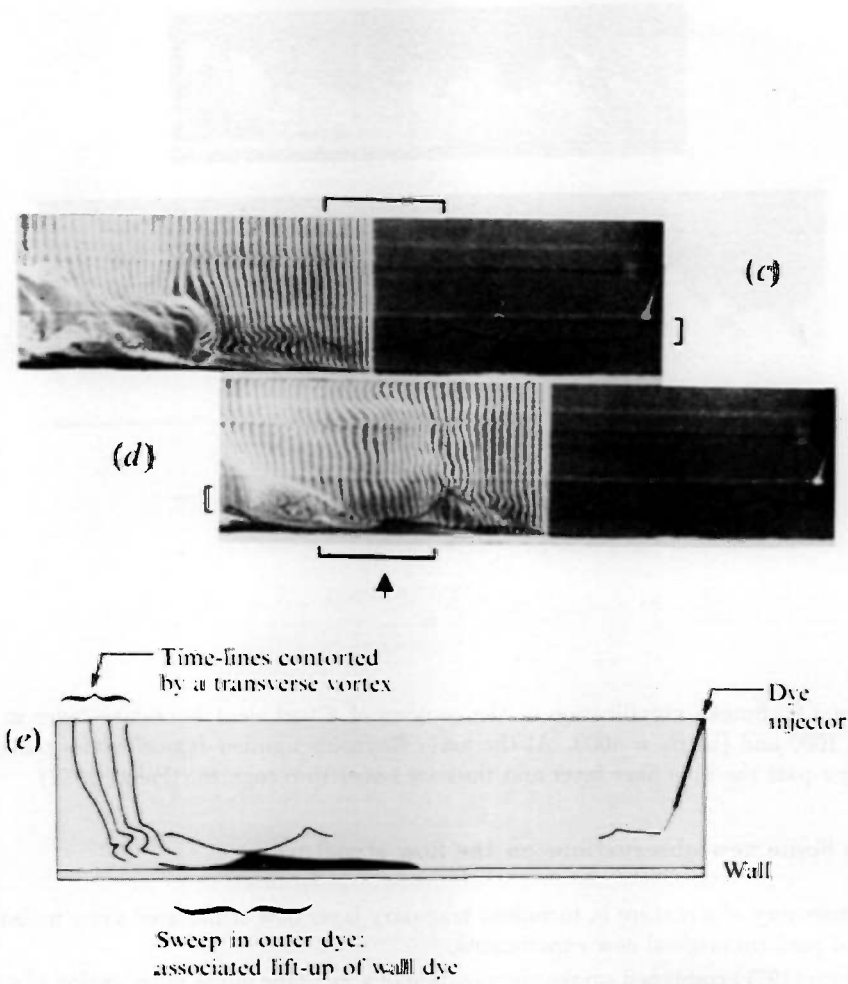
Figure 1.8: Consecutive pictures of a *sweep* and a *lift-up* as visualized using dye and vertical hydrogen-bubble time-lines. The flow is directed to the left. (Offen and Kline, 1974)
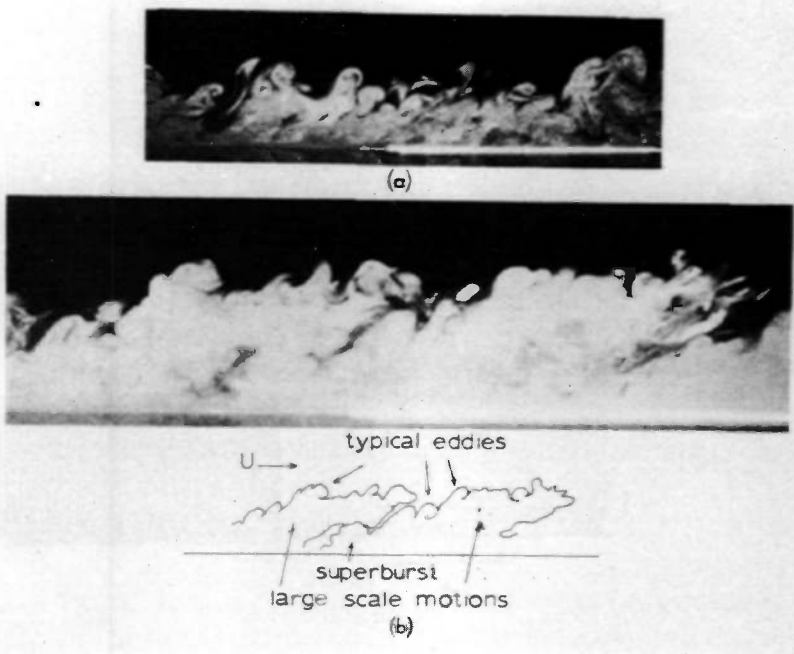
Figure 1.9: Smoke visualization of the contour of a turbulent boundary layer at (a) $R_\theta = 1000$ and (b) $R_\theta = 4000$. At the lower Reynolds number *typical eddies* make up a larger part the boundary layer and thus are easier to recognize. (Falco, 1977)

1.2.3 Some new observations on the flow structure

The discovery of structure in turbulent boundary layer flow stimulated some investigators to perform original new experiments.

Falco (1977) combined smoke visualization of a xy plane in the outer region of a turbulent boundary layer $(1000 < R_\theta < 4000)$ and two-component hot-wire anemometry. By simultaneously recording the film records and the hot-wire signals, he performed conditional sampling of the hot-wire signals to specific flow features. With the eyeball detection-technique he found that the outline of the turbulent boundary layer has the shape of *large-scale bulges*. Inside the bulges he distinguished two types of large-scale motion: those with an average speed less than the local mean (type 1) and those with an average speed greater than the local mean (type 2). At the upstream side of the bulges he visually identified coherent vortices: *typical eddies* (figure 1.9). The mushroom-shaped typical eddies contribute most to the production of Reynolds stress in the outer region. Since the frequency of the typical eddies scales with outer flow-variables, whereas their length scales with inner flow-variables, Falco hypothesized that
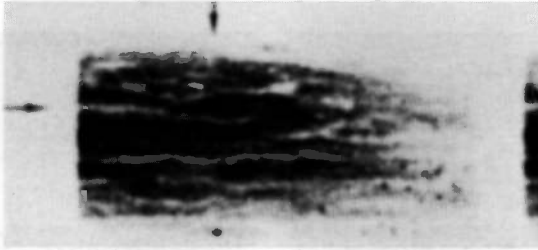
Figure 1.10: Top view of the structure of the wall layer visualized using smoke; the flow is from left to right. Two different structural elements are visible: streaks and *pockets* (located by the arrow). (Falco, 1978)

some relation exists between the structures in the wall layer and those in the outer region.

In subsequent smoke-visualization experiments, Falco (1978) visualized the xz plane of a turbulent boundary layer. He observed rapidly evolving structures whose scale is of the order of the streak spacing, and called them *pockets* (figure 1.10). Falco speculated that the pockets are the result of wall layer and outer region interactions: high-speed fluid approaches the wall, which results in the ejection of fluid out of the pocket. Furthermore, the wavy motion and break-up of low-speed streaks may be due to them being pushed around by the pockets.

Blackwelder and Eckelmann (1979) measured the streamwise and spanwise velocity components (u and v), and their gradients normal to the wall ($R_\theta = 400$). Using a splitting technique (for the velocity-vorticity correlations) and the VITA technique (for the detection of 'bursts'), they inferred that pairs of long *counter-rotating streamwise vortices* are present in the wall layer. Between these vortices a low-speed streak is present.

To provide more quantitative data on the high-speed fluid fronts associated with the sweep event described by Corino and Brodkey (1969), Kreplin and Eckelmann (1979) used hot-film sensors to measure the streamwise and spanwise velocity-components (u and w), and their gradients $\partial u/\partial y$ and $\partial w/\partial y$ at the wall in an oil channel. From simultaneous recordings of these signals they deduced that coherent flow-structures move downstream and are inclined to the wall. According to Kreplin and Eckelmann, space-time correlations implied that these structures are rotating. They also found that these structures are spaced at $50l_*$ in spanwise direction, and can be observed over a streamwise distance of at least $1000l_*$.

Using smoke and a light plane, Head and Bandyopadhyay (1981) discovered U-shaped vortex-loops in the outer region of a turbulent boundary layer (figure 1.11). These structures are arrayed at an angle of about 45° to the wall. Their cross-stream dimensions scale with the inner flow-variables, and their length seems to be limited only by the boundary layer thickness. The shape of these structures depends on the

(a)

Downstream light plane   Upstream light plane

(b)
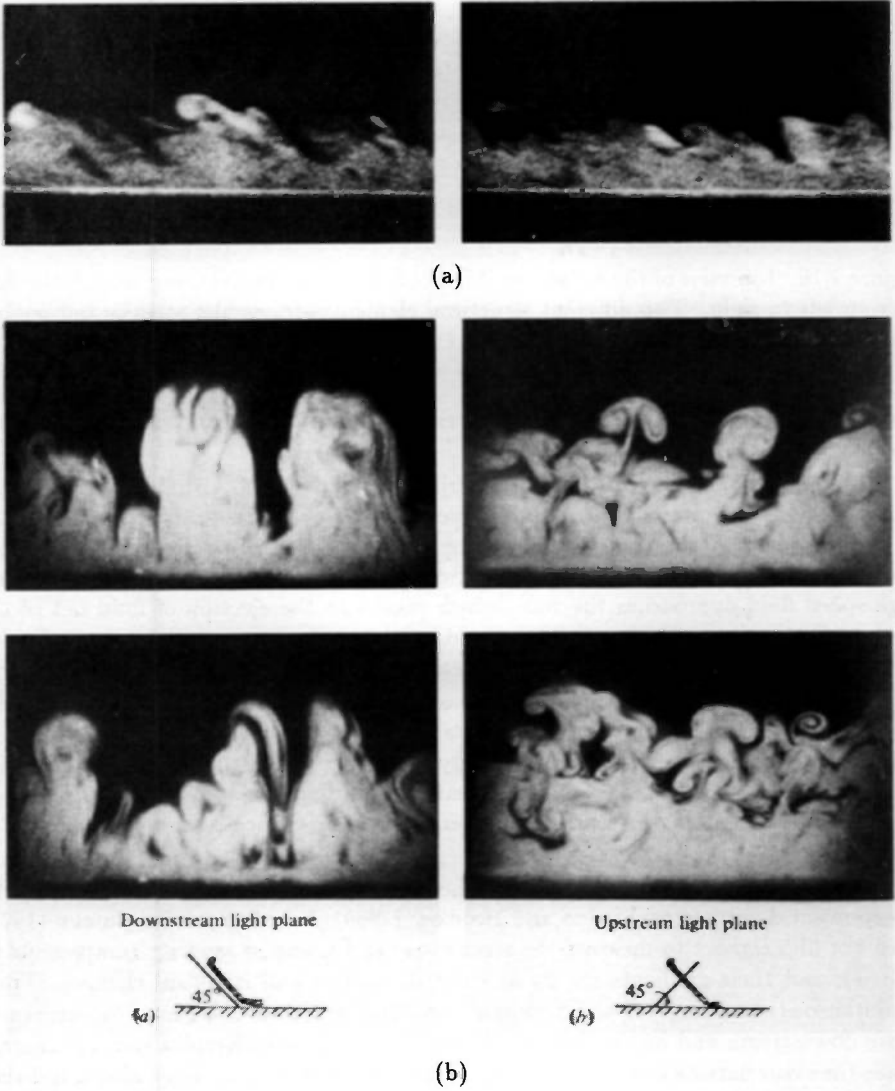
Figure 1.11: *U-shaped vortex-loops* determine the structure of the turbulent boundary layer $R_\theta \approx 600$, as is shown by smoke visualization with the light plane (a) in the xy plane, (b.a) inclined at 45° downstream, and (b.b) inclined at 45° upstream (Head and Bandyopadhyay, 1981)

Reynolds number: at low R_θ they consist of individual *vortex loops*, but at higher R_θ the loops become elongated, and appear as *horseshoes* or *hairpins*. At the highest Reynolds numbers the tips of the hairpins seem to lie on a line which makes an angle to wall less than 45°. Head and Bandyopadhyay concluded that the spacing of the streamwise streaks (as found in other studies) agrees with the cross-stream dimensions of the U-shaped vortex loops, and inferred that the occurrence of a 'burst' can be equated to the lifting of a vortex loop from the wall.

Although the types of motion presented in these investigations had not been observed before, they fit in the concept of coherent near-wall fluid motion.

1.2.4 Do different detection techniques reveal the same events?

After the discovery of non-random motion in the near-wall region of the turbulent boundary layer, various techniques (e.g. u-level, quadrant and VITA) were proposed to detect this motion in velocity traces (see section 1.2.2). A considerable amount of effort has been put in tuning these techniques such that the proper correspondence with visually observed fluid motion is obtained.

In order to compare various detection techniques (among which VITA and quadrant) to visual data, Offen and Kline (1973) combined hot-film anemometry and dye visualization at $y^+ = 15$ in a water channel flow ($R_\theta = 820$). Hardly any coincidence was found between probe detected and visually detected 'bursts'. They concluded that 'bursts' can be characterized by their spatial coherence, but may not be characterizable by a temporal record at one or two points.

The quadrant detection-technique was modified by Rajagopalan and Antonia (1982) in order to incorporate the attractiveness of quadrant decomposition with the potential of VITA to focus on the internal shear zone associated with the coherent flow structure. Their experimental results suggested that different techniques do not always detect structures with similar features. Moreover, motions which are coherent across the boundary layer and motions which contribute significantly to the Reynolds stress are not always identical. It was also found that the frequency of the ejections is nearly equal to that of the sweeps, but that, on average, a sweep does not follow an ejection, as was found by Corino and Brodkey (1969).

Using a hot-film sensor, Johansson and Alfredsson (1982) measured streamwise velocity signals, and detected deterministic events with the VITA technique. They demonstrated that this technique has a band-pass filter character: detection depends on the rate of change of the velocity, and the number of events detected decreases exponentially with the threshold level. The events occupy a wide range of time scales, which makes it impossible to define one unique frequency of occurrence or one unique duration of the events. The experiments also showed that two VITA events must be treated separately: accelerations ($\partial u/\partial t > 0$) and retardations ($\partial u/\partial t < 0$). The duration of the retardations typically is somewhat larger than that of the accelerations. Most of the events with a large amplitude nearly always correspond to accelerations.

In a subsequent study, Johansson and Alfredsson (1983) found that the number of events detected with the VITA technique depends strongly on the sensor length. They

saw this as an indirect indication for the spanwise extent of the structures associated with the 'bursting' event: ejections are laterally small, and will be greatly affected by spatial averaging over the length of a sensor, whereas sweeps, which have been observed to have a larger spanwise extension, are less affected by spatial averaging.

In order to examine the statistics and characteristics of low-speed streaks, Smith and Metzler (1983) observed in top view low-speed streaks which were visualized by hydrogen-bubble time-lines. A low-speed streak was detected when $u_{low}/u_{high} < 0.7$ (where u_{low} and u_{high} are the streamwise fluid velocity in the low and the high-velocity region, respectively). However, Smith and Metzler found that this acceptance criterion had only a weak effect on the streak-counting process. They found that at $y^+ = 5$ and for $740 < R_\theta < 5830$ the transversal streak-spacing λ_z is approximately lognormally distributed with a mean value $\lambda_z^+ \approx 100$. The streak spacing increases and its distribution becomes broader with distance from the wall. Smith and Metzler hypothesized that this effect is due to the merging of low-speed streaks. Furthermore, they found that the streaks are subject to the 'bursting' behaviour, but that generally an amount of low-speed fluid remains on the wall when a streak 'bursts'. This was observed to result in the reinforcement of the streak. Consequently, the streaks show a tremendous persistence, often maintaining themselves for time periods longer than the observed 'bursting' period.

The main objective of Smith and Schwartz (1983) was to visually verify the existence of counter-rotating streamwise vortices, whose presence was inferred from the experimental results of Blackwelder and Eckelmann (1979) and Kreplin and Eckelmann (1979). Smith and Schwartz generated hydrogen bubbles using a horizontal bubble-wire, and looked in upstream direction using a glassfiber optic lens. The bubble patterns showed that the low-speed streaks are discrete regions of outward motion (with the degree of activity varying with distance from the wall), and that rotating streamwise structures occur in the near-wall region (frequently appearing in counter-rotating pairs). It was also found that a low-speed streak is present when such a counter-rotating structure is observed.

In order to show the three-dimensional character of the flow in the near-wall region, Blokland and Krishna Prasad (1984) used transversal bubble-wires that are placed on the wall, in addition to horizontal and vertical bubble-wires. Vertical fluid motion was visualized by multi-colour illumination. They found that low-speed streaks in the wall layer have no distinct beginning or end, and, counter to the prevailing view, extend sometimes up to $y^+ = 120$, and do not break up.

Mainly to examine the effect of the sensor size on the spatial resolution of the near-wall flow events ($R_\theta = 6480$ and 9840), Willmarth and Sharma (1984) used hot wires smaller than the viscous length-scale. For 'burst' detection the VITA technique ($T = 10t_*$), with the addition of the slope detection criterion $\partial u/\partial t > 0$, was used. In order to avoid the detection of a multiple 'burst', the detection criteria were switched off following the first detection of a 'burst'. Willmarth and Sharma found that the 'bursting' frequency increases slowly with distance from the wall, reaching a maximum at $y^+ = 25$, and rapidly decreasing further from the wall. Furthermore, the 'bursting' frequency does not depend on the Reynolds number when scaled with inner flow-variables.

This result was contrary to the prevailing view at that time, but consistent with the independently obtained results of Blackwelder and Haritonides (1983). Willmarth and Sharma concluded that the VITA technique is a worth-wile method when the proper detection parameters and the proper sensor length are used.

Alfredsson and Johansson (1984) compared the VITA and the quadrant detection techniques, and found a close correspondence between VITA events and ejections detected with the quadrant method. Strong ejections often occurred at an inclination of $10°$ to the wall. A number of $u'v'$ peaks correspond only to VITA detections in the v' signal.

Bogard and Tiederman (1986) combined visualization and two-component hot-film anemometry ($R_\theta = 420$) in order to evaluate the effectiveness of various detection techniques (among which VITA, quadrant and u-level). Ejections were detected when dye in the wall layer touches the hot-film probe. The effectiveness of each of the schemes was found to be highly dependent on the threshold levels and the averaging times. Bogard and Tiederman concluded that the quadrant technique has the greatest reliability with a high probability of detecting the ejections and a low probability of false detections, provided that the optimum parameter setting is used ($H = 0.25...1.25$). Furthermore, it was found that ejections detected by the quadrant technique can be grouped into 'bursts' by analysing the probability distribution of the time between two ejections.

Simultaneous flow-visualization with hydrogen-bubble time-lines and Reynolds-stress measurements using a laser-doppler anemometer was performed by Talmon e.a. (1986). With a horizontal wire at $y^+ = 29$, they found that, at $R_\theta = 730$ and 770, the low-speed streaks are consistently longer than $490l_*$, and are $20...40l^*$ wide. They also observed an apparent disappearance and reappearance of the low-speed streaks. The disappearance of a streak was often accompanied by a *dark spot*, which is a small area within a streak from which the bubbles have disappeared (figure 1.12). From the simultaneous Reynolds-stress measurements Talmon e.a. concluded that the dark spots are related to second-quadrant events (i.e. ejections) with $(u'v')_2 > 2\overline{u'v'}$. Furthermore, they found that, on average, a low-speed streak contributes two second-quadrant events to the instantaneous Reynolds stress. Therefore, Talmon e.a. attributed detections with time intervals smaller than about $20t_*$ to the same 'burst'.

Kasagi e.a. (1986) used hydrogen-bubble clusters for the visualization of a turbulent channel flow at $R_\theta = 300$. End views of cluster patterns showed what they called streamwise pseudo-vortical motion near the wall. The diameter of each vortical structure is about $40l_*$, and their centers are located at $y^+ = 20...50$. For quantitative data reduction the cluster patterns were recorded by a movie camera. The data reduction yielded the normal and spanwise velocity components v and w, as well as the streamwise vorticity component ω_x. Near the wall the vorticity field showed quasi periodicity in the spanwise direction with the wavelength of the order of the streak spacing, and a conversion in the sign of ω_x in the region $y^+ = 15...40$.

Visualization by means of small polystyrene beads and digital image processing was employed by Utami and Ueno (1984 and 1987). With this method they obtained the three components of the velocity vector. These components were used to calculate the streamlines and the three components of the vorticity vector. Utami and Ueno
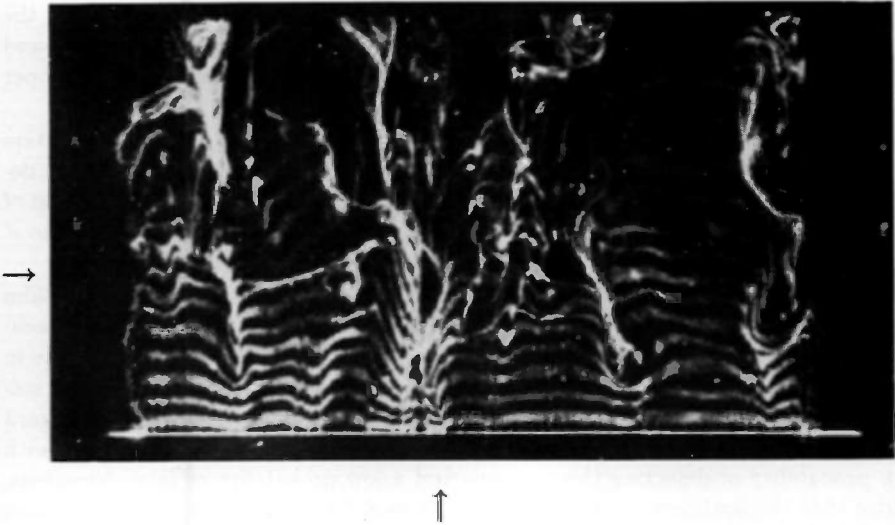
Figure 1.12: Top view of a turbulent channel flow (directed to the top). With horizontal hydrogen-bubble time-lines alternating low and high-speed streaks are visualized. A *dark spot* is indicated at the intersection of the arrows. (Talmon e.a., 1986)

concluded that the elementary unit of the coherent structure of turbulent flow near the wall is a horseshoe vortex with two trailing legs.

According to Luchik and Tiederman (1987), the second-quadrant, the VITA and the u-level techniques detect ejections. When the ejections detected with each of these techniques are grouped appropriately into 'bursts' (as proposed by Bogard and Tiederman, 1986), all of the techniques yield the same average time between 'bursts' as deduced from flow visualization. The results of the two-component laser-doppler measurements of Luchik and Tiederman showed that the inner flow-variables are the best candidates for the proper scaling of the average time between 'bursts'. The 'burst' events are closely related to slower-than-average moving fluid, moving both away from and towards the wall.

Johansson e.a. (1987) concentrated upon the buffer layer of an oil channel. They employed two hot-wire probes: a fixed probe at $y^+ = 15$ for the detection of events via the VITA technique, and a traversable probe for the examination of the detected structures. A second configuration was a traversable detector-probe in conjunction with a fixed wall shear-stress sensor. Johansson e.a. observed that *near-wall shear layers* are created due to the lift-up of low-speed streaks. From these layers a coherent flow structure developed which is confined to the wall layer (figure 1.13). The streamwise extent of the shear layer is $100l_*$, and it retains its identity over at least $500l_*$. Up to $y^+ = 30$ the streamwise propagation velocity is $13u_*$. Farther out this velocity increases and the structure becomes stretched. The shear layer is inclined to the wall

(a)

(b)
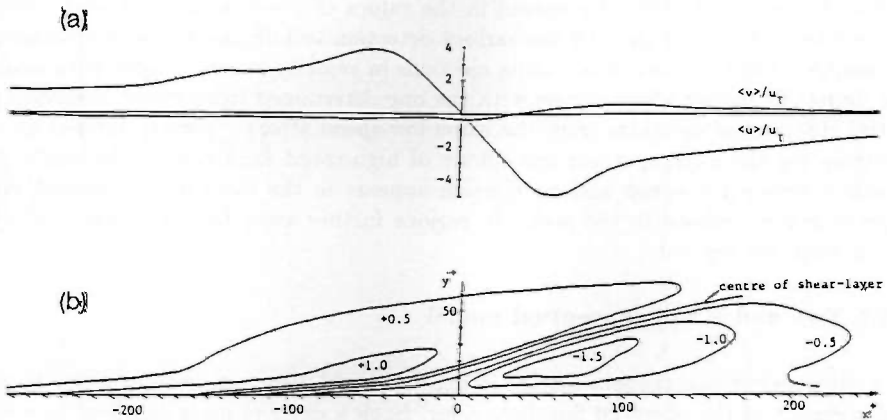
Figure 1.13: *Near-wall shear-layers* in the turbulent boundary layer. (a) Non-dimensional streamwise and normal velocity components as a function of x^+. (b) Isotachs in the xy plane. The velocities are non-dimensionized with local rms values. (Johansson e.a., 1987)

at a maximum angle of $20°$ at $y^+ = 20$ in the buffer layer.

The ejection was the subject of the study of Bogard and Tiederman (1987). An ejection was detected when a definite outward movement of a dye streak occurred near the hot-film probe. The velocity signals were averaged only for time periods during which the flow visualization indicated an ejection was in contact with the probe. Bogard and Tiederman found that some 80% of the contribution to $\overline{u'v'}$ is attributed to 'bursts' (which are closely spaced groups of ejections). The ejections are characterized by a rapid deceleration at the leading edge, followed by a strong acceleration at the trailing edge. The first ejection which occurs in a 'burst' is more intense than the following ejections. The distance between two ejection in a 'burst' is $180...230l_*$. Furthermore, Bogard and Tiederman found that the characteristics of the ensemble-averaged signals are highly dependent upon the phase alignment of the conditional samples. They concluded that the different 'burst' characteristics which are educed when different detection schemes are used, are not contradictory, but are due to phase alignment with different parts of the ejection.

The general picture which emerges from this enumeration of data is as follows. Near-wall turbulent flow is characterized by the presence of elongated regions with a lower-than-average fluid velocity: the *low-speed streaks*. Each streak is straddled by regions with *counter-rotating streamwise vorticity*. Generally, there occur *ejections* of low-speed fluid from the streaks, and several ejections from the same streak form a *'burst'*. Both the spanwise distance between low-speed streaks and the 'bursting' frequency scale with inner flow-variables. Although it is possible to determine an average streak-spacing and

'bursting'-frequency, there is a spread in the values of these parameters with respect to their respective averages. Of the various detection techniques, the second-quadrant technique is most reliable in detecting ejections in velocity traces. Essential to finding the 'burst' frequency which agrees with the one determined from visual observations, is the grouping of ejections from the same low-speed streak. Closely related to the ejections are the *sweeps*, which are inflows of high-speed fluid toward the wall. The interface between a sweep and an ejection appears in the form of an *internal shear layer* which is inclined to the wall. In regions further away from the wall *U-shaped vortex-loops* are present.

1.2.5 Two and a half conceptual model

The discovery of non-random motion in near-wall turbulence stimulated many to give a description of the observed flow-behaviour. Such a description is captured in a conceptual model. (A conceptual model gives an idealized account of the physics involved in the process under investigation.) Most of the published conceptual models present variations to the hairpin-vortex model which is originally due to Theodorsen (1955). The argument of Theodorsen is difficult to follow, but its essence is that the production and dissipation of turbulence in the near-wall region is governed by horseshoe vortices originating from near-wall regions of low-velocity fluid. In this subsection we represent the two models that seem to be the most complete in describing the observed behaviour of near-wall turbulence, and a suggestion of a mechanism by which the oscillation stage of streaks occurs.

Based on an extensive series of visualizations (e.g. Acarlar and Smith, 1984, 1987a and 1987b), Smith (1984) and Acarlar and Smith (1984) presented a cyclic model for the 'bursting' process (figure 1.14). The model cycle starts with the consideration of a *low-speed streak*, which is a concentration of low-momentum fluid. The streak grows in extent by continued accumulation of low-momentum fluid, until a disturbance originating from an earlier 'burst' impresses a streamwise pressure gradient upon it. The subsequent deceleration of the near-wall flow creates an inflectional velocity profile at the interface between the streak and the higher-speed fluid. Once an inflection develops, the streak is unstable to the small disturbances which are supplied by the background turbulence in the outer region, and the resulting perturbation in the shear layer which surrounds the low-momentum streaks leads to an oscillation of the streak. These perturbations grow by a process of concentration of vorticity, effecting in a roll-up of the shear layer. The number of vorticity concentrations per streak generally is 2 to 5. As the vortex sheet rolls up into three-dimensional vortices, the vortices take on the shape of horseshoes. Once a vortex concentration has a three-dimensional structure, Biot-Savart interactions create a self-induced movement of the head and the legs of the vortex away from the wall, and the vortex appears as a more elongated *hairpin vortex*. Since the trailing part of the legs must connect back to the vortex sheets flanking the streaks, they undergo stretching, resulting in an increase in vorticity. Due to this effect, between the legs of the hairpin vortex low-momentum fluid is accumulated and pumped away from the wall, which process maintains the streak. The stretched legs give rise to
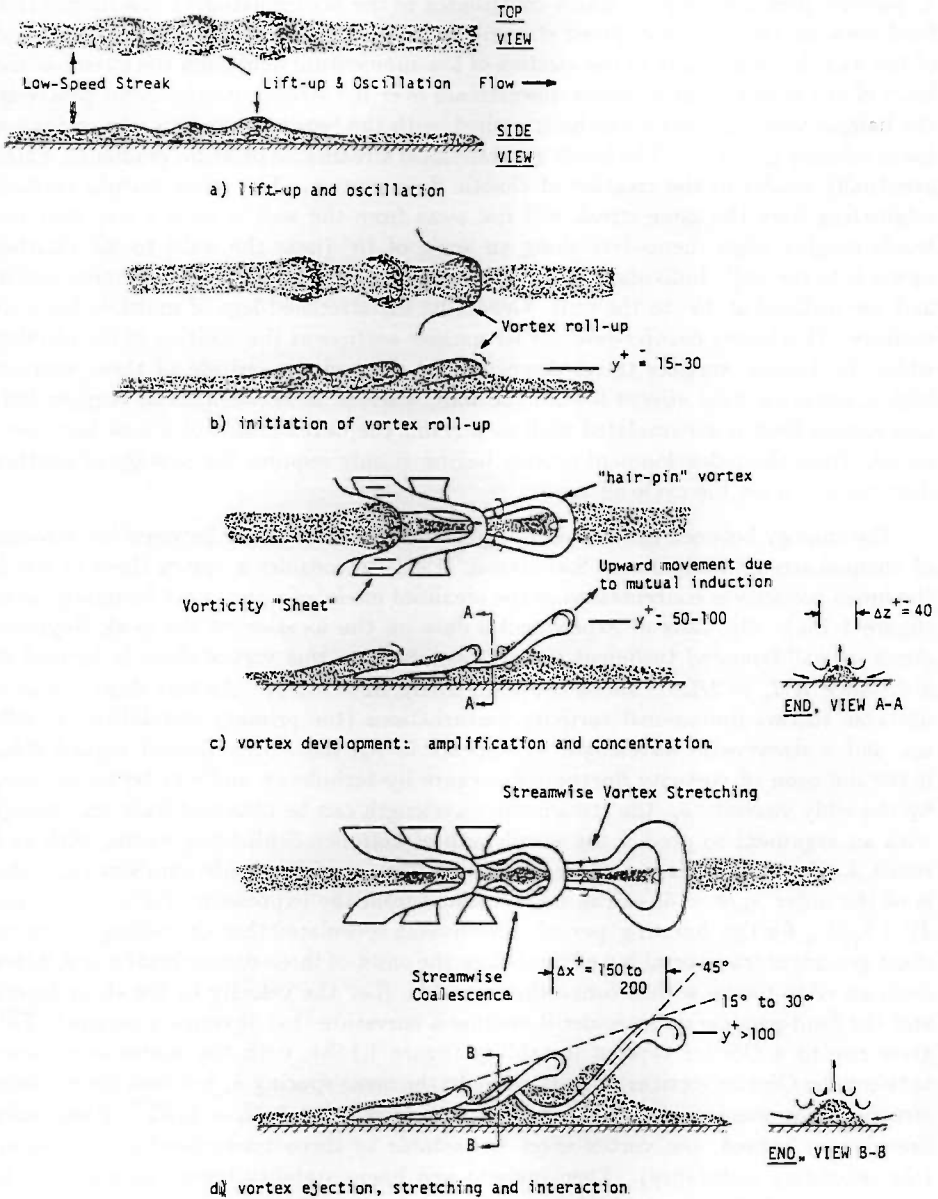
Figure 1.14: Representation of the hairpin model for the 'bursting' process, showing the creation of a hairpin vortex out of a low-speed streak. (Smith, 1984)

a spanwise pressure gradient which contributes to the accumulation of low-momentum fluid between the legs. A confined streamwise pressure gradient is created by the head of the hairpin, and results in the *ejection* of low-momentum fluid from the streak as the head of the hairpin vortex moves downstream over the streak. As the event proceeds, the hairpin vortices continue to be stretched, with the heads moving up into regions of lower velocity gradients. The heads generate local streamwise pressure gradients, which eventually results in the creation of chaotic fluid motion. The other hairpin vortices originating from the same streak will rise away from the wall in such a way that the heads roughly align themselves along an angle of 15° (near the wall) to 30° (farther upward) to the wall. Individual hairpins develop along the direction of maximum strain, and are inclined at 45° to the wall. Generally, the stretched legs of multiple hairpins coalesce. This leaves *counter-rotating streamwise vortices* at the position of the ejection while the hairpin vortices travel downstream. Around the outside of these vortices high-momentum fluid *sweeps* toward the wall, whereas in between these vortices low-momentum fluid is accumulated with as a result the development of a new low-speed streak. Once the redevelopment process begins, it only requires the passage of another disturbance to set the cycle off again.

The analogy between the near-wall region and the mixing layer between two streams of unequal strength stimulated Sreenivasan (1988) to consider a vortex sheet in which the mean vorticity is concentrated as the idealized model of a turbulent boundary layer (figure 1.15a). On basis of experimental data on the location of the peak Reynolds stress in wall-bounded turbulent flow, he argued that this vortex sheet is located at a distance $H/l_* = 2R_*^{-1/2}$ above the wall, where $R_* = u_*\delta/\nu$. As this sheet becomes unstable to two-dimensional vorticity perturbations (the primary instability), it rolls up, and a streamwise wavelength λ_x appears in the flow. Sreenivasan argued that, if the diffusion of vorticity fluctuations occurs by turbulence and can be represented by the eddy viscosity ν_e, the streamwise wavelength can be obtained from an analogy with an argument to predict the wavelength of Tollmien-Schlichting waves, with as a result $\lambda_x/\delta = 1.3\nu U_\infty/\nu_e u_*$. Over a significant range of Reynolds numbers this ratio is of the order $\lambda_x/\delta = 5$, as can be calculated from the expressions $T_b U_\infty/\delta = 5$ and $T_b = \lambda_x/U_\infty$ for the 'bursting' period. Sreenivasan speculated that the rolling-up vortex sheet generates transversal big eddies before the onset of three-dimensional instabilities. Such an eddy moves with a convection speed U_c (i.e. the velocity in the shear layer), and the fluid-particle paths under it assume a curvature that is concave upward. This gives rise to a Görtler type of instability (figure 1.15b), with the spanwise distance between the Görtler vortices corresponding to the mean spacing λ_z between the sublayer *streaks*. Using some assumptions, Sreenivasan inferred that $\lambda_z/l_* = 42R_*^{1/6}$. Eventually, Sreenivasan argued, the vortex sheet is unstable to three-dimensional perturbations (the secondary instability). Then inviscid and linear stability theory shows that the growth rates of those perturbations are largest for two distinct spanwise wavelengths: $\lambda_{z1}/\delta = 1.7R_*^{1/2}$ and $\lambda_{z2}/H = 17$. Since this implies that the rolling-up vortex sheet gets kinked on two distinct scales, two distinct scales of Λ-shaped vortices are created. Sreenivasan hypothesized that the smaller of the two wavelengths (λ_{z1}) corresponds to *hairpin vortices*, whereas the larger (λ_{z2}) corresponds to *counter-rotating vortices*.

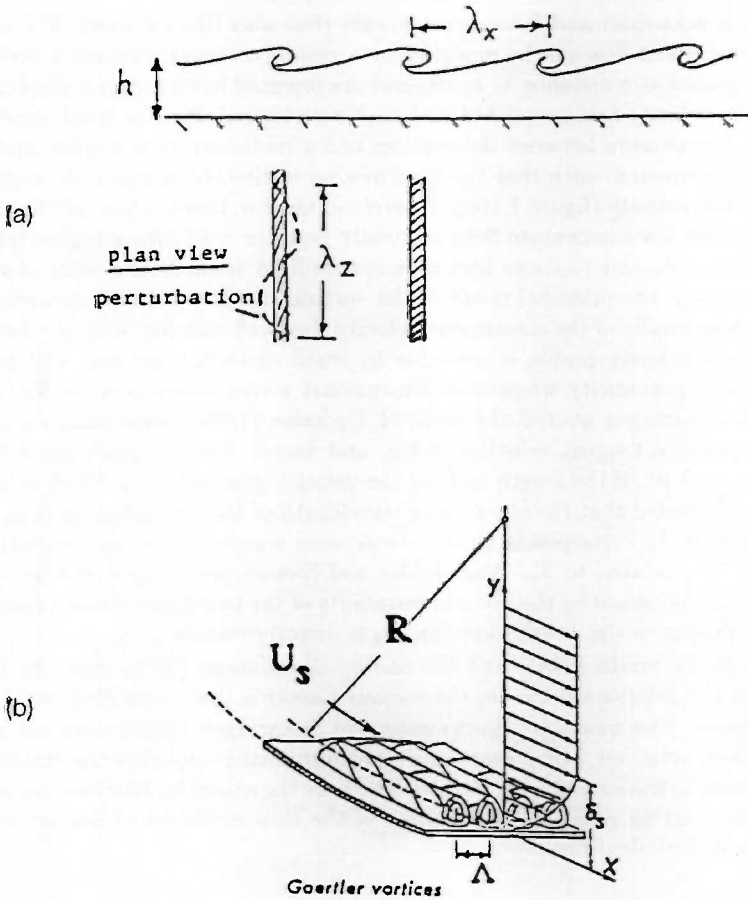Figure 1.15: (a) A vortex sheet as the idealized model of the turbulent boundary layer. Due to primary and secondary instabilities, perturbations appear with a streamwise wavelength λ_x and a spanwise wavelength λ_z. (b) Görtler vortices are created from upward moving fluid particles with concave upward particle paths, which gives rise to the creation of streaks. (Sreenivasan, 1988)

Sreenivasan concluded that the vortex-sheet model provides a rough but self-consistent description of several aspects of near-wall turbulence.

According to Blackwelder and Swearingen (1989) (but also Blackwelder, 1978 and 1983), near-wall turbulent flow can be modelled by a system of counter-rotating vortex pairs, which are spaced at a distance λ_z apart, and are oriented in streamwise direction (figure 1.16a). The velocity field associated with such a vortex pair has a normal velocity component with a maximum between the vortices and a minimum at the sides, and a spanwise velocity component such that the fluid motion is directed towards the region of maximum normal velocity (figure 1.16b). Therefore, the combined action of the two vortices is to displace low-momentum fluid originally near the wall into a region lying in between the vortices, and to move high-momentum fluid towards the sides of the vortices. Consequently, the principal result of the vortical motion is that it creates an inflectional spanwise profile of the streamwise velocity. Inviscid stability analysis shows that an inflectional velocity profile is unstable to small disturbances, and will give rise to a streamwise periodicity whose non-dimensional wavenumber is $\alpha_r = 2\pi/\lambda_x$. Blackwelder and Swearingen quoted the work of Michalke (1965), who analysed the stability of a hyperbolic-tangent velocity profile, and found that the most amplified wavenumber is $\alpha_r = 0.40$. If the length scale of the velocity gradient is Δ, Blackwelder and Swearingen concluded that the streamwise wavelength of the perturbation is $\lambda_x = 5\pi\Delta$. Assuming that λ_x corresponds to the streamwise wavelength of an oscillating *streak*, and that Δ is related to λ_z, Blackwelder and Swearingen suggested that the oscillation of a streak is caused by the inviscid instability of the two-dimensional velocity gradient that accompanies the streak, and that λ_x is directly related to λ_z.

Both the model by Smith (1984) and the one by Sreenivasan (1988) describe the dynamics of, and the relations between, the various elements that were discovered in near-wall turbulence. The model by Blackwelder and Swearingen (1989) does not account for all of these relations, but presents a simple argument to describe the stability of a low-speed streak in the xz plane. In chapter 3 we take the model by Blackwelder and Swearingen as the starting point of a description of the time-evolution of low-velocity regions in near-wall turbulent flow.

1.2.6 A shift of focus toward the spatial structure

In the first years of near-wall turbulence research most of the studies were aimed at a description of the spatial structure of the flow. Thereafter most of the experimental work was directed at the comparison of the various detection techniques, which resulted in knowledge on the temporal structure of the flow. Recently, some studies appeared which address the spatial structure again.

To measure instantaneous $u(y)$ and $u(z)$ profiles, Blackwelder and Swearingen (1989) used multiple hot-wire probes spanning the normal and spanwise (y and z) directions in a turbulent boundary layer ($R_\theta = 2200$). In both types of velocity profile numerous inflection points (i.e. points where $\partial^2 u/\partial^2 z = 0$) are present. By sampling the shear at the points of inflection, Blackwelder and Swearingen obtained the conditional probability of the shear rate. The distribution of the normal shear $\partial u/\partial y$ is asymmetrical
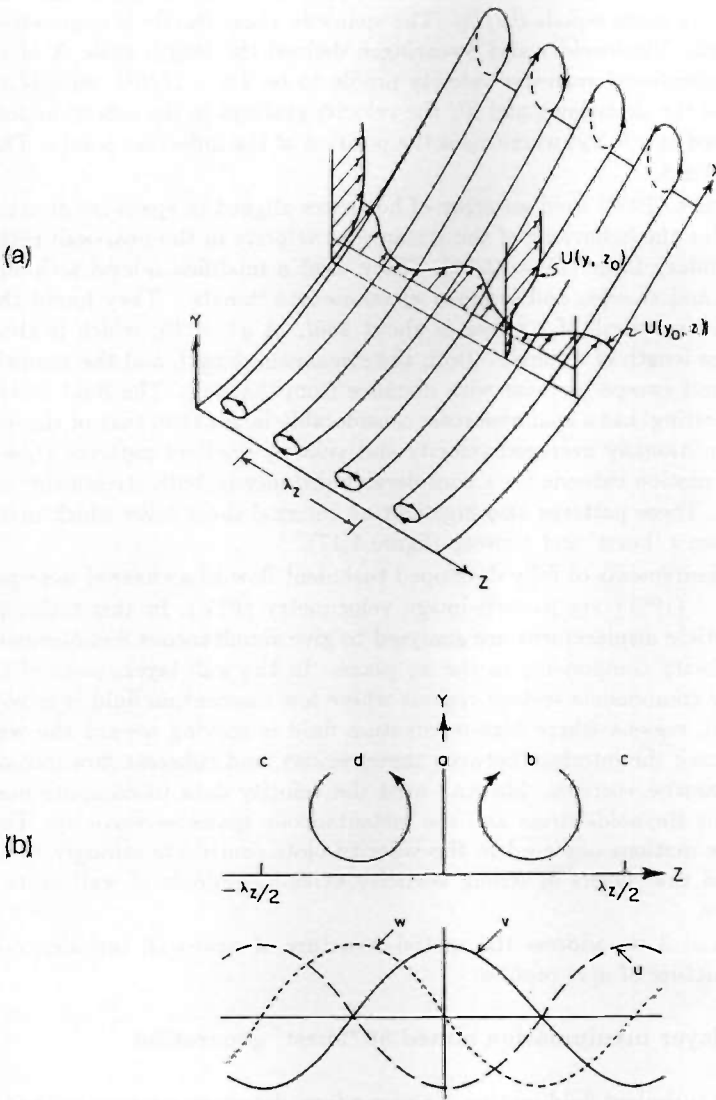
Figure I.16: (a) A system of streamwise vortices as the model of the flow in the near-wall region. The combined action of the vortices is to accumulate low-momentum fluid. (b) The velocity components as a function of the spanwise coordinate below a pair of streamwise vortices. (Blackwelder and Swearingen, 1989)

because of the mean shear in y direction. The most probable value of this shear is approximately 0, and its mean equals $\partial U/\partial y$. The spanwise shear $\partial u/\partial z$ is symmetrical and has a dual peak. Blackwelder and Swearingen defined the length scale Δ of the shear layer in an inflectional spanwise velocity profile to be $2\Delta = \mathcal{U}/\partial U$, with $\mathcal{U}$ the velocity difference in the shear layer and ∂U the velocity gradient in the inflection point (i.e. $\partial U/\partial z$ evaluated at $z = z_E$, where z_E is the position of the inflection point). They found that $\Delta^+ = 10 \pm 5$.

Antonia and Bisset (1990) used an array of hot wires aligned in spanwise direction in order to determine the behaviour of the streamwise velocity in the near-wall region of a turbulent boundary layer ($R_\theta \approx 2200$). They used a modified u-level technique to detect ejections and sweeps, and grouped ejections into 'bursts'. They found that the average streamwise length of a sweep is about $960l_*$ at $y^+ = 15$, which is about twice as large as the length of a 'burst'. Both the streamwise length and the spanwise extent of 'bursts' and sweeps increase with distance from the wall. The fluid motion associated with 'bursting' has a spanwise scale considerably larger than that of the low-speed streaks. Conditionally averaged velocity and velocity-gradient patterns showed that the organized motion extends for a considerable distance in both streamwise and spanwise direction. These patterns also highlight an internal shear layer which marks the interface between a 'burst' and a sweep (figure 1.17).

Whole-field measurements of fully developed turbulent flow in a channel were performed by Liu e.a. (1991) via particle-image velocimetry (PIV). In this technique photographs of particle displacement are analysed to give simultaneous measurements of the u and v velocity components in the xy plane. In the wall layer, plots of the fluctuating velocity components feature regions where low-momentum fluid is moving away from the wall, regions where high-momentum fluid is moving toward the wall, shear layers that mark the interface between these regions, and coherent flow-motions associated with spanwise vortices. Liu e.a. used the velocity data to compute maps of the instantaneous Reynolds-stress and the instantaneous spanwise vorticity. They found that the flow-motions observed in the velocity plots contribute strongly to the Reynolds-stress and that layers of strong vorticity extend hundreds of wall units in streamwise direction.

In chapters 2 and 3 we address the spatial structure of near-wall turbulence by considering the structure of $u(z)$ profiles.

1.2.7 Boundary-layer manipulation aimed at 'burst' generation

Although near-wall turbulent fluid-motion is non-random, detection schemes applied to velocity signals generally have failed to produce the characteristics of the coherent flow structure that is supposed to cause the observed events. This is mainly due to the fact that the hypothesized coherent flow structures appear randomly in a specific measuring position, and therefore are in different stages of development when detected. Evidently, no detection scheme is able to determine in which stage of development a structure is when it is detected, with as a consequence that any averaging procedure will yield a characteristic of the structure which is smeared out in phase. In order to remove this
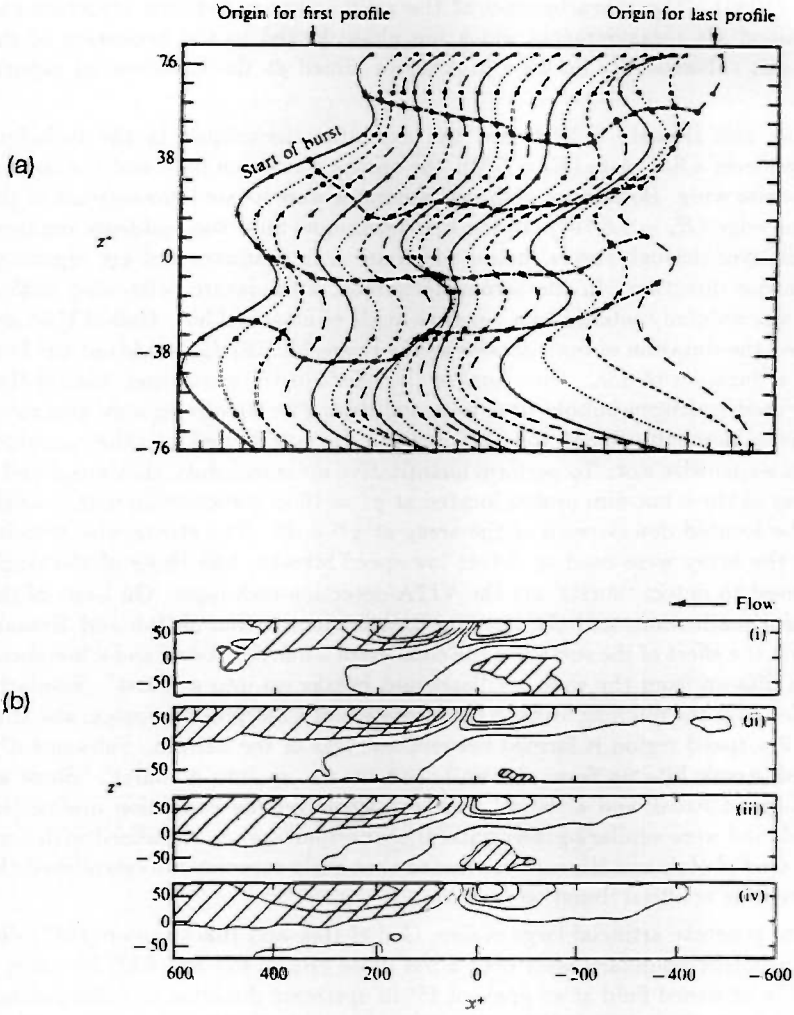
Figure 1.17: (a) Consecutive instantaneous spanwise profiles of the streamwise velocity during a 'burst'. The time step is $1.08t_*$. (b) The characteristic patterns of the streamwise fluid velocity at the beginning of a 'burst' at (i) $y^+ = 10$, (ii) $y^+ = 15$, (iii) $y^+ = 30$, and (iv) $y^+ = 40$. (Antonia and Bisset, 1990)

deficiency, the concept of artificially generated 'bursting' was introduced by Gad-el-Hak and Hussain (1986). The characteristics of the artificially created flow structure can then be obtained via measurements which are phase locked to the excitation of the 'burst', and can subsequently be used in schemes aimed at the detection of natural 'bursts'.

Gad-el-Hak and Hussain (1986) used two excitation techniques in the turbulent boundary layer over a flat plate ($R_\theta = 520$): the abrupt suction of fluid and the sudden pitching of a delta wing. Both types of 'burst' generator were located downstream of the plate's leading edge ($R_x = 1.6 \; 10^5$). In the first technique, fluid was suddenly removed from the wall layer through several holes, which are l_* in diameter and are separated $100l_*$ in spanwise direction. In the second technique, a miniature delta-wing with a span of $80l_*$ was suddenly pitched to a negative angle of attack of 30°. Gad-el-Hak and Hussain varied the duration of both actions in the range 10...167 t_*, but found the best results with a duration of $15t_*$. To visualize the effect of the excitation, Gad-el-Hak and Hussain used hydrogen-bubble time-lines and dye. The time-lines were generated either parallel or perpendicular to the wall, and the dye was seeped into the boundary layer through a spanwise slot. To perform quantitative measurements, they employed a spanwise array of three hot-film probes located at $y^+ = 10$ in combination with a single hot-film probe located downstream of the array at $y^+ = 20$. The streamwise velocity signals from the array were used to detect low-speed streaks, and those of the single probe were used to detect 'bursts' via the VITA-detection technique. On basis of the results of the visualizations and the hot-film measurements, Gad-el-Hak and Hussain concluded that the effect of the suction is the creation of a hairpin vortex and a low-speed streak which lifts up from the wall, oscillates and breaks up into a 'burst'. Similarly, they concluded that the pitching leads to the formation of a hairpin-like vortex, and that an unstable low-speed region is formed between the legs of the hairpin. Subsequently, the low-speed streak lifts up from the wall, and breaks up into a 'burst'. Since an artificial low-speed streak and a 'burst' appeared whenever the excitation mechanism was activated, and were similar to their natural counterparts when visualized with time lines or dye, Gad-el-Hak and Hussain concluded that their experiments established the proof-of-concept of artificial 'burst' generation.

In order to generate artificial large eddies, Gad-el-Hak and Blackwelder (1987) disturbed the turbulent boundary layer over a flat plate ($R_\theta = 455$ and 632) by using a cyclic jet. This jet issued fluid at an angle of 45° in upstream direction to collect turbulent fluid for a finite time period. When the jet was turned off, all of the collected fluid was released instantaneously in one large eddy that convected downstream. The flow was visualized by either mixing dye with the fluid to be issued from the injection slot or seeping dye from a second spanwise slot located further downstream. To measure the streamwise velocity component, hot-film probes were employed. With an injection velocity of approximately U_∞ and a perturbation frequency U_∞/δ (which is the one of the naturally occurring large eddies), Gad-el-Hak and Blackwelder found that large eddies qualitatively similar to the natural ones were produced. Furthermore, on basis of the flow visualization and 'burst' detection via the VITA technique, they concluded that an artificially generated eddy seems to trigger a 'burst'-like event in the wall region (figure
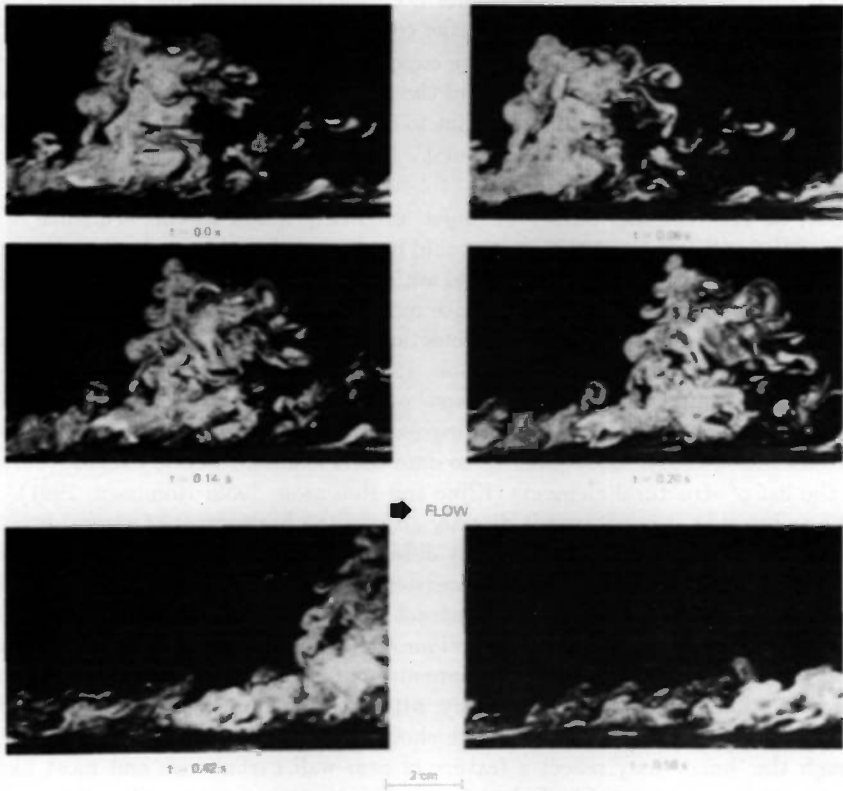
Figure 1.18: A 'burst'-like event in a turbulent boundary layer, triggered by the passing of an artificially generated large eddy. (Gad-el-Hak and Blackwelder, 1987)

1.18). These 'bursting' events are phase-locked with the trailing edge of the artificial eddies, and, consequently, appear more regularly than the natural 'bursts'. Gad-el-Hak and Blackwelder concluded that their disturbance mechanism is capable of producing periodic structures in both the outer and the inner region of a turbulent boundary layer.

The concept of the artificial generation of periodic fluid motion is the topic of chapter 4 of this thesis.

1.3 Evaluation of the knowledge and objectives of this study

In the evaluation of the knowledge on the structure of near-wall turbulence, it is essential to consider three levels of knowledge: the experimental results (i.e. the data), the

interpretation of the experimental results (i.e. the inferences), and the model which relates the data and the inferences (i.e. the coherent view).

Of primary concern in evaluating the experimental results is the question whether a specific result is a fact (i.e. a feature of the flow) or an artefact (i.e. a feature of the investigative technique). To illustrate that to date this point is not clear, we give three examples, respectively involving the 'burst', the counter-rotating streamwise vortices and the low-speed streak.

First, we consider the 'burst'. A 'burst' originally was a specific sequence of dye-streak motions (Kline e.a., 1967) which could hardly be related to probe detected events (Offen and Kline, 1973). However, several authors claimed that 'bursts' can be detected in velocity traces (see section 1.2.4). Since most of these authors used different 'burst' definitions, and consequently different detection techniques, the usefulness of 'bursting' is questionable (Johansson and Alfredsson, 1982; Robinson, 1991). Moreover, some of the techniques are deficient: e.g. the 'burst' period found by Rao e.a. (1971) is a function of the threshold-discriminator setting (see Lu and Willmarth, 1973; Blackwelder and Haritonides, 1983). Consequently, to date there is a tendency to exclude 'bursting' from the list of structural elements (Kline and Robinson, 1989; Robinson, 1991). May this be as brave as it is because it directly attacks the brainwaves of several investigators, it does not address the question why different detection techniques gave consistent results. Our point of view is that this consistency is due to the availability of detection parameters (e.g. the hole size in the quadrant technique, but also the algorithm which groups ejections into 'bursts' in the technique of Bogard and Tiederman (1986)), whose setting is not dictated by physical arguments, but by the willingness to confirm the findings of other investigators. Obviously, with creative data handling one can always obtain such a result, but it is what one should not do. We therefore conclude that although the 'burst' may reflect a feature of near-wall turbulence, and most likely is related to the production of turbulent kinetic energy, it is not a significant measure of near-wall turbulence.

As a second example we consider the counter-rotating streamwise vortices, whose existence was inferred from near-wall velocity measurements (Blackwelder and Eckelmann, 1979) and hydrogen-bubble flow-visualization (Smith and Schwartz, 1983). Unfortunately, the evidence for the existence of these vortices is weak because the symmetry found by Blackwelder and Eckelmann is due to a symmetry in their measurement technique (Blackwelder and Swearingen, 1989; Robinson, 1991), and the conclusion of Smith and Schwartz seems to be based more on the desire to validate Blackwelder and Eckelmann's result than on a fair evaluation of their own data. Moreover, Runstadler e.a. (1963), who were keen to detect streamwise vorticity in low-speed streaks, were forced to conclude that there is no clear evidence of vorticity in a streak. This example therefore shows that a defective measurement technique may lead to an erroneous interpretation, which subsequently confuses other investigators. Moreover, it shows that opposite views may exist regarding the role of a specific fluid motion and, consequently, a conceptual model may be based on only a selection of the available data.

As a final example we consider the low-speed streaks. Since the initial near-wall experiments (Kline and Runstadler, 1959) the prevailing interpretation has been that

these streaks are elongated regions with slower-than-average-moving fluid. However, what one sees if one visualizes the near-wall region is the convergence of fluid marker (either dye or time lines), and the presence of elongated low-velocity regions is a possible mechanism for the convergence of the fluid marker. That this explanation might not be clear was shown by Morrison e.a. (1971), who reasoned that the convergence of fluid marker is caused by sublayer waves. However, as indicated, the low-velocity region interpretation is the prevailing one although it has never been critically evaluated; to the best of our knowledge the streak advocates have never referred to the alternative view of Morrisson e.a. Furthermore, the popular view is that the streaks are spaced at approximately 100 wall units apart. The origin of this deceptive idea is the investigation of Schraub and Kline (1965), who experimentally found that two spanwise scales exist in the near-wall region: the spanwise distance $80l_*$ between convergence zones as determined with the counting scheme of Runstadler e.a. (1963), and the spanwise distance $130l_*$ between low-velocity regions in spanwise velocity profiles as it follows from a spatial spectral-analysis of these profiles. If one assumes that these different values are equivalent (and that is what Kline e.a. (1967) did), one finds an average streak spacing of the order of $100l_*$. Clearly, this result is a direct consequence of the hypothesis that Kline e.a. wanted to prove, and not an independently established experimental result on the observed phenomena. Moreover, it is not clear what is a streak and what is not: Smith and Metzler (1983) could not reproduce the mean spacing of $100l_*$ without the use of an acceptance criterion, whereas Kline e.a. did not use one. May this be as serious as it is, any emphasis on the value $100l_*$ masks that in reality a band of spacings characterizes the near-wall flow (Schraub and Kline, 1965). Finally, the popular view is that the convergence zones are subject to the 'bursting' process. But, who established the proof that the convergence zones are equivalent to the dye streaks, and are therefore subject to the same kind of fluid motion? Both Kline e.a. (1967) and Kim e.a. (1971) want us to believe that these are equivalent, but in our opinion this statement is a hypothesis and not a fact.

These three examples show that data might not be correct, inferences might not be appropriate, and opposite views may exist. This is a point of considerable interest because if the data and the interpretations are wrong, the concept of coherent near-wall turbulence is erroneous and misleading. In fact, this is the ultimate consequence of the proposal of Kline and Robinson (1989) to re-evaluate the knowledge on near-wall turbulence; however Kline and Robinson failed to reach this consequence for reasons unknown. Even so, at the moment it is too early to decide on the significance of the concept of coherent motion in the turbulent boundary layer. In this thesis it is therefore assumed that the knowledge on the structure of the turbulent boundary layer is reliable and significant.

Taking into account these considerations, we think that up to now coherent-structure investigations have been hampered by three factors: the limitations of flow-visualization and probe measurements, the lack of a deterministic model, and the random occurrence of the coherent motions in a specific position.

Although flow visualization provides knowledge on the spatial extent of the flow structures, it is necessarily qualitative in character. On the other hand, probe measure-

ments yield quantitative temporal data, which however is limited to one (or at most several) spatial positions. Time-line flow-visualization combines the best of the two, and enables velocity profiles to be measured. Traditionally, the evaluation of time-line images was a laborious task, but this has changed since the emergence of digital image processing techniques. This re-opens the door to experiments on the structure of spanwise profiles of the streamwise velocity. In particular, it presents an opportunity to compare the results with the findings of e.g. Kline e.a. (1967), and determine both the temporal and the spatial structure of the coherent fluid motions.

Secondly, there is no theory which rigorously explains whether the boundary-layer equations for the mean and the fluctuating velocity components have quasi-periodic and/or coherent solutions, and if so, what is the character of such a solution. Similarly, there is no theory which explains what happens to a given structure as it is exposed to the flow conditions in a turbulent boundary layer. These are severe limitations because they imply that many an interpretation of experimental results is pure conjecture, and limit the application of the concept of coherent motions to flows of practical interest. May a complete deterministic model be far away, a simple model which captures the essential physics will be as useful in explaining why things work as they do. In particular, we think that the ideas of Blackwelder and Swearingen (1989) on the stability of low-velocity regions may provide the basis of such a simple model.

Finally, most coherent motions have escaped detailed observation because they appear randomly in a specific measuring position. This causes a smearing of their characteristics, which results in a frustration of schemes aimed at their detection. However, in principal, it should be possible to artificially generate coherent flow motion (Gad-el-Hak and Hussain, 1986; Gad-el-Hak and Blackwelder, 1987). This should force the quasi-periodic motions to be in a location where their signature can be captured at controlled times.

If these factors can be addressed properly, it might be possible to measure and predict coherent motions, and, consequently, come to an understanding of some of the mysteries of near-wall turbulent flow. Therefore, the objectives of this study are to

- Develop a technique which measures at consecutive time instants spanwise profiles of the streamwise fluid velocity (chapter 2),

- Evaluate the structure of spanwise profiles of the streamwise fluid velocity (chapter 2),

- Determine the evolution in time of the flow in the low-velocity regions (chapter 3),

- Develop a model which describes the time-evolution of the low-velocity regions (chapter 3),

- Develop a method by which non-random fluid motion can be generated artificially (chapter 4).

Chapter 2

The spanwise structure of a turbulent boundary layer

The hydrogen-bubble time-line technique is a useful method to measure mean fluid-velocities in regions not too close to (i.e. more than, say, 15 wall units above) the wall of a turbulent boundary layer. However, it fails when it is used to measure mean fluid velocities close to the wall, and velocity variances in the entire boundary layer. Moreover, its reliability is poor because of the intrinsic errors; especially those due to the presence of the bubble-generating wire and the velocity gradient in the flow.

The structure of near-wall turbulence is expressed in length scales based on the positions of the velocity extremes and inflection points in spanwise profiles of the streamwise fluid velocity. It appears that near-wall turbulence is spatially quasi-periodical with the mean values representing a range of values. The numerical values of these length scales are different from the generally accepted ones: e.g. the mean distance between low-velocity regions is 70 rather than 100 wall units, and on average the low-velocity regions are as wide as the high-velocity regions.

2.1 The quantitative analysis of hydrogen-bubble time-lines

The hydrogen-bubble technique has been used extensively in studying the structure of the turbulent boundary layer (e.g. Kline and Runstadler, 1959; Kline e.a., 1967; and Smith and Metzler, 1983). In some studies the hydrogen bubbles were only used to visualize the flow, and the conclusions of these studies are, consequently, qualitative and for a great deal subjective. Other studies were aimed at a quantitative analysis by employing hydrogen-bubble time-lines (Schraub e.a., 1965). In particular, spanwise profiles of the streamwise fluid velocity can be measured by dividing the displacement of the time line in a time interval through the time interval, and by compensating for the effects of the wake of the bubble-generating wire and the velocity gradient in the boundary layer.

In this chapter we present a method to measure spanwise profiles of the streamwise fluid velocity, and evaluate the structure of these profiles. First, we address the fundamentals of the hydrogen-bubble technique (section 2.2), and formulate a correct estimate of the fluid velocity based on the displacement of hydrogen-bubble time-lines (section 2.3). Then we present our technique to digitally process time-line images, and test its performance by comparing velocity means and variances obtained with time lines with those obtained with a hot-film sensor (section 2.4). We use this technique to express the structure of a turbulent boundary layer in four length scales that can be identified in spanwise profiles of the streamwise velocity (section 2.5). Finally, we evaluate the use of hydrogen-bubble time-lines (section 2.6).

2.2 The hydrogen-bubble technique revisited

2.2.1 Synopsis of the technique

For the synopsis of the hydrogen-bubble technique we follow closely the description by Merzkirch (1987, pp. 69...75). The hydrogen-bubble technique is based on the electrolysis of water. If a voltage is applied between two electrodes in water, hydrogen bubbles are formed at the cathode (negative pole) and oxygen bubbles at the anode (positive pole). Since the hydrogen bubbles are smaller than the oxygen bubbles, the hydrogen bubbles suit best as tracers. If the cathode is a thin wire placed normal to the mean flow, and if a short voltage pulse is applied, a row of bubbles (generally called bubble line) is formed along the wire. This bubble line is carried away with the flow, and deformed according to the local velocity profile. By pulsing the voltage at constant time intervals, successive bubble lines are produced. In the flow these lines mark curves separated by a constant time interval. Since their position coincided at a given instant with the position of the wire, the bubble lines are time lines. Each time line is a measure of the local velocity profile integrated over the time lapse since the generation of the time line, but does not provide information about the trajectories of fluid elements.

Generally, the wires are made of platinum or stainless steel, and have diameters of the order of 10...70 μm. As a rule for such small wires, the bubble size is of the order of the diameter of the wire. However, the bubble size also depends on other parameters, e.g. the conductivity and the hardness of the water, and the magnitude and the duration of the voltage pulses. Usually, the 'quality' of the generated bubbles deteriorates after a few minutes of continuous operation, presumably as the result of the deposition of contaminating materials at the wire. This can be corrected by reversing the polarity in the electric circuit for a few seconds.

Two effects diminish the usefulness of hydrogen bubbles as fluid markers. First, although the overall flow pattern is not seriously disturbed by the wire, the local flow field is changed by the wake of the wire. If the bubbles move in this wake, they experience a velocity defect with respect to the undisturbed velocity (i.e. the fluid velocity in the absence of the wire). The magnitude of the wake defect will be large at short distances behind the wire. Second, the bubbles rise in the fluid due to buoyance. If the bubbles are small, the Reynolds number associated with their rising motion is low, and the terminal rise velocity v_r is determined by Stokes law. As a rule of thumb, $v_r = gd^2/12\nu$, with g the acceleration of gravity, d the diameter of the wire, and ν the kinematic viscosity of the fluid. The rise velocity causes the bubble motion to be different from the motion of fluid elements. This can lead to a velocity surplus in an estimate of the fluid velocity if the bubbles travel in a flow region with a large velocity gradient in the direction of the rise velocity.

Another factor which restricts the usefulness of hydrogen bubbles is that the period of time during which the bubbles can be observed is limited by the dissolution of the hydrogen in the flow. Diffusion of the bubbles is very rapid in turbulent flows, especially if the bubbles are small. Clearly, this limits the use of the hydrogen-bubble technique to regions not too far behind the wire.

The amount of light needed to illuminate the bubbles depends on their size and on the exposure time of the recording system. In general, the amount of light scattered decreases with the bubble diameter, and a large intensity is needed if the bubbles are small. Short exposure times are needed in order to minimize blurring due to the motion of the bubbles. Mechanical or electro-optical shutters are used to generate light pulses which are synchronized with the camera, and give the appropriate exposure time. To reduce the uncertainty in the position of the bubble lines, only a thin plane must be illuminated. This light sheet can be produced either with a conventional light source and a projection condenser system, or with a laser and an anamorphic optical system. Due to the scattering characteristics of the bubbles, most of the incident light is scattered in forward direction at an angle of about 65° between illuminating and viewing direction. If one consequently employs a large angle between object plane and image plane, one must correct the bubble-line images for perspective distortion.

The evolution of the bubble lines can either be recorded on film or video. If the bubble-line pictures are digitized, they can be processed and analysed with digital image processing and pattern recognition techniques.

When the motion of a bubble line is analysed quantitatively, fluid velocity values are obtained by dividing the displacement of the bubble line in a time interval through the time interval. The measuring error is therefore contained in the measured displacement and the measured time interval. The associated uncertainty can be large and will be discussed in section 2.2.2.

2.2.2 On the errors and uncertainties of the technique

A number of error sources add up to the total uncertainty associated with the quantitative use of the hydrogen-bubble technique in a turbulent boundary layer (Schraub e.a., 1965). Here we consider two types of error: 1) errors that are intrinsic to the use of hydrogen-bubble time-lines, and 2) errors that have to do with the recording and the processing of the hydrogen-bubble time-lines.

The errors intrinsic to the method originate from the use of non-ideal fluid markers in a flow that is not one-dimensional. There are two main contributing factors. First, the vertical velocity of the bubbles causes the bubbles to move into regions with a larger fluid velocity. This vertical velocity is the sum of the terminal rise velocity of the bubbles and the rms value of the fluctuations in the vertical velocity component of the flow. It was reported that this effect can lead to a velocity surplus of about 2.5% (Schraub e.a., 1965). Second, the wake of the wire causes the bubbles to move with too low a streamwise velocity. There is some controversy on the magnitude of this velocity defect: values have been reported in the range from 0% (Schraub e.a., 1965) up to 20% (Grass, 1971) beyond 70 wire diameters. Due to these two effects, the streamwise velocity of a bubble can be different from the streamwise velocity of a fluid element. We consider both effects important enough to warrant the development of a model that quantifies their influence. This model is presented in section 2.3.

There are also four minor contributions to the intrinsic error. First, the fluctuations in the spanwise velocity component of the flow cause the bubbles occasionally to move

in a direction parallel to the wire. If so, positions on the wire are related to the wrong positions on the bubble line. For a typical turbulent boundary layer this yields an uncertainty of the order of 1% in the displacement (Schraub e.a., 1965). Second, it is the question whether the bubbles will follow the flow. Since the bubbles are small, it is assumed that there is no lag between bubble speed and fluid velocity. (For a qualitative proof, which unfortunately does not hold for gas bubbles in a fluid, see Merzkirch, 1987, p. 39.) Third, due to their inertia, the bubbles might not follow the fluctuations in a turbulent flow. However, by assuming an oscillating flow, it can be shown that bubbles 25 μm in diameter lag less than 3% for fluctuations up to 2000 Hz (Schraub e.a., 1965). Fourth, a hydrogen-bubble time-line can not resolve turbulent fluctuations whose scales are smaller than the displacement of the time line and the time interval in which the displacement took place (Schraub e.a., 1965). Moreover, flow patterns of short length and short duration will be attenuated because the bubble-line patterns need a certain time to develop (Pulles, 1988). Together this gives the hydrogen-bubble technique the character of a band-pass filter, and care must be taken in inferring fluctuating quantities from hydrogen-bubble data.

The errors that have to do with the recording and the processing of the hydrogen-bubble time-line pictures concern the uncertainty in determining the time interval and the displacement. The analysis we have in mind is the frame-to-frame method, in which the displacement of a specific time line is measured from one movie or video frame to another. Then the time interval is determined by the frame speed of the camera, which is known to a high degree of accuracy. When the displacement of a time line is actually measured, there is a principal uncertainty of 1 pixel in counting the number of pixels between the two positions of the time line.

However, three other factors contribute to the uncertainty in the measured displacement. First, in an automated analysis the time-line pictures must be digitized before they can be processed. The resulting loss of accuracy is of the order of the smallest length scale in a digitized picture: 1 pixel. Second, if the time lines were recorded at a large angle between the camera axis and the axis normal to the object plane, the pictures must be corrected for perspective distortion. The angles over which the image plane must be rotated are determined by control grid matching (Castleman, 1979, p. 116). This procedure also yields the scale factor, which converts distance-in-pixels to distance-in-meters. For a well-defined control grid the uncertainty in the scale factor is determined by the uncertainty in the number of pixels between two control grid points, and can be of the order of 2%. Note that control grid matching also captures effects that are hard to quantify, such as the refraction of the light rays at the water-air interface. Third, usually the time-line pictures must be filtered in order to remove noise. Since the filtering operations affect the shape of the time lines, the uncertainty in their position increases with 2 pixels.

If the number of observations is small, the total uncertainty is determined by the cumulative effect of the individual error sources (external error estimate). Then the square of the total relative uncertainty is equal to the sum of the squares of the contributing relative uncertainties. Given the contributions of the various error sources, the total uncertainty of the hydrogen-bubble time-line technique is large. On the other

hand, a smaller uncertainty can be reached if it can be determined from the actual data (internal error estimate). This necessitates the processing of a large amount of time-line pictures, which is a laborious task even if automated processing techniques are used. Furthermore, this makes it difficult to discriminate between fluctuations due to uncertainty and fluctuations due to turbulence.

2.3 The wake velocity defect and the gradient velocity surplus

2.3.1 Existing views on the influence of the wire and the gradient

At the introduction of the hydrogen-bubble technique as a method to measure fluid velocities, it was recognized that the wake of the wire influences the motion of the bubbles (Schraub e.a., 1965). Measurements showed that the magnitude of the velocity defect is in agreement with a prediction based on the laminar-wake solution for an infinite circular cylinder, provided that the wire is not generating bubbles. In this case the defect is on the centerline:

$$\frac{U_0 - U(x)}{U_0} = C(\frac{x}{d})^{-\frac{1}{2}}, \tag{2.1}$$

with U_0 the undisturbed fluid velocity, x the distance downstream of the wire, $U(x)$ the fluid velocity in the wake, and d the diameter of the wire. However, Schraub e.a. observed that the velocity defect is markedly reduced when bubbles are being generated, and is not present beyond 70 wire diameters. They attributed the defect reduction to the presence of a gas film around the wire, which serves to reduce the drag force on the wire. On the other hand, from an examination of empirical data it was suggested that $C \approx 1.3$ for $3 < R_d < 40$ (Abernathy e.a., 1977). Experiments showed that $C = 1.5$ provides a reasonable compensation for the velocity defect when fluid velocities are to be measured via hydrogen-bubble time-lines (Lu and Smith, 1985).

In a later investigation, the velocity of the hydrogen bubbles was measured as a function of the distance behind the wire (Grass, 1971). Although the defect was less than predicted by laminar-wake theory, it was larger than reported before. Grass considered the defect sufficiently large to warrant compensation of his experimental data with the empirical formula:

$$\frac{U_0 - U(x)}{U_0} = 3.62(\frac{x}{d})^{-0.729}. \tag{2.2}$$

Note however that this result was obtained with a partially insulated wire.

Experiments in which the fluid velocity was simultaneously measured with hydrogen-bubble time-lines and a laser-doppler anemometer, also showed that the bubble velocity is systematically lower than the fluid velocity (Pulles, 1988). A quantitative explanation was found by integrating the equation for the laminar flow around an infinite cylinder (Thijssen, 1988). With respect to the undisturbed flow, the presence of the wire causes a deficiency in the position of the bubbles downstream of the wire. The true fluid velocity is therefore found by dividing the sum of the position defect and the displacement of the

bubbles through the time interval in which the displacement took place. The position defect can empirically be found from a plot of the displacement versus the product of the fluid velocity and the time interval.

Although the effect of the vertical velocity of the bubbles in a boundary layer was also recognized, it was not considered to be large enough to warrant compensation (Schraub e.a., 1965; Grass, 1971). However, the resulting surplus in the streamwise velocity of the bubbles can be large, especially if the bubbles move in a shear layer with a large velocity gradient.

In section 2.3.2 we develop a model which describes the effects of the wake of the wire and the velocity gradient in a boundary layer.

2.3.2 A model for the wake defect and the gradient surplus

Due to the small fluid velocities and the small diameter of the bubble generating wire, generally the Reynolds number of the flow around the wire is low ($R_d = 1...10$). Consequently, at first glance the wake of the wire should be treated by laminar flow theory. However, the wire is placed in a turbulent flow, and therefore the flow in its wake is turbulent. Here we consider the instantaneous undisturbed fluid velocity u_0 and the resulting velocity $u(x)$ in the wire wake.

By assuming similarity between velocity profiles in subsequent positions downstream of a cylinder in an otherwise non-turbulent flow, it can be shown that in the wake the distribution of the velocity is determined by

$$\frac{u_0 - u(x)}{u_0} \propto (\frac{x}{d})^{-\frac{1}{2}} \exp(-\frac{u_0 d}{4\epsilon_m}\xi_2^2),$$ (2.3)

(Hinze, 1975, p. 496), with x the position downstream of the wire, $u(x)$ the fluid velocity in the wake, u_0 the undisturbed fluid velocity, ϵ_m the eddy diffusity, and $\xi_2 = y/\sqrt{xd}$ the similarity parameter (figure 2.1).

Suppose now the cylinder is a thin wire oriented parallel to the wall of a boundary layer, and orientated such that the buoyance force and the velocity gradient are in the same direction. Furthermore, suppose that the wire is generating fluid markers in the form of hydrogen bubbles. The off-axis position of a bubble initially at the center line is $y = vt$, where v is the vertical velocity of the bubble (figure 2.2). Since the bubble moves into regions with a different streamwise fluid velocity, it experiences a modified undisturbed fluid velocity. This modified undisturbed fluid velocity $u(t)$ is determined by the law that governs the shear layer. If we assume that the eddy diffusity is constant and given by $\epsilon_m = \frac{1}{61}u_0 d$ (Hinze, 1975, p. 507), it follows from (2.3) that the downstream motion of the bubbles is determined by

$$\frac{dx}{dt} = u(t) \left(1 - (\frac{x}{d})^{-\frac{1}{2}} \exp(-c\frac{v^2 t^2}{xd})\right),$$ (2.4)

with $c \approx \frac{61}{4}$. The solution of this differential equation gives the position x of the bubble in the wake as a function of time, its vertical velocity v, the diameter of the wire d, and
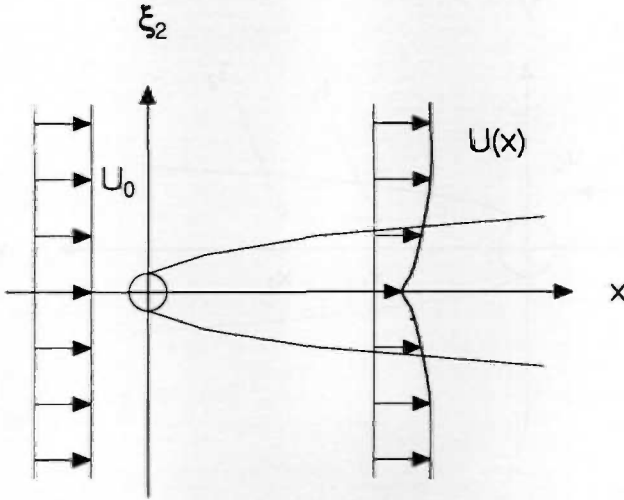
Figure 2.1: Schematic of the wake of a circular cylinder. In the wake the fluid velocity $U(x)$ differs from the undisturbed fluid velocity U_0.

via the modified undisturbed fluid velocity $u(t)$, the true undisturbed fluid velocity u_0 (i.e. the fluid velocity at the wire).

In order to simplify (2.4), we assume that the bubble travels from $x = x_1$ at $t = t_1$ to $x = x_2$ at $t = t_2$. Then its average position in the time interval (t_1, t_2) is $\bar{x} = (x_2 + x_1)/2$, which is reached at $\bar{t} = (t_2 + t_1)/2$. Consequently, the differential equation (2.4) can be written as

$$\frac{dx}{dt} = u(t)f(x), \tag{2.5}$$

with

$$f(x) = 1 - \left(\frac{x}{d'}\right)^{-\frac{1}{2}} \tag{2.6}$$

and

$$d' = d\exp\left(-c\frac{2v^2\bar{t}^2}{\bar{x}d}\right). \tag{2.7}$$

Equation (2.7) shows that the bubble experiences a virtual wire diameter, which is smaller than the actual wire diameter. This effect reduces the influence of the wake. Equation (2.5) can be separated, and

$$\int_{x_1}^{x_2} \frac{1}{f(x)}dx = \int_{t_1}^{t_2} u(t)dt \tag{2.8}$$
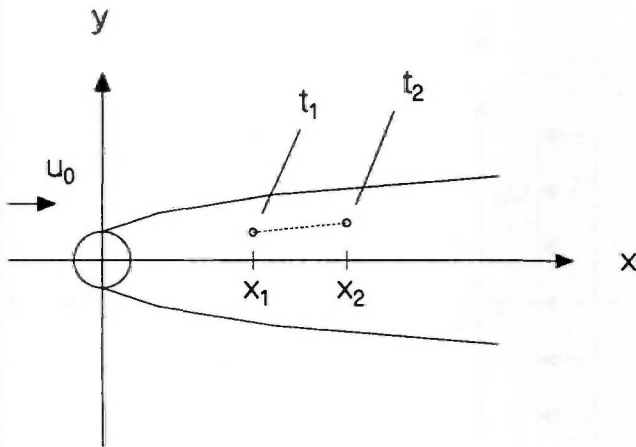
Figure 2.2: Schematic of the motion of a hydrogen bubble in the wake of the bubble generating wire. The bubble, initially in $x = x_0$, moves to $x = x_1$ and $x = x_2$ at later instances. The true undisturbed fluid velocity is u_0.

is its formal solution.

The left-hand side of (2.8) describes the influence of the wake of the wire on the position of the bubble. Since

$$\int \frac{1}{1 - (\frac{x}{a})^{-\frac{1}{2}}} dx = a((\frac{x}{a})^{\frac{1}{2}} - 1)^2 + 4a((\frac{x}{a})^{\frac{1}{2}} - 1) + 2a\ln((\frac{x}{a})^{\frac{1}{2}} - 1) \qquad (2.9)$$

for $x/a > 1$, it follows that

$$\int_{x_1}^{x_2} \frac{1}{f(x)} dx = x_2 - x_1 + 2d'\left((\frac{x_2}{d'})^{\frac{1}{2}} - (\frac{x_1}{d'})^{\frac{1}{2}} + \ln((\frac{x_2}{d'})^{\frac{1}{2}} - 1) - \ln((\frac{x_1}{d'})^{\frac{1}{2}} - 1)\right) \qquad (2.10)$$

is its solution.

The right-hand side of (2.8) describes the effect of the velocity gradient on the actual streamwise velocity of the bubble. If y_0 is the position of the bubble at $t = 0$ (which necessarily coincides with the position of the wire), the off-axis position of the bubble is $y(t) = y_0 + vt$ (figure 2.3). Next, we treat separately the effect of the velocity gradient in the three regions of the turbulent boundary layer.

In the viscous sublayer the mean fluid velocity obeys the linear law $U(y) = u_*^2 y/\nu$, with u_* the viscous velocity and ν the kinematic viscosity of the fluid. Substituting the position of the bubble as a function of time gives $u(t) = u_*^2(y_0 + vt)/\nu$. Then the true
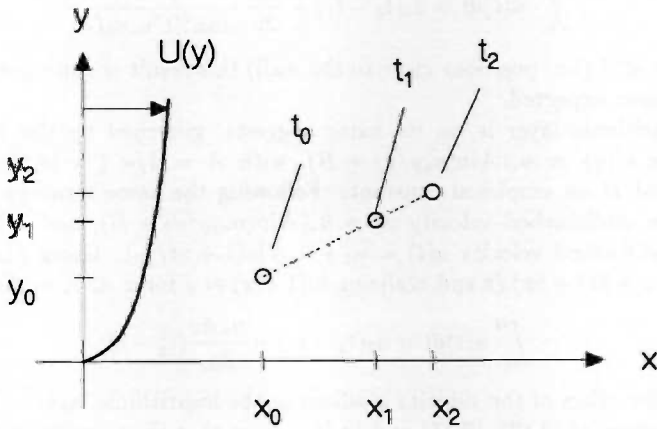
Figure 2.3: Schematic of the motion of a hydrogen bubble in a shear layer $U(y)$. The bubble experiences an increasing fluid velocity when it moves from $y = y_1$ to $y = y_2$.

undisturbed velocity can be determined to be $u_0 = u_*^2 y_0/\nu$, which yields the modified undisturbed velocity

$$u(t) = u_0 + \frac{u_*^2 v}{\nu} t. \tag{2.11}$$

Thus

$$\int_{t_1}^{t_2} u(t)dt = u_0(t_2 - t_1) + \frac{u_*^2 v}{2\nu}(t_2^2 - t_1^2) \tag{2.12}$$

gives the effect of the velocity gradient on the bubble motion in the viscous sublayer. In the buffer layer the mean velocity profile is approximated by $U(y) = u_* \tanh(Cu_*y/\nu)/C$, with C (not to be confused with c) an empirical constant that can be determined by matching the hyperbolic-tangent law and the logarithmic law in a specific position. Proceeding as for the viscous sublayer, we find via $u(t) = u_* \tanh(Cu_*(y_0+vt)/\nu)/C$ for the true undisturbed velocity: $u_0 = u_* \tanh(Cu_*y_0/\nu)/C$. With $\tanh x - \tanh y = \tanh(x-y)(1 - \tanh x \tanh y)$ we find for $y_0 > vt$ (i.e. a small vertical displacement of the bubble with respect to the position of the wire):

$$u(t) - u_0 \approx \frac{u_*}{C} \tanh(Cu_*vt/\nu)\left(1 - \tanh^2(Cu_*y_0/\nu)\right), \tag{2.13}$$

which yields the modified fluid velocity

$$u(t) = u_0 + \frac{u_*}{C}\frac{\tanh(Cu_*vt/\nu)}{\cosh^2(Cu_*y_0/\nu)}. \tag{2.14}$$

Using $\int \tanh x\, dx = \ln \cosh x$, and realizing $\cosh x \approx 1 + \frac{1}{2}x^2$ and $\ln(1 + x) \approx x$ for $x \ll 1$, we find the effect of the velocity gradient in the buffer layer:

$$\int_{t_1}^{t_2} u(t)dt = u_0(t_2 - t_1) + \frac{u_*^2 v}{2\nu} \frac{t_2^2 - t_1^2}{\cosh^2(Cu_* y_0/\nu)}. \tag{2.15}$$

For $Cu_* y_0/\nu \ll 1$ (i.e. positions close to the wall) this result is equivalent to (2.12), as could have been expected.

The logarithmic layer is, as its name suggests, governed by the mean fluid velocity profile $U(y) = u_*(A\ln(u_* y/\nu) + B)$, with $A = 1/\kappa$ (κ is the von-Karman constant) and B an empirical constant. Following the same strategy as before, we find the true undisturbed velocity $u_0 = u_*(A\ln(u_* y_0/\nu) + B)$, and subsequently the modified undisturbed velocity $u(t) = u_0 + u_* A\ln(1 + vt/y_0)$. Using $\int \ln(a + bx)dx = ((a + bx)\ln(a + bx) + bx)/b$ and realizing $\ln(1 + x) \approx x$ for $x \ll 1$, we find

$$\int_{t_1}^{t_2} u(t)dt = u_0(t_2 - t_1) + \frac{u_* A v}{2y_0}(t_2^2 - t_1^2) \tag{2.16}$$

to describe the effect of the velocity gradient in the logarithmic layer.

A comparison of (2.12), (2.15) and (2.16) shows that they are equivalent to

$$\int_{t_1}^{t_2} u(t)dt = u_0(t_2 - t_1) + \frac{du_0}{dy}\frac{v}{2}(t_2^2 - t_1^2), \tag{2.17}$$

with du_0/dy the gradient of the true undisturbed fluid velocity at the position of the wire. Equation (2.17) is equivalent to the result which one obtains by linearizing and integrating the hyperbolic tangent or the logarithmic law.

Substituting (2.10) and (2.17) in (2.8) gives after rearranging terms the true undisturbed fluid velocity at the wire:

$$u_0 = \frac{x_2 - x_1}{t_2 - t_1} +$$
$$\frac{2d'}{t_2 - t_1}\left(\left(\frac{x_2}{d'}\right)^{\frac{1}{2}} - \left(\frac{x_1}{d'}\right)^{\frac{1}{2}} + \ln\left(\left(\frac{x_2}{d'}\right)^{\frac{1}{2}} - 1\right) - \ln\left(\left(\frac{x_1}{d'}\right)^{\frac{1}{2}} - 1\right)\right) -$$
$$\frac{du_0}{dy}\frac{v}{2}(t_2 + t_1). \tag{2.18}$$

The first term on the right is due to the displacement of the bubble in the time interval. The second term specifies the influence of the velocity defect due to the wake of the wire, and the third term specifies the velocity surplus due to the vertical motion of the bubble in the shear layer. Note that for specific values of the groups $(x_2, x_1, t_2, t_1, v, d)$ and $(t_2, t_1, v, du_0/dy)$ the two correction terms may be of equal order and opposite sign. In that case $u_0 = (x_2 - x_1)/(t_2 - t_1)$, which supports claims that no correction is needed under proper conditions (see e.g. Schraub e.a., 1965). However, in general both corrections are needed.

Equation (2.18) shows that the true undisturbed fluid velocity can be estimated from the motion of a hydrogen bubble by

$$u_0 = u_{raw} + u_{def} - u_{sur}, \tag{2.19}$$

with

$$u_{raw} = \frac{x_2 - x_1}{t_2 - t_1},$$ (2.20)

$$u_{def} = \frac{2d'}{t_2 - t_1} \left((\frac{x_2}{d'})^{\frac{1}{2}} - (\frac{x_1}{d'})^{\frac{1}{2}} + \ln((\frac{x_2}{d'})^{\frac{1}{2}} - 1) - \ln((\frac{x_1}{d'})^{\frac{1}{2}} - 1) \right),$$ (2.21)

and

$$u_{sur} = \frac{du_0}{dy} \frac{v}{2} (t_2 + t_1).$$ (2.22)

The two terms u_{def} and u_{sur} compensate for the effects of the wire wake and the velocity gradient, respectively. We see that the velocity defect can be kept small if the diameter of the wire is small, the bubble is not too close to the wire, and $x_2 \approx x_1$. On the other hand, the velocity surplus can be kept small if the bubble has a small vertical velocity, and is not too far away from the wire. Note that in a boundary layer the hydrogen-bubble time-line technique can not be used as a stand-alone technique because the compensation for the wake defect necessitates the presence of knowledge on the velocity gradient. In sections 2.4, 2.5 and 3.2 we use (2.19) to estimate instantaneous fluid velocities via this technique.

As a numerical example we consider the wake velocity defect and the gradient velocity surplus in a turbulent boundary layer whose logarithmic layer is defined by $U^+ = 2.5 \ln y^+ + 5.0$, with $u_* = 6.5$ mm/s and $\nu = 1.1 \ 10^{-6}$ m^2/s. Matching the logarithmic and the buffer layer in $y^+ = 35$ yields for the constant in the hyperbolic-tangent law $C = 7.1 \ 10^{-2}$. If we take a 40 μm thick wire, and assume that it produces hydrogen bubbles with a diameter of 40 μm, the bubbles have a terminal rise velocity of about 1.2 mm/s. For $t_1 = 40$ ms and $t_2 = 80$ ms, we find the velocity defect ranging from 5.2% at $y^+ = 5$ (the top of the linear layer) to 6.1% at $y^+ = 35$, and the velocity surplus ranging from 8.5% at $y^+ = 5$ to 0.1% at $y^+ = 35$ (figure 2.4). We see that the gradient surplus dominates below the buffer layer, whereas the wake defect dominates beyond the buffer layer. Note also that the buffer layer is the region of little net effect.

2.3.3 The velocity mean and variance

Generally, when fluid markers are employed, a fluid velocity is to be determined from the displacement of the fluid marker in a time interval. Let (t_1, t_2) be this time interval, with $t_2 > t_1$, $t_1 > t_0$ and $t = t_0$ the instant at which the fluid marker is generated. Consider a fluid marker, initially in $x = x_0$ (at $t = t_0$), and at later instances in $x = x_1$ (at $t = t_1$) and $x = x_2$ (at $t = t_2$). Now we would like to estimate from the positions x_1 and x_2 the mean fluid velocity U_0 and the velocity variance $\overline{u_0'^2}$ at $t = t_0$ (figure 2.5). (Note that this configuration is the one of the general application of the hydrogen-bubble time-line technique: after the generation of the time line its position is measured at two time instants in order to estimate the fluid velocity in the absence of the wire.)

The motion of the fluid marker is determined by

$$\frac{dx}{dt} = u(t),$$ (2.23)
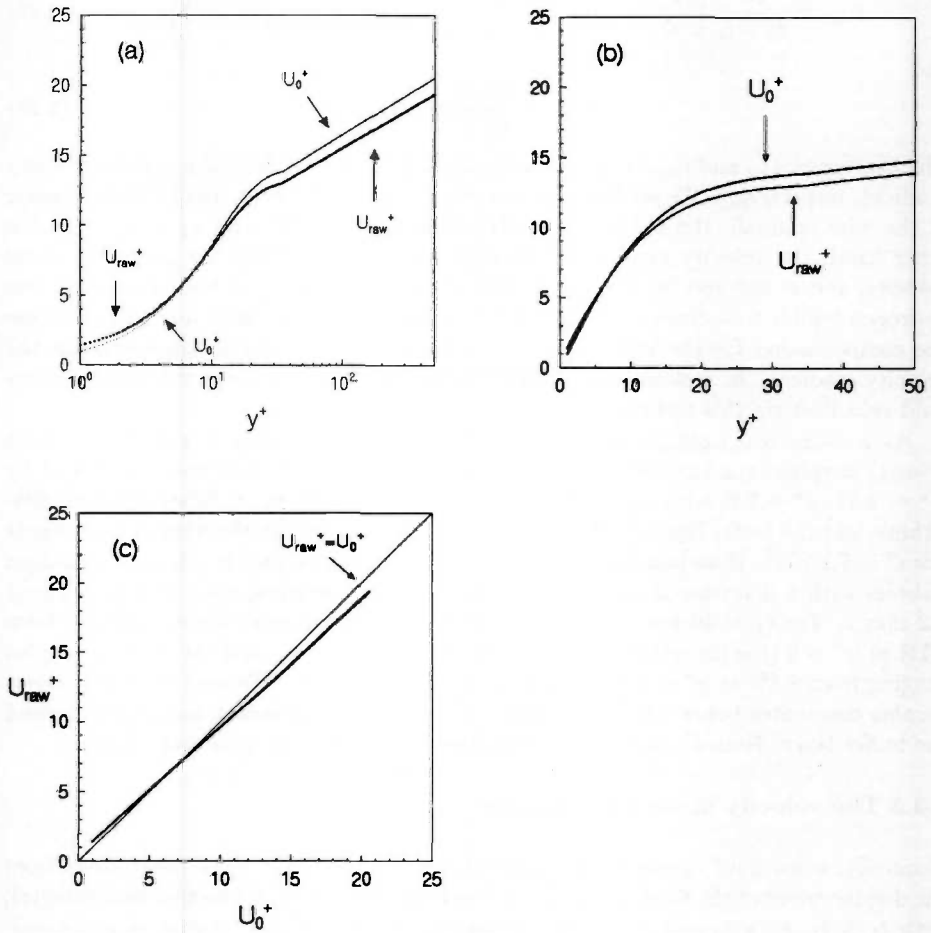
Figure 2.4: Numerical example of the influence of the wire wake and the velocity gradient. (a) Model turbulent boundary layer with logarithmic layer $U^+ = 2.5 \ln y^+ + 5.0$ for $y^+ \geq 35$ and hyperbolic-tangent layer $U^+ = \tanh(Cy^+)/C$ (with $C = 7.1 \ 10^{-2}$) for $y^+ \leq 35$. The mean true fluid velocity is $U_0^+ = U^+$; the mean velocity of the hydrogen bubbles is U_{raw}^+. (b) Same as (a), but with emphasis on the region $0 \leq y^+ \leq 60$. (c) The correlation of the mean true fluid velocity U_0^+ and the mean bubble velocity U_{raw}^+.
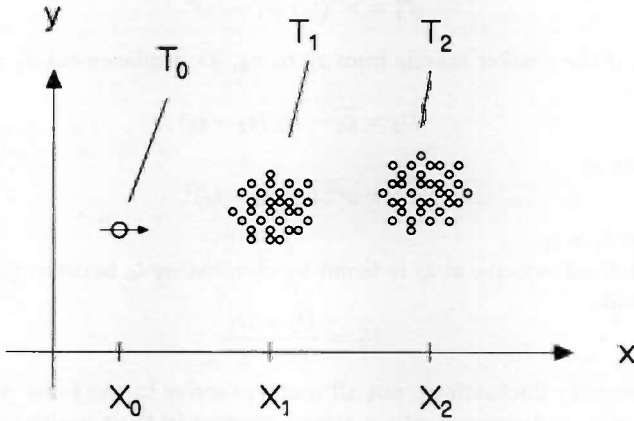
Figure 2.5: Schematic of the motion of fluid markers in a time-dependent but spatially homogeneous flow. Due to the velocity fluctuations a spread appears in the position that the markers reach after a specific time lapse since their generation.

with $u(t)$ the time-dependent but spatially homogeneous fluid velocity. If the marker travels from x_0 to x_1 in the time interval (t_0, t_1), (2.23) gives:

$$\int_{x_0}^{x_1} dx = \int_{t_0}^{t_1} u(t)dt. \tag{2.24}$$

Using the trapezoidal rule gives as the approximate solution of (2.24):

$$x_1 - x_0 = \frac{u(t_1) + u(t_0)}{2}(t_1 - t_0). \tag{2.25}$$

Let $d_1 = x_1 - x_0$ be the displacement of the marker, and suppose that the fluid velocity fluctuates: $u(t) = U_0 + u'(t)$. Then

$$d_1 = \left(U_0 + \frac{u'(t_1) + u'(t_0)}{2}\right)(t_1 - t_0). \tag{2.26}$$

Taking the time average of (2.26) gives

$$D_1 = \overline{d_1} = U_0(t_1 - t_0). \tag{2.27}$$

Time averaging the square of (2.26), and subtracting the square of (2.27) yields

$$\overline{d_1'^2} = \overline{d_1^2} - D_1^2 = \frac{1}{4}\left(\overline{u'^2(t_1)} + 2\overline{u'(t_1)u'(t_0)} + \overline{u'^2(t_0)}\right)(t_1 - t_0)^2. \tag{2.28}$$

By assuming homogeneous fluctuations (i.e. $\overline{u'^2(t_1)} = \overline{u'^2(t_0)}$) and for $t_1 \approx t_0$ we get $\overline{u'(t_1)u'(t_0)} = \overline{u'^2(t_0)}$. Then (2.28) becomes

$$\overline{d'^2_1} = \overline{u'^2(t_0)} \, (t_1 - t_0)^2. \tag{2.29}$$

Similarly, if the marker travels from x_0 to x_2, its displacement $d_2 = x_2 - x_0$ has a mean of

$$D_2 = \overline{d_2} = U_0 \, (t_2 - t_0) \tag{2.30}$$

and a variance of

$$\overline{d'^2_2} = \overline{u'^2(t_0)} \, (t_2 - t_0)^2, \tag{2.31}$$

provided that $t_2 \approx t_0$.

The mean fluid velocity at t_0 is found by eliminating t_0 between (2.27) and (2.30), with as a result

$$U_0 = \frac{D_2 - D_1}{t_2 - t_1}. \tag{2.32}$$

Due to the velocity fluctuations, not all markers arrive in the same positions at both $t = t_1$ and $t = t_2$, and consequently a spread appears in their positions: $x_2 = X_2 + x'_2$ and $x_1 = X_1 + x'_1$. Although we should also consider the spread in the time instants because generally not all fluid markers leave their starting position $x = x_0$ at $t = t_0$, we assume $t_1 = T_1$ and $t_2 = T_2$. Inserting this into (2.32) gives the well-known estimate for the mean fluid-velocity

$$U_0 = \frac{X_2 - X_1}{T_2 - T_1}. \tag{2.33}$$

The variance of the fluid velocity at t_0 is found by eliminating t_0 between (2.29) and (2.31), which gives

$$\overline{u'^2_0} = \overline{u'^2_0(t_0)} = \frac{\overline{d'^2_2} + \overline{d'^2_1} - 2\sqrt{\overline{d'^2_2}\,\overline{d'^2_1}}}{(t_2 - t_1)^2}. \tag{2.34}$$

Since $x_0 = X_0$ (all markers start in the same position) we have $\overline{d'^2_2} = \overline{x'^2_2}$ and $\overline{d'^2_1} = \overline{x'^2_1}$, which means that (2.34) becomes

$$\overline{u'^2_0} = \frac{\overline{x'^2_2} + \overline{x'^2_1} - 2\sqrt{\overline{x'^2_2}\,\overline{x'^2_1}}}{(T_2 - T_1)^2}. \tag{2.35}$$

When in sections 2.4, 2.5 and 3.2 fluid velocities are measured via time lines, equation (2.33) is used for the mean values and equation (2.35) for the variances.

It is instructive to compare (2.33) and (2.35) with the intuitive estimates for U_0 and $\overline{u'^2_0}$ that follow from merely considering the displacement of the fluid marker in the time interval (t_1, t_2). If $d = d_2 - d_1$ is this displacement, we get

$$D = \overline{d} = \overline{d_2} - \overline{d_1} = X_2 - X_1 \tag{2.36}$$

and

$$\overline{d'^2} = \overline{d^2} - D^2 = \overline{x'^2_2} + \overline{x'^2_1} - 2\overline{x'_2 x'_1}. \tag{2.37}$$

From these two equations follow the intuitive estimate for the mean velocity

$$U_0 = \frac{D}{T_2 - T_1},$$
(2.38)

and the intuitive estimate for the velocity variance

$$\overline{u'^2_0} = \frac{\overline{d'^2}}{(T_2 - T_1)^2}.$$
(2.39)

The intuitive estimate (2.38) for the mean velocity is equivalent to (2.33). On the other hand, since $\sqrt{(\overline{x'^2_2}\ \overline{x'^2_1})} \geq \overline{x'_2 x'_1}$ (Schwartz inequality), the intuitive estimate (2.39) for the velocity variance is larger than the one of (2.35). Recalling that the presence of the wire forced us to estimate velocities at $t = t_0$ from measurements at $t = t_1$ and $t = t_2$, we see that this procedure causes a problem when rms fluid velocities are to be determined through the use of fluid markers. In particular, the rms velocities should not be based on the rms values of the displacements. This is not generally recognized.

The difference between (2.35) and (2.39) can be explained by considering the spread in the positions x_1 and x_2. The spread in x_1 originates from the integrated effect of the velocity fluctuations $u'(t)$ in the time interval (t_0, t_1). Similarly, the spread in x_2 originates from the fluctuations in the interval (t_0, t_2). However, the spread in the displacement $d = x_2 - x_1$ accounts twice for the velocity fluctuations in the time interval (t_0, t_1). Therefore, the cross correlation of the positions is determined by $\sqrt{(\overline{x'^2_2}\ \overline{x'^2_1})}$ and not by $\overline{x'_2 x'_1}$.

Note also that the marker forgets the initial fluctuations in the fluid velocity if the correlation between the fluid velocities at t_2 and t_0, and t_1 and t_0 decreases, i.e. if the turbulence intensity is large. In a turbulent flow it is therefore difficult to estimate the velocity variance $\overline{u'^2_0}$ from measurements of the rms positions $\overline{x'^2_2}$ and $\overline{x'^2_1}$ of fluid markers.

2.4 Measurements on the velocity mean and variance[1]

2.4.1 The experimental facility

The turbulent boundary layer under investigation in this study is generated over a flat plate mounted in an open water channel. This water channel, which was used for combined hydrogen-bubble visualization and laser-doppler anemometry, is described elsewhere (Talmon e.a., 1986). Modification since then resulted in less vibrations in the test section, and a higher water level. In the test section it allows for free-stream velocities up to 19 cm/s with a turbulence intensity of 1.5%.
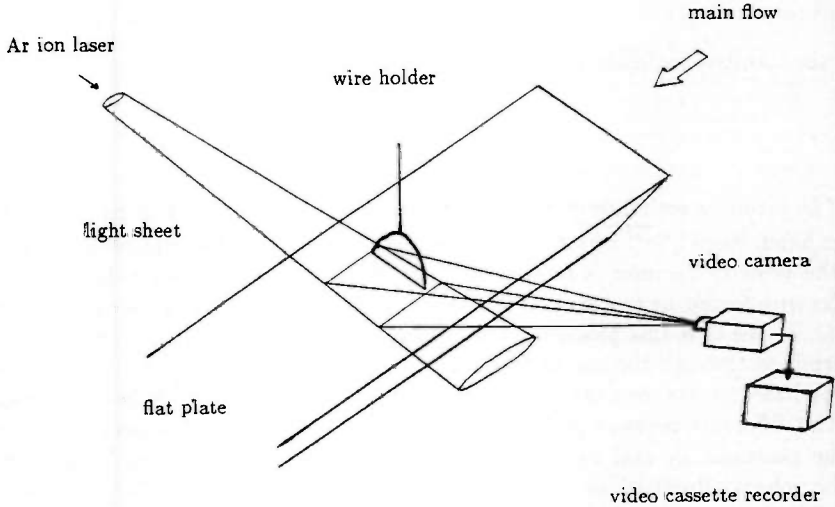
Figure 2.6: Schematic of the experimental facility.

The flat plate is 175 cm long and 60 cm wide. It has a sharp leading edge, and an adjustable flap at its end in order to control boundary-layer transition and separation. The plate is made of 2 cm thick perspex. The surface of the plate is mounted at a height of 6.5 cm above the bottom of the water channel. A 7 mm thick tripping wire, mounted 25 cm downstream of the leading edge, is used to create a turbulent boundary layer. Figure 2.6 shows the experimental facility.

Hydrogen bubbles are generated at a 40 μm thick and 17.5 cm long platinum wire, which is oriented perpendicular to the mean flow and parallel to the surface of the flat plate. The wire holder is traversable in horizontal (x and z) and vertical (y) direction. The bubbles have a vertical terminal velocity of about 1.2 mm/s. (We assume that the size of the bubbles is of the order of the diameter of the wire.)

The bubbles are illuminated with light from a 5 W Ar-ion laser (Spectra Physics Model 2020). A special fiber-optic cable transports the light to an anamorphic optical system that produces a thin light sheet[2]. In the test section of the water channel the sheet measures 100x1 mm. (These beam diameters are based on the $1/e^2$-intensity points of the 'gaussian' laser beam.)

The light scattered by the bubbles is recorded with a standard CCD video camera

---

[2]The light sheet was developed by J.M. Bessem

(High Technology Holland MX). An electro-optical shutter (Displaytech Model PV-050C) appropriately synchronizes the light for the camera (i.e. a light pulse of 4 ms duration every 20 ms). The recordings are stored on video tape. In order to optimize the amount of light scattered into the camera, the angle between the camera axis and the axis of the light sheet is about 40°. The viewing field is about 35 mm in streamwise direction, and about 85 mm in spanwise direction.

Hydrogen-bubble time-lines are created by applying to the wire voltage pulses of 20 ms duration and 30 V amplitude. If the water quality is 'improved' by adding 0.1% kitchen salt to the water, this results in extremely thin bubble lines: about 2 mm with the wire at $y^+ = 27$. Single bubble lines are generated at intervals of 1 s because we want a new bubble line to be generated when the previous line is convected out of the viewing field.

2.4.2 The data handling

A frame grabber (Data Translation DT 2851), mounted in a personal computer (Hewlett Packard Vectra RS/20), is used to digitize the bubble-line pictures that are stored on video tape. With help of the 'still/advance' function of the video tape recorder, the operator grabs a video frame from tape, and stores it in a video buffer. The picture is then available in a format of 512x512 non-square pixels and 256 grey values. Standard and customized commands[3] in an image-processing software-package (PC Semper) are used for processing of the digitized pictures.

The pictures are re-sampled on a 128x128 grid in order to reduce storage requirements and computation times. This has as additional (and not unwelcome) side effect that image flicker due to the interlaced and non-ideal video signal is removed. Furthermore, the pictures are aligned in order to correct for random offsets in the origin of their coordinate system. These offsets are caused by misfits between the synchronization signals of the frame grabber and the video-tape recorder. Next, a recording of the background is subtracted from the bubble-line pictures. This results in an improved contrast. Uneven illumination is taken care of by applying a minmax filter to the pictures (Rosenfeld and Kak, 1982, Vol. 1, p. 261).

Due to the large angle between the camera axis and the light sheet, the viewing field is geometrically distorted. Control grid matching is used to obtain a value for the angle over which the image field must be rotated in order to rectify the images. After this transformation the image plane corresponds to a xz plane in the boundary-layer coordinate system.

Next, the binary versions of the pictures are created. (A binary picture has only two grey values: 0 and 1.) This is possible because the pictures generally contain just one object (the bubble line) and the background. The binary bubble-line pictures allow for logical and morphological processing (see appendix A). An opening of size 1, followed by a closing of size 1, is used to remove 'salt-and-pepper noise', and to smooth the boundaries of the bubble lines. The thickness of the lines is then reduced to the size of one pixel with the rim-west function. This gives the position of the bubble line at the

---

[3]The minmax and the distortion-correction commands were implemented by J. Westerweel

instant the light switched on.

After successive processing of the recordings of a bubble line during its voyage through the viewing field, we create the picture that contains the position of the line at intervals of 40 ms. This is done by taking the 'inclusive or' of the thinned bubble-line pictures. Then the $u(z)$ velocity profiles at consecutive time steps can be obtained. For this purpose the distance between the line and the wire is measured at each scan line. This data is used to compute the raw, the defect and the surplus velocity, which together yield the estimate (2.19) for the true fluid velocity (see section 2.3.2). Due to the errors introduced at the preceding stages, the uncertainty in the spanwise velocity profiles will be about 10% for u and about 1 grid unit for z. The velocity profiles are stored as data files which are available for post-processing.

In general, the $u(z)$ profiles suffer from holes which originate from parts of the bubble line that have moved out of the light sheet. Therefore, the profiles are restored via cubic-spline interpolation. Also outliers are removed. (Outliers are data points u for which $|u - \mu_u| > 2\sigma_u$, with μ_u the mean velocity of the profile and σ_u its standard deviation.)

Figure 2.7 shows some of the image-processing stages which are applied when a velocity profile is determined from two recordings of a hydrogen-bubble time-line.

2.4.3 The velocity mean and variance

In order to test the performance of the method to measure turbulent fluid velocities via hydrogen-bubble time-lines, we performed experiments at $x \approx 100$ cm downstream of the plate's leading edge and with a free-stream velocity $U_\infty \approx 14.3$ cm/s. A hot-film anemometer[4] (Dantec probe 55R32 with bridge 56C01) was used to measure the fluid velocity in positions ranging from $y^+ \approx 1.9$ to $y^+ \approx 366.4$ (figure 2.8). Fitting the data points near the wall to the linear law yielded $u_* = 7.1$ mm/s. This value of the viscous velocity was used to estimate the empirical constant B in the logarithmic law, with as a result $U^+ = 2.5 \ln y^+ + 5.0$. (Note that we used $\kappa = 0.40$.) The lowest point in the logarithmic layer was determined to be $y^+ = 70$, which shows that we have a rather unusual turbulent boundary layer. Matching the logarithmic law and the hyberbolic-tangent law $U^+ = \tanh(Cy^+)/C$ in this point gave $C = 6.4 \ 10^{-2}$.

Hydrogen-bubble time-lines were generated during periods of about 300 s and at intervals of 1 s, and recorded with the wire mounted in 7 positions ranging from $y^+ \approx 11.1$ to $y^+ \approx 49.4$. At each scan line of each picture the raw fluid velocity (2.20) was computed from the displacement of the line in the time interval of 40 ms. The data from the velocity profile (i.e. u_*, κ, B and C), the fluid (ν), the wire (d) and the bubbles (v) was used to compute the wake velocity defect (2.21) and the gradient velocity surplus (2.22). Together with the raw fluid velocity, this yielded the estimate (2.19) for the true fluid velocity at the position of the wire (see section 2.3.2).

Figure 2.9 shows the mean fluid velocities that were determined from the motion of the time lines. The raw fluid velocity has the behaviour predicted before: close to the wall it is too large, whereas farther away it is too small (see the numerical example in

---

[4]The hot-film measurements were performed by A.K. Wemmers.
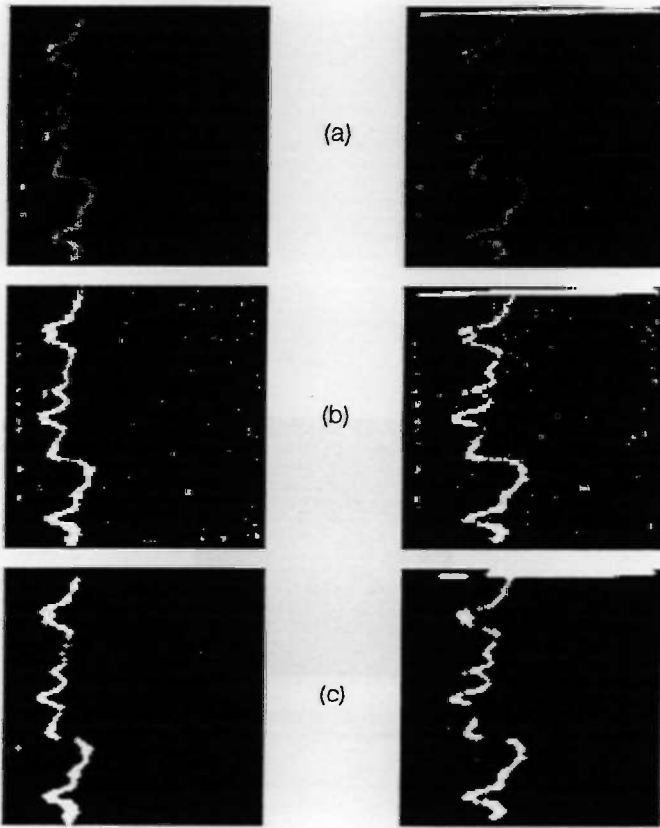
Figure 2.7: Illustration of some of the image-processing stages which are used to obtain a spanwise velocity profile from the motion of a hydrogen-bubble time-line. (a) Grey value picture of the time line at $t = t_1$ (left) and $t = t_2$ (right). The flow is from left to right. (b) Binary versions of the time lines. Due to segmentation errors salt-and-pepper noise appears. (c) The effect of opening and closing on the binary time-lines.
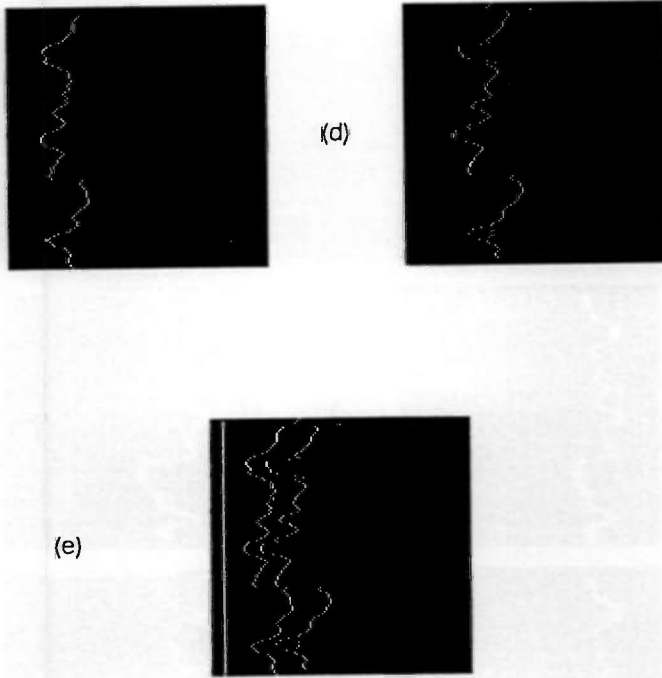
Figure 2.7: (d) Rimmed and restored versions of the previous pictures; the time lines are thinned to the size of 1 pixel. (e) Composite picture of the position of the time lines at t_0 (which coincides with the position of the wire), t_1 and t_2.
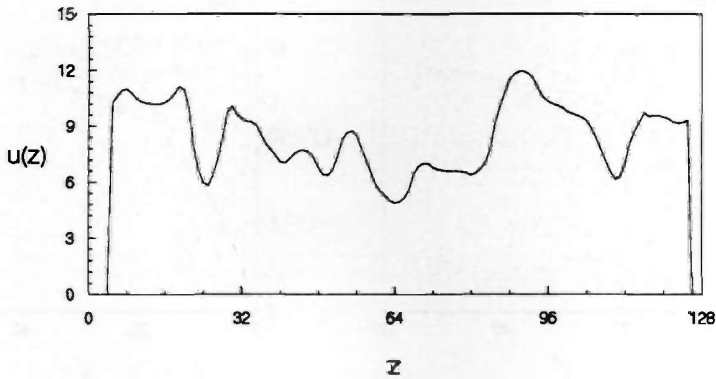
Figure 2.7: (f) The velocity profile obtained from the composite time-line picture, with z in grid units and $u(z)$ in cm/s. One grid unit corresponds to 0.52 mm.
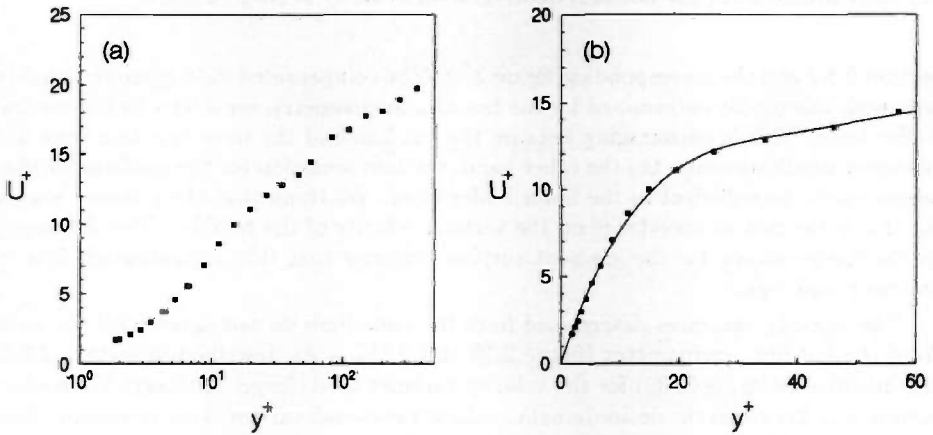
Figure 2.8: The mean velocity profile $U^+(y^+)$ of the turbulent boundary layer as measured with a hot-film anemometer; (a) whole profile, (b) emphasis on the buffer layer, with a least-square fit of the data.
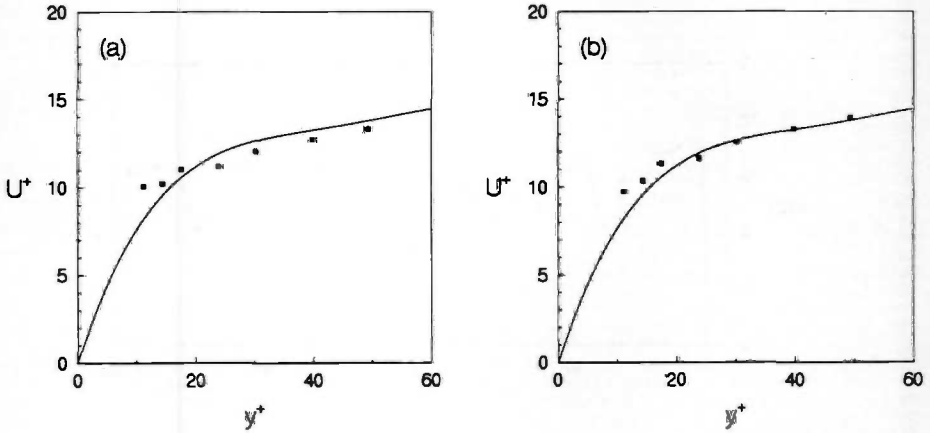
Figure 2.9: The mean fluid velocity in the turbulent boundary layer as measured with hydrogen-bubble time-lines. (a) The raw fluid velocity U_{raw}^+ as determined by dividing the displacement of the bubbles in the time interval through the time interval. (b) The true fluid velocity U_0^+ as determined by compensating via (2.19) the motion of the bubbles for the influence of the wire wake and the velocity gradient. The curves denote the least-square fit of the hot-film data. The uncertainty is $\Delta U_0^+ \approx \pm 1.4$.

section 2.3.2 and the corresponding figure 2.4). The compensated data agree reasonably well with the profile determined by the hot-film anemometry, especially in the central buffer layer. This is encouraging because the hot film and the time-line data were not obtained simultaneously. On the other hand, the compensation for the gradient surplus seems not to be sufficient in the lower buffer layer. We think that the primary reason for this is the lack of knowledge on the vertical velocity of the bubbles. The deficiency in the compensation for the gradient surplus indicates that this compensation fails in the near-wall region.

The velocity variances determined from the time lines do not agree with the data from the hot-film anemometer (figure 2.10 and 2.11). As described in section 2.3.3, the intuitive estimate (2.39) for the velocity variance is too large. Although the correct estimate (2.35) yields the desired smaller values, the overall variances are too small. This indicates that the hydrogen-bubble time-line technique underestimates the fluctuations in a turbulent flow. Probably, the cause for this effect is the inability of the bubbles to resolve fluctuations whose time scale is smaller than the time interval between two exposures.

We therefore conclude that the hydrogen-bubble time-line technique is a useful method to measure mean fluid velocities in regions not too close to (i.e. more than, say,
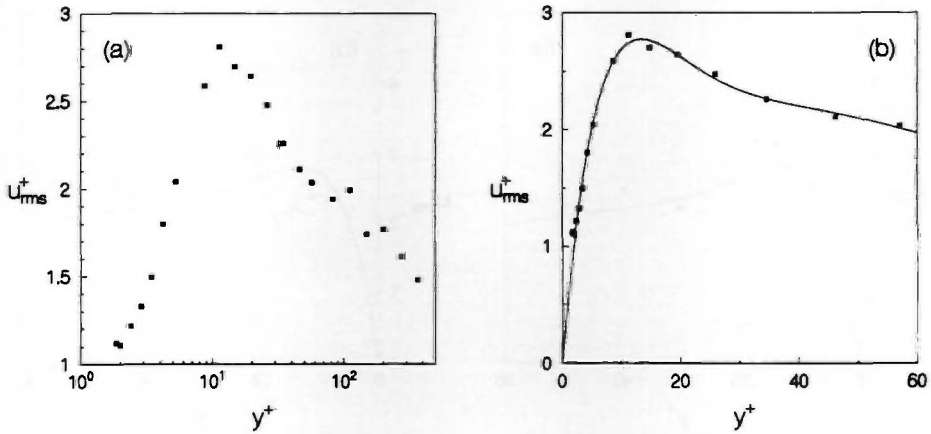
Figure 2.10: The profile of the turbulence intensity $\sqrt{\overline{u'^2_0}}/u_*$ in the turbulent boundary layer as measured with a hot-film anemometer; (a) whole profile, (b) emphasis on the buffer layer, with a least-square fit of the data.

$15l_*$ above) the wall of a turbulent boundary layer. However, this technique fails when it is used to measure mean fluid velocities close to the wall, and velocity variances in the entire boundary layer.

2.5 On the structure of spanwise velocity profiles[5]

2.5.1 Recapitulation of relevant knowledge

The structure of turbulent boundary-layer flow is dominated by elongated regions with a lower-than-average velocity (figure 2.12a). These so-called low-speed streaks have a mean spanwise spacing $<\lambda^+_z> \approx 100$ (Kline e.a., 1967) and a mean width $<\lambda^+_L> \approx$ 20...40 (Blackwelder, 1978; Talmon e.a., 1986). (Lengths are non-dimensionized with the viscous length scale $l_* = \nu/u_*$, with ν the kinematic viscosity and u_* the viscous velocity.) The streaks can have a very large streamwise extent (Blokland and Krishna Prasad, 1984). The high-speed regions neighbouring the streaks are reported to be considerably wider: $<\lambda^+_H> \approx 40...110$ (Talmon e.a., 1986; Robinson e.a., 1989).
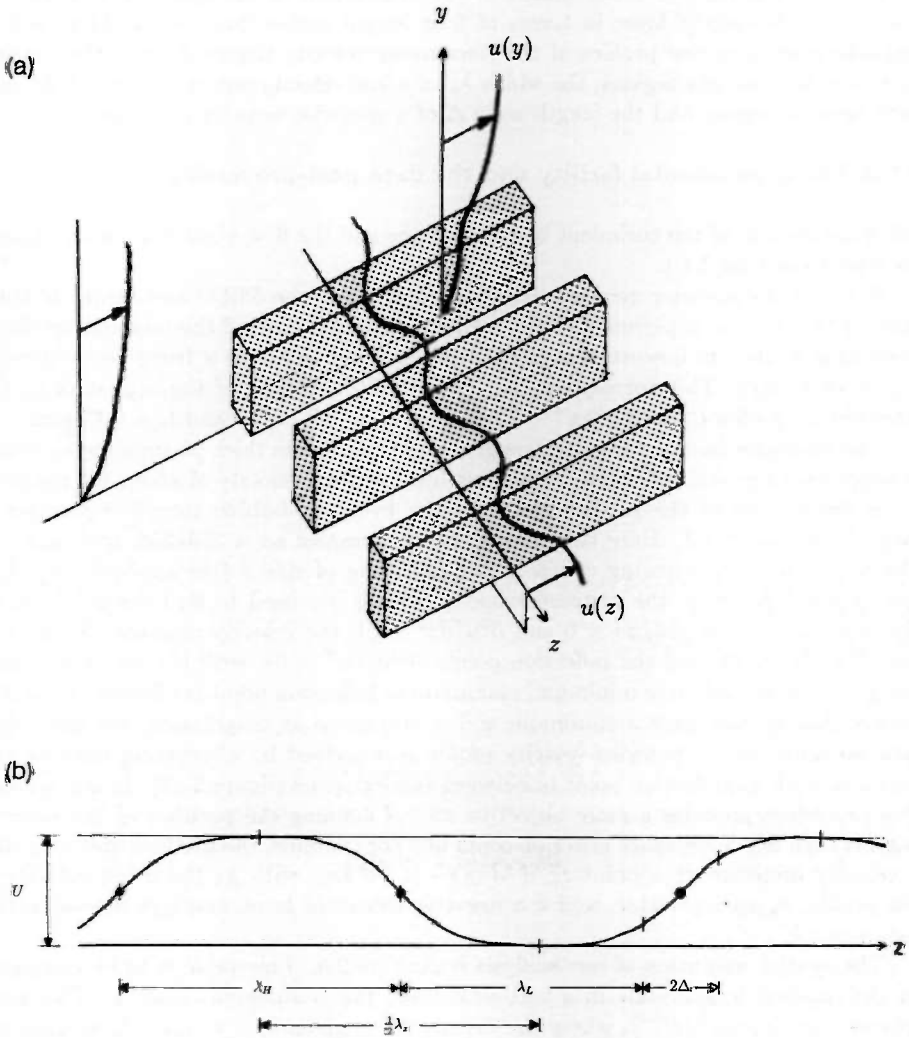
Figure 2.12: (a) Schematic of the structure of turbulent boundary layer flow. Low-velocity regions (indicated grey) appear as inflectional instantaneous $u(z)$ and $u(y)$ profiles. (b) A model for an inflectional $u(z)$ profile, with the four associated length scales: the half-spacing of two low-velocity regions $(\frac{1}{2}\lambda_z)$, the width of a low and a high-velocity region (λ_L and λ_H), and the length scale of the spanwise velocity gradient (Δ).

Here we report on a study aimed at the description of the spanwise structure of a turbulent boundary layer in terms of four length scales that can be identified in instantaneous spanwise profiles of the streamwise velocity (figure 2.12b): the spacing λ_z of two low-velocity regions, the width λ_L of a low-velocity region, the width λ_H of a high-velocity region, and the length scale Δ of a spanwise velocity gradient.

2.5.2 The experimental facility and the data post-processing

For a description of the turbulent boundary layer and the flow-visualization equipment we refer to section 2.4.1.

Hot-film anemometer measurements[6] (with DISA probe 55R32 and bridge 55M01) showed that for the experiments reported here $R_\theta = 978$ (with θ the momentum thickness) at $x \approx 100$ cm downstream of the leading edge, and with a free-stream velocity $U_\infty = 18.0$ cm/s. This corresponds to $R_x = 1.7\ 10^5$. Fitting of the $u(y)$ data to the 'theoretical' profile $U^+ = 2.5 \ln y^+ + 5.0$ yielded $u_* = 8.2$ mm/s and $l_* = 0.13$ mm.

The hydrogen-bubble time-lines are generated at a 20 μm thick platinum wire, which is supposed to generate bubbles with a vertical terminal velocity of about 0.5 mm/s.

A description of the pre-processing of the hydrogen-bubble time-line pictures is given in section 2.4.2. Here the pictures are re-sampled on a 256x256 grid, and the filtering involves an opening of size 2 and a closing of size 2 (see appendix A). The least-square splines of the restored velocity profiles are used to find the positions of the velocity minima ($\partial u/\partial z = 0$ and $\partial^2 u/\partial z^2 > 0$), the velocity maxima ($\partial u/\partial z = 0$ and $\partial^2 u/\partial z^2 < 0$), and the inflection points ($\partial^2 u/\partial z^2 = 0$); with the restriction that per grid interval only one minimum, maximum or inflection point is allowed. Inflection points that do not have a minimum and a maximum as neighbours, are not taken into account. So, a spanwise velocity profile is described by alternating minima and maxima, with an inflection point in between two extremes (figure 2.13). In our opinion this procedure provides a more objective way of defining the position of low-velocity regions than any acceptance criterion could do. For example, the method that identifies a velocity minimum in a point z_E if $u(z_E) - \mu_u < k\sigma_u$, with μ_u the mean velocity of the profile, σ_u its rms value, and k a negative threshold level, employs the subjective parameter k.

The spatial resolution of our analysis is $\Delta z^+ \approx 2.6$. This value is to be compared to the smallest length scale in a turbulent flow: the Kolmogorov scale η. This scale follows from $\eta = (\nu^3/\varepsilon)^{0.25}$, where the dissipation is given by $\varepsilon = u_r^3/\ell$. If we take the characteristic velocity fluctuation $u_r \sim 0.2U_\infty$ and the characteristic eddy scale $\ell \sim y$, this gives $\eta^+ \approx 1$ at $y^+ = 27$. This means that we have a spatial resolution which is almost sufficient to resolve the smallest length scale.

2.5.3 The spanwise structure in terms of four length scales

To measure spanwise profiles of the streamwise fluid velocity, the wire was mounted at $y^+ = 27, 20, 12$ and 8. At each height bubble lines were generated during a period of

---

[6]The hot-film measurements were performed by H.J.M. Vollebregt
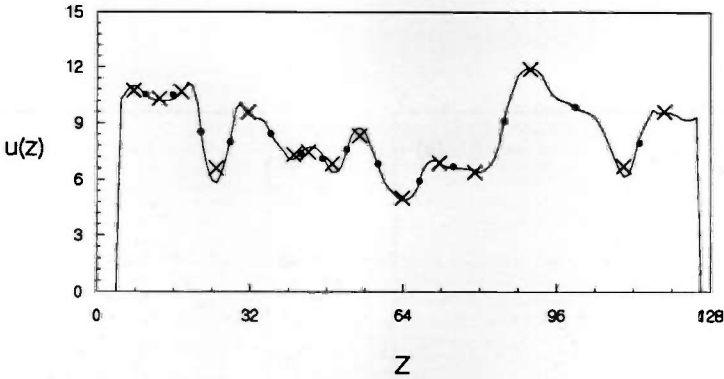
Figure 2.13: Example of the structure of an instantaneous spanwise velocity profile (see figure 2.7f) in terms of the position of velocity extremes ($\times$) and inflection points ($\bullet$).

about 300 s, and at intervals of 1 s. From most of the bubble lines recorded in this period we obtained a spanwise velocity profile. This yielded respectively 254, 300, 281 and 270 profiles, in which a total amount of 1822, 2170, 2169 and 2123 low-velocity regions were detected.

Figure 2.14 presents the histograms of the four length scales λ_z, λ_L, λ_H and Δ that were determined in the profiles at $y^+ = 20$. It is clear that there is a large variation in individual values for each scale, and that the histograms are skewed towards values lower than the mean. Therefore, we computed three statistical quantities: the mean, the median, and the interval in which 95% of the data lies. Table 2.1 summarizes these results.

The mean spacing $<\lambda_z^+> \approx 70$ is low compared to the generally accepted value $<\lambda_z^+> \approx 100$. However, the latter value is based on the spacing of elongated regions in which the bubbles have actually accumulated (Kline e.a., 1967). Obviously, not all spanwise gradients cause the bubbles to accumulate in streaks. Furthermore, most streak-count schemes (implicitly or explicitly) applied an acceptance criterion of the form $u_{low}/u_{high} < \alpha$, with as a result that the streaks originating from small gradients are ignored. Therefore, although these schemes may identify the correct streaks (i.e. those spaced at 100 wall units), they underestimate the influence of the small local spanwise velocity gradients. Note that we can not decide on the effect of our low R_θ because we did not vary R_θ. However, there is some evidence that $<\lambda_z^+> < 100$ for $R_\theta < 1000$ (Sreenivasan, 1988). Note also that we obtained u_* from the logarithmic layer; this procedure generally yields a larger u_* than the linear layer, and consequently larger values of λ_z^+.

From the variation of $<\lambda_z^+>$ with y^+, it is clear that the spacing of the low-velocity regions does not depend on the distance above the wall. This result is in contrast with the observed increase of $<\lambda_z^+>$ with y^+ for $y^+ > 5$ (Smith and Metzler, 1983).
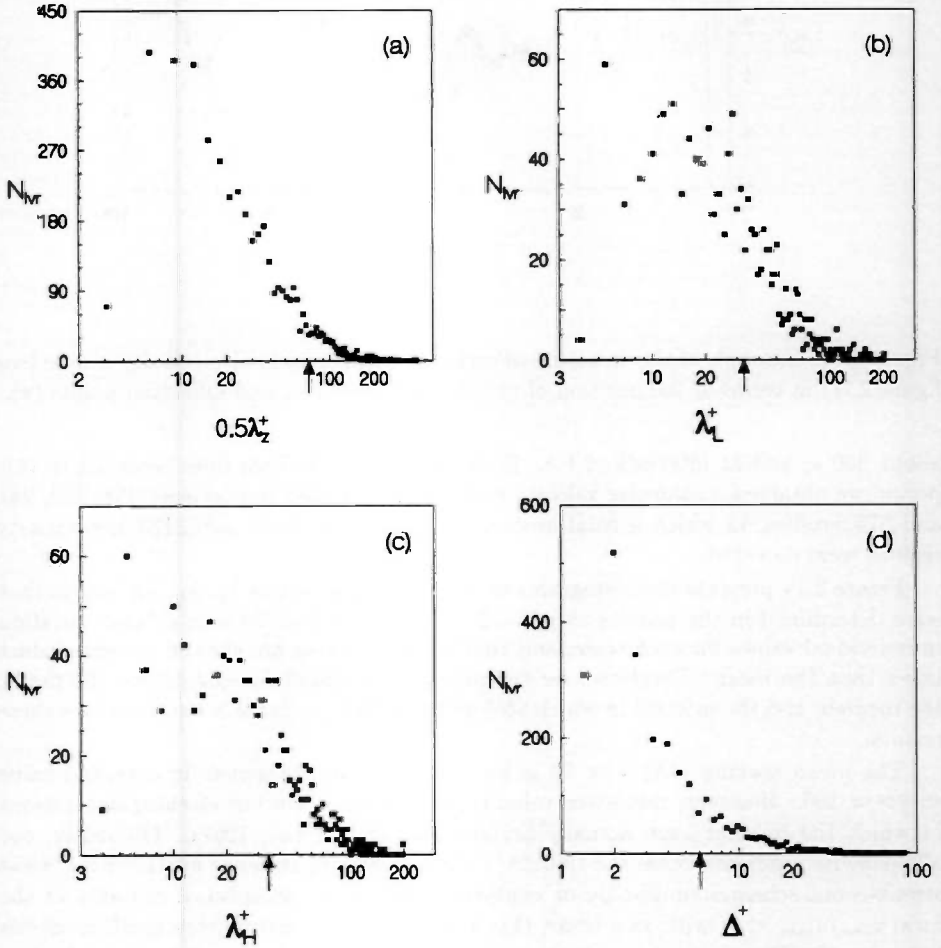
Figure 2.14: Histograms of the dimensionless length scales at $y^+ = 20$. (a) The half-spacing of low-velocity regions ($\frac{1}{2}\lambda_z^+$). (b) The width of low-velocity regions (λ_L^+). (c) The width of high-velocity regions (λ_H^+). (d) The length scale of the spanwise velocity gradient (Δ^+). The arrows indicate the mean values.

(a)	y^+	$<\lambda_z^+>$	$<\lambda_L^+>$	$<\lambda_H^+>$	$<\Delta^+>$
	27	71	32	33	6
	20	72	33	34	6
	12	69	31	33	6
	8	68	32	31	6
(b)	y^+	$\overline{\lambda_z^+}$	$\overline{\lambda_L^+}$	$\overline{\lambda_H^+}$	$\overline{\Delta^+}$
	27	48	25	26	4
	20	49	27	27	3
	12	47	26	26	3
	8	47	26	26	3
(c)	y^+	λ_z^+	λ_L^+	λ_H^+	Δ^+
	27	10...267	5...92	5...98	1...26
	20	10...263	5...105	5...102	1...29
	12	10...249	5...92	5...98	1...31
	8	9...249	5...95	5...86	1...28

Table 2.1: Dimensionless spacing of low-speed regions (λ_z^+), width of low and high-speed regions (λ_L^+ and λ_H^+), and gradient length scale (Δ^+) at different heights above the wall; (a) mean values, (b) median values, and (c) 95% interval.

From a comparison of the median and the mean spacings it follows that smaller spacings occur more often than larger spacings. The 95% interval quantifies this observation. What should be surprising about λ_z is not its mean or median, but the range of values that occurs. However, this certainly is not a new observation (Kline e.a., 1967). We note that, due to our fine spatial resolution, the small scales (in an absolute sense) have a large relative weight in the averaging procedure. Indeed, we found $<\lambda_z^+> \approx 110$ from velocity profiles that were median filtered such that the spatial resolution was reduced to $\Delta z^+ \approx 28$.

The mean widths of the low and the high-velocity regions are almost equal: $<\lambda_L^+> \approx <\lambda_H^+>$. This result is considerably different from the generally accepted values $<\lambda_L^+> \approx 20$ (Blackwelder, 1978; Talmon e.a., 1986) and $<\lambda_L^+> / <\lambda_H^+> \approx 2...5$ (Talmon e.a. 1986; Robinson e.a., 1989). Again this is due to a difference in concept: the latter values are based on the width of the regions in which the bubbles have accumulated, whereas ours are based on the distance between inflection points in the velocity profile. This illustrates that one should be careful in explaining flow phenomena in terms of the behaviour of fluid markers: the low-speed streaks are regions in which fluid markers have

accumulated, and need not be elongated and narrow low-velocity regions. Evidently, the low-speed streaks do exist, but the low-velocity regions are dynamically important to the near-wall region.

The value of the mean gradient length scale $<\Delta^+> \approx 6$ is in agreement with the value $<\Delta^+> \approx 5...15$ that was found with a rake of hot-wire sensors in a wind tunnel turbulent boundary layer (Blackwelder and Swearingen, 1989). It was shown that inflectional $u(z)$ profiles with gradient length scale Δ produce disturbances with streamwise wavelength $\lambda_x = 5\pi\Delta$ (Blackwelder and Swearingen, 1989). If we assume that these disturbances travel with a convection velocity $u_c = 15u_*$ (Robinson e.a., 1989), then an observer stationary in the boundary layer finds a dimensionless time between two disturbances $T^+ = \lambda_x^+/u_c^+ \sim \Delta^+$. Since this is of the order of the reported time between two 'bursts', it suggests that there is a large variability in values of the time between 'bursts' (Kim e.a., 1971). Furthermore, it suggests that the distribution of this time interval is skewed towards the smaller values.

May the differences in the numerical values be as they are, the general picture which emerges form these measurements is in agreement with the concept of a quasi-periodic near-wall flow-structure.

2.6 Evaluation of the use of hydrogen-bubble time-lines

In evaluating results obtained with the hydrogen-bubble time-line technique in a turbulent boundary layer, a primary concern is the reliability of the technique. Generally, this reliability is poor because of the errors intrinsic to the technique; especially those due to the presence of the bubble-generating wire and the velocity gradient in the boundary layer. Although we have compensated our data for the latter two effects, our results show that these compensations fail in the region close to the wall. This shows that one should not be too confident in the reliability of this technique in the region that is of most interest to turbulence structure research.

In particular, when using hydrogen-bubble time-lines, there is a principal uncertainty in the knowledge on the position of the time line with respect to the wire. This is because, generally, the bubbles move out of the plane of the wire. Since, on average, one can deal with this motion by considering the rise velocity of a bubble and the rms vertical fluid velocity, it is possible to measure the correct mean fluid velocity. However, in practise, the bubble also experiences the instantaneous fluid velocity component. Together with the rise velocity this component determines the motion of the bubble, and, consequently, the motion of individual bubbles is different from the mean motion.

It is not generally recognized that the uncertainty in the position of a time line might hamper the evaluation of its motion. If, for example, at the wire the local instantaneous fluid velocity is directed wallwards, the bubble which is part of the time line moves into a region with a mean streamwise velocity which is lower than the one at the position of the wire, and, consequently, moves slower than a bubble which stayed in the plane of the wire. An investigator observing the slower moving bubble might therefore conclude that a low-velocity region is present at the position of the wire, which obviously is erroneous.

This example again illustrates that one should be careful in interpreting fluid-marker data in terms of flow structure, and that alternative hypotheses are highly desirable in order to test the usefulness of the prevailing ones.

May this be as it is, the conclusion of the structural analysis of our time-line data is that near-wall turbulence is quasi-periodical in spanwise direction, and that the mean values represent a broad range of values. This is in agreement with the general view.

As to alternative hypotheses on the origin of spatial periodicity in hydrogen-bubble time-line patterns in near-wall turbulence, one might consider the periodicity to be the direct effect of vibration modes of the wire which are excited by random fluctuations in the drag force on the wire. If so, observations which are interpreted as the feature of near-wall turbulence should be interpreted as the feature of forced vibrations in a string. One might also consider that, when time lines are used to visualize homogeneous and isotropic turbulence, due to the random fluid motions a structure will appear in the time-line patterns (see e.g. Monin and Yaglom, 1975, section 24.5). Obviously, no investigator would conclude that homogeneous and isotropic turbulent flow is quasi-periodical.

Fortunately, formulating and testing alternative hypotheses is beyond the scope of this thesis, and we will stick to the prevailing ones.

Chapter 3

Time evolution of low-velocity regions in a turbulent boundary layer

The time evolution of the fluid velocity in the low-velocity regions of near-wall turbulence is found by connecting the velocity extremes in the consecutive velocity profiles determined from the motion of a hydrogen-bubble time-line. It appears that the flow in a low-velocity region can be treated as an almost parallel and time-independent viscous basic flow, and that a sinusoidal profile may model its shear layer. A stability analysis of this basic flow shows that always one unstable mode exists. The behaviour of the growth rate of this mode as a function of the parameters of its basic flow is in agreement with the one found experimentally, and suggests that in practise this mode is a temporal one. Furthermore, it is found experimentally that the distance between two low-velocity regions seems to depend on the 'age' of the time line from which the velocity profile is determined.

3.1 The two-dimensional treatment of a low-velocity region

Near the wall the structure of a turbulent boundary layer is dominated by the presence of alternating regions of low and high-velocity fluid. The low-velocity regions are generally known as low-speed streaks, and are spaced at a distance λ_z (Kline e.a., 1967). A top view of the boundary layer (i.e. a cross cut in the xz plane) shows that the low-velocity regions meander over ranges of the order of their width, are very persistent, and extend for large distances in streamwise direction (Smith and Metzler, 1983; Blokland and Krishna Prasad, 1984). On the other hand, a side view (i.e. a cross cut in the xy plane) shows that the low-velocity regions migrate slowly away from the wall as they move downstream, and occasionally lift up in a more rapid motion. In a later stage the lifted low-velocity fluid undergoes oscillations, and finally breaks up into smaller scales (Kline e.a., 1967; Kim e.a., 1971; Corino and Brodkey, 1971). Associated with the oscillation motion is the streamwise wavelength λ_x.

Blackwelder and Swearingen (1989) suggested a mechanism for the oscillation stage by considering the instability of the shear layer which forms the interface between the low-velocity fluid in the streak and the surrounding high-velocity fluid. (A flow is said to be unstable if a disturbance is amplified; by definition the perturbation is the resulting divergence from the undisturbed flow.) By assuming a hyperbolic-tangent profile for the shear layer, inviscid stability theory to be valid, and the most amplified wavelength to correspond to the observed one, Blackwelder and Swearingen argued that there is a relation between the length scale Δ associated with the spanwise velocity gradient in the flow and the streamwise wavelength λ_x of the perturbation: $\lambda_x = 5\pi\Delta$.

This result leads to two hypotheses. First, since the length scale Δ of the shear

layer is related to the spanwise wavelength λ_z of the flow, it follows that the spanwise and the streamwise wavelengths are related: $\lambda_x \propto \lambda_z$. Second, if it is assumed that the perturbations travel with a convection velocity u_c, an observer stationary in the flow will find a time interval $T \propto \lambda_x/u_c$ between the passage of two perturbations. If it is subsequently assumed that 'bursts' are travelling perturbations, it follows that the time interval between two 'bursts' is related to the streamwise wavelength λ_x, and therefore to the spanwise wavelength λ_z, i.e. the streak spacing. (Note also that if the convection velocity u_c is a function of the distance to the wall, the time interval between two 'bursts' too depends on the distance to the wall.) Although Blackwelder and Swearingen did not propose to relate both the streamwise wavelength and the time interval between two 'bursts' to the streak spacing, these ideas are a direct consequence of their work.

Moreover, the ideas of Blackwelder and Swearingen (1989) lead to a model which makes it possible to treat in a the quasi-deterministic manner localized regions in near-wall turbulent flow. Therefore, consider a low-velocity region, and decompose its instantaneous flow into a basic flow and a perturbation. When a classic stability analysis is performed on this configuration, it will provide both the most amplified wavenumber and the growth rate of the perturbation as a function of the parameters of the basic flow. Consequently, if one has detected a low-velocity region and determined its basic-flow parameters, it might be possible to predict the magnitude of the perturbation at a later instant. At this later instant the instantaneous flow follows by superimposing the basic flow and the perturbation.

Evidently, this strategy only works if the low-velocity region exists long enough to allow the decomposition of the flow into a parallel stationary basic flow and a two-dimensional time-dependent velocity perturbation. Also, we emphasize that the internal shear-layer which surrounds the low-velocity region is principally three-dimensional. Fortunately, inviscid stability theory shows that three-dimensional instabilities grow more slowly than two-dimensional instabilities (Squire's theorem; see Drazin and Reid, 1981, p. 129), which suggests that two-dimensional instabilities determine the dynamics of the low-velocity region. Therefore, a proper treatment of the two-dimensional stability of a low-velocity region should consider the stability in both the xz and the xy plane, and address the coupling between the two. Consequently, our strategy is too simple to give a full account of near-wall turbulence, but we believe that it captures enough of the essential physics.

This chapter deals with experimental and theoretical considerations on the time evolution of the flow in the low-velocity regions of near-wall turbulence. First, we present hydrogen-bubble time-line measurements which quantify the basic flow and the life time of the low-velocity regions (section 3.2). Next, we develop a model which describes the instability of low-velocity regions in terms of its basic-flow parameters (section 3.3). Finally, we compare experiment and theory, and evaluate our findings (section 3.4).

3.2 Measurements on the evolution of low-velocity regions[7]

3.2.1 The connectivity of extremes and inflection points

In order to study the time evolution of the low-velocity regions which are present in the velocity profiles obtained from time-line patterns, we must determine the connectivity of the velocity extremes and the inflection points. (The scheme to detect these points is described in section 2.5.2.)

First, we consider the connectivity algorithm for the extremes (figure 3.1). Let $z_E^{(i,j)}$ denote the position of extreme j in velocity profile i, with $i = 1, 2, ..., M$ (M is the number of velocity profiles) and $j = 1, 2, ..., N_i$ (N_i is the number of extremes in profile i). The sign of the second velocity derivative $\partial^2 u_E^{(i,j)}$ determines whether the extreme is a maximum ($\partial^2 u_E^{(i,j)} < 0$) or a minimum ($\partial^2 u_E^{(i,j)} > 0$). Furthermore, let

$$d_{jk} = |z_E^{(i,j)} - z_E^{(i+1,k)}| \tag{3.1}$$

(with $k = 1, 2, ..., N_{i+1}$) be the 'distance' between extreme j in profile i and extreme k in profile $i + 1$, with as a constraint

$$\partial^2 u_E^{(i,j)} \, \partial^2 u_E^{(i+1,k)} > 0. \tag{3.2}$$

Then the smallest 'distance' between the extreme k^* in profile $i + 1$ and the extreme j in profile i is

$$d_{jk^*} = \min(d_{jk})_n \tag{3.3}$$

where $\min(d_{jk})$ is the smallest term of the sequence d_{jk}. By introducing the threshold

$$d_{thr} = \min(|z_E^{(i,j)} - z_E^{(i,j+1)}|, |z_E^{(i,j)} - z_E^{(i,j-1)}|), \tag{3.4}$$

the condition for the extreme k^* in profile $i + 1$ to be connected with the extreme j in profile i is

$$d_{jk^*} < d_{thr}. \tag{3.5}$$

This condition ensures that the extreme j in profile i is connected with the 'nearest' extreme in profile $i+1$, without exceeding the limits which are imposed by the positions of its neighbours $j + 1$ and $j - 1$ (see figure 3.1).

A set of connected velocity extremes is defined to be a low-velocity region if the extremes are velocity minima, and a high-velocity region if the extremes are velocity maxima. Two adjacent sets of connected velocity extremes form a pair of low and high-velocity regions. A pair of low and high-velocity regions is said to merge at profile l if at profile $l + 1$ no extremes exist that can be connected to the extremes of the pair. A pair is said to split at profile l if at profile l extremes exist that cannot be connected to the extremes of the pair which are present in profile $l - 1$ (figure 3.2). The length L_{ij}

---

[7]This section was presented at the First European Fluid Mechanics Conference, Cambridge, September 1991. The material in section 3.2.2 was also presented at Euromech Colloquium 279, Delft, July 1991
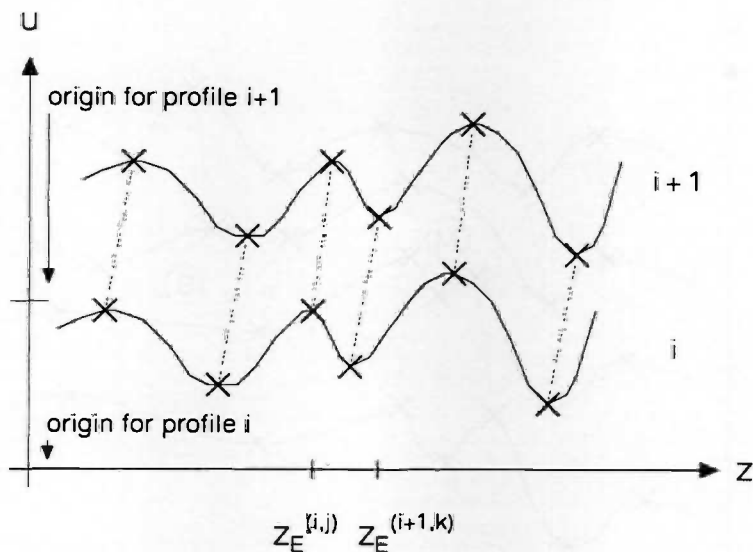
Figure 3.1: The positions z_E of the extremes ($\times$) in the profile pattern which consists of the velocity profiles i and $i+1$. The connectivity algorithm ensures that the extreme j of profile i is connected with the 'nearest' extreme of profile $i+1$.

of the low/high-velocity region which starts at extreme j in profile i is determined by the number of velocity profiles that is actually connected ($L_{ij} \leq M$).

In an analogous way, the connectivity algorithm for the inflection points $z_{IP}^{(i,j)}$ can be described; the only difference being the measurement of the distance d_{jk} between inflection point j in profile i and inflection point k in profile $i+1$. This distance is to be determined with as a constraint

$$\partial u_{IP}^{(i,j)} \; \partial u_{IP}^{(i+1,k)} > 0, \tag{3.6}$$

with $\partial u_{IP}^{(i,j)}$ the velocity derivative in inflection point j of profile i. A set of connected inflection points is defined to be a shear layer. For the definitions of the length, the splitting and the merging of a shear layer we refer to the corresponding definitions for the velocity extremes.

The basic flow of a low-velocity region is defined to be the inclusion of the low-velocity region, the shear layers adjacent to the low-velocity region, and the high-velocity regions adjacent to those shear layers (figure 3.3). Therefore, each low-velocity region has two basic flows associated with it, which in general are not symmetrical.
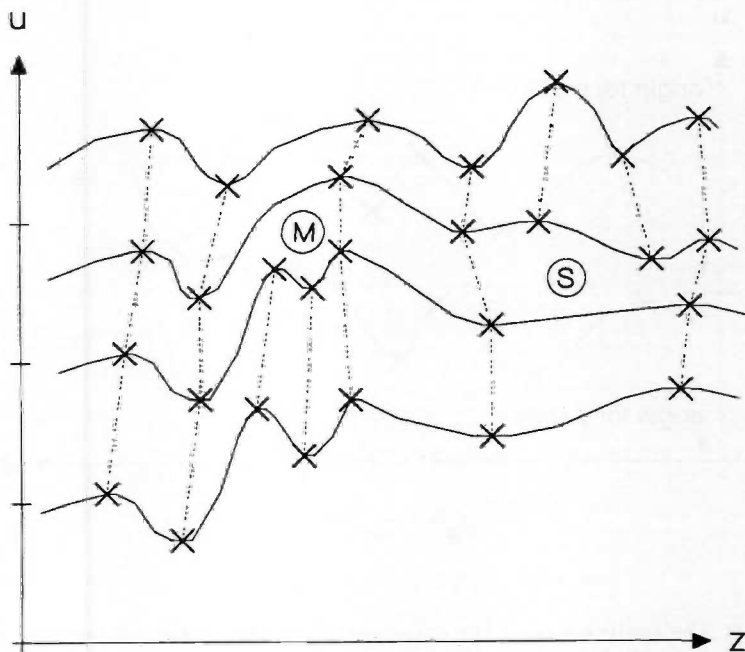
Figure 3.2: The connectivity of the velocity extremes ($\times$) in a velocity-profile pattern. Indicated are the splitting (S) and the merging (M) of a low-velocity region.

In general, a velocity gradient can be described in terms of three parameters: the local mean fluid velocity U_b, the magnitude (i.e. the velocity difference) U_0 and the wavenumber $k_z = 2\pi/\lambda_z$, with λ_z the wavelength (see figure 3.4). When these parameters are used to describe the flow in a low-velocity region, they will be referred to as the basic-flow parameters of the low-velocity region. (In section 3.3 the basic-flow parameters of a low-velocity region are used to analyse its stability.)

In the following, we determine the parameters of the basic flow which is located at the right of the low-velocity region that starts in the extreme j of profile i (i.e. $\partial^2 u_E^{(i,j)} > 0$ and $\partial^2 u_E^{(i,j+1)} < 0$). Let $z^{(m,n^*)}$ denote the set of points which are connected to the point n (either an extreme or an inflection point) in profile m, and L_{mn} the number of connected points. Then the wavenumber of the low-velocity region is defined to be

$$k_z^{(i,j)} = \frac{1}{L_{ij}} \sum_{l=i}^{i+L_{ij}-1} \frac{\pi}{\left| z_E^{(l,j^*)} - z_E^{(l,j^*+1)} \right|} \tag{3.7}$$
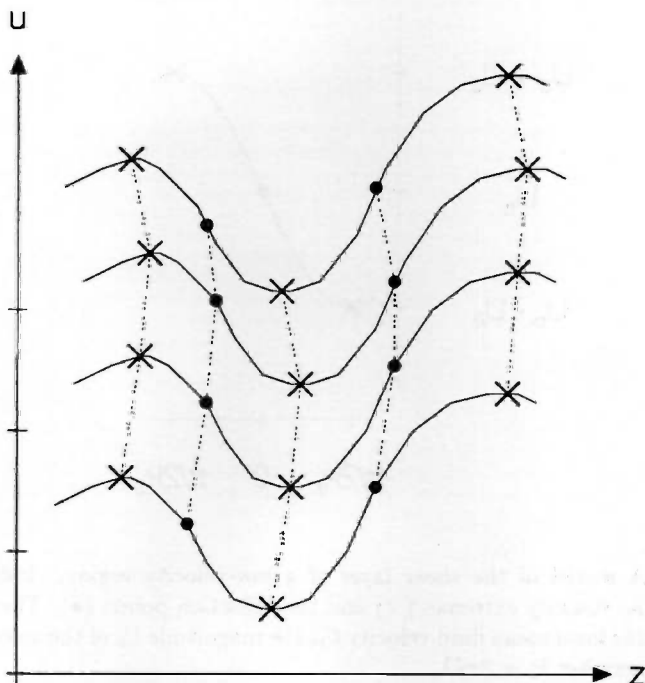
Figure 3.3: The basic flows of a low-velocity region consist of the low-velocity region itself, and the adjacent shear layers and high-velocity regions. The low-velocity region is the set of connected velocity minima, the two shear layers are the two sets of connected inflection points, and the two high-velocity regions are the two sets of connected velocity maxima. Indicated are the positions of the velocity extremes ($\times$) and the inflection points ($\bullet$).

with $z_E^{(m,n)}$ the position of the extreme n of profile m. Its local mean fluid velocity is defined as

$$U_b^{(i,j)} = \frac{1}{L_{ij}} \sum_{l=i}^{i+L_{ij}-1} u_{IP}^{(l,j^*)}, \tag{3.8}$$

with $u_{IP}^{(m,n)}$ the fluid velocity in the inflection point which is confined between the extremes n and $n+1$ of profile m. (Note that the inflection point with label j must be located at the right of the velocity minimum with label j: $z_E^{(i,j)} < z_{IP}^{(i,j)}$.) Similarly, the
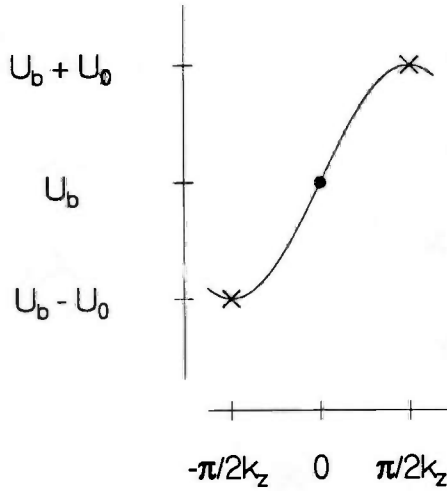
Figure 3.4: A model of the shear layer of a low-velocity region. Indicated are the positions of the velocity extremes ($\times$) and the inflection points ($\bullet$). The basic-flow parameters are the local mean fluid velocity U_b, the magnitude U_0 of the velocity difference, and the wavenumber $k_z = 2\pi/\lambda_{z}$.

magnitude of the low-velocity region is defined to be

$$U_0^{(i,j)} = \frac{1}{L_{ij}} \sum_{l=i}^{i+L_{ij}-1} |u_E^{(l,j^*)} - u_E^{(l,j^*+1)}|, \tag{3.9}$$

with $u_E^{(m,n)}$ the fluid velocity in the extreme n of profile m.

In addition to these parameters, we define the length scale of the velocity gradient of the low-velocity region which is located at the right of the extreme j of profile i:

$$\Delta^{(i,j)} = \frac{1}{L_{ij}} \sum_{l=i}^{i+L_{ij}-1} \frac{u_E^{(l,j^*+1)} - u_E^{(l,j^*)}}{\partial u_{IP}^{(l,i^*)}}, \tag{3.10}$$

with $\partial u_{IP}^{(m,n)}$ the velocity gradient in the inflection point that is confined between the extremes n and $n + 1$ of profile m. (Note that this definition of Δ yields values twice as large as the one of Blackwelder and Swearingen, 1989; see section 2.5.1.)

The equations for the basic-flow parameters and the gradient length-scale on the left of the low-velocity region (i.e. extremes such that $\partial^2 u_E^{(i,j)} > 0$ and $\partial^2 u_E^{(i,j-1)} < 0$) are similar to (3.7)...(3.10), provided that $j^* - 1$ is substituted for $j^* + 1$.

Figures 3.5f and 3.5g illustrate how low/high-velocity regions and shear layers are identified by connecting the velocity extremes and the inflection points that are present in the velocity-profile pattern determined from a moving time line. (For a description of the method to obtain a velocity-profile pattern we refer to section 3.2.2.) These figures show that the time evolution of the structure of a spanwise velocity profile is determined by the connectivity of the velocity extremes and the inflection points, and hence by the presence of low/high-velocity regions and shear layers.

3.2.2 The experimental conditions and the data reduction

A general description of the experimental facility is given in section 2.4.1. In the present experiments hydrogen-bubble time-lines were generated with the wire mounted at $y^+ \approx$ 23 in the turbulent boundary layer ($U_\infty \approx 17.1$ cm/s and $\nu \approx 1.1 \ 10^{-6}$ m^2/s). By fitting the fluid velocities near the wall to the linear law, it was found that $u_* \approx 8.5$ mm/s. The time lapse between two time-line generations was 1 s, which proved to be sufficient to have at most one time line in the viewing field. Time lines were recorded during a period of approximately 300 s.

For the description of the pre-processing involved in the creation of binary time-line pictures, we refer to sections 2.4.2 and 2.5.2. The processed recordings of a time line at consecutive instants are used to create a picture that contains the position of the time line at intervals of 40 ms (figure 3.5a and 3.5c).   To avoid the merging of the recordings of the time line due to small displacements, the 'inclusive or' operation is performed with a preshift which adds a multiple of 16 grid units to the position of each picture. In general, due to the local fluid velocity and the extent of the viewing field, 6 recordings of the time line are present in one picture (figure 3.5b and 3.5d). In each scanline the distance between the time lines is measured and compensated for the preshift. This data is used to compute the corresponding $u(z)$ velocity profiles via equation (2.19), which gives a profile pattern in which each profile contains the estimate of the fluid velocity at the position of the wire at a specific time instant. (The consecutive time instants occur in intervals of 40 ms.)

After the restoration stage the profiles are median and lowpass filtered in order to remove small-scale velocity fluctuations. Velocity extremes and inflection points are detected by differentiating the least-square splines that approximate the datapoints of each profile (see section 2.5.2). Due to the character of the least-square splines, the detection stage introduces an additional amount of smoothing, which unfortunately is hard to quantify. Figure 3.5e shows this effect: some of the extremes and inflection points are separated from the spline. In each profile the positions of the velocity extremes z_E, together with the fluid velocities u_E and the values of the second velocity derivative $\partial^2 u_E$ in the extremes are stored for post-processing purposes. Similarly, the positions of the inflection points z_{IP}, and the corresponding values of the fluid velocity u_{IP} and the velocity derivative ∂u_{IP} are stored. Finally, the extreme and the inflection point connectivity schemes (see section 3.2.1) are used to detect the low and high-velocity regions and the shear layers (figure 3.5f and 3.5g).

(a)

(b)
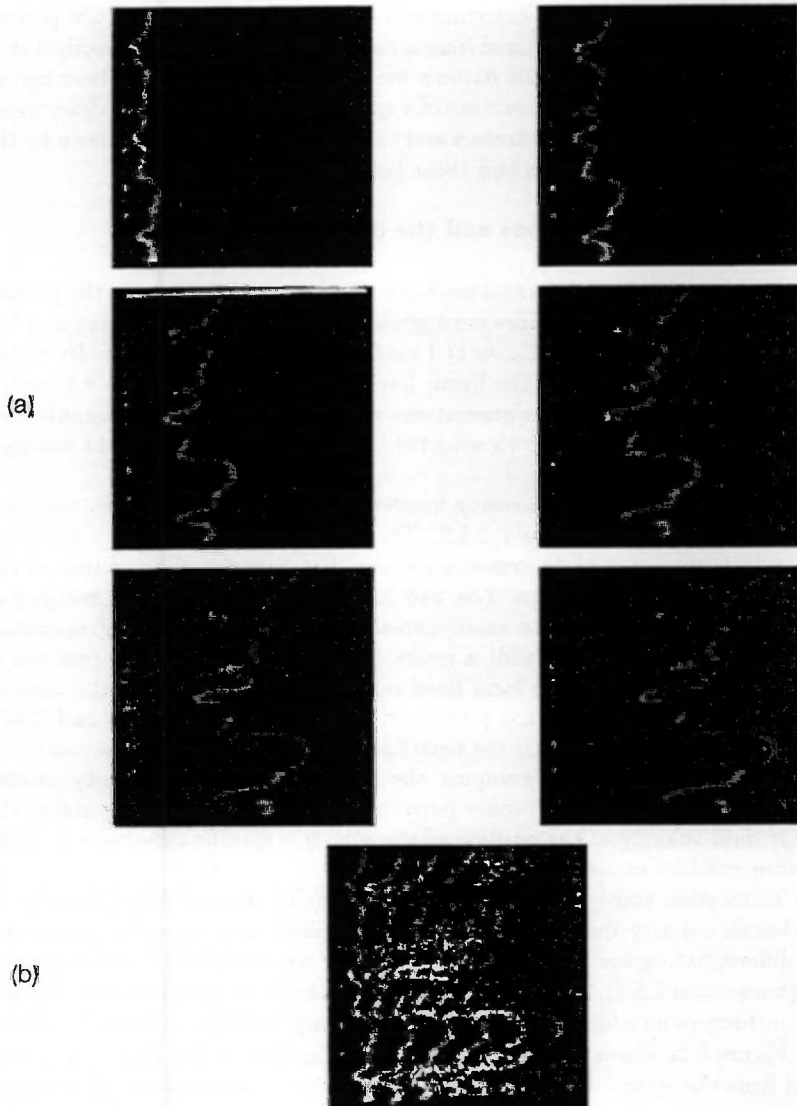
Figure 3.5: The stages involved in the detection of low/high-velocity regions and shear layers in a spanwise velocity-profile pattern. (a) Six consecutive recordings of the position of a time line. (b) Composite grey-value picture of the lime lines. Three 'low-speed streaks' can be identified visually.
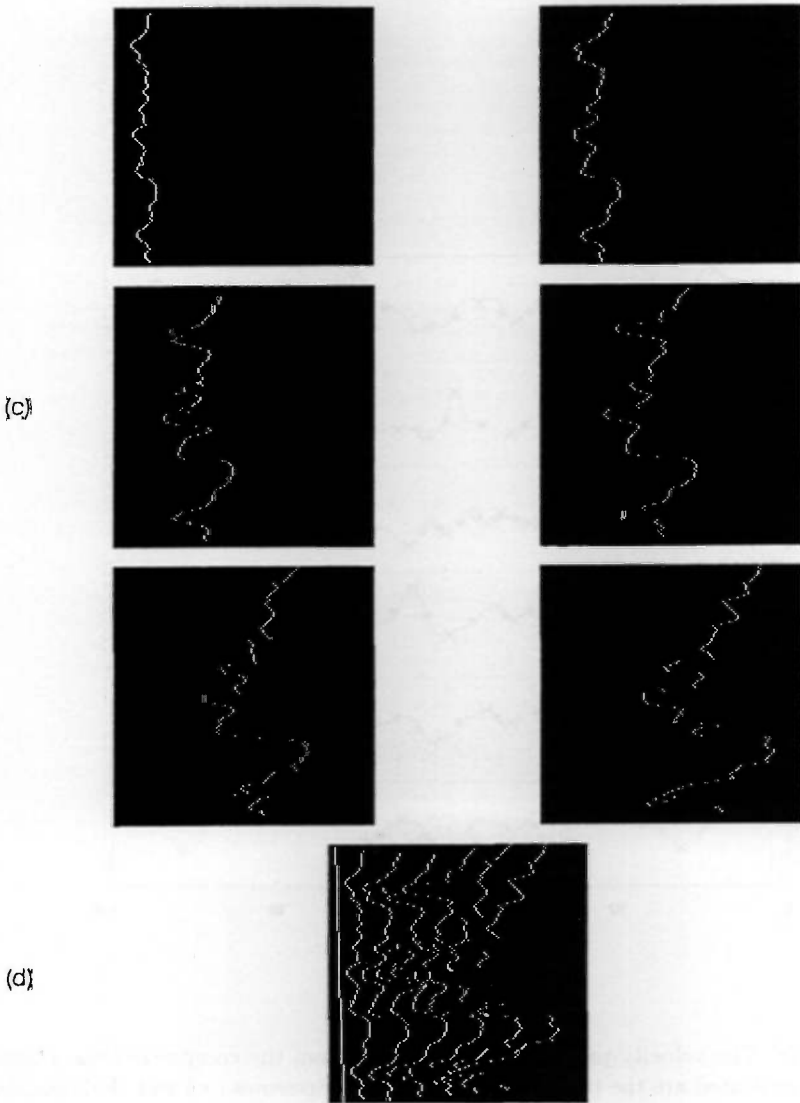
Figure 3.5: (c) Binary versions of the time-line images. (d) Composite binary image, obtained by taking the 'inclusive or' of the binary time-line images.
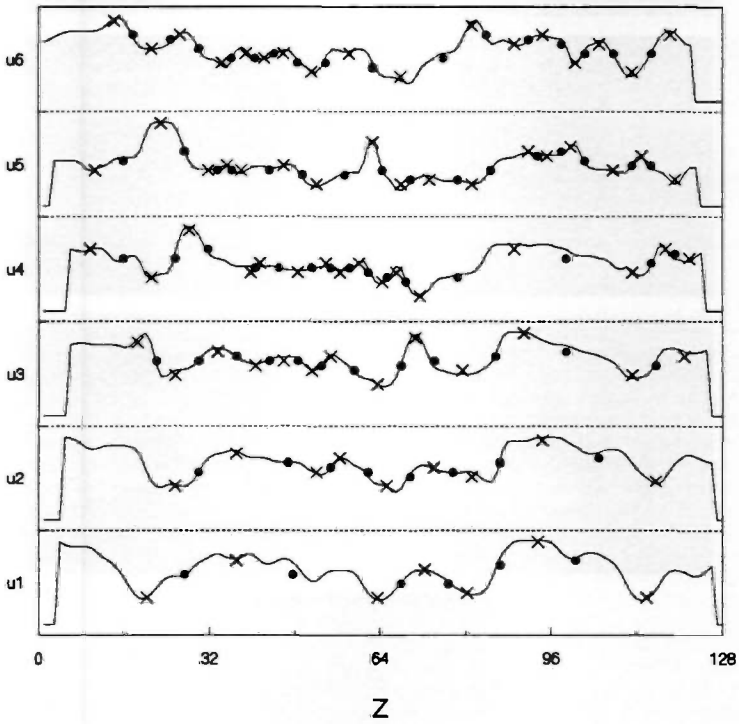
Figure 3.5: (e) The velocity-profile pattern obtained from the composite binary time-line image. Indicated are the positions of the velocity extremes ($\times$) and the inflection points ($\bullet$).
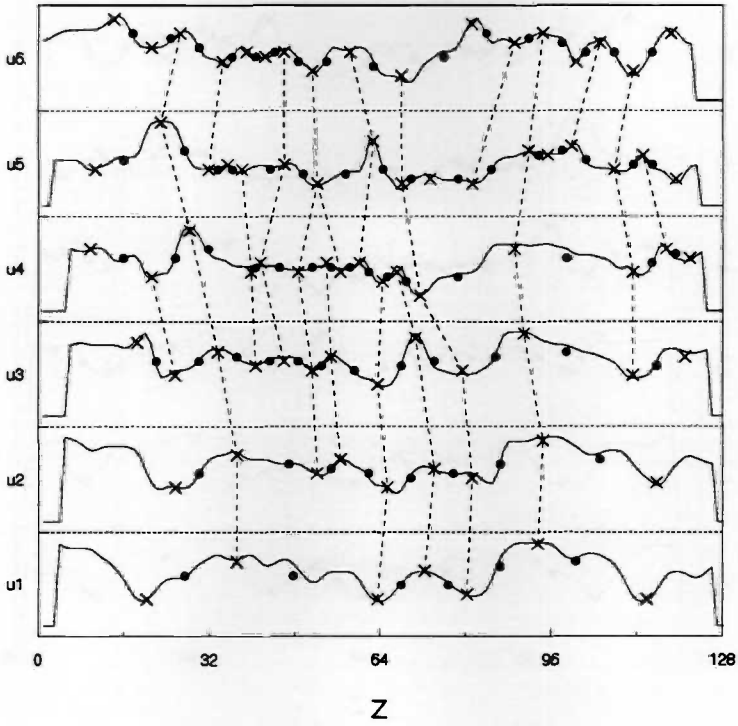
Figure 3.5: (f) The connectivity diagram of the extremes showing the detected low and high-velocity regions.
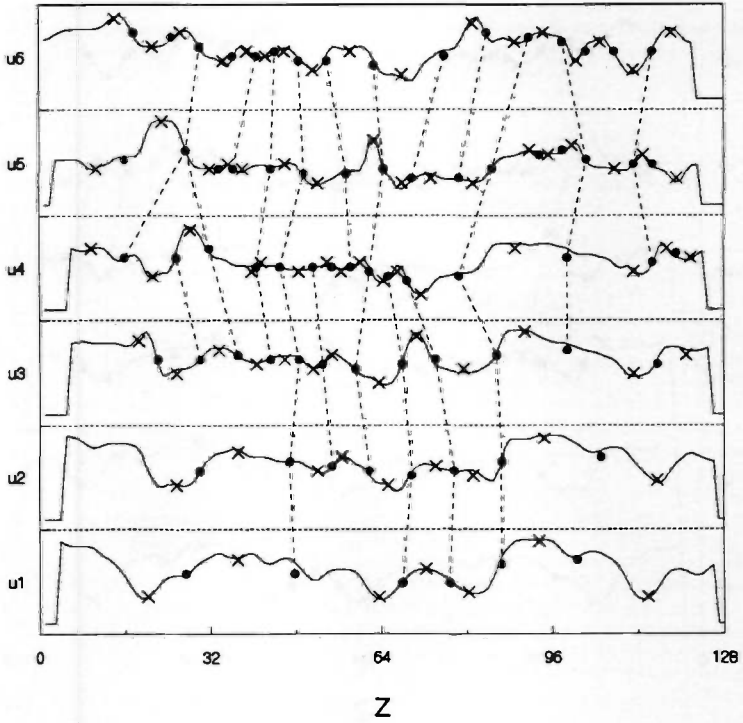
Figure 3.5: (g) The connectivity diagram of the inflection points showing the detected shear layers.

A comparison of figures 3.5b and 3.5f shows that the positions of the detected low-velocity regions agree reasonably well with those of the 'low-speed streaks' that are observed visually.

3.2.3 The time evolution of the structure of spanwise velocity profiles

In order to determine the time evolution of the flow in the low-velocity regions of near-wall turbulence, we generated approximately 300 time lines, and managed to obtain 85 time-line patterns. This set of patterns yielded 22 velocity profile patterns which proved to be consistent.

In these patterns we selected the low-velocity regions with length 5 and 6, which yielded an amount of 40 low-velocity regions. Subsequently, we determined the basic-flow parameters U_b (the local mean fluid velocity), U_0 (the magnitude) and k_z (the wavenumber) of these low-velocity regions, and the length scale Δ of the velocity gradient. (See section 3.2.1 for the definitions of these parameters).

Figure 3.6 presents the correlations of U_b^+, U_0^+ and k_z^+. (Recall that each low-velocity region has two basic flows associated with it; therefore figure 3.6 contains 80 datapoints.) The ensemble average $< U_b^+ > \approx 9.4$ is in agreement with the mean fluid velocity at $y^+ \approx 23$. Similarly, the variance of U_b^+ is of the order of the variance of the fluid velocity. The magnitudes of the low-velocity regions have as an ensemble averaged value $< U_0^+ > \approx 1.7$, and a standard deviation of 23% of $< U_0^+ >$. Since the value of the corresponding correlation coefficient is 0.08, it follows that there is no correlation between the values of U_b^+ and U_0^+. The ensemble average of the wavenumber is $< k_z^+ > \approx 4.5 \ 10^{-2}$, which corresponds to $< \lambda_z^+ > \approx 140$. Compared to the mean width of the low-velocity regions, as determined from the distance between neighbouring inflection points (see section 2.5.3), this value is considerably larger. Most probably, this is caused by the smoothing due to the use of the filters and the least-square splines. The median value of k_z^+ is of the order of its ensemble average, which indicates that the wavenumbers are not skewed towards the lower values. (Note that this is counter to our finding in section 2.5.3.) The correlations of k_z^+ versus U_b^+, and k_z^+ versus U_0^+ show that these parameters too are not related; the values of the correlation coefficient are -0.44 and -0.11, respectively.

The ensemble average of the gradient length scale is $< \Delta^+ > = 24$, which is somewhat larger than the value of 20 found by Blackwelder and Swearingen (1989). (Recall that our definition (3.10) of Δ yields values twice as large as Blackwelder's; see sections 2.5.1 and 3.2.1.) This larger value of $< \Delta^+ >$ is a direct consequence of our small wavenumber $< k_z^+ >$. Figure 3.7 presents the correlation of Δ^+ and the wavenumber k_z^+. By substituting the basic-flow profile $U(z) = U_b + U_0 \sin k_z z$ in the definition (3.10) of Δ, and non-dimensionizing the result with wall units, we find the relation $\Delta^+ = 2/k_z^+$. The mean deviation of the values of Δ^+ with respect to the 'theoretical' value is 1%, which shows that the agreement is quite good. We therefore conclude that the gradient length scale Δ is not independent of k_z. Unfortunately, Blackwelder and Swearingen (1989) did not measure k_z in their dataset, so we can not compare our findings with theirs. Furthermore, we conclude that a sinusoidal profile can be used to model the
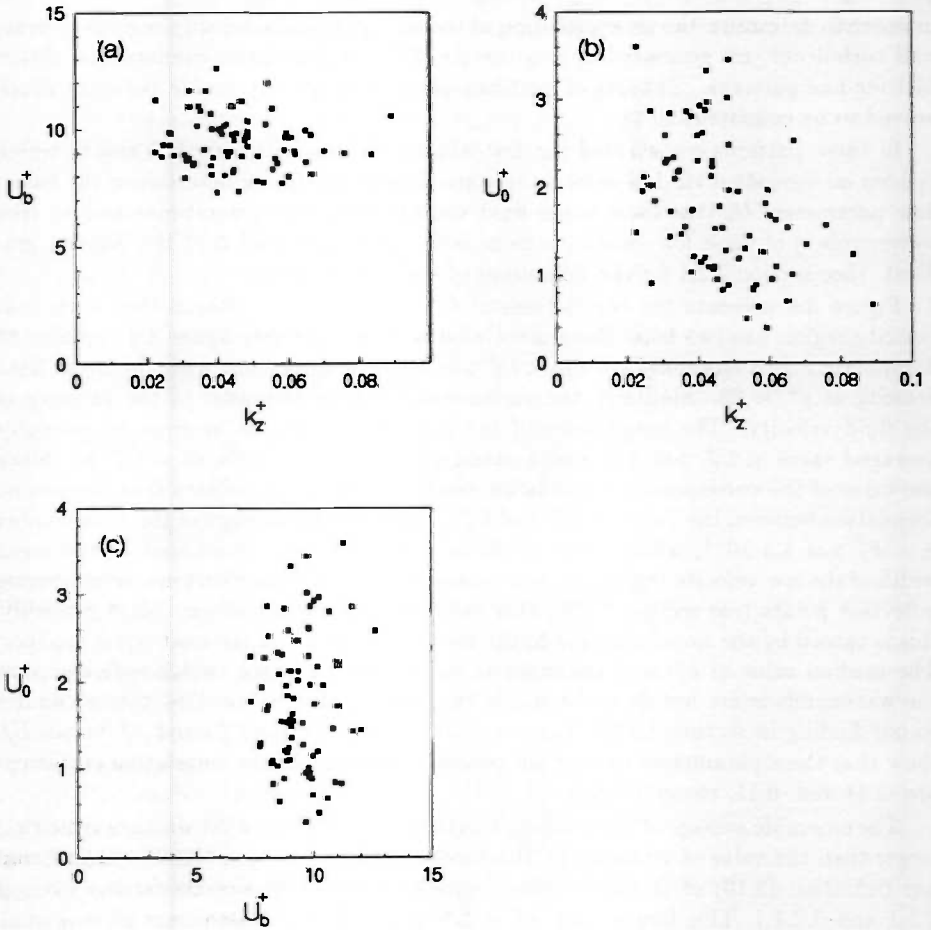
Figure 3.6: Correlations of the basic-flow parameters non-dimensionized with the viscous scales u_* and l_*; (a) U_b^+ versus k_z^+, (b) U_0^+ versus k_z^+, and (c) U_0^+ versus U_b^+.
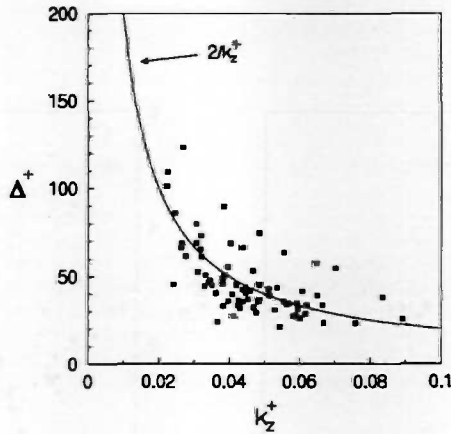
Figure 3.7: The gradient length scale Δ^+ as a function of the wavenumber k_z^+ of the basic flow. Indicated is the relation which is valid for a sinusoidal basic flow. The lengths are non-dimensionized with the viscous length scale l_*.

shear layer of a low-velocity region.

The asymmetry of a low-velocity region is expressed by the ratio of the basic-flow parameters in the two parts of the low-velocity region; e.g. k_z^R/k_z^L (with k_z^R such that $z_E > z_{IP}$) specifies the asymmetry in the wavenumber. The more this ratio diverges from 1, the more the low-velocity region is asymmetrical. Figure 3.8 shows that there are almost no symmetric low-velocity regions: just 2.6% of the low-velocity regions has k_z^R/k_z^L, U_b^R/U_b^L or U_0^R/U_0^L in the range 0.9...1.1. The standard deviations of these ratios with respect to 1.0 are 0.47, 0.14 and 1.41, respectively. This illustrates that the local mean velocity U_b is the most symmetric parameter. More surprising however is the large asymmetry in U_0, which shows that large and small velocity differences may exist in flow regions which are close together. Consequently, we conclude that a model of a low-velocity region must treat the two shear layers separately. The correlations of k_z^R/k_z^L, U_b^R/U_b^L and U_0^R/U_0^L also show that there is some indication that large wavenumbers k_z occur together with small magnitudes U_0, whereas small wavenumbers occur together with large magnitudes. (The corresponding correlation coefficients are -0.77 and -0.61, respectively.)

The Reynolds number $R = \mathcal{U}\mathcal{L}/\nu = 2\pi U_0/\nu k_z$ is a measure of the basic flow associated with a low-velocity region. Figure 3.9a presents the values of R for the detected low-velocity regions. It is clear that a large range of values occurs: 90% of the R's lies in the range 60...530. The ensemble average is $<R>\approx 280$, and the standard deviation is 62% of $<R>$. These low Reynolds numbers force us to conclude that the stability
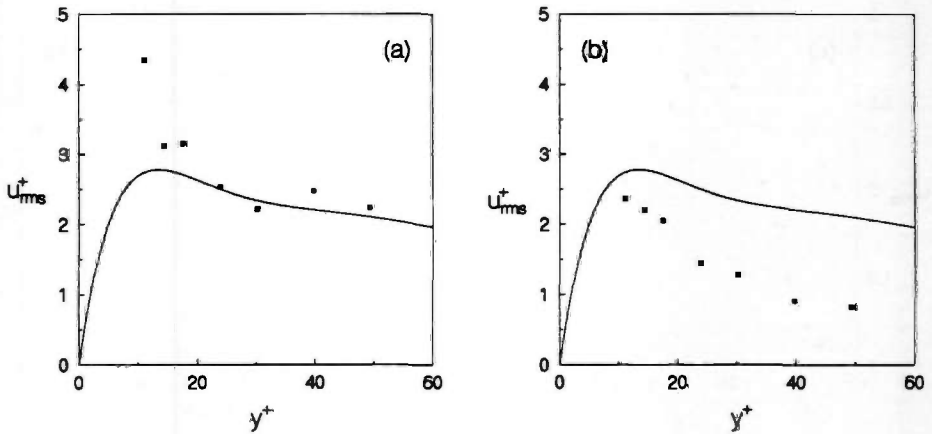
Figure 2.11: The turbulence intensity $\sqrt{\overline{u_0'^2}}/u_*$ in the turbulent boundary layer as measured with hydrogen-bubble time-lines; (a) values based on the intuitive estimate (2.39) of the velocity variance, (b) values based on the correct estimate (2.35) of the velocity variance. The curves denote the least-square fit of the hot-film data.

The low-speed streaks appear as local minima in the spanwise profiles of the streamwise velocity. Associated with these minima are inflection points that mark the position of the shear layers that surround the low-speed streaks. Since these shear layers might be unstable (Rayleigh's and Fjørtoft's theorems for inviscid flows, see Drazin and Reid, 1981, p. 131 and 132), the 'bursting of low-speed streaks' (Kline e.a., 1967) is hypothesized to be the sudden development of hairpin vortices from unstable streaks (Smith, 1984). However, this process is not well understood. To explain some of its dynamics, it was suggested to model a spanwise velocity gradient with a hyperbolic-tangent profile (Blackwelder and Swearingen, 1989). This showed that there is a relation between the length scale Δ associated with this gradient and the streamwise wavelength λ_x of the disturbances in the flow. Experimentally it was found that $<\Delta^+> \approx 5...15$ (Blackwelder and Swearingen, 1989), where $2\Delta = \mathcal{U}/\partial U$ with $\mathcal{U}$ the velocity difference in the shear layer and ∂U the velocity gradient in the inflection point.

The quantitative analysis of hydrogen-bubble time-line visualizations gives instantaneous local velocity profiles (Schraub e.a., 1965). Compared to the use of multiple sensors, this technique has a finer spatial resolution, especially if digital image processing methods are used. For example, in a wind tunnel turbulent boundary layer a typical spatial resolution is $\Delta z^+ \sim 30$ for a rake of hot-wire sensors (Blackwelder and Swearingen, 1989; Antonia and Bisset, 1990), whereas in a water channel turbulent boundary layer $\Delta z^+ \sim 1$ can easily be obtained with help of appropriate image processing.
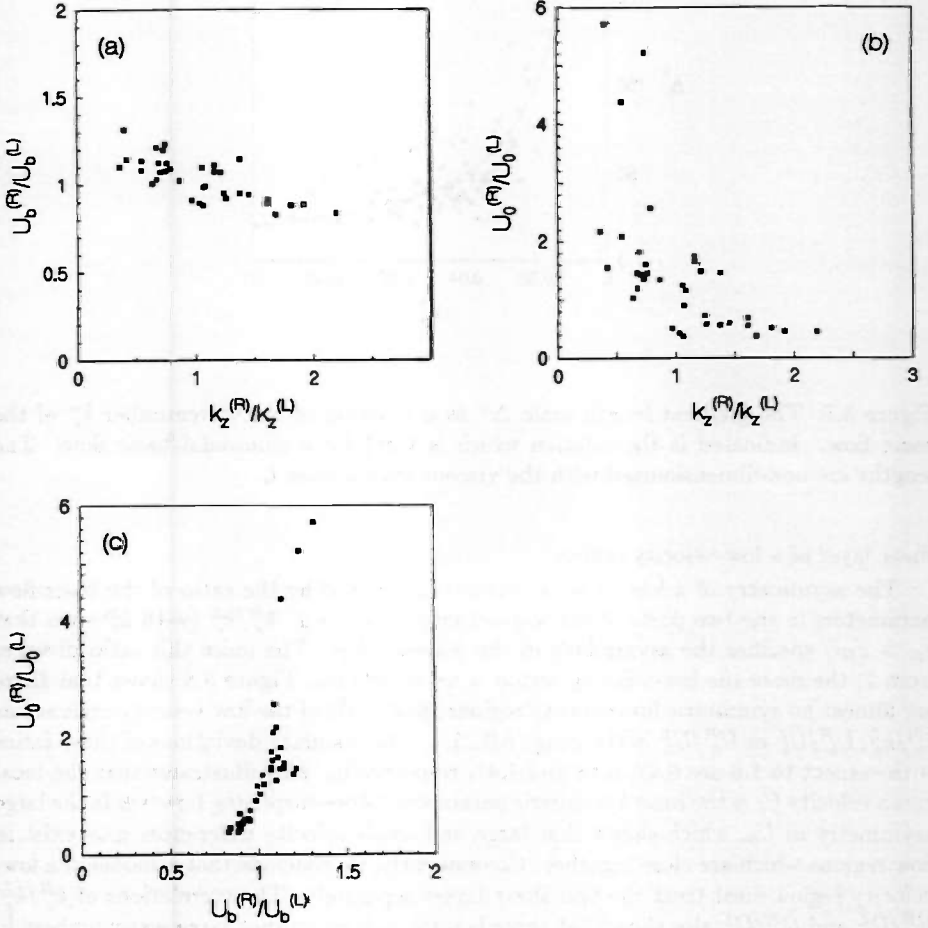
Figure 3.8: The asymmetry of the low-velocity regions as expressed by the ratio of the basic-flow parameters in the left (L) and the right (R) part of the region. Presented are correlations of the ratios of (a) U_b versus k_z, (b) U_0 versus k_z, and (c) U_0 versus U_b.
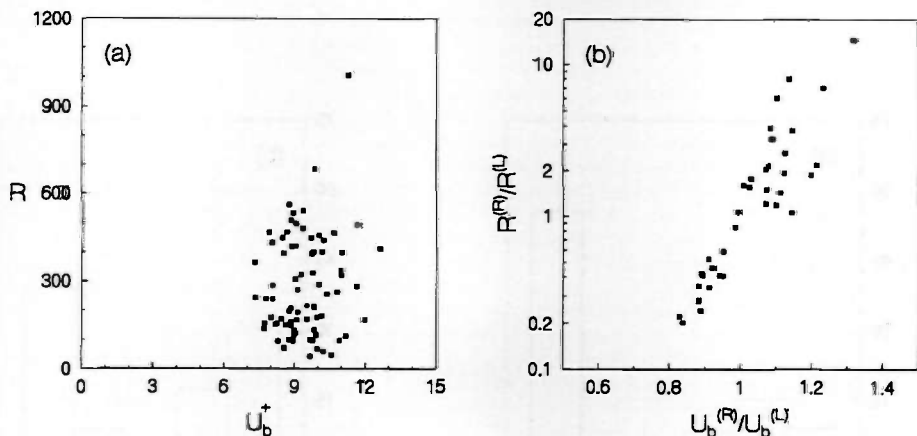
Figure 3.9: (a) The Reynolds number R of the low-velocity region as a function of the local mean velocity U_b. (b) The asymmetry of the low-velocity regions expressed in R and U_b.

of a low-velocity region must be treated via a viscous stability analysis. The Reynolds number R can also be used to express the asymmetry of a low-velocity region. Figure 3.9b shows that, generally, the lower values of R occur together with the lower values of the local mean velocity U_b. This picture is in agreement with the conclusions drawn from the parameter ratios.

On basis of these results we conclude that, at least for time lapses up to 6 time units (i.e. about $15t_*$), it is possible to treat the flow in a low-velocity region as an almost parallel and time-independent basic flow. Having said this, we complete our analysis of the low-velocity regions with length 5 and 6, and return to the total dataset.

The length of a low-velocity region is a measure of its life time. Figure 3.10 shows the distribution of the life times of the low-velocity regions that originate from a specific profile. Generally speaking, there are two peaks in each of the histograms: one corresponding to the smallest life times which are possible, and the other corresponding to the largest life time that can actually be found for the profile under consideration. The first peak indicates the presence of low-velocity regions which are short lived and have disappeared after at most 2 time steps. The second peak should correspond to the low-velocity regions which are dominately present in a profile pattern.

Figure 3.11 shows the relation between the life time of a low-velocity region and the instantaneous values of k_z^+, U_b^+ and U_0^+ that occur in the profile in which the low-velocity region originates. If a new velocity minimum has a large wavenumber (say $k_z^+ > 0.15$), it is most likely to merge immediately. On the other hand, it can achieve
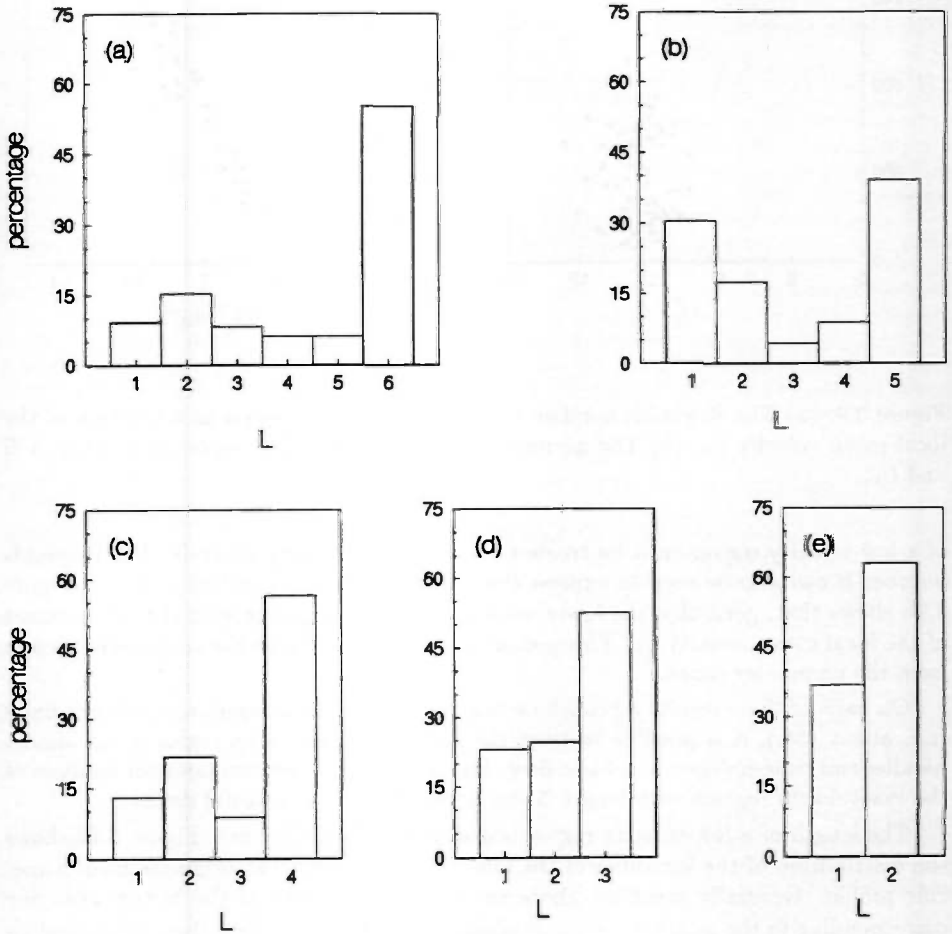
Figure 3.10: The distribution of the life times L of the low-velocity regions originating from (a) the first, (b) the second, (c) the third, (d) the fourth and (e) the fifth profile of the profile patterns.
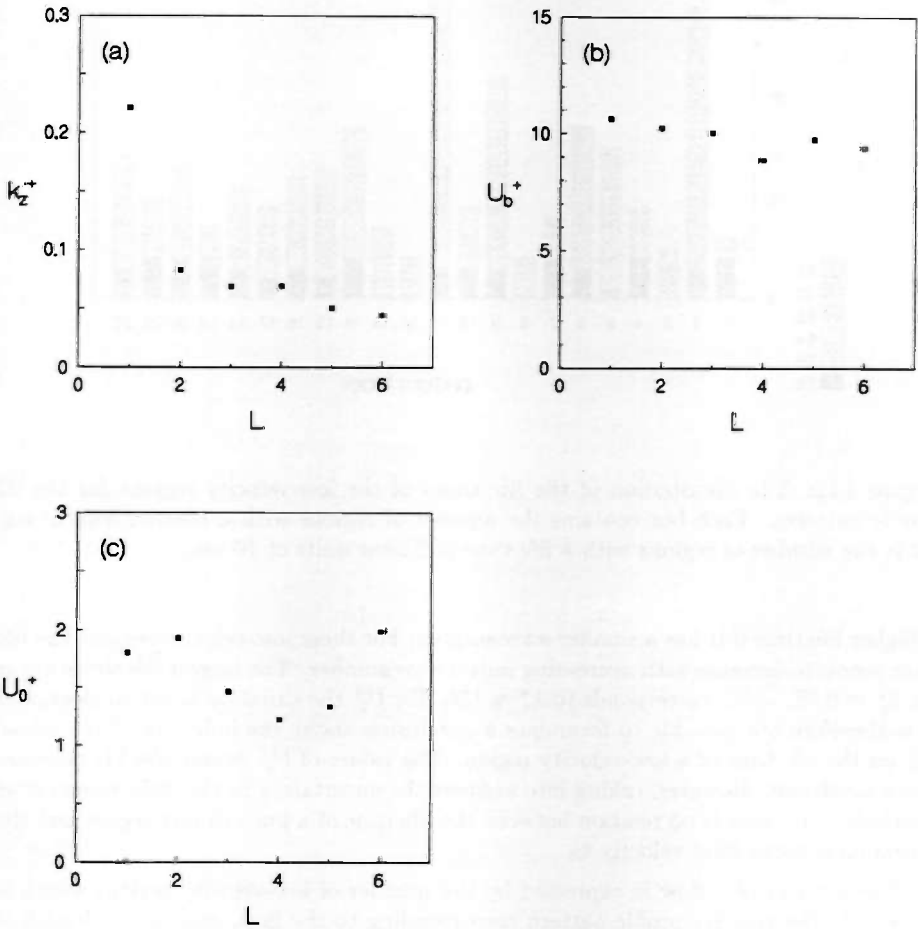
Figure 3.11: The life time L of a low-velocity region as a function of the non-dimensional basic-flow parameters (a) k_z^+, (b) U_b^+ and (c) U_0^+.
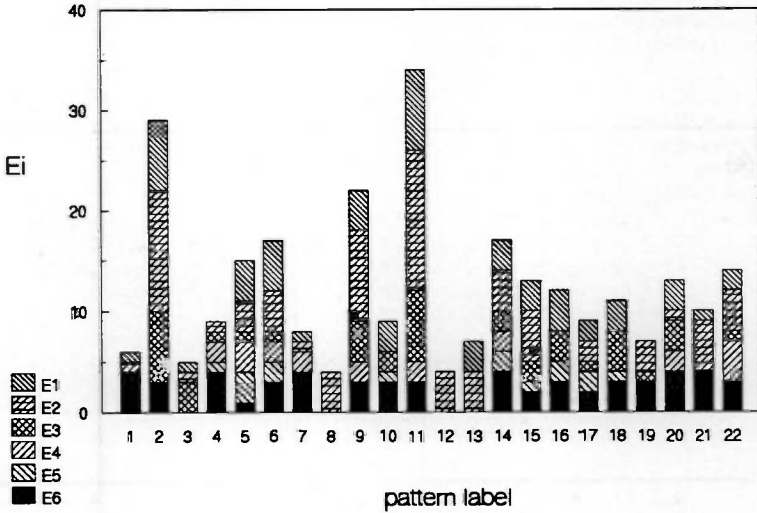
Figure 3.12: The distribution of the life times of the low-velocity regions for the 22 profile patterns. Each bar contains the number of regions with a specific length; e.g. E2 is the number of regions with a life time of 2 time units of 40 ms.

a higher life time if it has a smaller wavenumber. For these low-velocity regions the life time seems to increase with decreasing initial wavenumber. The largest life times occur for $k_z^+ \approx 0.05$, which corresponds to $\lambda_z^+ \approx 126$. For U_0^+ the situation is not so clear, and it is therefore not possible to formulate a conclusion about the influence of the initial U_0^+ on the life time of a low-velocity region. The values of U_b^+ versus the life time are more consistent. However, taking into account the uncertainty in the fluid velocity, we conclude that there is no relation between the life time of a low-velocity region and the initial local mean fluid velocity U_b.

The activity of a flow is expressed by the number of low-velocity regions which is present in the velocity-profile pattern corresponding to the flow, and by the length of individual low-velocity regions. The flow is said to be not active when the flow structure consists of long-lived low-velocity regions in the absence of noise (i.e. extremely short-lived low-velocity regions) and short-lived low-velocity regions. Figure 3.12 shows that the activity of each of the 22 profile patterns is determined by a large amount of short-lived low-velocity regions: 22% (in profile pattern 4) to 100% (in profile patterns 3, 8, 12 and 13) of the low-velocity regions have a length of 3 or less time units. However, most of the profile patterns have at least one long-lived (i.e. length 5 or 6) low-velocity region.
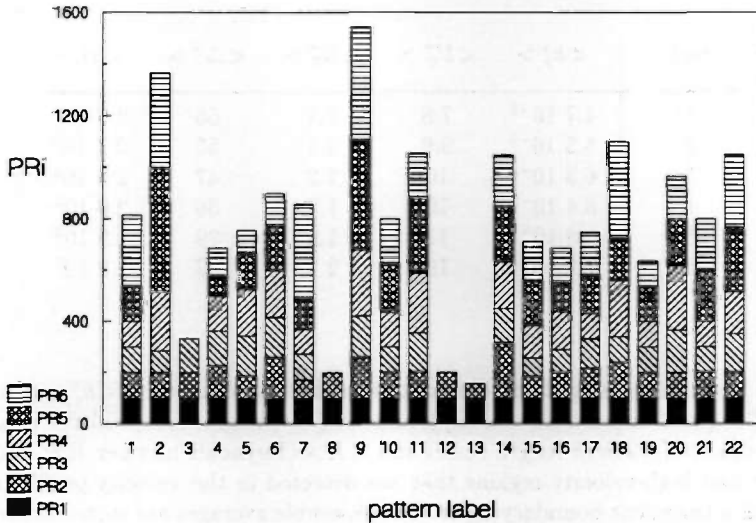
Figure 3.13: The change in the number of extremes in a profile with profile rank. The number of extremes in the first profile of the pattern is equated to 100; e.g. PR2 denotes the number of extremes in the second profile of a pattern.

Another measure of the flow activity is found by counting the number of extremes in a specific profile of a profile pattern, and by expressing this number relative to the number of extremes in the first profile of the pattern. Figure 3.13 presents the relative change of the number of extremes with the profile rank. (For ease of comparison the number of extremes in the first profile of a pattern is equated to 100.) For most (i.e. 77%) of the profile patterns no large change (i.e. less than 20% per step) occurs in the number of extremes during the initial 2 time steps. After the initial time steps the number of extremes changes considerably, with as a result that two classes of velocity profiles can be identified: those with less and those with more than the initial amount of extremes. In the latter class the splitting of low-velocity regions generally has led to a doubling of the number of extremes (with occasional excursions to larger multiplication rates).

A direct consequence of the observed increase in the number of extremes with profile rank is that it renders useless measuring the wavenumber k_z based on one velocity profile alone (as was done in section 2.5.3 and in a number of other studies). This is illustrated by determining the ensemble averaged k_z per profile (table 3.1). It is observed that $<k_z^+>$ has doubled after 5 time steps, which corresponds to a decrease of the spanwise distance $<\lambda_z^+>$ between two low-velocity regions from about 131 to about

rank	$<k_z^+>$	$<U_b^+>$	$<U_0^+>$	$<\Delta^+>$	$<R>$
1	$4.7\ 10^{-2}$	7.8	1.4	56	$2.8\ 10^2$
2	$5.5\ 10^{-2}$	9.0	1.4	55	$2.7\ 10^2$
3	$6.3\ 10^{-2}$	10	1.2	47	$2.0\ 10^2$
4	$8.4\ 10^{-2}$	10	1.7	36	$2.0\ 10^2$
5	$1.8\ 10^{-1}$	11	1.9	29	$1.9\ 10^2$
6	$1.2\ 10^{-1}$	10	2.1	33	$2.2\ 10^2$

Table 3.1: Ensemble averaged non-dimensional basic-flow parameters $<k_z^+>$ (wavenumber), $<U_b^+>$ (local mean fluid velocity), and $<U_0^+>$ (magnitude); and the related parameters $<\Delta^+>$ (gradient length scale) and $<R>$ (Reynolds number $R = 2\pi U_0/\nu k_z$) of the low and high-velocity regions that are detected in the velocity-profile patterns obtained in a turbulent boundary layer. The ensemble averages are sorted according to the profile rank in which they appear.

51. Since the $<k_z^+>$ determined from the basic flow of low-velocity regions (which are connected low-velocity minima) corresponds to the $<k_z^+>$ of the first profile, we infer that applying the connection scheme leads to conserving a specific set of extremes, and that it therefore yields higher values of $<k_z^+>$. Furthermore, we infer that the 'age' of a time line determines the number of velocity extremes that are present in the corresponding velocity profile, and therefore the spanwise distance between low-velocity regions.

The splitting and the merging of low and high-velocity regions is a feature of the velocity-profile patterns. In order to specify the conditions for the splitting of a low-velocity region to occur, we obtained the wavenumber k_z, the local mean velocity U_b, the magnitude U_0, the gradient length scale Δ and the Reynolds number R of the low-velocity region which serves as the 'parent' of the new low-velocity region (table 3.2a). A comparison of these instantaneous values with the corresponding ensemble averages shows that, in general, the splitting occurs when the wavenumber k_z^+ of the 'parent' low-velocity region is smaller, and when its magnitude U_0^+ is larger than the ensemble average. The values of the instantaneous Δ^+ and R are in agreement with this observation. On the other hand, the value of the local mean velocity U_b^+ does not seem to play a role. Furthermore, the conditions for a low or a high-velocity region to split seem not to be different (see table 3.2a). The same conclusions hold when the parent low-velocity regions are sorted according to their profile rank (table 3.3a; for reference data see table 3.1).

Similarly, in order to specify the conditions for the merging of a low-velocity region to occur, we obtained the instantaneous k_z, U_b, U_0, Δ and R of the velocity minimum where

(a)	type	$<k_z^+>$	$<U_b^+>$	$<U_0^+>$	$<\Delta^+>$	$<R>$
	LVR	$5.3\ 10^{-2}$	10	3.8	54	$6.6\ 10^2$
	HVR	$6.0\ 10^{-2}$	9.3	3.6	60	$5.5\ 10^2$
(b)	type	$<k_z^+>$	$<U_b^+>$	$<U_0^+>$	$<\Delta^+>$	$<R>$
	LVR	$1.5\ 10^{-1}$	11	3.8	44	$4.8\ 10^2$
	HVR	$1.1\ 10^{-1}$	10	3.0	34	$3.5\ 10^2$
(c)	type	$<k_z^+>$	$<U_b^+>$	$<U_0^+>$	$<\Delta^+>$	$<R>$
	LVR	$1.0\ 10^{-1}$	9.9	1.8	39	$2.2\ 10^2$
	HVR	$1.0\ 10^{-1}$	9.7	1.7	40	$2.2\ 10^2$

Table 3.2: The conditions for the splitting or merging of low and high-velocity regions to occur. Presented are the ensemble averages of the wavenumber k_z^+, the local mean fluid velocity U_b^+, the magnitude U_0^+, the gradient length scale Δ^+ and the Reynolds number $R = 2\pi U_0 / \nu k_z$ of the velocity minima and maxima (a) which serve as the parent of a new low or high-velocity region (referred to as LVR and HVR, respectively), (b) where a low or high-velocity region is terminated, and (c) which serve as the set of reference data.

the low-velocity region is terminated (table 3.2b). The merging of a low-velocity region generally occurs when the instantaneous wavenumber k_z^+ is larger than the ensemble average $< k_z^+ >$. The values of the local mean velocity U_b^+ and the magnitude U_0^+ do not seem to play a role. As in the case of splitting, the conditions for a low or a high-velocity region to merge seem not to be different (table 3.2b). This view agrees with the conclusion obtained by comparing the refence data (table 3.1) with the data sorted according to profile rank (table 3.3b).

To summarize, we present the main conclusions of our experiments on the time evolution of the flow in low-velocity regions. First, it is possible to distinguish an almost parallel and time-independent basic flow in a low-velocity region. Second, a stability analysis of a low-velocity region must treat the two shear layers separately, and consider the effect of viscosity. (In section 3.3 we use these findings as the basis of our model for the stability of a low-velocity region.) Third, the number of extremes in a velocity profile, and therefore the distance between two low-velocity regions, seems to depend on the 'age' of the time line from which the velocity profile is determined. (In section 3.2.4 we address the origin of this effect.)

(a)	rank	$<k_z^+>$	$<U_b^+>$	$<U_0^+>$	$<\Delta^+>$	$<R>$
	1	$4.3\ 10^{-2}$	6.9	3.4	64	$8.6\ 10^2$
	2	$4.3\ 10^{-2}$	8.4	2.8	83	$6.9\ 10^2$
	3	$5.1\ 10^{-2}$	9.9	3.4	53	$5.3\ 10^2$
	4	$6.7\ 10^{-2}$	10	4.3	50	$6.0\ 10^2$

(b)	rank	$<k_z^+>$	$<U_b^+>$	$<U_0^+>$	$<\Delta^+>$	$<R>$
	1	$7.6\ 10^{-2}$	8.9	2.4	46	$4.5\ 10^2$
	2	$5.5\ 10^{-2}$	9.5	2.7	73	$5.5\ 10^2$
	3	$8.4\ 10^{-2}$	11	3.5	55	$6.1\ 10^2$
	4	$1.0\ 10^{-1}$	10	3.4	32	$3.4\ 10^2$
	5	$2.0\ 10^{-1}$	12	3.9	23	$3.5\ 10^2$

Table 3.3: (a) The conditions for the splitting of low and high-velocity regions to occur, sorted according to the rank of the profile which is the parent of the region. (b) The conditions for the merging of low and high-velocity regions to occur, sorted according to the rank of the profile in which the region is terminated. Presented are the ensemble averages of the wavenumber k_z^+, the local mean fluid velocity U_b^+, the magnitude U_0^+, the gradient length scale Δ^+ and the Reynolds number $R = 2\pi U_0/\nu k_z$. For reference data see table 3.1.

3.2.4 On the origin of the increase in the number of extremes

The increase in the number of extremes with profile rank is an unequivocal feature of the velocity-profile patterns, and directly influences the mean spanwise distance between low-velocity regions. Therefore, in evaluating the observations of section 3.2.3, a primary concern is the origin of this effect.

First, we consider the analysis stages of our data handling. (These stages are described in sections 2.5.2 and 3.2.2.) Since the extreme-detection scheme is universally applied to each velocity profile of a profile pattern, it can be ruled out as the potential origin. For the same reason the filtering stages (i.e. the use of the median and the lowpass filters, and the least-square splines) can be ruled out, the more so as filtering usually results in a decrease in the number of extremes. The restoration stage is a more probable origin because a hole in a velocity profile is more likely to occur in a high-ranking velocity profile. (The older a time line the more its quality deteriorates due to dissolution and motion perpendicular to the light plane.) To investigate the effect of the restoration stage, we measured in the 22 restored patterns the variance in the

displacement of the time line after the first and the sixth time step, and compared it to the corresponding variance in the not-yet compensated pattern. Generally, for both the patterns the variance in the displacement in the profile of rank 6 is larger than the variance in the profile with rank 1. Consequently, we conclude that the restoration stage does not add to the profiles noise in the form of velocity fluctuations. Similarly, we investigated the effect of the compensations for the wake of the wire and the velocity gradient in the flow. A comparison of the velocity-variance ratios of the compensated and the not-yet compensated patterns shows that the compensated profiles of rank 6 generally have a velocity variance which is somewhat larger than the one of the not-yet compensated profiles of rank 6. However, when the compensated patterns are median and low-pass filtered, the differences in the variances disappear. So, we conclude that the compensation stage too does not add to the velocity fluctuations in the profiles.

Next, we consider the pre-processing stages (see section 2.4.2). We rule out the morphological operations rimming, closing and opening because they apply equally on each binary time-line. However, the situation is entirely different for the segmentation stage because the grey-value gradient in the edges of a time line determines the uncertainty in the position of the edges after application of the threshold. Although the grey-value gradient is kept to a maximum by rescaling the grey values of a time-line picture into the range 0...255 (recall that in this stage one time line is present in a picture), the grey-value gradient generally decreases with the age of the time line. Consequently, the uncertainty in the position of the time line increases with its age. However, a comparison of the variances of the width of the binary time-lines of age 6 and 1 does not show a larger value of this variance for the older time lines. So, we see that the segmentation stage does not add to the variance in the high-ranking profiles.

On basis of this assessment, we conclude that the analysis and the pre-processing stages (in particular the restoration, compensation and the segmentation stages) are not the origin of the increase in the number of extremes with profile rank. Consequently, we infer that this effect is a feature of the time lines and not of the investigative technique, and that it might indicate a feature of the flow. However, recall that always a structure appears in a time-line pattern when time lines are used to visualize turbulent flow (see section 2.6). Furthermore, we emphasize that the uncertainties in the present results are large due to the use of the hydrogen-bubble technique to obtain fluid velocities (see section 2.2.2), and the limited amount of profile patterns.

3.3 The stability of a two-dimensional viscous shear layer

3.3.1 Outline of the stability analysis

On basis of our experimental results on the time evolution of the flow in the low-velocity regions of near-wall turbulence (see section 3.2.3), we have concluded that (at least for short time lapses, i.e. less than about $15t_*$) it is possible to model this flow by an almost parallel and time-independent basic flow. Furthermore, we concluded that in an analysis of the stability of these low-velocity regions the two shear layers must be treated

separately, and the effect of viscosity must be included. In this section we assume that the flow in a low-velocity region can be modelled by a parallel and time-independent basic flow, and present an analysis of its stability. First, we represent the basics of viscous stability theory (section 3.3.2). Next, we present a model for the shear layer of a low-velocity region (section 3.3.3). Finally, we develop a model which expresses the stability of a low-velocity region in terms of the parameters of its basic flow (section 3.3.4).

3.3.2 The equation for the amplitude of two-dimensional perturbations

The flow of a viscous fluid is determined by the vorticity equation (Batchelor, 1967, p. 267)

$$\frac{D\underline{\tilde{\omega}}}{D\tilde{t}} = \underline{\tilde{\omega}} \cdot \nabla\underline{\tilde{u}} + \nu\nabla^2\underline{\tilde{\omega}} , \tag{3.11}$$

with $\underline{\tilde{u}}$ the fluid velocity vector, $\underline{\tilde{\omega}} = \nabla \times \underline{\tilde{u}}$ the vorticity vector, $\tilde{t}$ the time and ν the kinematic viscosity of the fluid. In two dimensions (3.11) reduces to the two-dimensional vorticity equation

$$\frac{D\tilde{\omega}_2}{D\tilde{t}} = \nu\nabla^2\tilde{\omega}_2 , \tag{3.12}$$

with $\tilde{\omega}_2 = \frac{\partial \tilde{u}_1}{\partial \tilde{z}} - \frac{\partial \tilde{u}_3}{\partial \tilde{x}}$; $\tilde{u}_1$ and $\tilde{u}_3$ denoting the x and z components of the fluid velocity vector $\underline{\tilde{u}} = (\tilde{u}_1, 0, \tilde{u}_3)$. If $\mathcal{U}$ and $\mathcal{L}$ are the velocity and the length scale of the flow, (3.12) can be cast in non-dimensional form:

$$\frac{D\omega_2}{Dt} = \frac{1}{R}\nabla^2\omega_2 , \tag{3.13}$$

with $R = \mathcal{U}\mathcal{L}/\nu$ the Reynolds number of the flow.

Suppose now the instantaneous flow is the superposition of a basic flow and a perturbation (Lin, 1955, p. 28):

$$
\begin{aligned}
u_1(x,z,t) &= U_1(z) + \varepsilon u_1'(x,z,t) \\
u_3(x,z,t) &= \varepsilon u_3'(x,z,t) \\
\omega_2(x,z,t) &= \Omega_2(z) + \varepsilon\omega_2'(x,z,t),
\end{aligned}
\tag{3.14}
$$

with $\Omega_2 = dU_1/dz$. By substituting (3.14) in (3.13), and assuming the perturbations to be small (i.e. $\frac{u_1'}{U_1} \ll \varepsilon^{-1}$ and $\frac{\partial\omega_2'/\partial z}{\partial\Omega_2/\partial z} \ll \varepsilon^{-1}$), we obtain the linearized viscous perturbation equation

$$\frac{\partial\omega_2'}{\partial t} + U_1\frac{\partial\omega_2'}{\partial x} + u_3'\frac{\partial\Omega_2}{\partial z} = \frac{1}{R}\left(\frac{\partial^2\omega_2'}{\partial x^2} + \frac{\partial^2\omega_2'}{\partial z^2}\right). \tag{3.15}$$

Since the perturbations are two-dimensional, it is possible to introduce a stream-function $\psi(x,z,t)$ such that

$$u_1' = \frac{\partial\psi}{\partial z} \quad \text{and} \quad u_3' = -\frac{\partial\psi}{\partial x} , \tag{3.16}$$

and thus satisfy the continuity equation $\frac{\partial u'_1}{\partial z} + \frac{\partial u'_3}{\partial z} = 0$. By assuming a perturbation to have the character of a wave, we get

$$\psi(x, z, t) = \phi(z)\, e^{i\alpha(x-ct)}, \tag{3.17}$$

with $\phi(z)$ the amplitude of the streamfunction which describes the velocity perturbation. From (3.16) and (3.17) it follows that the streamwise and the spanwise component of the velocity perturbation are

$$u'_1(x, z, t) = Re[\frac{d\phi}{dz}\, e^{i\alpha(x-ct)}] \tag{3.18}$$

and

$$u'_3(x, z, t) = Re[-i\alpha\phi\, e^{i\alpha(x-ct)}]. \tag{3.19}$$

Similarly, we assume that the vorticity perturbation has a wavy character:

$$\omega'_2(x, z, t) = w(z)\, e^{i\alpha(x-ct)}, \tag{3.20}$$

with $w(z)$ the amplitude of the vorticity perturbation.

In general, both α and c are complex: $\alpha = \alpha_r + i\alpha_i$ with $\alpha_r = 2\pi/\lambda_x$ the streamwise wavenumber, and $c = c_r + ic_i$ with c_r the phase velocity. The period of the perturbation is $T = 2\pi/\alpha_r c_r$. The quantities $g_t = \alpha_r c_i + \alpha_i c_r$ and $g_x = -\alpha_i$ are the temporal and the spatial growth rate, respectively. If $g_x = 0$ and $g_t \neq 0$, the amplitude of the perturbation does not depend on x, and we have the timewise case. On the other hand, for $g_t = 0$ and $g_x \neq 0$, the amplitude of the perturbation does not depend on time, and we have the spacewise case. Here we consider the most general case: the perturbations are localized in space ($g_x \neq 0$) and their amplitude depends on time ($g_t \neq 0$).

Inserting (3.16b), (3.17) and (3.20) in the linearized viscous perturbation equation (3.15) yields

$$\alpha \left(U_1 - c - i\frac{\alpha}{R} \right) w(z) + i\frac{1}{R}\frac{d^2 w}{dz^2} - \alpha\frac{d^2 U_1}{dz^2}\phi(z) = 0. \tag{3.21}$$

By inserting (3.16) and (3.17) in the definition of the vorticity perturbation $\omega'_2 = \frac{\partial u'_1}{\partial z} - \frac{\partial u'_3}{\partial x}$, we find

$$w(z) = -\alpha^2\phi(z) + \frac{d^2\phi}{dz^2}. \tag{3.22}$$

Eliminating $w(z)$ between (3.21) and (3.22) gives

$$i\frac{1}{R}\frac{d^4\phi}{dz^4} + \alpha \left(U_1 - c - i\frac{2\alpha}{R} \right) \frac{d^2\phi}{dz^2} - \alpha \left(\alpha^2 \left(U_1 - c - i\frac{\alpha}{R} \right) + \frac{d^2 U_1}{dz^2} \right) \phi = 0, \tag{3.23}$$

which is the equation for the amplitude of the streamfunction which describes the velocity perturbation in the xz plane. Since the derivation of (3.23) is equivalent to the derivation of the Orr-Sommerfeld equation for the amplitude of velocity perturbations in the xy plane (see e.g. Drazin and Reid, 1981, p. 156), in this thesis it will be referred to as the Orr-Sommerfeld equation for the amplitude of velocity perturbations in the xz plane.

3.3.3 The sinusoidal basic velocity profile

Before we start with the analysis of the stability of a low-velocity region, we must determine the profile of the basic flow. Inspection of instantaneous spanwise profiles of the streamwise velocity in a natural turbulent boundary layer (see e.g. figure 2.7f; but also figure 13, Kline e.a., 1967; and figure 10, Blackwelder and Swearingen, 1989) suggests that the basic flow $U(z)$ of a low-velocity region can be modelled by the sinusoidal velocity profile

$$U(z) = U_b - U_0 \cos k_z z \quad \text{for} \quad -\frac{\pi}{k_z} \leq z \leq \frac{\pi}{k_z}, \tag{3.24}$$

with U_b the local mean fluid velocity, U_0 the magnitude of the low-velocity region, and $k_z = 2\pi/\lambda_z$ its wavenumber.

Furthermore, what the before mentioned figures also suggest is confirmed by our experimental results (see section 3.2.3): the low-velocity regions are highly asymmetrical. It is therefore more appropriate to model separately each shear layer of a low-velocity region (figure 3.4). Thus we take as the velocity profile for a shear layer:

$$U(z) = U_b + U_0 \sin k_z z \quad \text{for} \quad -\frac{\pi}{2k_z} \leq z \leq \frac{\pi}{2k_z}. \tag{3.25}$$

Note that the shear layer is aligned such that $z = 0$ is its inflection point.

Clearly, inspection by the eye is not enough to decide on the usefulness of the sinusoidal profile. In order to give a quantitative assessment, we define the gradient length scale Δ and the gradient velocity scale Υ (see figure 3.14):

$$\Delta = \frac{\mathcal{U}}{\partial U_{IP}} \quad \text{and} \quad \Upsilon = \mathcal{L} \, \partial U_{IP}, \tag{3.26}$$

with $\mathcal{U} = U_{E2} - U_{E1}$ the velocity scale of the low-velocity region (U_{E2} and U_{E1} are the fluid velocity in the maximum and minimum, respectively), $\mathcal{L} = z_{E2} - z_{E1}$ the length scale of the low-velocity region (z_{E2} and z_{E1} are the position of the velocity maximum and minimum, respectively), and ∂U_{IP} the velocity gradient in the inflection point. (Note that (3.26) differs from the definition of Δ by Blackwelder and Swearingen (1989) by a factor 2 in the denominator.) The sinusoidal basic flow (3.25) yields $\mathcal{U} = 2U_0$, $\mathcal{L} = \pi/2k_z$ and $\partial U_{IP} = k_z U_0$. Inserting this in (3.26), we find

$$\frac{\Delta}{\mathcal{L}} = \frac{2}{\pi} \quad \text{and} \quad \frac{\Upsilon}{\mathcal{U}} = \frac{\pi}{2} \tag{3.27}$$

for the corresponding dimensionless gradient length and velocity scales.

In order to compare the 'predicted' values (3.27) with the ones found experimentally, we used hydrogen-bubble time-lines, generated with a wire at $y^+ \approx 20$, to measure instantaneous spanwise profiles of the streamwise velocity, and applied the inflection-point detection-scheme to find the shear layers of the low-velocity regions. (See sections 2.4.2 and 2.5.2 for a description of the data handling.) A plot of Δ versus $\mathcal{L}$ (figure 3.15a) shows 87% of the inflection points to have the ratio $\Delta/\mathcal{L}$ within $\pm 13\%$ of the desired value $2/\pi$. Similarly (see figure 3.15b), for 86% of the inflection points $\Upsilon/\mathcal{U}$ lies
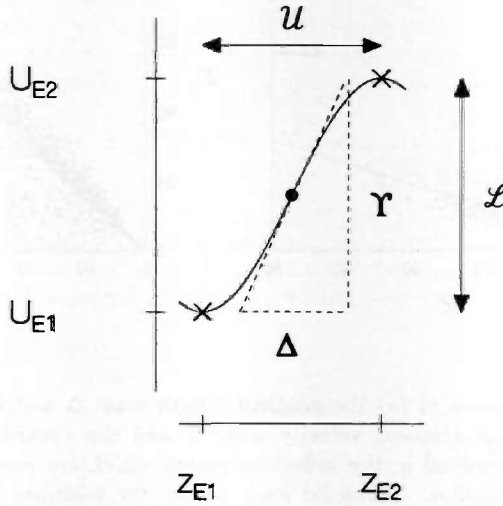
Figure 3.14: The scales of a shear layer of a low-velocity region: the gradient length scale Δ, the shear-layer length scale $\mathcal{L}$, the gradient velocity scale Υ and the shear-layer velocity scale $\mathcal{U}$.

within $\pm 13\%$ of $\pi/2$. Consequently, we conclude that the sinusoidal basic flow (3.25) may serve as a model for the shear layer of a low-velocity region in a turbulent boundary layer.

3.3.4 On the stability of the sinusoidal and viscous shear layer

a The equation for the perturbation amplitude

Here we turn to the analysis of the stability of the sinusoidal and viscous basic flow. In the shear layer

$$U(z) = U_b + U_0 \sin k_z z \quad \text{for} \quad -\frac{\pi}{2k_z} \le z \le \frac{\pi}{2k_z} \tag{3.28}$$

the amplitude of the perturbation is governed by the Orr-Sommerfeld equation (3.23). Substituting the basic flow (3.28) in (3.23), and rearranging terms yields

$$a_4 \frac{d^4\phi}{dz^4} + (a_2 + b_2 \sin k_z z) \frac{d^2\phi}{dz^2} + (a_1 + b_1 \sin k_z z)\, \phi = 0, \tag{3.29}$$
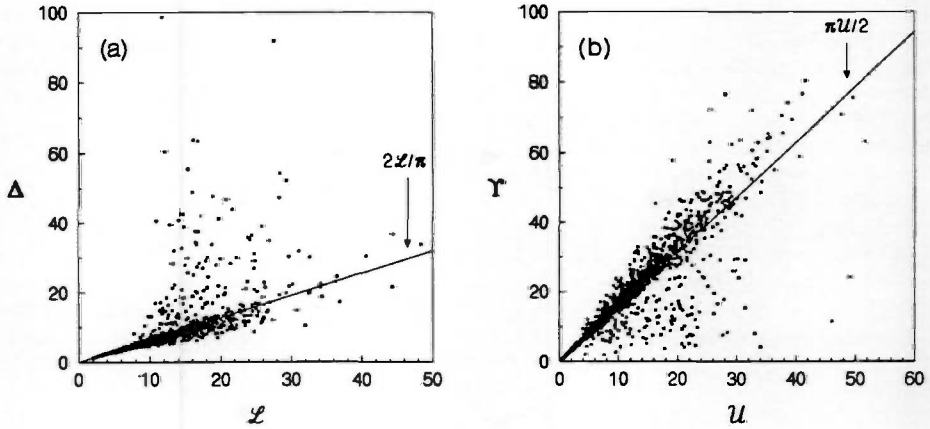
Figure 3.15: The ratios of (a) the gradient length scale Δ and the shear-layer length scale $\mathcal{L}$, and (b) the gradient velocity scale Υ and the shear-layer velocity scale $\mathcal{U}$ of the flow as determined in the inflection points which are present in instantaneous spanwise velocity profiles. The solid lines denote the relations for a sinusoidal basic flow: $\Delta = 2\mathcal{L}/\pi$ and $\Upsilon = \pi\mathcal{U}/2$.

with $a_4 = i/R$, $a_2 = \alpha\,(U_b - c - i2\alpha/R)$, $a_1 = -\alpha^3\,(U_b - c - i\alpha/R)$, $b_2 = \alpha\,U_0$ and $b_1 = \alpha\,(k_z^2 - \alpha^2)\,U_0$. Since $z = 0$ is an ordinary point of (3.29), the solution of (3.29) can be expressed as the infinite series

$$\phi(z) = \sum_{n=0}^{\infty} c_n\,z^n. \tag{3.30}$$

Using $\sin x \approx x - \frac{1}{6}x^3 + \frac{1}{120}x^5$ for $-\frac{\pi}{2} \leq x \leq \frac{\pi}{2}$, and substituting (3.30) in (3.29), we find (see appendix B.1)

$$\phi(z) = c_0\phi_0(z) + c_1\phi_1(z) + c_2\phi_2(z) + c_3\phi_3(z) \tag{3.31}$$

with

$$\phi_0(z) = 1 + A_4z^4 + A_5z^5 + A_6z^6 + A_7z^7 + \dots , \tag{3.32}$$

$$\phi_1(z) = z + \frac{1}{5}A_4z^5 + \frac{1}{3}A_5z^6 + \frac{1}{7}A_6z^7 + \dots , \tag{3.33}$$

$$\phi_2(z) = z^2 + C_4z^4 + C_5z^5 + C_6z^6 + C_7z^7 + \dots , \tag{3.34}$$

$$\phi_3(z) = z^3 + \frac{3}{5}C_4z^5 + C_5z^6 + \frac{3}{7}C_6z^7 + \dots \tag{3.35}$$

the four linearly independent solutions of (3.29). The coefficients of the powers of z in these solutions are

$$A_4 = -\frac{1}{24}\left(i\alpha^3 R(U_b - c) + \alpha^4\right), \tag{3.36}$$

$$A_5 = -\frac{1}{120}i\alpha R(\alpha^2 - k_z^2)k_z U_0, \tag{3.37}$$

$$A_6 = \frac{\alpha^4 R^2}{720}\left((U_b - c)^2 - i\frac{3\alpha}{R}(U_b - c) - \frac{2\alpha^2}{R^2}\right), \tag{3.38}$$

$$A_7 = \frac{k_z U_0}{5040}(\alpha^2 R^2(4\alpha^2 - k_z^2)(U_b - c) - i\alpha^3 R(5\alpha^2 - 2k_z^2)$$
$$+ i\alpha R(\alpha^2 - k_z^2)k_z^2), \tag{3.39}$$

and

$$C_4 = \frac{1}{12}\left(i\alpha R(U_b - c) + 2\alpha^2\right), \tag{3.40}$$

$$C_5 = \frac{1}{60}i\alpha R k_z U_0, \tag{3.41}$$

$$C_6 = \frac{1}{360}\left(-\alpha^2 R^2(U_b - c)^2 + i3\alpha^3 R(U_b - c) + 3\alpha^4\right), \tag{3.42}$$

$$C_7 = \frac{k_z U_0}{2520}\left(-4\alpha^2 R^2(U_b - c) + i\alpha R(5\alpha^2 + 2k_z^2)\right). \tag{3.43}$$

(See appendix B.1.)

b The dispersion relation

We require that at the boundaries of the shear layer the velocity perturbations vanish. Therefore, according to (3.18) and (3.19), the boundary conditions are

$$\phi(\pm\frac{\pi}{2k_z}) = 0 \quad \text{and} \quad D\phi(\pm\frac{\pi}{2k_z}) = 0, \tag{3.44}$$

with $D\phi(z) = d\phi(z)/dz$. A non-zero solution of the equations (3.44) exists only if

$$\begin{vmatrix} \phi_0(\frac{\pi}{2k_z}) & \phi_1(\frac{\pi}{2k_z}) & \phi_2(\frac{\pi}{2k_z}) & \phi_3(\frac{\pi}{2k_z}) \\ \phi_0(-\frac{\pi}{2k_z}) & \phi_1(-\frac{\pi}{2k_z}) & \phi_2(-\frac{\pi}{2k_z}) & \phi_3(-\frac{\pi}{2k_z}) \\ D\phi_0(\frac{\pi}{2k_z}) & D\phi_1(\frac{\pi}{2k_z}) & D\phi_2(\frac{\pi}{2k_z}) & D\phi_3(\frac{\pi}{2k_z}) \\ D\phi_0(-\frac{\pi}{2k_z}) & D\phi_1(-\frac{\pi}{2k_z}) & D\phi_2(-\frac{\pi}{2k_z}) & D\phi_3(-\frac{\pi}{2k_z}) \end{vmatrix} = 0. \tag{3.45}$$

The solution of (3.45) expresses α and c, and therefore the wavenumber and the growth rates of the perturbation, in terms of the basic-flow parameters U_b, U_0 and k_z, and the dimensionless viscosity of the fluid R (see section 3.3.1).

Provided that $\alpha_r < k_z$, $\alpha_i < k_z$, $R > \alpha_r/U_0$ and $R > \alpha_i/U_0$, it can be shown that (3.45) is equivalent to

$$-\frac{192 k_z^2}{\pi^2}\left(K_{00}(U_b - c)^2 + 1\right)\left(-M_{10} + \frac{\pi}{2k_z}\right)\begin{vmatrix} e_{20} & e_{30} \\ e_{22} & e_{32} \end{vmatrix} = 0, \qquad (3.46)$$

with

$$\begin{aligned}
e_{20} =\ & \frac{\pi^4}{192}\frac{i\alpha R}{k_z^4}(U_b - c) + M_{20} + \frac{\pi^2}{4k_z^2} - \\
& \frac{\frac{\pi^4}{576}\frac{i\alpha R}{k_z^4}(U_b - c) + \frac{\pi^2}{6k_z^2}}{K_{00}(U_b - c)^2 + 1}(M_{00} + 2) + \\
& \frac{K_{20}(U_b - c)^2 + \frac{\pi^4}{288}\frac{i\alpha R}{k_z^4}(U_b - c) + \frac{\pi^2}{12k_z^2}}{-M_{10} + \frac{\pi}{2k_z}}\left(L_{10}(U_b - c) + \frac{3\pi}{2k_z}\right), \qquad (3.47)
\end{aligned}$$

$$\begin{aligned}
e_{22} =\ & \left(L_{20} - \frac{\pi^4}{96}\frac{i\alpha R}{k_z^4}\right)(U_b - c) - \frac{\pi^2}{2k_z^2} - \\
& \frac{\frac{\pi^4}{576}\frac{i\alpha R}{k_z^4}(U_b - c) + \frac{\pi^2}{6k_z^2}}{K_{00}(U_b - c)^2 + 1}(L_{00}(U_b - c) - 3) + \\
& \frac{K_{20}(U_b - c)^2 + \frac{\pi^4}{288}\frac{i\alpha R}{k_z^4}(U_b - c) + \frac{\pi^2}{12k_z^2}}{-M_{10} + \frac{\pi}{2k_z}}\left(K_{10}(U_b - c)^2 - \frac{\pi}{k_z}\right), \qquad (3.48)
\end{aligned}$$

$$e_{30} = L_{30}(U_b - c) + \frac{\pi^3}{4k_z^3} - \frac{-M_{30} + \frac{\pi^3}{8k_z^3}}{-M_{10} + \frac{\pi}{2k_z}}\left(L_{10}(U_b - c) + \frac{3\pi}{2k_z}\right), \qquad (3.49)$$

and

$$e_{32} = K_{30}(U_b - c)^2 - \frac{\pi^3}{8k_z^3} - \frac{-M_{30} + \frac{\pi^3}{8k_z^3}}{-M_{10} + \frac{\pi}{2k_z}}\left(K_{10}(U_b - c)^2 - \frac{\pi}{k_z}\right) \qquad (3.50)$$

(see appendix B.2). The coefficients in the determinant elements (3.47)...(3.50) are

$$K_{00} = \frac{\pi^6}{46080}\frac{\alpha^4 R^2}{k_z^6}, \quad L_{00} = -\frac{\pi^7}{645120}\frac{\alpha^2 R^2 U_0}{k_z^4}, \quad \text{and } M_{00} = 1 + \frac{\pi^5}{3840}\frac{i\alpha R U_0}{k_z^2}; \qquad (3.51)$$

$$K_{10} = \frac{\pi^7}{645120}\frac{\alpha^4 R^2}{k_z^7}, \quad L_{10} = -\frac{\pi^5}{3840}\frac{i\alpha^3 R}{k_z^5}, \quad \text{and } M_{10} = \frac{\pi}{2k_z}\left(1 + \frac{\pi^5}{11520}\frac{i\alpha R U_0}{k_z^2}\right); \qquad (3.52)$$

$$K_{20} = -\frac{\pi^6}{23040}\frac{\alpha^2 R^2}{k_z^6}, \quad L_{20} = \frac{\pi^4}{192}\frac{i\alpha R}{k_z^4}\left(1 + \frac{\pi^3}{420}\frac{i\alpha R U_0}{k_z^2}\right), \quad \text{and } M_{20} = \frac{\pi^2}{4k_z^2}\left(1 + \frac{\pi^3}{480}\frac{i\alpha R U_0}{k_z^2}\right); \qquad (3.53)$$

and

$$K_{30} = -\frac{\pi^7}{107520}\frac{\alpha^2 R^2}{k_z^7}, \quad L_{30} = \frac{\pi^5}{640}\frac{i\alpha R}{k_z^5}, \quad \text{and } M_{30} = \frac{\pi^3}{8k_z^3}\left(1 + \frac{\pi^3}{480}\frac{i\alpha R U_0}{k_z^2}\right). \qquad (3.54)$$

Equation (3.46), together with the determinant elements (3.47)...(3.50), is the viscous dispersion relation for the sinusoidal shear layer. Note that the conditions for (3.46) to be valid are $\tilde{\lambda}_z < \tilde{\lambda}_x$ and $\tilde{\lambda}_x < 2\pi\nu/\tilde{U}_0$. Near the wall of a turbulent boundary layer there is experimental evidence for the validity of the first condition (see e.g. Smith and Metzler, 1983 and Blackwelder and Swearingen, 1989), but, unfortunately, no evidence exists for the second condition.

c The asymptotic behaviour of the dispersion relation

Next, we study the asymptotic behaviour of (3.46). In the long-wave and high Reynolds-number approximation ($|\alpha| \to 0$ and $R > \frac{23040}{\pi^5} \frac{k_z^2}{|\alpha|U_0}$) equation (3.46) reduces to

$$(U_b - c)^4 + \frac{\pi^4}{360}U_0^2(U_b - c)^2 - 8\left(\frac{7\pi^2}{288} - 1\right)\frac{ik_z^2U_0^2}{\alpha R}(U_b - c) + \frac{224}{\pi^2}\frac{k_z^4U_0^2}{\alpha^2 R^2} = 0 \quad (3.55)$$

(see appendix B.3).

c.1 The long-wave and inviscid behaviour

For very large Reynolds numbers ($R \to \infty$) we find the inviscid limit of the dispersion relation (3.55):

$$(U_b - c)^4 + \frac{\pi^4}{360}U_0^2(U_b - c)^2 = 0. \quad (3.56)$$

This equation has three different roots:

$$U_b - c = \pm\frac{\pi^2}{6\sqrt{10}}iU_0 \quad \text{and} \quad U_b - c = 0, \quad (3.57)$$

the latter being two coincident roots. Taking the real and the imaginary part of the first and the second root gives

$$c_i = \mp\frac{\pi^2}{6\sqrt{10}}U_0 \quad \text{and} \quad c_r = U_b, \quad (3.58)$$

from which follow the temporal growth rates

$$g_t = \alpha_r c_i + \alpha_i c_r = \mp\frac{\pi^2}{6\sqrt{10}}\alpha_r U_0 + \alpha_i U_b. \quad (3.59)$$

Similarly, the third root gives

$$g_t = \alpha_i U_b. \quad (3.60)$$

Therefore, in the inviscid limit three different stability modes exist for the sinusoidal shear layer.

This analysis shows that for the timewise case ($g_x = -\alpha_i = 0$) the third mode (3.60) vanishes and the two modes (3.59) reduce to

$$g_t = \mp\frac{\pi^2}{6\sqrt{10}}\alpha_r U_0. \quad (3.61)$$

We see that in the inviscid limit and for small wavenumbers one unstable and one stable mode exist for the sinusoidal shear layer. It is instructive to compare these modes with the ones of a bounded shear layer in an inviscid flow (see Drazin and Reid, 1981, p. 147). If it is assumed that the velocity profile in the shear layer is linear and the long-wave approximation is valid, it is found that the thickness of the shear layer determines whether the flow is stable or not. That is to say: one unstable and one stable mode exist if the thickness of the shear layer is less than a critical value, and the temporal growth rates of these modes depend on this thickness. On the other hand, if the shear layer is thicker than the critical value, the flow is stable. We therefore conclude that the sinusoidal shear layer does not have a stabilizing effect on the flow, as one might have expected from the analogy with the linear shear layer.

Equation (3.59) tells us that, for small wavenumbers and in the inviscid limit, if $\alpha_i = 0$, the temporal growth rate is proportional to the wavenumber α_r of the perturbation and the magnitude U_0 of the shear layer. On the other hand, if $\alpha_i \neq 0$, the temporal growth rate is also proportional to the spatial decay rate α_i and the local mean fluid velocity U_b. Consequently, if it is found experimentally that these asymptotic conditions are valid and the temporal growth rate depends on the local mean fluid velocity, necessarily it follows that $\alpha_i \neq 0$. Then one might conclude that the perturbations are localized in space (see section 3.2.1).

The second mode (3.59b) is unstable for all wavenumbers α_r. A sufficient condition for the first mode (3.59a) to be unstable is

$$\alpha_r < \frac{6\sqrt{10}}{\pi^2} \alpha_i \frac{U_b}{U_0}. \tag{3.62}$$

Consequently, for a given spatial decay rate α_i only the perturbations with

$$\lambda_x > \frac{\pi^3}{3\sqrt{10}} \frac{1}{\alpha_i} \frac{U_0}{U_b}. \tag{3.63}$$

will not be damped.

Due to both the temporal and the spatial growth rate, the perturbation amplitude is amplified by a factor $\exp(g_x x + g_t t)$ within a wavelength λ_x and a period T. Therefore, the time lapse for an unstable mode to grow by a factor e is $1/g_t$. If we define the life time τ of a perturbation as the time lapse since the initial occurrence of the perturbation, it follows that

$$\tau \propto \frac{1}{g_t}. \tag{3.64}$$

Therefore, from (3.59) and (3.60) it follows that in the inviscid limit the life times of the perturbation modes are

$$\tau \propto \mp \frac{6\sqrt{10}}{\pi^2} \frac{1}{\alpha_r U_0} \left(1 \mp \frac{6\sqrt{10}}{\pi^2} \frac{\alpha_i}{\alpha_r} \frac{U_b}{U_0} \right) \tag{3.65}$$

and

$$\tau \propto \frac{1}{\alpha_i U_b}; \tag{3.66}$$

with (3.65) holding for $\frac{\alpha_r}{\alpha_i} < \frac{6\sqrt{10}}{\pi^2}\frac{U_b}{U_0}$. We see that, under the prevailing asymptotic conditions, both an increase in U_0 and a decrease in U_b leads to a decrease of the life time of the perturbation, provided that the first mode is unstable. The second mode has the same behaviour, but for all wavenumbers.

c.2 The long-wave and high Reynolds-number approximation

Since in real-life near-wall turbulence we have to deal with non-infinite Reynolds-numbers (see section 3.2.3), we have to include the effect of viscosity in the expressions for the growth rates and the life times of the perturbations. For Reynolds numbers which are neither small nor large ($\frac{23040}{\pi^5}\frac{k_z^2}{|\alpha|U_0} < R < \infty$), the four roots of (3.55) are

$$U_b - c = \mp\frac{\pi^2}{12\sqrt{10}}iU_0\left(1 + Y\frac{k_z^2}{\alpha RU_0}\right) \pm \frac{\pi^2}{12\sqrt{10}}iU_0\left(1 + Z_\pm\frac{k_z^2}{\alpha RU_0}\right), \quad (3.67)$$

with

$$Z_\pm = Y - \frac{720}{\pi^4}X'' \pm \frac{17280\sqrt{10}}{\pi^6}\left(\frac{7\pi^2}{288} - 1\right). \quad (3.68)$$

The constants in (3.68) are

$$Y = \frac{360^2 4320\sqrt{3}}{\pi^{12}}X', \quad X'' = \frac{360^2 12\sqrt{3}}{\pi^8}X' \quad \text{and} \quad X' = \sqrt{\frac{224\pi^{14}}{2160^4} + \frac{\pi^{12}X}{2160^3}}, \quad (3.69)$$

and

$$X = \frac{28\pi^2}{135} + 8\left(\frac{7\pi^2}{288} - 1\right)^2. \quad (3.70)$$

(See appendix B.4.) Note that the second sign duality in (3.67) is independent of the first and the third. By taking the real and the imaginary parts of (3.67), we find the corresponding four temporal growth rates:

$$g_t = \pm\frac{\pi^2}{12\sqrt{10}}\left(\alpha_r U_0 + 2Y\frac{k_z^2}{R}\right) \mp \frac{\pi^2}{12\sqrt{10}}\left(\alpha_r U_0 + 2Z_\pm\frac{k_z^2}{R}\right) + \alpha_i U_b; \quad (3.71)$$

or to be more specific

$$g_t = \mp\frac{\pi^2}{6\sqrt{10}}\alpha_r U_0 - \frac{2880}{\pi^4}\left(1 - \frac{7\pi^2}{288}\right)\frac{k_z^2}{R} + \alpha_i U_b,$$

$$g_t \approx \frac{1583\pi^2}{96\sqrt{10}}\frac{k_z^2}{R} + \alpha_i U_b, \quad (3.72)$$

$$g_t \approx -\frac{401\pi^2}{192\sqrt{10}}\frac{k_z^2}{R} + \alpha_i U_b.$$

The approximations in (3.72c) and (3.72d) follow from simplifying the coefficients $Y - Z_+$ and $-Y + Z_-$, respectively. For $R = \infty$, (3.72) yields the three modes (3.59) and (3.60) of the inviscid approximation. A comparison of (3.72) with these modes shows
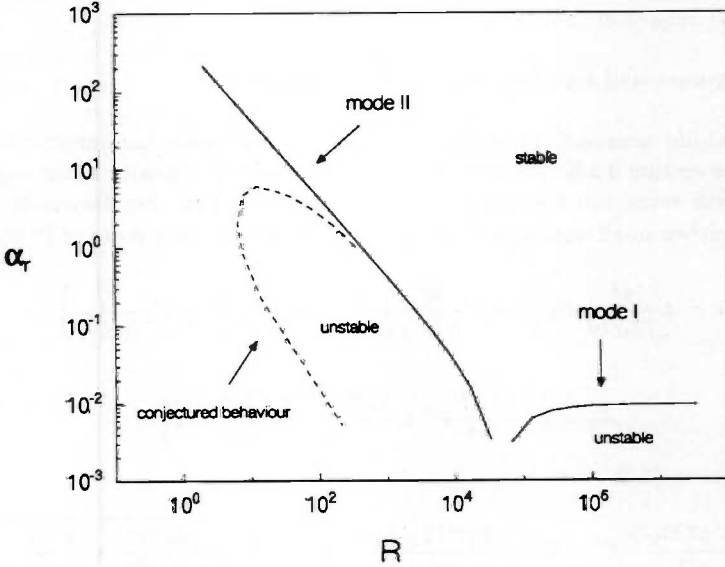
Figure 3.16: The stability diagram for the sinusoidal basic flow in the long-wave and high Reynolds-number approximation.

that the effect of the viscosity appears in the terms that are proportional to k_z^2/R. For three modes the viscosity has a stabilizing effect, whereas it has a destabilizing effect for the other one. Similarly, an increase in the wavenumber k_z of the basic flow leads to a smaller g_t for three modes, and a larger g_t for the other mode. Equation (3.72) also shows that (3.72c) is the most unstable mode.

Using (3.72a) and (3.72b) to calculate the neutral curves $g_t = 0$, we find

$$\alpha_r = \mp \frac{6\sqrt{10}}{\pi^2} \left(\frac{2880}{\pi^2} \left(1 - \frac{7\pi^2}{288} \right) \frac{k_z^2}{RU_0} - \alpha_i \frac{U_b}{U_0} \right). \tag{3.73}$$

Since we are only interested in perturbations traveling in the direction of the basic flow, we restrict ourselves to $\alpha_r > 0$. The stability diagram (figure 3.16) then shows the smaller wavenumbers α_r to be more unstable than the larger ones. Recalling that here we have the long-wave and high Reynolds-number approximation, we conclude that this behaviour is qualitatively in agreement with the one of the general stability diagram of a viscous shear layer. (See e.g. Drazin and Reid, 1981, p. 241.) From (3.73a) it follows

that instability occurs if

$$\lambda_x > \pm \frac{\pi^3}{3\sqrt{10}} \frac{1}{\alpha_i} \frac{U_0}{U_b} \left(1 + \frac{2880}{\pi^4}\left(1 - \frac{7\pi^2}{288}\right)\frac{k_z}{\alpha_i R U_0}\right). \tag{3.74}$$

On comparing (3.74) and (3.73), we find that the second mode (i.e. the unstable mode of the inviscid case) might be stable, and that the first mode (i.e. the stable mode of the inviscid case) might be unstable for appropriate values of the Reynolds number. This shows that (for the governing approximations) viscosity has a damping effect. Note however that for very small wavelengths λ_x and Reynolds numbers R the perturbations are likely to be stable, as can be conjectured by comparing figure 3.16 with the general stability diagram for a viscous shear layer.

The viscous perturbation life-times follow from (3.72):

$$\begin{aligned}
\tau &\propto \mp \frac{6\sqrt{10}}{\pi^2}\frac{1}{\alpha_r U_0}\left(1 \mp \frac{17280\sqrt{10}}{\pi^6}\left(1 - \frac{7\pi^2}{288}\right)\frac{k_z^2}{\alpha_r R U_0} \pm \frac{6\sqrt{10}}{\pi^2}\frac{\alpha_i}{\alpha_r}\frac{U_b}{U_0}\right) \\
\tau &\propto \frac{1}{\alpha_i U_b}\left(1 - \frac{1583\pi^2}{96\sqrt{10}}\frac{k_z^2}{\alpha_i R U_b}\right), \\
\tau &\propto \frac{1}{\alpha_i U_b}\left(1 + \frac{401\pi^2}{192\sqrt{10}}\frac{k_z^2}{\alpha_i R U_b}\right).
\end{aligned} \tag{3.75}$$

The approximations are justified by the high Reynolds-number approximation (see appendix B.3). For the most unstable mode (3.75c) the effect of both the viscosity and the wavenumber of the basic flow is to decrease the life time of the perturbation.

d The general behaviour of the dispersion relation

In the general case ($\alpha_r < k_z$ and $R > \alpha_r/U_0$) it is difficult to evaluate the dispersion relation (3.46) analytically. Instead, we numerically solved (3.46) for Reynolds numbers in the range $R = 2^6...2^{17}$, and with the parameter setting $\mathcal{U} = 2U_0$, $\mathcal{L} = \frac{1}{4}\lambda_z$, $\alpha_r = \frac{1}{10}k_z$, $\alpha_i = \frac{1}{10}\alpha_r$ and $U_b = 1$. We find that this seventh-order equation has only six different roots (which are labeled I, II, ... ,VI). Figure 3.17 shows the corresponding six temporal growth rates g_t as a function of the Reynolds number of the low-velocity region. For large Reynolds numbers R we find one stable (I) and five unstable modes. When R decreases, the stable mode stabilizes further, whereas the most unstable mode (III) gives larger values of g_t. However, the least stable mode (IV) gives lower values of g_t. There is no strong effect of R on the other modes (II, V and VI). In general, this picture is in agreement with (3.72); the difference being the two 'new' modes that originate from the roots of the factor $(U_b - c)^2$ which is absent in (3.46). For smaller values of the Reynolds number the unstable modes II, V and VI stabilize, with as a result that for (say) $R < 256$ instability occurs only for mode III. We see that for this mode the viscosity has a destabilizing effect. Recalling that (3.46) is valid for $R > \alpha_r/U_0$, we conclude that this mode determines the stability of the basic flow. (Although the small Reynolds numbers are not covered by the governing approximations, we conjecture that mode III stabilizes for small Reynolds numbers.)
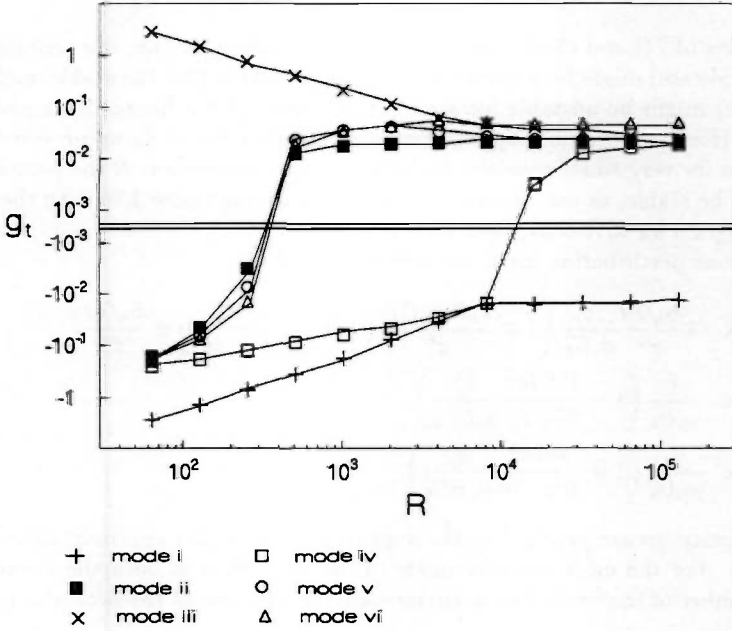
Figure 3.17: The temporal growth rates g_t of the stability modes of the dispersion relation (3.46) as a function of the Reynolds number R for the parameter setting $\mathcal{U} = 2\tilde{U}_0$, $\mathcal{L} = \frac{1}{4}\tilde{\lambda}_z$, $\alpha_r = \frac{1}{10}k_z$, $\alpha_i = \frac{1}{10}\alpha_r$ and $U_b = 1$.

This analysis leads to the following general picture. If both the wavelength of the perturbation and the Reynolds number of the basic flow is large, there always exists a number of different modes which cause the flow to be unstable. The number of unstable modes decreases with decreasing Reynolds number, and below a specific value of the Reynolds number only one unstable mode exists. In the range of intermediate Reynolds numbers the temporal growth-rate g_t of the perturbations is determined by the most unstable mode. The corresponding perturbation life-time τ increases with decreasing basic-flow wavenumber k_z and increasing Reynolds number R. Since there is no a-priori reason to restrict ourselves to the timewise case ($\alpha_i = 0$), in general τ is also inversely proportional to the local mean velocity U_b. Finally, although the life time of the most unstable mode does not depend on the magnitude U_0 of the low-velocity region, the life time of one unstable mode is inversely proportional to U_0.

3.4 Evaluation of the evolution of a spanwise velocity profile

Several studies have been performed in order to investigate the spanwise structure of the turbulent boundary layer, but to the best of our knowledge none of these involved the time evolution of the flow in a low-velocity region.

Connecting the extremes in a velocity profile pattern leads to the identification of two classes of extremes: those that are connected and those that are not. A further analysis shows that the class of connected extremes consists of two subclasses: the short-lived and the long-lived extremes. Associated with the long-lived extremes is the mean distance between low-velocity regions $< \lambda_z^+ > \approx 140$, whereas ensemble averaging all the extremes (whether connected or not) gives $< \lambda_z^+ > \approx 60$. We therefore conclude that the structure of an instantaneous profile is determined by all the extremes present, whereas the structure of a profile pattern is determined by the long-lived extremes. This conclusion emphasizes that the mean distance between low-velocity regions, as determined from the distance between inflection points (see section 2.5.3), is a measure of the instantaneous structure, which partly explains its low value as compared to the 'streak spacings' reported in other studies (e.g. Kline e.a., 1967; Smith and Metzler, 1983). If the short and extremely-short lived extremes are considered to be noise, the $< \lambda_z >$ determined from the long-lived extremes should be associated to the low-velocity regions that dominate the flow structure. However, the value $< \lambda_z^+ > \approx 140$ is larger than the well known value $< \lambda_z^+ > \approx 100$. At present, we do not have a satisfactory explanation for the difference.

Note however that merely separating connected and non-connected extremes leads to a difference of a factor 2 in $< \lambda_z >$. This shows that even a seemingly objective concept as extreme detection contains a great deal of subjectivity. Note also that the overall dynamics of the flow is determined by both the short and the long-lived extremes. Therefore, selecting the long-lived extremes reflects a choice by the investigator which might not reflect a feature of the flow.

May the differences in the numerical values be as they are, the qualitative picture given by the velocity profile patterns is in agreement with the knowledge on the spatial spanwise structure of the turbulent boundary layer. Our results show that this structure has a spatially quasi-periodic character, with the ensemble averaged wavenumber $< k_z >$ representing a band of dominant wavenumbers.

However, of more interest is the information which emerges from the basic-flow parameters k_z, U_b and U_0, and the Reynolds number R of the detected low-velocity regions (section 3.2.3). The wavenumber k_z, the local mean velocity U_b and the magnitude U_0 of a specific basic flow are mutually independent. However, the gradient length scale Δ seems to be uniquely determined by k_z. Furthermore, the two basic flows of a low-velocity region are asymmetrical. Generally, if in one of the basic flows large values of k_z occur together with small values of U_0, then in the other basic flow small values of k_z occur together with large values of U_0. The Reynolds number of the flow in the low-velocity regions is too low to consider this flow as inviscid. On basis of our observations, we concluded that (at least for short time lapses) it is possible to model the flow in a low-velocity region by a sinusoidal basic flow (section 3.3.2).

A viscous stability analysis shows that, for the prevailing values of the Reynolds number, one unstable mode exists for perturbations with a large streamwise wavelength (see section 3.3.3). Our measurements show that the life time of a low-velocity region is inversely proportional to k_z, and seems not to depend on U_b and U_0 (see section 3.2.3). If we assume that the most unstable viscous mode (3.75c) determines the dynamics of the low-velocity region, the behaviour of k_z and U_0 is qualitatively in agreement with the prediction. The behaviour of U_b suggests the spatial decay rate α_i to be small, which means that in practise only temporal modes occur.

Another feature of our experiments is that we found that the number of extremes in a velocity profile increases with profile rank. Associated with this effect are the splitting and the merging of low-velocity regions; a low-velocity region generally splits when k_z is small and U_0 is large, whereas it generally merges when k_z is large. The latter observation qualitatively agrees with the effect of k_z on the perturbation life-time of the most unstable viscous mode (3.75c) (see section 3.3.3).

The interpretation of our measurements is hampered by the limited temporal extent of the profile patterns. Regarding the life time of the low-velocity regions, it is observed that the peak which should correspond to the low-velocity regions which are dominately present in a profile pattern occurs at the largest life time possible. Unfortunately, we were not able to include more time-line recordings in a picture, so we can not tell in which position the second peak appears when the time evolution involves, say, twice as many time steps. Instead, we formulate two hypotheses: 1) The time scale of the observation determines to what extent a low-velocity region is present in a multiple velocity profile, and 2) The low-velocity regions have a life time which is considerably longer than the temporal extent of the present experiments. Regarding the increase in the number of extremes with profile rank, we formulate two mutually excluding hypotheses which describe what may happen after 6 time steps: 1) The splitting of low-velocity regions continues in subsequent time steps, and is not compensated by the merging of low-velocity regions, with as a net result an 'unbounded' increase of the number of extremes, and 2) The splitting of low-velocity regions continues in subsequent time steps, but is compensated by the merging of low-velocity regions, with as a result that after a certain number of time steps a steady number of extremes is present in a specific high-ranking velocity profile. In order to test these hypotheses, measurements should be performed with a larger temporal extent and a smaller uncertainty.

For two reasons the limitations of our experimental technique forced us to exclude from our presentation in section 3.2.3 measurements on the value of the streamwise wavenumber α_r of the perturbations. First, during 6 time steps the streamwise displacement of a time line is too small to resolve one streamwise wavelength. Second, the uncertainty in the fluid velocities, as determined from the moving time lines, is large, and might be of the order of the magnitude of the velocity perturbation (or worse), with as a result that it is not possible to distinguish between noise and velocity perturbation. Note also that we could not present in section 3.3.3 a prediction of the value of the most amplified streamwise wavenumber α_r as a function of the basic-flow parameters and the Reynolds number because we could only treat (3.46) in the long-wave approximation.

Chapter 4

Response of a turbulent boundary layer to artificial disturbances[8]

With periodic fluid-injection through small slots, a turbulent boundary layer is artificially disturbed on scales that are of the order of those of the natural quasi-periodic events. The periodic phase-average of the streamwise fluid velocity is determined from hot-film measurements, and used to find the coherent velocity component as defined by the triple decomposition. It appears that, when a disturbance is active, the generated flow pattern is very similar to the one caused by the interaction of a crossflow and a jet. However, when it is terminated, the turbulent boundary layer returns to its undisturbed state. In particular, there occurs no large increase in the fluid velocity which cannot be attributed to the disturbance itself; which increase one might expect if the disturbance initiates an artificial 'burst'.

4.1 The concept of disturbing the turbulent boundary layer

In a turbulent boundary layer the fluid velocity decreases from U_∞ (the free-stream velocity) to 0 (at the wall), and is characterized by fluctuations in its instantaneous value. If the fluid velocity is averaged over a specific time interval, it can be shown both theoretically and experimentally that the turbulent boundary layer consists of four distinctive layers (see e.g. Schlichting, 1979, chapters 19 and 20): the viscous sublayer, the buffer layer, the logarithmic layer and the wake region. According to the classic view, in each of these regions the fluid velocity is a random variable which can only be characterized by its mean and rms values. However, if the time interval is smaller than the one needed for the moments to converge, experiments have shown that the flow has a quasi-periodic character (see e.g. Robinson, 1991). According to the modern view, the fluid motion is coherent in space and time for scales which are larger than the smallest, but smaller than the largest scales of the flow.

May the structure of a turbulent boundary layer be well established, few experiments have been performed on the response of a turbulent boundary layer to artificial disturbances whose scales are of the order of the ones of the quasi-periodic events in a natural (i.e. undisturbed) turbulent boundary layer.

Gad-el-Hak and Hussain (1986) used two techniques to disturb a turbulent boundary layer: the abrupt suction of fluid and the sudden pitching of a small delta-wing. On basis of flow visualization and hot-film measurements, Gad-el-Hak and Hussain concluded that the effect of both these actions is the generation of a hairpin vortex and a low-

speed streak, and that the low-speed streak breaks up into a 'burst'.

Gad-el-Hak and Blackwelder (1987) used a cyclic jet to disturb a turbulent boundary layer. The jet issued fluid in upstream direction, and collected boundary layer fluid. When it was 'turned off', all of the collected fluid was released instantaneously in one large eddy that convected downstream. The results of flow visualization and hot-film measurements led Gad-el-Hak and Blackwelder to conclude that these large eddies are qualitatively similar to the natural ones, and seem to trigger 'burst'-like events in the wall region.

Although these investigations have shown that the fluid motion in a turbulent boundary layer can be organized, they have not given much quantitative information on the generated flow patterns, and therefore on the response of the flow to the disturbances. As was pointed out by Gad-el-Hak and Hussain (1986), this response can be studied via measurements which are phase locked to the initiation of the disturbance. Since each response to a disturbance will be smeared out differently due to the background turbulence, the responses must be phase averaged in order to eliminate the influence of the background turbulence. If the disturbances are periodical in time, the periodic phase average and the triple decomposition can be used to obtain the coherent part of the response (Hussain, 1983).

Sierputowsky (1991) used this procedure to study the flow structure due to the disturbances caused by an oscillating element in the wall of a turbulent boundary layer. On basis of hot-wire anemometry, Sierputowsky concluded that the disturbances lead to organized motion in the near-wall region.

The objective of the present investigation is to study the response of a turbulent boundary layer to artificially generated disturbances with time and length scales of the order of the ones of the quasi-periodic events in a natural turbulent boundary layer. That is to say: the time interval between two disturbances is of the order of the time interval between two 'bursts' (see e.g. Kim e.a., 1971), the spanwise distance between two disturbances is of the order of the spanwise distance between two low-speed streaks (see e.g. Kline e.a., 1967), and the width of the disturbance is of the order of the width of a low-speed streak (see e.g. Blackwelder, 1978).

In this chapter we report on this study on the response of a turbulent boundary layer to artificial disturbances. To disturb the turbulent boundary layer, we periodically injected fluid through small spanwise slots. We examined the response of the flow to the disturbance in terms of the coherent component of the streamwise fluid velocity, which was obtained from measurements that were phase locked to the initiation of the disturbance. First, we describe our experimental procedure (section 4.2). Then we present the results of the measurements on the response (section 4.3) and, finally, the evaluation of our experiments (section 4.4).

4.2 The experimental procedure

4.2.1 The experimental apparatus and methods

The turbulent boundary layer in which we performed our experiments is generated over a flat plate mounted in an open water channel. This channel, which was used for combined hydrogen-bubble visualization and laser-doppler anemometry, is described elsewhere (Talmon e.a., 1986). Modification since then resulted in less vibrations in the test section and a higher water level. The channel allows for free-stream velocities U_∞ up to 19 cm/s with a turbulence level of 1.5%.

The flat plate is 175 cm long and 60 cm wide (figure 4.1a). It has an adjustable flap at its end in order to control boundary-layer transition and separation. The plate is made of 2 cm thick perspex. The surface of the plate is mounted at a height of 6.5 cm above the bottom of the water channel. A 7 mm thick tripping wire, mounted 32 cm downstream of the leading edge, is used to create a turbulent boundary layer.

The disturbances are generated by a mechanism[9] which injects amounts of fluid into the turbulent boundary layer. For this purpose three arrays of four holes each are mounted at $x = 85$, 105 and 125 cm downstream of the leading edge of the plate (figure 4.1a). Each hole is provided with a plug in which a small slot was drilled. The total layout is such that its sizes scale with the length scales of the quasi-periodic events in a natural turbulent boundary layer. This means that the spanwise spacing of two slots is about $100 l_*$ (which corresponds to the mean spanwise distance between two low-speed streaks; Kline e.a. (1967)), and the spanwise extent of a slot is about $20 l_*$ (which corresponds to the mean width of a low-speed streak; Blackwelder (1978)). (Recall $l_* = \nu/u_*$ is the viscous length scale.) In order to keep the streamwise scale of the disturbances as small as possible, the streamwise extent of each slot is about $3 l_*$. Therefore, for example, at $x = 105$ cm the slots measure 3.0x0.5 mm, and are spaced 14.7 mm apart.

The injection mechanism is driven by pressurized air (figure 4.1b). To visualize the disturbances, the water in this mechanism can be replaced by dye (methylene blue). The electro-magnetic solenoid valves of the injection mechanism are controlled by a logic control unit (Siemens S5-100U), which enables us to set independently the injection period T (i.e. the time interval between the start of two injections) and the injection duration T_i (i.e. the time interval during which the valve is open). The injection period T is of the order of the mean time interval $5\delta/U_\infty$ (with δ the boundary layer thickness) between two 'bursts' in a natural turbulent boundary layer (Kim e.a., 1971). The injection duration T_i must be smaller than the injection period, but larger than the smallest time scale $t_* = \nu/u_*^2$. For the present experiments $T = 1.5$ s or $T = 4.0$ s, and $T_i = 0.5$ s is used (see section 4.3.1). The injection velocity can be precisely set in the range $V_i = 0...1000$ mm/s with a 20-turn valve.

A personal computer (Hewlett Packard Vectra ES/12) with specific data acquisition hardware (Data Translation DT 2820) controls the experiments via the logic control unit. A hot-film probe (DISA/Dantec 55R32 with bridge 55M01 or 56C01), calibrated

---

[9]The injection mechanism was designed by H.F.Th. Tichelman
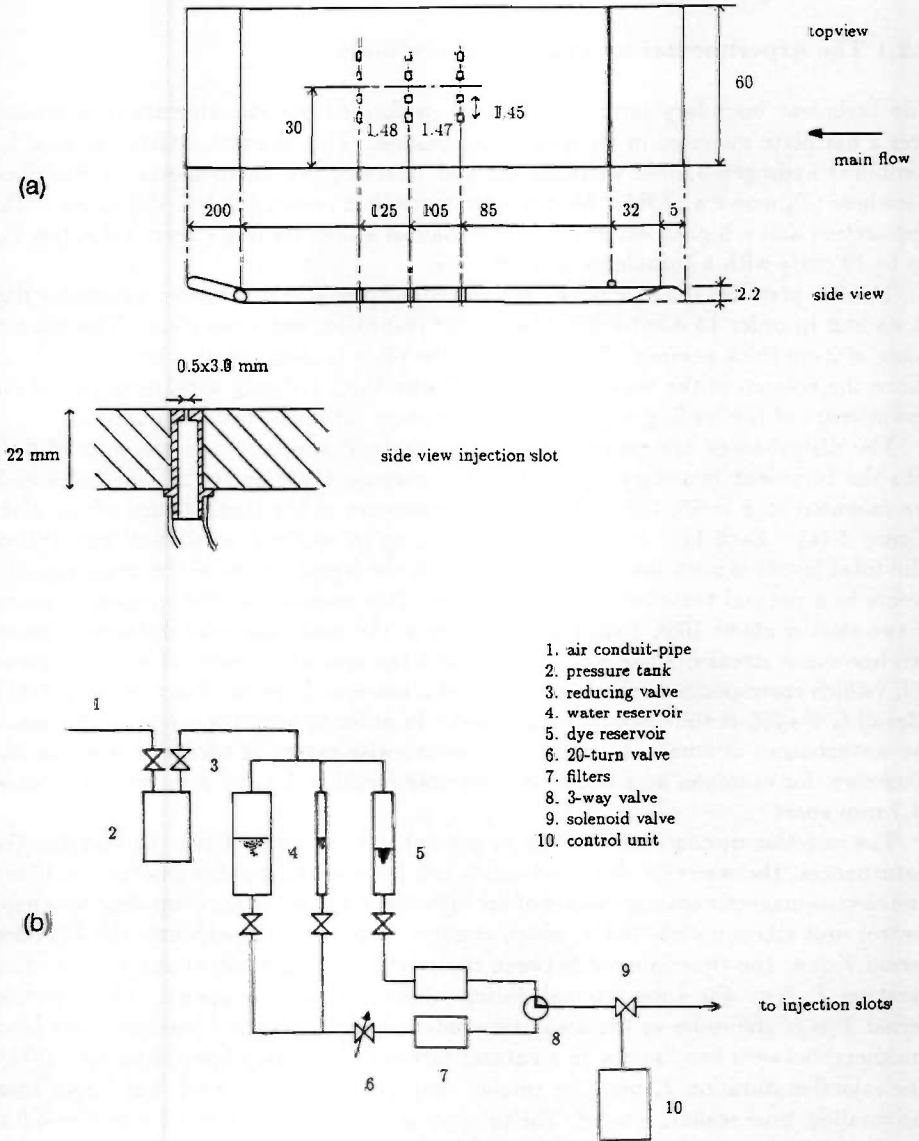
Figure 4.1: A schematic of (a) the flat plate, with a detailed side view of an injection slot, and (b) the injection mechanism. Sizes are in cm, unless else stated.
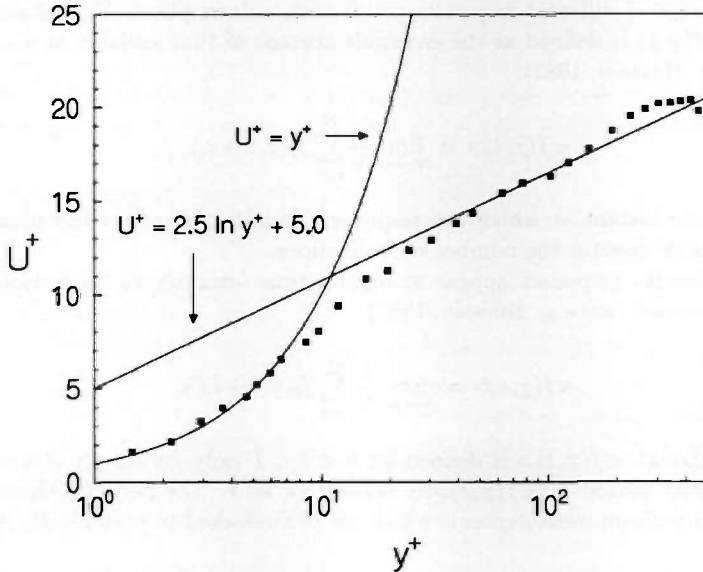
Figure 4.2: Dimensionless mean velocity profile in the turbulent boundary in the absence of disturbances.

in a Poiseuille flow, is used to measure streamwise velocities. The signals from this probe are processed by the computer through customized programs[10] in a data processing software package (Asyst).

Before we performed the injection experiments, we determined the characteristic parameters of the flow. With a free-stream velocity U_∞ of 16.7 cm/s we found $Re_\theta = 769$ (with θ the momentum thickness) at $x = 85$ cm ($Re_x = 1.33 \; 10^5$). The viscous scales are $u_* \approx 8.1$ mm/s, $l_* \approx 0.13$ mm and $t_* \approx 16$ ms. (We determined u_* by fitting the 'theoretical' profile $U^+ = 2.5 \ln y^+ + 5.0$ to the $U(y)$ profile.) The boundary layer thickness is $\delta = 48$ mm (with δ the distance above the wall where the mean velocity is $0.99 U_\infty$). The turbulent boundary layer has a linear profile up to $y^+ = 9$, and a logarithmic profile for $35 < y^+ < 180$ (figure 4.2).

4.2.2 The data reduction

In general, each response to a disturbance evolves differently because of the influence

---

[10]Parts of the data analysis software were coded by W.H. van Sorge

of the background turbulence. As a consequence, the characteristics of the response at a specific phase (i.e. the time lapse since the initiation of the disturbance) are smeared out. However, the description of the response must be independent of this effect. Taking the phase average of different responses yields such a description. The phase average of a variable $f(\underline{x}, t)$ is defined as the ensemble average of that variable at a particular phase (see e.g. Hussain, 1983):

$$<f(\underline{x}, t)> = \lim_{N \to \infty} \frac{1}{N} \sum_{i=1}^{N} f_i(\underline{x}, t + t_i), \qquad (4.1)$$

with t_i the time instant at which the response $\bar{i}$ is initiated, and t the phase of the response. Here N denotes the number of realizations.

When successive responses appear at regular time intervals T, the periodic phase average can be used (see e.g. Hussain, 1983):

$$<f(\underline{x}, t)> = \lim_{N \to \infty} \frac{1}{N} \sum_{i=1}^{N} f_i(\underline{x}, t + iT). \qquad (4.2)$$

Note that, although $<f(\underline{x}, t)>$ is defined for $0 < t < T$ only, by simply stating that it is periodical with period T, $<f(\underline{x}, t)>$ is defined for all t. The periodic phase average can be used to perform measurements which are phase-locked to periodically generated disturbances.

In practice, the number of realizations does not reach infinity. The periodic phase average is then approximated by:

$$<f(\underline{x}, t)> \sim \frac{1}{N} \sum_{i=1}^{N} f_i(\underline{x}, t + iT). \qquad (4.3)$$

Then

$$\delta_f(\underline{x}, t) = \left(\frac{\sum_{i=1}^{N} (<f(\underline{x}, t)> - f_i(\underline{x}, t + iT))^2}{N(N-1)} \right)^{\frac{1}{2}} \qquad (4.4)$$

gives the error $\delta_f(\underline{x}, t)$ in the value of the phase-averaged response $<f(\underline{x}, t)>$.

Having defined the periodic phase average of a variable f, we can decompose f into three components: the time independent or mean component f_m, the coherent component f_c, and the random or incoherent component f_r. This decomposition is called the triple decomposition (Hussain, 1983):

$$f(\underline{x}, t) = f_m(\underline{x}) + f_c(\underline{x}, t) + f_r(\underline{x}, t). \qquad (4.5)$$

The following relations hold:

$$f_m = \overline{f}, \quad f_c = <f> - \overline{f}, \quad \text{and} \quad f_r = f - <f>, \qquad (4.6)$$

with $\overline{f}$ the time average and $< f >$ the phase average of f. Note that f_m is time independent, f_c is periodical with period T, and f_r is a random function of time. So,

the coherent component of the response to periodic disturbances can be determined from measurements of the periodic phase average and the time average of the responses.

The random component f_r of a variable can be used to estimate the error in its periodic phase average:

$$\delta_f(\underline{x}, t) \sim \frac{1}{N} \left(\sum_{i=1}^{N} f_r^2(\underline{x}, t + iT) \right)^{\frac{1}{2}}. \qquad (4.7)$$

This follows from taking into account that $f_i - <f> = f_r$, and assuming a large number of realizations N.

4.3 Measurements on the response[11]

4.3.1 The setting of the disturbance amplitude

In order to test the performance of the phase-averaging procedure, and to determine the effect of the injection velocity V_i, fluid was injected into the turbulent boundary layer ($U_\infty = 18.6$ cm/s) at velocities between 1 and 45 cm/s. The hot-film sensor was positioned downstream of the slots at $x = 105$ cm, and at the position $(x^+, y^+, z^+) = (77, 23, 113)$ relative to the slots. (See figure 4.3 for the definition of this coordinate system.) During each injection period 50 velocity samples were taken. Each measurement series consisted of 288 periods. An example of a part of the measured streamwise velocity signal is shown in figure 4.4a.

From (4.6) it follows that the mean velocity component u_m is needed to compute the coherent component u_c of the response: $u_c = u_m - <u>$, where $<u>$ is the periodic phase average of the fluid velocity. In the case of the disturbed turbulent boundary layer, u_m is the average velocity in the absence of disturbances. Figure 4.4b shows that the level of $<u>$ remains constant (i.e. $u_c < \delta u_c$) for $t/T > 0.8$. We therefore concluded that for $t/T > 0.8$ the turbulent boundary layer is in its undisturbed state, and obtained u_m from the last 10 velocity samples of each injection period:

$$u_m = \frac{1}{10} \sum_{i=41}^{50} <u(T\frac{i}{50})>, \qquad (4.8)$$

where i denotes an individual sample. This choice ensured that an ensemble average of u_m over a sufficiently large number of realizations yields the average fluid velocity in the absence of disturbances; which average corresponds to the statistical mean of the fluid velocity in the undisturbed turbulent boundary layer. (We used the statistical mean to obtain the data in figure 4.2.) Note, however, that the response depends on four quantities, viz. V_i, U_∞, T_i and T. So for a different value of the group (V_i, U_∞, T_i, T) a different set of last velocity samples might be needed to obtain a significant u_m, or, even worse, no significant u_m might be obtained at all.

---

[11]The experiments reported on in this section were performed by H.J.M. Vollebregt and A.K. Wemmers
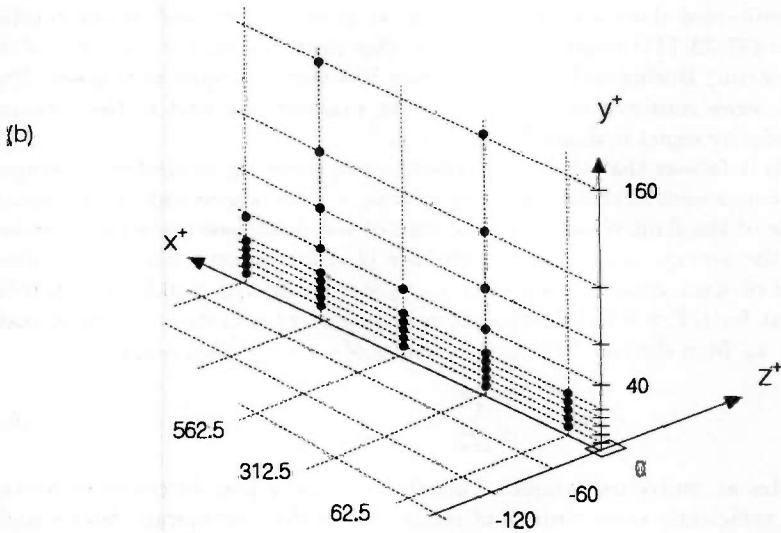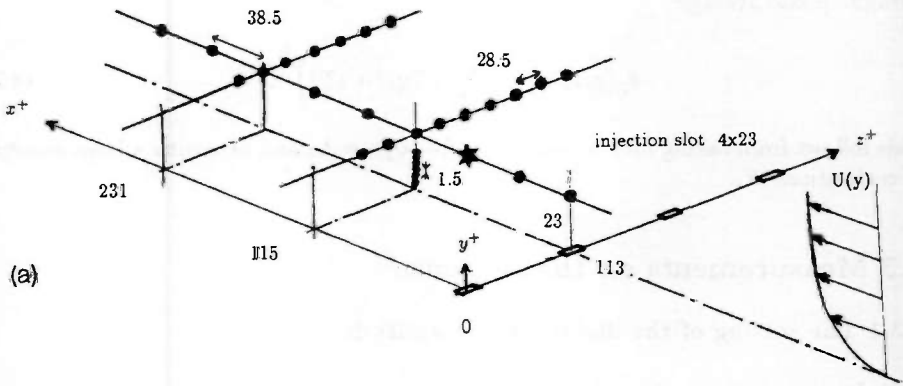
Figure 4.3: (a) The coordinate system with respect to the injection slots and the four sets of measuring positions used in the case of moderate disturbances. The * denotes the position $(x^+, y^+, z^+) = (77, 23, 113)$. (b) A guide to the measuring positions used in the case of strong disturbances. For clarity only the measuring positions in the xy plane are shown. Sizes are in viscous length scales ν/u_*.
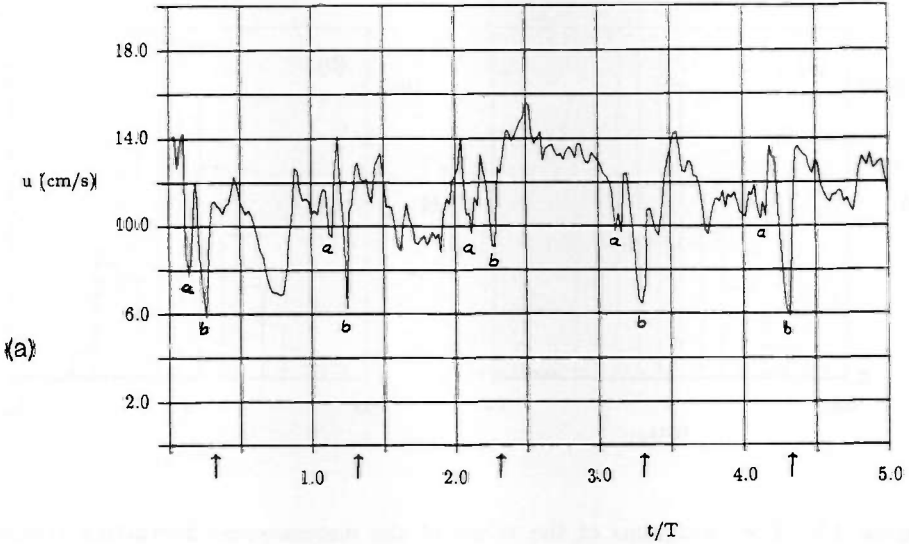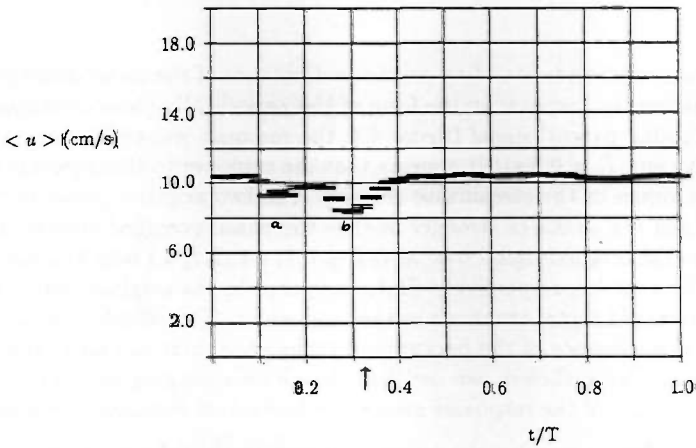
Figure 4.4: An example of (a) the streamwise velocity signal u, and (b) its periodic phase average $<u>$. The lowercase characters denote the two minima. The signal was measured at $(x^+, y^+, z^+) = (77, 23, 113)$ with the parameter setting $V_i = 130$ mm/s, $T_i = 0.5$ s and $T = 1.5$ s. In this and subsequent figures the arrow indicates the phase at which the disturbance is terminated.
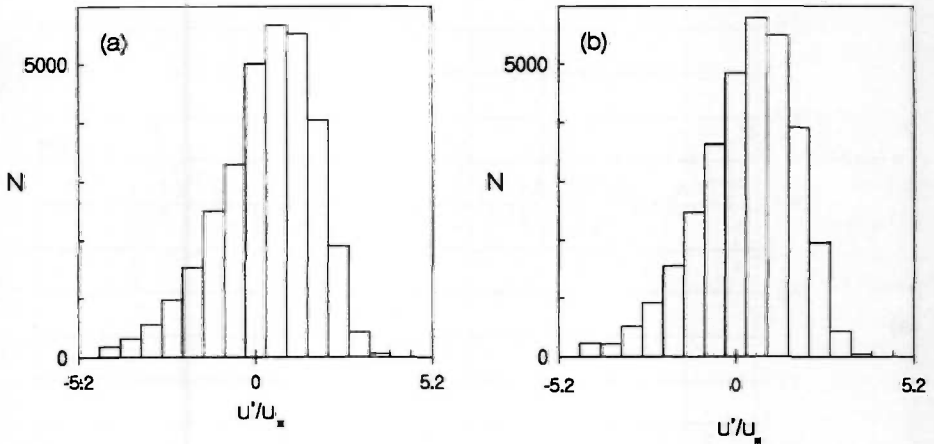
Figure 4.5: The histograms of the values of the dimensionless fluctuating component u'/u_* of the Reynolds decomposition as obtained in the measuring position $(x^+, y^+, z^+) = (77, 23, 113)$ in the turbulent boundary layer (a) without and (b) with disturbances ($V_i/U_\infty = 0.75$).

We may gain some understanding on the performance of the phase-averaging procedure by comparing the response in the form of the periodically phase-averaged velocity trace $<u(t)>$ to its 'parent' signal (figure 4.4; the response was obtained with $V_i = 13$ cm/s, $T = 1.5$ s and $T_i = 0.5$ s). It appears that the response to the injection is characterized by low values of the streamwise velocity. The two negative peaks at $t/T \approx 0.1$ (a weak one) and $t/T \approx 0.3$ (a stronger one) in the phase-averaged velocity signal can be identified in the original signal too: at $t/T \approx 0.1$, 1.1, 2.1, 3.1 and 4.1, and at $t/T \approx 0.3$, 1.3, 2.3, 3.3 and 4.3, respectively. But, compared to the original peaks, the peaks in the phase-averaged signal are much weaker and wider. This effect is caused by phase jitter: due to the influence of the background turbulence there are no responses which are totally equal. Nevertheless, we see that the phase-averaging procedure is able to capture the signature of the responses even if the individual responses are smeared out.

In fact, the phase-averaging procedure is the most powerful procedure to achieve this goal. This is illustrated in figure 4.5, which shows the histograms of the Reynolds fluctuating component of the streamwise fluid velocity, as it was obtained without and with disturbances. It appears that the negative velocity peaks due to the disturbances (which are present in the phase-averaged velocity traces) did not cause a change in the shape of the histograms, as one might have expected.

As a measure of the magnitude of the response of the flow to the disturbances we
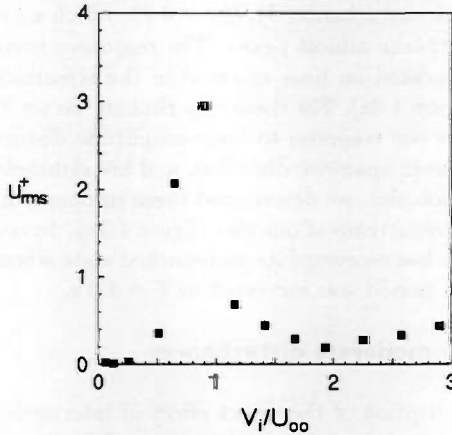
Figure 4.6: The measure of the dimensionless response $u_{rms} = \overline{u_c^2}^{\frac{1}{2}}/u_*$ due to the disturbance as a function of the dimensionless injection velocity V_i/U_∞; the response was measured at $(x^+, y^+, z^+) = (77, 23, 113)$.

took

$$\overline{u_c^2}^{\frac{1}{2}} = \left(\frac{1}{50} \sum_{i=1}^{50} u_c^2 \left(T\frac{i}{50}\right)\right)^{\frac{1}{2}}, \qquad (4.9)$$

which is the rms value of u_c in the measuring position. Figure 4.6 shows the response $\overline{u_c^2}^{\frac{1}{2}}$ to the disturbances as a function of the injection velocity V_i. It appears that four regions of interest are present: 1) For small injection velocities ($V_i/U_\infty < 0.3$) there is no significant response. 2) When the injection velocity is increased to a value in the range $0.3 < V_i/U_\infty < 1.0$, the response is strong and roughly proportional to V_i. 3) However, for still larger values ($1.0 < V_i/U_\infty < 2.0$) the response decreases with the injection velocity. 4) Finally, for $V_i/U_\infty > 2.0$ the response is weak but increases slowly with the injection velocity.

Since taking the phase average is the most powerful method to capture a response (even for the values of V_i/U_∞ where a strong response occurs; cf. figures 4.6 and 4.5), the absence of any response for small disturbance amplitudes strongly suggests that a weak disturbance is dissipated by the turbulent flow before it reaches the measurement station. For larger amplitudes, the response to a disturbance is caused by the interaction of the flow and the disturbance. As is revealed by dye visualization of the injected fluid (not shown), the strong responses in the range $0.3 < V_i/U_\infty < 1.0$ are caused by injected fluid that passes the measuring position, and, consequently, are a characteristic of the disturbance itself. However, for very large injection velocities the disturbance penetrates

the turbulent boundary layer, and passes over the measuring position.

We did not explore further the response to small-magnitude disturbances, and in the following we will treat the other two cases separately. Section 4.3.2 presents the response to intermediate-amplitude disturbances $V_i/U_\infty = 0.75$, which amplitude corresponds to the one for which the response almost peaks. The responses themselves were obtained in measuring positions located on lines oriented in the streamwise, the spanwise and the normal direction (figure 4.3a). For these experiments we set $T = 1.5$ s and $T_i = 0.5$ s. Section 4.3.3 presents the response to large-amplitude disturbances $V_i/U_\infty = 2.5$. Since the responses repeat in spanwise direction, and are symmetrical with respect to a plane through the injection slot, we determined these responses in positions located on a grid in the halfspace downstream of one slot (figure 4.3b). In order to ensure that the turbulent boundary layer has recovered its undisturbed state when the next disturbance is initiated, the injection period was increased to $T = 4.0$ s.

4.3.2 The response to moderate disturbances

To get a qualitative description of the direct effect of intermediate magnitude disturbances $V_i/U_\infty = 0.75$, we used dye rather than water as injection fluid. Figure 4.7 shows the digitized versions of 4 of the about 40 consecutive video frames that were recorded during one injection period. The frames at $t/T = 0.05$, 0.11, 0.16 and 0.21 were digitally low-pass filtered, rescaled and compensated for uneven illumination in order to improve their quality, and laser printed with a grey-value resolution of 16 levels. The sideviews of the dye plume show that the disturbance itself is very similar to a jet which is active during a short time lapse.

In order to obtain a quantitative description of the response to intermediate-magnitude disturbances, we performed measurements on lines in the streamwise, the spanwise and the normal direction, as indicated in figure 4.3a.

Nine measuring positions were located on a line oriented in the streamwise direction at $y^+ = 23$ and $z^+ = 113$. Figure 4.8a shows the nine coherent velocity components as a function of phase, and figure 4.8b shows the corresponding lines of equal u_c. By carefully examining these graphs, two 'valleys' can be found in u_c. These valleys correspond to the two negative peaks which characterize the response to the injection (one weak and the other strong; see section 4.3.1 and figure 4.4).

In figure 4.9 the positions of the coherent-velocity minima are plotted as a function of the phase. The convection velocity determined from the weak minimum is 10.7 cm/s. This value corresponds to the one of the local mean velocity at $y^+=23$, which is $\overline{u} = 10.5$ cm/s. The convection velocity determined from the strong minimum is 7.2 cm/s, which corresponds to $0.7\overline{u}$. Therefore, the strong minimum indicates the presence of a low-velocity region travelling at a speed less than the local mean velocity.

A measure of the magnitude of the coherent velocity component of the response at a specific phase is

$$u_c^{mag}(t/T) = \left(\frac{1}{9}\sum_{i=1}^{9} u_c^2(X_i, t/T)\right)^{\frac{1}{2}}, \tag{4.10}$$

where X_i denotes the measuring position i. Note that here the averaging takes place in

(a)   (b)

(c)   (d)
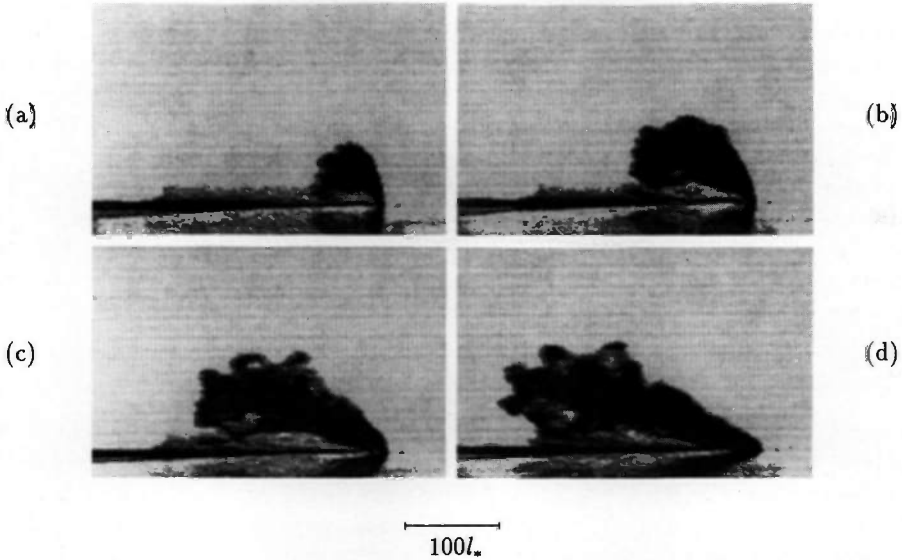
$100l_*$

Figure 4.7: Four sideview snapshots of a moderate disturbance $V_i/U_\infty = 0.75$ at (a) $t/T = 0.05$, (b) 0.11, (c) 0.16, and (d) 0.21; the flow is from right to left. The injection lasts for $T_i = 500$ ms and has a period of $T = 1500$ ms. The bar denotes a distance of $100l_*$.

space rather than in time. Figure 4.10 presents u_c^{mag} as a function of the phase. It can be seen that the magnitude of the coherent velocity component rises during the first half of the injection period ($0 < t/T < 0.17$), and decays afterwards ($0.17 < t/T < 0.50$). For $t/T > 0.67$ the coherent velocity does not change significantly, and the turbulent boundary layer is back in its undisturbed state. The decay depends exponentially on the phase:

$$u_c^{mag}(t/T) = C \exp(-t/\tau) \qquad (4.11)$$

with τ the time scale of the decay. From the slope of the solid line in figure 4.10 it follows that $\tau/T \sim 0.11$, which is equivalent to $\tau u_*^2/\nu \sim 11$.

In order to obtain the spanwise flow pattern due to the injected fluid, we performed measurements on two lines oriented in the spanwise direction: one with nine measuring positions at $y^+ = 23$ and $x^+ = 115$, and the other with seven measuring positions at $y^+ = 23$ and $x^+ = 231$. The phase axes were transformed into spatial axes using $x_1 = -U_{conv}(t - T_i)$, with U_{conv} the convection velocity of the strong low-speed region ($U_{conv} = 7.2$ cm/s) (figure 4.11; note that $x_1^+ = 400$ corresponds to $t = 0$).

From figure 4.11a it appears that for $220 < x_1^+ < 400$ the spanwise flow pattern is
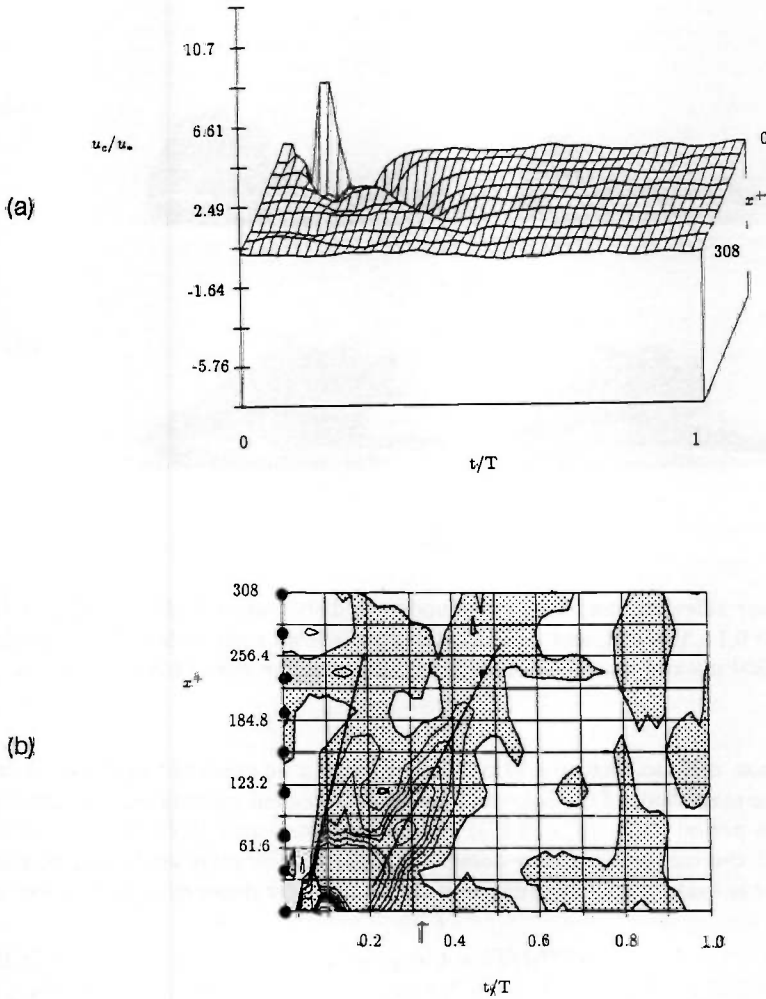
Figure 4.8: (a) A graph and (b) a contour plot of the dimensionless coherent velocity u_c/u_* due to a moderate disturbance, as measured in positions on a streamwise line at $y^+ = 23$, $z^+ = 113$. A ● indicates a measuring position. The contour lines denote $u_c/u_* = 2.0$, 1.0, 0.5, 0.0 (fat line), -0.5, -1.0 and -2.0. In the grey region $u_c/u_* < 0$. The straight lines indicate the valleys where u_c/u_* reaches a minimum value.
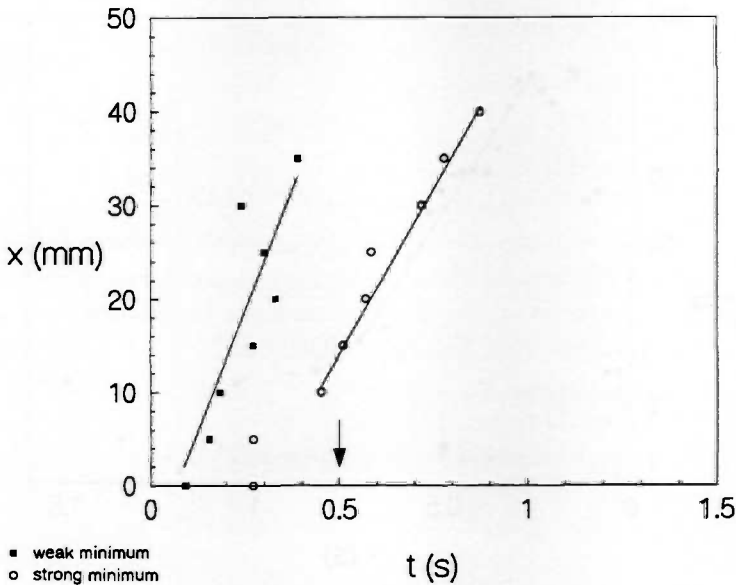
Figure 4.9: The location of the minima of figure 4.8b as a function of phase. The straight lines are linear least square fits for (1) the weak minimum, and (2) the strong minimum. The latter gives the convection velocity for the low-velocity regions.

dominated by the presence of a wide region with a small negative value of the coherent velocity component. This region travels with the higher convection velocity $\overline{u}$. For $x_1^+ <$ 220 elongated regions with a larger negative value of the coherent velocity component are present. These regions are located behind the injection slots, and obtain their minimum at $x_1^+ \approx 100$. They travel with the convection velocity of about $0.7\overline{u}$. However, at the measuring positions located at z^+=85, 141, 198 and 254 the flow pattern is characterized by a region with a large positive coherent velocity component. The peaks of these regions are at $x_1^+ \approx 180$.

The strong low-velocity regions and the high-velocity regions (which are at $x_1^+ \approx 100$ and $x_1^+ \approx 180$, respectively) arrive at different phase instants in a specific position. The difference can be attributed to the different convection velocities: the low-velocity regions travel with the lower convection velocity $0.7\overline{u}$.

The elongated low-velocity regions that are clearly present at $x^+ = 115$ (figure 4.11a) have almost completely disappeared at x^+=231 (figure 4.11b). On the other hand, the high-speed regions seem to have merged: the two regions at z^+=141 and 198 ($x^+ = 115$) have become one large high-velocity region at z^+=168 ($x^+ = 231$).
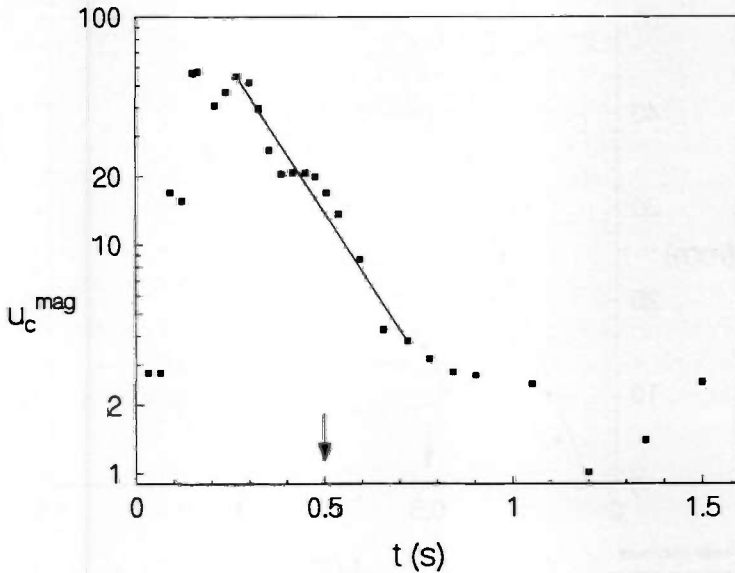
Figure 4.10: The magnitude of the coherent velocity u_c^{mag} as a function of phase. The straight line is a linear least square fit from which follows the decay rate of the low-velocity region.

Ten measuring positions were located on a line oriented normal to the wall at $x^+ = 115$ and $z^+ = 113$. The measurements performed here yield the near-wall flow pattern due to the injected amounts of fluid. Figure 4.12a shows the ten coherent velocity components as a function of the phase. The coherent part of the velocity first decreases to $u_c/u_* \approx -0.5$ at $t/T \approx 0.1$, and then increases to $u_c/u_* \approx +0.5$ at $t/T \approx 0.3$. Figure 4.12b presents, at five consecutive phase instants, the instantaneous profiles of the coherent velocity as a function of the distance y^+ to the wall. For $t/T < 0.3$ the flow is dominated by the presence of the disturbance, and is characterized by a large negative coherent velocity with a peak at $y^+ \approx 8$. In the interval $0.3 < t/T < 0.4$ a large change occurs: during this short period large positive coherent velocities are present. For $t/T > 0.6$ the flow returns to its undisturbed state, which is characterized by $u_c/u_* = 0$.
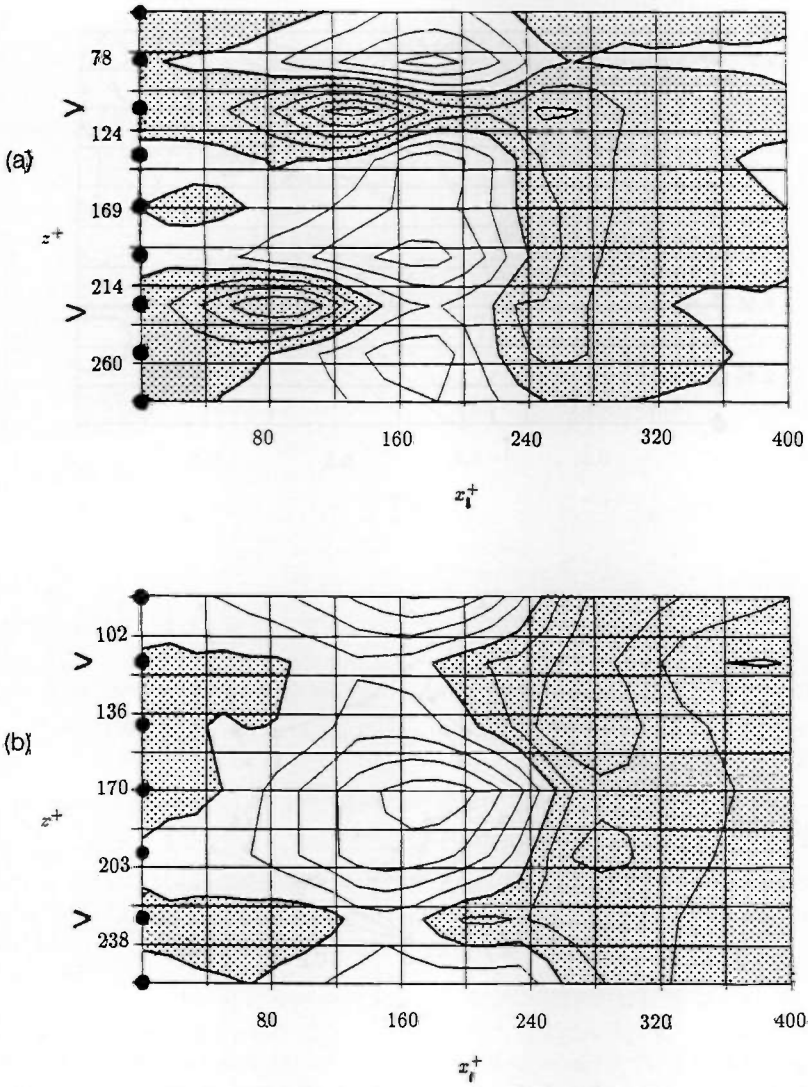
Figure 4.11: The contour plots of the spanwise structure of the coherent velocity due to a moderate disturbance as measured in (a) $x^+ = 115$, $y^+ = 23$, and (b) $x^+ = 231$, $y^+ = 23$. Phase has been transformed into distance with $x_1 = -U_{conv}(t - T)$. A • indicates a measuring position and a > the position of an injection slot. In the grey region $u_c/u_* < 0$.
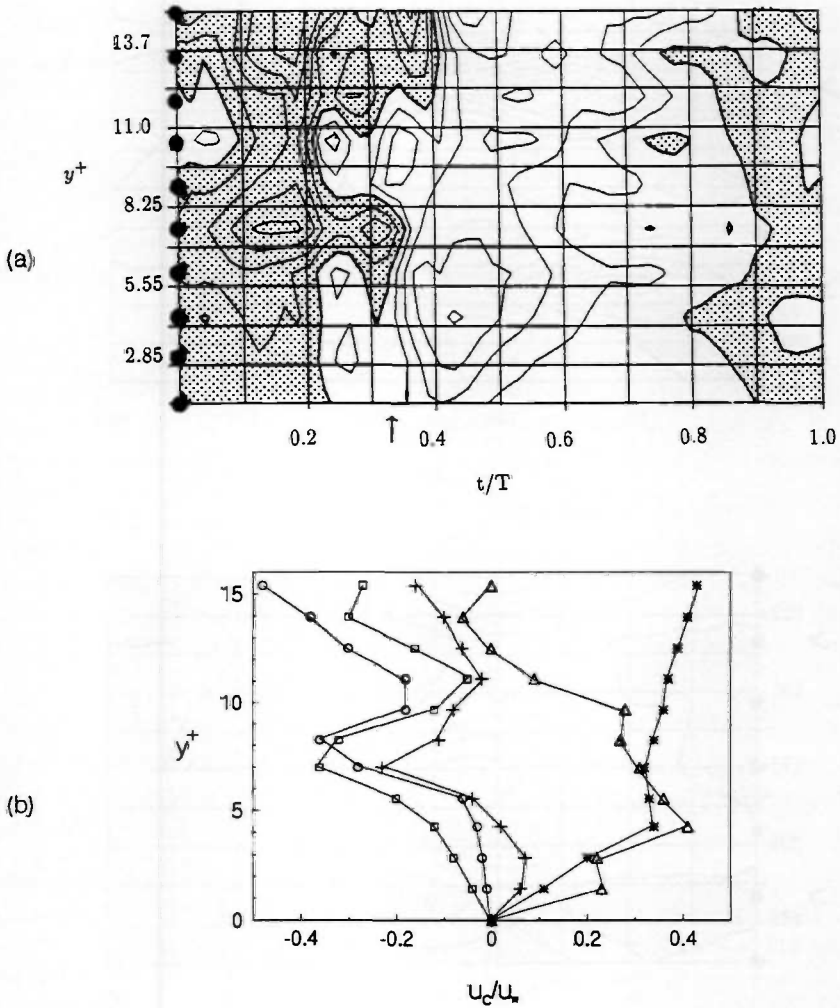
Figure 4.12: (a) A contour plot of the dimensionless coherent velocity u_c/u_* due to a moderate disturbance, as measured in locations on a line normal to the wall at $x^+ = 115$, $z^+ = 113$. The fat line denotes $u_c/u_* = 0$ and the contour interval is $u_c/u_* = 0.12$. A ● indicates a measuring position. In the grey region $u_c/u_* < 0$. (b) The dimensionless coherent velocity u_c/u_* due to the generated disturbance as a function of the dimensionless distance to the wall y^+. The profiles were obtained from figure 4.12a at the intersection of 11 y^+ levels and the phases $t/T = 0.1$ (□), 0.2 (○), 0.3 (+), 0.4 (△) and 0.5 (⋆).

4.3.3 The response to strong disturbances

In order to obtain the response to large-magnitude disturbances $V_i/U_\infty = 2.5$, we performed measurements in 135 positions in a halfspace downstream of an injection slot (figure 4.3b). Only a selection of the measured coherent velocity components at the various cross sections will be presented here.

First, we consider the responses obtained in the plane of symmetry $(z^+ = 0)$. Figure 4.13a shows the phase evolution of the coherent components of the fluid velocity which were obtained in five positions on the streamwise line at $y^+ = 5$. It appears that in positions near the slot the response is characterized by two peaks: one negative and the other positive. The peaks level out for large values of the phase and the streamwise coordinate. However, the situation is different for the streamwise lines at $y^+ = 15$ and $y^+ = 25$. Figures 4.13b and 4.13c show that the negative peak is still present, whereas the positive peak has disappeared. Furthermore, the negative peak is wider, and is present in positions further downstream. By plotting the positions of the velocity minima as a function of the phase, the convection velocities U_{conv} are found to be 5.9 cm/s at $y^+ = 5$, 5.0 cm/s at $y^+ = 15$, and 4.6 cm/s at $y^+ = 25$.

The responses off the plane of symmetry were obtained in positions on three streamwise lines (at $y^+ = 5$, $y^+ = 15$ and $y^+ = 25$) at $z^+ = -60$ and $z^+ = -120$ (figure 4.14 and 4.15, respectively). In general, at $y^+ = 5$ these responses are similar to those obtained at $z^+ = 0$. However, the negative peak is wider, whereas the positive peak is less wide. Both peaks have a smaller amplitude. At $y^+ = 15$ and $y^+ = 25$ the response is characterized by a weak velocity minimum, which is followed by a weak velocity maximum. This behaviour is different from the one observed at $y^+ = 5$.

As observed from the maxima at $t/T \approx 0.19$, 0.44 and 0.69 in figures 4.13a and 4.14a, the response to strong disturbances is characterized by an oscillation with a period of the order of $T/4$. Since 1) the amplitude of the oscillation is larger than the uncertainty in u_c^+, and 2) observations of fluid injections into still water indicated that neither the injection mechanism nor the data reduction introduces a periodicity with a period of $T/4$, it is reasonable to interpret the oscillation as a feature of the interaction between the flow and the disturbance. Note, however, that the streamwise extent of the oscillation scales with the resolution in x^+ direction, as can be found by inspection of figure 4.3b. Even so, to date we do not have an explanation for this oscillation, and we will not speculate on its origin or significance.

The near-wall flow-pattern as a function of the phase was determined in positions on three lines perpendicular to the wall at $x^+ = 300$ and $z^+ = 0$, $z^+ = -60$, and $z^+ = -120$, respectively. Figure 4.16a shows the flow behaviour in the plane of symmetry. In the region near the wall $(y^+ < 15$, say) the fluid velocity first increases, and then returns to its undisturbed state. However, further away form the wall $(15 < y^+ < 70)$ the fluid velocity decreases before it returns to the undisturbed state. The latter behaviour can also be found for all measuring positions off the plane of symmetry (figures 4.16b and 4.16c).
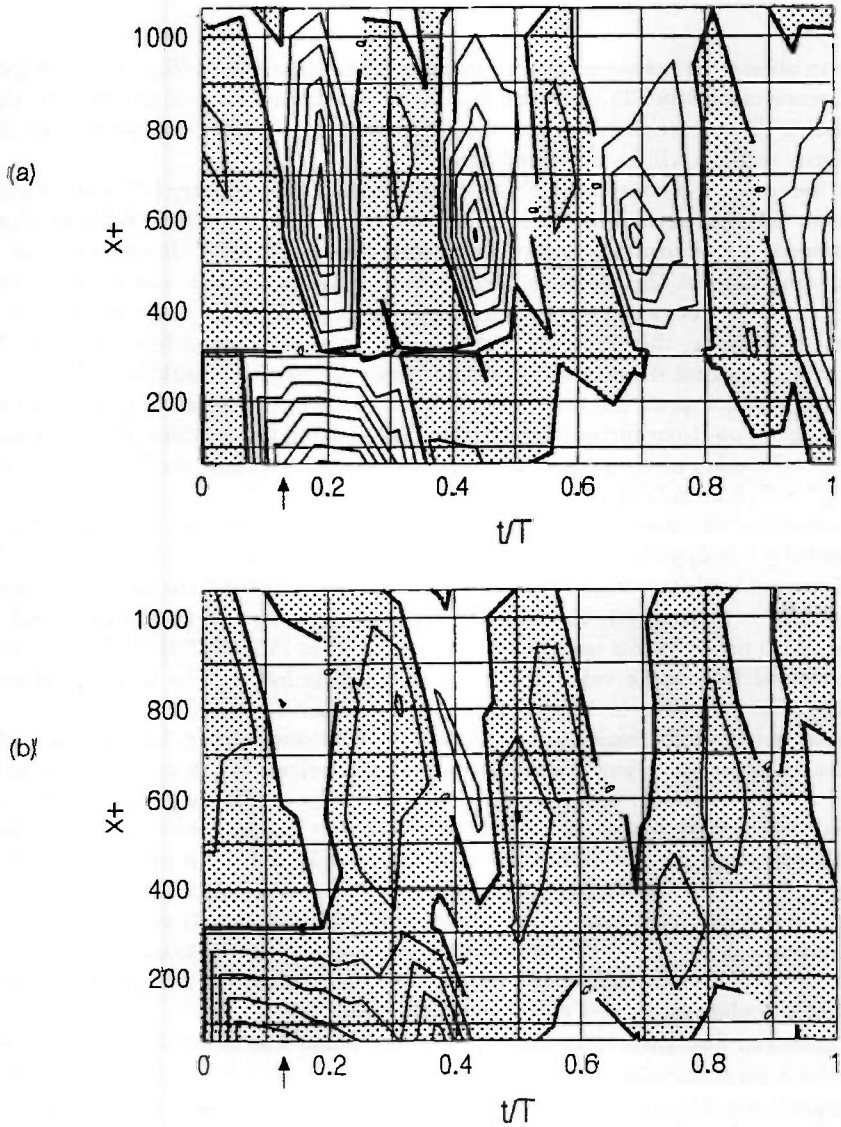
Figure 4.13: The contour plots of the dimensionless coherent velocity u_c/u_* due to a strong disturbance as a function of the phase, as measured in the plane of symmetry $z^+ = 0$ in positions on a streamwise line at (a) $y^+ = 5$, (b) $y^+ = 15$, and (c) $y^+ = 25$. The fat line denotes $u_c/u_* = 0$, and the contour interval is $u_c/u_* = 0.5$. In the grey region $u_c/u_* < 0$.
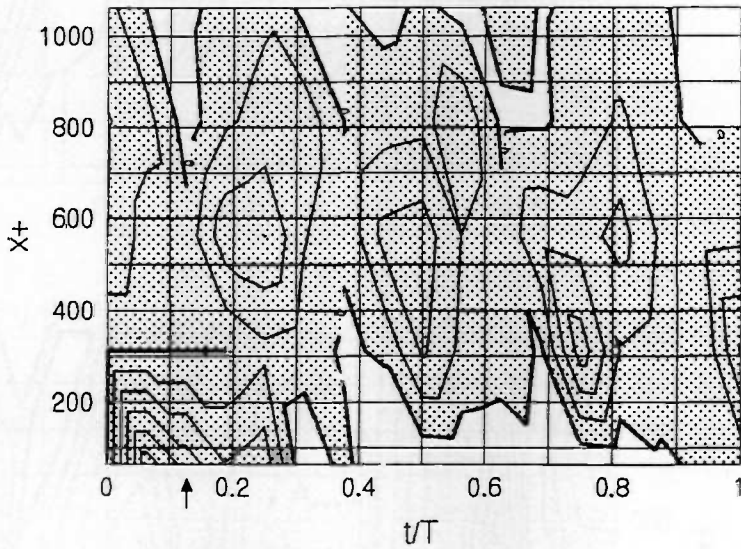
Figure 4.13: (c) For caption see previous page.
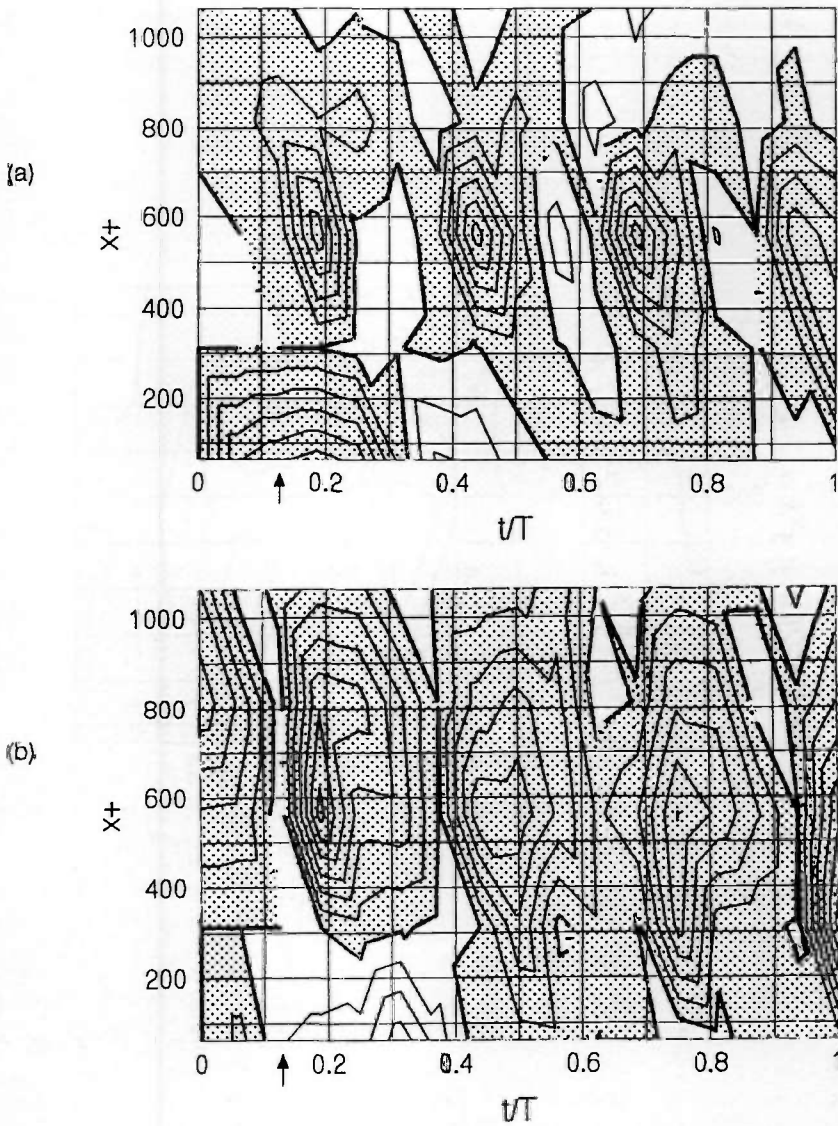
Figure 4.14: The contour plots of the dimensionless coherent velocity u_c/u_* due to a strong disturbance as a function of the phase, as measured in the plane at $z^+ = -60$ in positions on a streamwise line at (a) $y^+ = 5$, and (b) $y^+ = 25$. The fat line denotes $u_c/u_* = 0$, and the contour interval is $u_c/u_* = 0.25$. In the grey region $u_c/u_* < 0$.
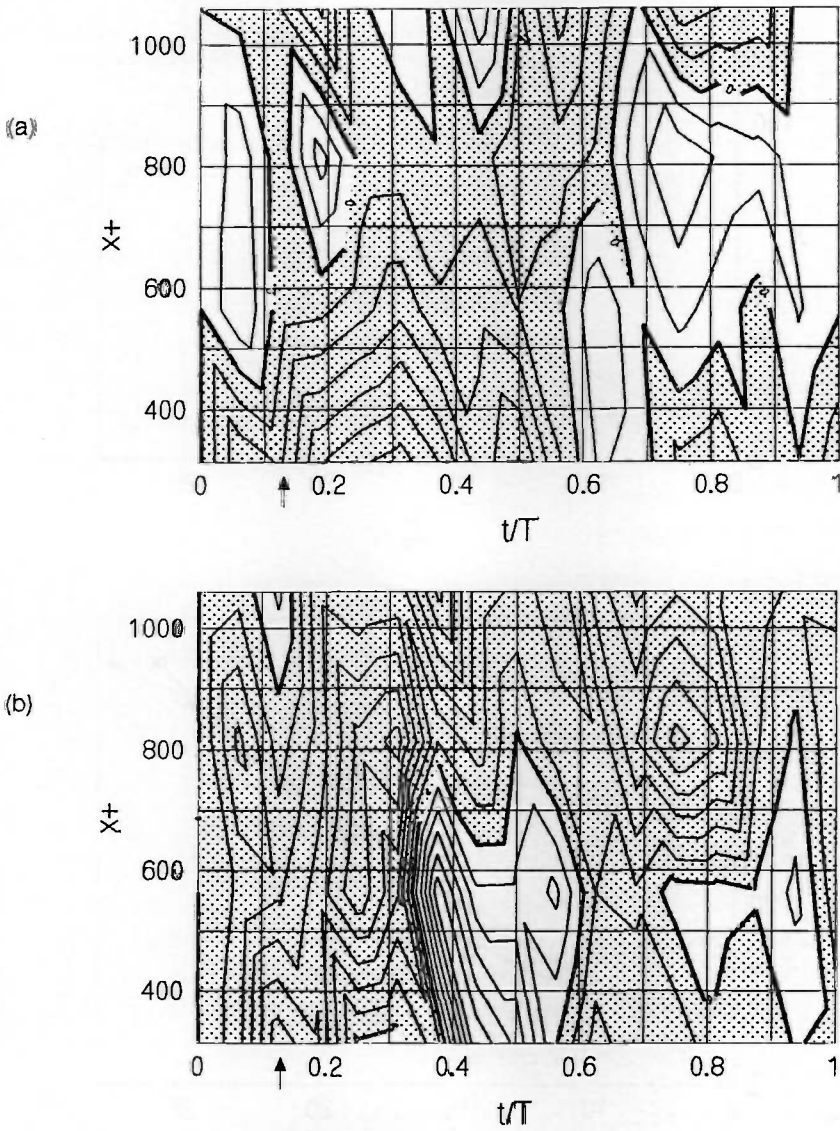
Figure 4.15: As figure 4.14, but for measuring positions in the plane at $z^+ = -120$ and with contour interval $u_c/u_* = 0.1$.
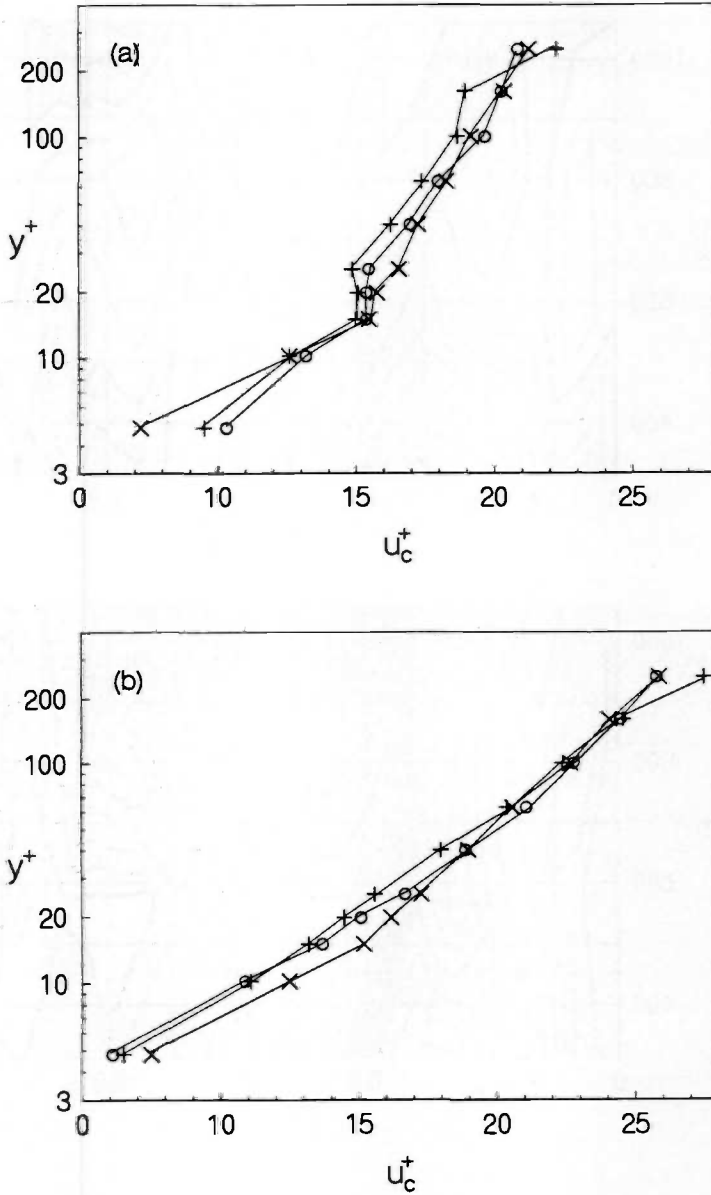
Figure 4.16: The profile of the dimensionless coherent velocity u_c/u_*. The measuring positions were at $x^+ = 300$ and (a) $z^+ = 0$, (b) $z^+ = -60$ and (c) $z^+ = -120$. The profiles were obtained at $t/T = 0.25$ (+), 0.44 (o), and 0.88 (×).
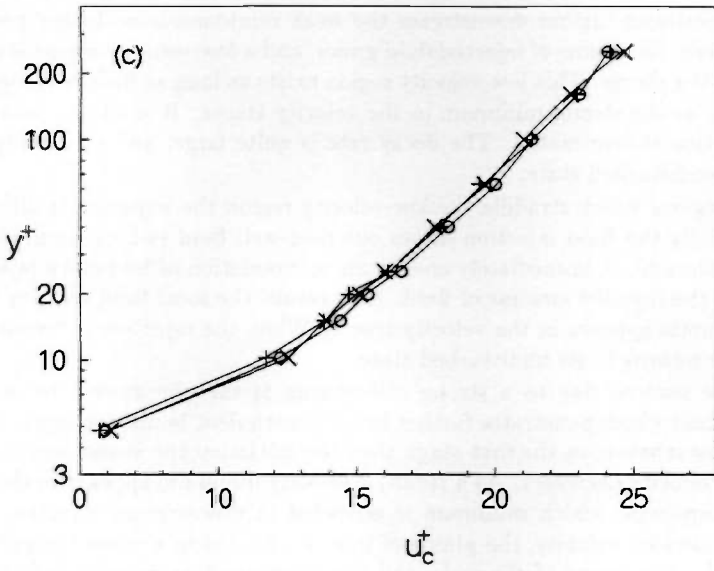
Figure 4.16: (c) For caption see previous page.

4.4 Evaluation of the response

4.4.1 The nature of the generated flow pattern

The flow pattern due to both the moderate and the strong disturbances can be described as the flow pattern caused by an amount of fluid which is injected into a turbulent boundary layer.

In the first instants after the initiation of a moderate disturbance, a small amount of fluid drives out the near-wall fluid, and, consequently, the streamwise component of the local fluid velocity decreases. The weak minimum in the coherent velocity component traces which are obtained near the slots is the result of this effect. Due to advection by the local mean flow, this amount of fluid, together with the weak velocity minimum, is transported in downstream direction. However, this effect is so small that in the measuring positions further downstream the weak minimum is no longer present. As phase proceeds, the plume of injected fluid grows, and a low-velocity region is created in the wake of the plume. This low-velocity region exists as long as fluid is being injected, and appears as the strong minimum in the velocity traces. It starts to decay as soon as the injection is terminated. The decay rate is quite large, and eventually the flow reaches its undisturbed state.

In the regions which straddle the low-velocity region the situation is different. Although initially the fluid injection drives out near-wall fluid (which results in a weak velocity minimum), it immediately creates an accumulation of boundary layer fluid at the sides of the injected amount of fluid. As a result, the local fluid velocity increases, and a maximum appears in the velocity traces. When the injection is terminated, the flow quickly returns to its undisturbed state.

The flow pattern due to a strong disturbance is the one caused by an injected amount of fluid which penetrates further into the turbulent boundary layer. As for the moderate disturbance, in the first stage after the initiation the streamwise component of the fluid velocity decreases. As a result, a velocity minimum appears in the coherent velocity component, which minimum is advected in downstream direction. Due to the larger injection velocity, the plume of injected fluid is in a more upright position. Consequently, the extent of the wake and the corresponding velocity deficit is larger, and a strong velocity minimum appears in the coherent velocity components which are obtained at some distance from the wall. The low pressure in the wake induces an inward motion of fluid, which creates a region with a higher fluid velocity. This is the cause of the maximum in the coherent velocity component near the wall and in the plane of symmetry. These low and high-velocity regions exist as long as fluid is being injected, and their magnitudes decrease with distance from the injection slot. When the injection is terminated, these regions start to decay, and eventually the flow reaches its undisturbed state.

In fact, when the disturbance is active, the flow pattern is very similar to the one due to the interaction of a jet and a crossflow. For example, the experiments of Andreopoulos and Rodi (1984) showed that a stationary jet in a crossflow creates an extensive wake, and that close to the wall a reverse flow occurs which causes a local increase in the fluid

velocity in the wake.

We therefore conclude that the response of a turbulent boundary layer to artificially generated disturbances in the form of injected amounts of fluid is very similar to the interaction of a crossflow and a jet when the disturbance is active. Furthermore, we conclude that the overall character of the response depends on the disturbance amplitude. If the disturbance amplitude is small, the disturbance is dissipated by the turbulent flow, and no response occurs. For larger values of the disturbance amplitude, the generated flow pattern is mainly caused by the disturbance itself when the disturbance is active, and returns to its undisturbed state when the disturbance is terminated. In particular, the feature of the response to moderate disturbances is the presence of a low-velocity region which travels at a convection velocity of about 70% of the local mean velocity, and decays exponentially with a time scale $\tau^+ \approx 11$.

4.4.2 Artificial organized fluid motion and beyond

One of the features of near-wall turbulent flow motion is the quasi-periodic production of turbulent kinetic energy (e.g. Kline e.a., 1967; Corino and Brodkey, 1969). This process is generally known as the 'bursting' process, and is characterized by the quasi-periodic occurrence of a large increase in the streamwise fluid velocity and a quasi-periodic outflow of near-wall fluid. According to at least one hypothesis, each 'burst' is caused by a local flow instability which is triggered by a 'burst' in a more upstream position (see e.g. Smith, 1984).

For this hypothesis to be valid, it is necessary that before the 'burst' occurs the local flow can be decomposed into a basic flow and a perturbation. If the basic flow is unstable, any disturbance will cause the perturbation to grow exponentially. Consequently, this hypothesis implies that there exist coherent flow regions which serve as the cradle of new 'bursts'. We will refer to these regions as unstable coherent eddies. Here we assume that in a natural turbulent boundary layer numerous unstable coherent eddies are present, and that the disturbances which trigger the 'bursts' are provided by the environment of the eddy.

In principal, it should be possible to overrule the natural disturbances by introducing artificial ones. If the hypothesized mechanism is appropriate, the artificial disturbances will perturb the unstable coherent eddies, and, as a result, a response will occur which is characterized by a large increase in the streamwise fluid velocity and/or a large outflow of near-wall fluid. If so, it might be possible to interpret this part of the response as an artificially generated 'burst', and we might conclude that 'bursts' are related to local flow instabilities.

Because of the function of a disturbance, it is obvious that it must mimic the hypothesized natural burst-driving mechanism in the form of the outflow of near-wall fluid. Consequently, to get the desired disturbance, fluid must be suddenly injected from a hole in the wall into the turbulent boundary layer. If an unstable coherent eddy is present in a position downstream of the jet, the jet will impress a pressure gradient upon it, with as a result the sudden deceleration and, consequently, the initiation of the perturbation of the eddy. Because of the character of the desired disturbances,

their time and length scales must be of the order of those of the hypothesized natural burst-driving mechanism, which means that they must be of the order of those of the quasi-periodic events in a natural turbulent boundary layer. In particular, it follows that the time interval between two disturbances must be of the order of the time interval between two 'bursts', the spanwise distance between two disturbances must be of the order of the spanwise distance between two low-speed streaks, and the width of the disturbance must be of the order of the width of a low-speed streak.

The response of the flow to a disturbance can be studied via measurements which are phase locked to the initiation of the disturbance. Since each response will be smeared out differently due to the background turbulence, the responses must be phase averaged in order to eliminate the influence of the background turbulence. In fact, when the disturbances are periodical in time, the periodic phase-average can be used to obtain the coherent part of the response (Hussain, 1983).

A comparison of the experimental set-up just described and the one described in section 4.1 shows that the two set-ups are equivalent. It is therefore instructive to evaluate the results of section 4.3 in terms of the mechanism proposed in the first part of this section.

Unfortunately, our measurements have shown (see section 4.3) that, when the turbulent boundary layer is disturbed by amounts of injected fluid, there occurs no large increase in the streamwise component of the fluid velocity which cannot be attributed to the disturbance itself. This means either that there is no unstable coherent eddy in the neighbourhood of the disturbance, or, more likely, that the proposed mechanism is not appropriate. Moreover, this means that one should be careful in interpreting the response to disturbances in terms of specific flow events which are not directly related to the disturbance itself.

As to artificially generated flow events, Gad-el-Hak and Hussain (1986) claimed that abrupt suction of near-wall-fluid and the sudden pitching of a miniature delta wing generates a hairpin vortex and a low-speed streak, and that subsequently the streak lifts up from the wall and breaks up into a 'burst'. It therefore seems that these mechanisms are the only ones which can generate artificial 'bursts'. But, then we have to be sure that the prevailing explanation of Gad-el-Hak and Hussain's experimental results is appropriate and unique, and, in particular, that their artificial flow events are not directly related to the excitation. In the following we present an alternative explanation of their experimental results.

In the experiments of Gad-el-Hak and Hussain (1986), the initial effect of the abrupt suction through two holes is the withdrawal of an amount of fluid from the near-wall region. Due to continuity, this amount is replaced by fluid from regions higher in the turbulent boundary layer, and, as a result, a velocity surplus is created above each suction hole. As a consequence, the effect of the suction is the creation of a spanwise low-velocity region with its velocity minimum in between the holes and its velocity maxima above the two holes. This low-velocity region is advected in downstream direction, and appears as a characteristic streak when dye or horizontal time-line flow-visualization is used. Moreover, it is detected in the velocity traces obtained with a spanwise array of hot-film sensors when a pattern recognition technique is used which is designed

to identify low-velocity regions. The amount of fluid set in wallward motion by the suction is also transported in downstream direction, and appears as a trace of spanwise vorticity when vertical time-line flow-visualization is used. When a pattern recognition technique is used which identifies large changes in the fluid velocity (i.e. the VITA detection-technique), the gradient in the streamwise velocity component created by the downflow is detected in the velocity traces obtained with a hot-film sensor.

Similarly, the effect of the pitching of the delta wing is the creation of a low-velocity region, and consequently the downflow of fluid from regions higher in the turbulent boundary layer.

This argument shows that the concept of a hairpin vortex is not needed to explain the flow behaviour observed by Gad-el-Hak and Hussain (1986), and, in particular, that the detected 'burst' might be caused by the advection of the created streamwise velocity gradient, and not by the break up of the created low-velocity region. We therefore conclude that the interpretation of the experimental results by Gad-el-Hak and Hussain (1986) might be erroneous, and that the proof-of-concept of artificial 'burst'-generation is not established.

Conclusion

In conclusion, we recapitulate the major findings of our experiments and analyses, and present the points which are open for further research.

The hydrogen-bubble time-line technique is a useful method to measure mean fluid-velocities in regions not too close to (i.e. more than, say, 15 wall units above) the wall of a turbulent boundary layer. However, this technique fails when it is used to measure fluid velocities close to the wall, and velocity variances in the entire boundary layer. Moreover, the reliability of this technique is poor because of the intrinsic errors; especially those due to the presence of the bubble-generating wire and the velocity gradient in the flow. This means that one should not be too confident in the reliability of the hydrogen-bubble technique in the region close to the wall.

When the structure of near-wall turbulence is expressed in length scales that can be identified in spanwise profiles of the streamwise fluid velocity, it appears that near-wall turbulence is spatially quasi-periodical with the mean values representing a range of values. The numerical values of these length scales are different from the generally accepted ones. For example, the mean distance between low-velocity regions is 70 rather than 100 wall units. Most probably, this effect is due to the lower spatial resolution of the measurement technique, as compared to the ones used by other investigators. Moreover, on average the low-velocity regions are as wide as the high-velocity regions.

The most prominent feature of a top view of the near-wall turbulence structure are the elongated regions with a lower-than-average velocity: the low-speed streaks. At least for short time lapses (i.e. less than 15 wall time-units), the flow in a low-velocity region can be treated as an almost parallel and time-independent basic flow. Generally, a low-velocity region has two highly asymmetric shear layers and a Reynolds number in the range 60 ... 530. This means that a stability analysis of a low-velocity region must treat the two shear layers separately, and consider the effect of viscosity. However, the number of extremes in a spanwise velocity profile, and therefore the distance between two low-velocity regions, seems to depend on the 'age' of the time line from which the velocity profile is determined. This effect is a feature of the time lines and not of the investigative technique, and might indicate a feature of the flow. Associated with the increase in the number of extremes is the splitting and the merging of a low-velocity region.

Comparing the measured values of the dimensionless gradient length and velocity scales with the values of those scales according to a sinusoidal velocity profile leads to the conclusion that a sinusoidal velocity profile may serve as a model for the shear layer of a low-velocity region. A viscous stability analysis of the sinusoidal basic flow shows that always one unstable mode exists. The behaviour of the growth rate of this mode as a function of the basic-flow parameters is in agreement with the one found experimentally,

and suggests that in practise this mode is a temporal one.

The response of a turbulent boundary layer to artificially generated periodic disturbances in the form of injected amounts of fluid is very similar to the interaction of a crossflow and a periodic jet. The overall character of the response depends on the disturbance amplitude. When the disturbance amplitude is small, the disturbance is dissipated by the turbulent flow, and no response occurs. For larger values of the disturbance amplitude, the generated flow pattern is mainly caused by the disturbance itself when the disturbance is active, and returns to its undisturbed state when the disturbance is terminated. The feature of the response to the intermediate amplitude disturbances is an artificial low-velocity region which travels at a convection velocity of about 70% of the local mean velocity, and decays exponentially with a time scale of 11 wall units. In particular, in the response there occurs no large increase in the streamwise fluid velocity which cannot be attributed to the disturbance itself; which increase one might expect if the disturbance initiates an artificial 'burst'. It therefore follows that care should be taken in interpreting the response to a disturbance in terms of a specific flow event which is not related to the disturbance.

These findings on the measurement, prediction and manipulation of the turbulent boundary layer flow over a flat plate summarize our contribution to a better understanding of near-wall turbulence.

However, we emphasize that the uncertainty in the hydrogen-bubble time-line data is large. Consequently, one should be careful in generalizing the results obtained from the time lines, especially those regarding the basic-flow parameters and the life times of the low-velocity regions. In fact, the basic-flow parameters and the life times should be measured with a technique which is truly two-dimensional, and has a small intrinsic uncertainty.

To date such a technique is available: particle image velocimetry (PIV). With PIV it should be possible to determine to a high accuracy the instantaneous streamwise and spanwise velocity components in a plane parallel to the wall and at several consecutive time instants. Subsequently, it should be possible to identify the low-velocity regions, and to decompose the flow in these regions into an almost parallel and time-independent basic flow and a two-dimensional velocity perturbation. When the parameters of the basic flow are determined and a model of its stability is available, it should be possible to compute the streamwise wavelength and the growth rate of the velocity perturbation, and to predict the instantaneous flow at a later instant. Then the predicted flow field can be compared with the measured one.

Therefore, the points open for future research are to

- Use particle image velocimetry (PIV) to measure at several consecutive time instants the instantaneous streamwise and spanwise velocity components in a plane parallel to the wall,

- Use the results of PIV measurements to verify the existence of an almost parallel and time-independent basic flow in the near-wall low-velocity regions,

- Develop a model which expresses the streamwise wavelength and the growth rate of the two-dimensional velocity perturbation in the low-velocity region in terms of the basic-flow parameters,

- Test the performance of the model by comparing the predicted and the measured flow fields.

With this strategy it might be possible to prove that near-wall turbulence contains regions which are highly deterministical, and solve some of its mysteries.

Symbols

Roman and calligraphic:

A	-	empirical constant in the logarithmic law
B	-	empirical constant in the logarithmic law
c	-	complex phase-velocity of a velocity perturbation
c_r	m/s	phase velocity of a velocity perturbation
c_i	m/s	imaginary part of the complex phase-velocity of a velocity perturbation
C	-	empirical constant in the hyperbolic-tangent law
d	m	diameter of the bubble-generating wire
d	m	diameter of a hydrogen bubble
d	m	displacement of a fluid marker
d'	m	virtual diameter of the bubble-generating wire
g	m/s^2	acceleration of gravity
g_t	1/s	temporal growth-rate of a velocity perturbation
g_x	1/m	spatial growth-rate of a velocity perturbation
H	-	threshold level of the Quadrant Splitting detection-technique
H	m	position above the wall of the vortex sheet that models a turbulent boundary layer
k	-	threshold level of the VITA detection-technique
k_z	1/m	spanwise wavenumber of a low-velocity region
l_*	m	viscous length scale
L	-	threshold level of the u-level detection-technique
L	-	length or life time of a low-velocity region
$\mathcal{L}$	m	length scale of a shear layer
R	-	Reynolds number of a low-velocity region
R_d	-	Reynolds number of the bubble-generating wire
R_x	-	Reynolds number of a boundary layer based on the free-stream velocity and the distance to the leading edge
R_θ	-	Reynolds number of a boundary layer based on the free-stream velocity and the momentum thickness
R_*	-	Reynolds number based on the friction velocity and the boundary layer thickness
t	s	time
t	s	phase
t_*	s	viscous time scale

T	s	time interval between two artificial disturbances
T	s	averaging time of the VITA technique
T_b	s	time interval between two near-wall events; 'burst' period
T_i	s	duration of an artificial disturbance
u	m/s	velocity component in streamwise direction
$\underline{u}$	m/s	velocity vector
u_c	m/s	convection velocity
u_c^{mag}	m/s	magnitude of the coherent velocity component at a specific phase instant
u_{conv}	m/s	convection velocity
u_{def}	m/s	defect in the velocity of a time line due to the wake of the wire
u_{high}	m/s	streamwise velocity in a high-velocity region
u_{low}	m/s	streamwise velocity in a low-velocity region
u_{raw}	m/s	velocity of a time line determined from its displacement in a time interval
u_{rms}	m/s	magnitude of the coherent velocity component at a specific spanwise position
u_{sur}	m/s	surplus in the velocity of a time line due to the velocity gradient in a boundary layer
u_0	m/s	undisturbed fluid velocity
u_*	m/s	friction velocity; viscous velocity scale
U_b	m/s	local mean velocity in a low-velocity region
U_0	m/s	velocity difference in a low-velocity region
U_∞	m/s	free-stream velocity
$\mathcal{U}$	m/s	velocity difference in a shear layer
v	m	velocity component normal to the wall
v	m/s	vertical velocity of a hydrogen bubble
v_r	m/s	terminal rise velocity of a hydrogen bubble
V_i	m/s	injection velocity
w	m	velocity component in spanwise direction
x	m	streamwise coordinate
x_1	m	coordinate in streamwise direction as it follows from applying Taylor's hypothesis to phase
y	m	coordinate normal to the wall
z	m	spanwise coordinate

Greek:

α	-	complex streamwise wavenumber of a velocity perturbation
α_r	1/m	streamwise wavenumber of a velocity perturbation
α_i	1/m	spatial decay rate of a velocity perturbation
δ	m	boundary layer thickness
∂U	1/s	velocity gradient in a specific point
$\partial^2 U$	1/ms	second velocity derivative in a specific point
Δ	m	length scale of a velocity gradient
ϵ_m	m^2/s	eddy diffusivity
ε	m^2/s^3	viscous dissipation
η	m	Kolmogorov length scale
θ	m	momentum thickness
κ	-	von Karman constant
λ_x	m	wavelength in streamwise direction
λ_z	m	wavelength in spanwise direction; distance between two low-velocity regions; distance between two low-speed streaks
λ_L	m	width of a low-velocity region
λ_H	m	width of a high-velocity region
ν	m^2/s	kinematic viscosity of the fluid
ξ_2	-	similarity parameter
τ	s	life time of a perturbation
τ	s	temporal decay rate of an artificial disturbance
Υ	m/s	velocity scale of a velocity gradient
ϕ	-	amplitude of the streamfunction which describes a two-dimensional velocity perturbation
ψ	-	streamfunction describing a two-dimensional velocity perturbation
$\underline{\omega}$	1/s	vorticity vector

Decompositions:

f	instantaneous value
F	time-independent value
f'	fluctuation with respect to the time-averaged value
$\overline{f}$	time-averaged value; median value (section 2.5 only)
$<f>$	phase-averaged value; ensemble-averaged value
f_c	coherent value
f_m	time-independent value
f_r	random value

Dimensions:

f	dimensional quantity
f	quantity non-dimensionized with the scales of a low-velocity region (section 4.3 only)
$\tilde{f}$	dimensional quantity (section 4.3 only)
f^+	quantity non-dimensionized with the viscous scales

Nomenclature

Artificially created structure/event: A structure/event generated by manipulation of the boundary layer.

Average: The statistical mean of a quantity over a stated number of realizations; $\overline{f} = \frac{1}{N} \sum_{i=1}^{N} f(t_i)$.

Basic flow: A region of almost parallel and time-independent flow which might be unstable to small disturbances. In case the basic flow is a shear layer the basic-flow parameters are: the local mean velocity U_b, the magnitude (i.e. the velocity difference) U_0 and the wavenumber $k_z = 2\pi/\lambda_z$ (where λ_z is the wavelength).

Basic-flow parameters: See basic flow.

Biot-Savart interaction: See induction.

Black spot: An area devoid of fluid markers; probably related to the ejection.

Boundary layer flow: The flow in the region over a wall where the velocity increases from 0 (at the wall) to U_∞ (which corresponds to frictionless flow).

Boundary layer thickness: The measure δ of the distance between the wall and the frictionless flow as defined by $U(\delta)/U_\infty = 0.99$.

Buffer layer: See statistical description.

Bulge: A large-scale eddy at the outside edge of a turbulent boundary layer.

Burst: A quasi-periodic sequence of events in a confined region. It involves a higher production of turbulent energy and/or Reynolds stress than average, and/or a large increase in the streamwise velocity and the outflow of low-momentum fluid. Its measures are the *bursting period* T_b and the *bursting frequency* $f_b = 1/T_b$.

Channel flow: The flow over a wall with a free surface.

Coherent: The state of having a significant correlation over space and/or time.

Coherent structure: A region of flow with a significant correlation over its spatial and/or temporal extent; also referred to as *structure*.

Conditional average: The statistical mean of a quantity over the realizations of a conditional sample.

Conditional sample: One or more single realizations that meet a specified condition regarding the properties or the character of the realizations.

Connectivity: The relation between the velocity extremes or inflection points of the consecutive profiles of a velocity profile pattern.

Coordinate axes: x (in the direction of the free-stream flow), y (normal to the wall), and z (in spanwise direction). Names as axes: streamwise (longitudinal, axial), normal and spanwise (transversal, lateral), respectively. Names as viewing direction: end, plan (top) and side view, respectively.

Correlation: A measure for the relation between the values of a quantity at the same instant but at different spatial positions, or at the same spatial position but in different instants.

Counter-rotating vortex pair: Two nearly parallel vortices with opposite signs of rotation.

Deterministic: Occurring such that a future value can be predicted via an explicit mathematical expression.

Disturbance: The actual manipulation of the boundary layer in order to create an artificial structure/event.

Eddy: A region of flow with some coherence, often in the form of rotational motion.

Ejection: A rapid fluid motion away from the wall.

Ensemble: A collection of realizations chosen for a pre-determined common property or characteristic.

Ensemble average: The statistical mean of a quantity over the realizations of an ensemble.

Event: See flow event.

Fjørtoft's theorem: A necessary condition for instability of an inviscid flow is that the basic flow $U(z)$ should have an inflection point z_{IP}, and that the basic flow should satisfy $U''(z)(U(z) - U(z_{IP})) \leq 0$, with $U''(z) = \partial^2 U(z)/\partial z^2$.

Flow event: The flow behaviour identified by a specific conditional sampling scheme.

Fluctuating value: The difference between the instantaneous value of a quantity and its time average.

Fluid motion: The flow behaviour revealed by a specific flow-visualization method.

Free-stream velocity: The fluid velocity U_∞ that corresponds to frictionless flow.

Friction velocity: The velocity scale u_* which is defined by the shear stress at the wall as $\rho u_*^2 = \tau_w$, with τ_w the wall shear stress and ρ the density of the fluid.

Görtler instability: See Taylor-Görtler instability.

Hairpin vortex: An U-shaped vortex with pinched-in legs.

High-velocity region: A region in a spanwise velocity profile with streamwise velocity higher than the mean. The width of a high-velocity region is λ_H.

Horseshoe vortex: An U-shaped vortex with its legs rather wide apart; also known as Λ *vortex* and *vortex loop*.

Hydrogen-bubble technique: The method to visualize water flow via the generation of hydrogen bubbles at a thin wire. If hydrogen-bubble time-lines are created, profiles of the instantaneous fluid velocity can be estimated by dividing the displacement of parts of the time line in a specific time interval through the time interval.

Induction: The motion of a vortex caused by its interaction with the surrounding flow field (*self induction*), or by the presence of one or more other vortices (*mutual induction*).

Inflection point: The point z_{IP} in a velocity profile $U(z)$ where the second velocity derivative vanishes: $\partial^2 U(z_{IP})/\partial z^2 = 0$.

Inner flow-variables: See viscous scales.

Inner scales: See viscous scales.

Instability: An oscillation that, once initiated, grows continuously at a rate and frequency determined by the parameters of the system.

Instantaneous value: The value of a quantity at a specific instant.

Instantaneous velocity vector: $\underline{u} = (u, v, w) = (u_1, u_2, u_3)$ where u, v and w are the instantaneous components of the fluid velocity in streamwise, normal and spanwise direction, respectively.

Instantaneous vorticity vector: $\underline{\omega} = (\omega_1, \omega_2, \omega_3)$ with components $\omega_i = \frac{\partial u_k}{\partial x_j} - \frac{\partial u_j}{\partial x_k}$.

Internal shear layer: A region of fluid with a shear rate which is higher than average.

Kelvin-Helmholtz instability: The instability arising in two-dimensional steady flows with an inflection point in the mean velocity profile. It leads to vortices with their axes transverse to the mean motion.

Lin's theorem: For perturbations with a wavelength beyond a certain lower limit, there is always a finite range of Reynolds numbers for which the motion is unstable.

Logarithmic layer: See statistical description.

Low-speed streak: An elongated streamwise region of fluid with streamwise velocity lower than the one of the mean flow. Its measures are the spanwise streak spacing λ_z and the streak width λ_L.

Low-velocity region: A region in a spanwise velocity profile with streamwise velocity lower than the mean. The distance between two low-velocity regions is λ_z and the width of a low-velocity region is λ_L.

Momentum thickness: The measure θ of the momentum loss in the boundary layer with respect to the approaching flow as defined by $\theta = \int (U(y)/U_\infty)(1 - U(y)/U_\infty)dy$.

Motion: See fluid motion.

Natural boundary layer: The undisturbed boundary layer flow of a newtonian fluid over a flat plate.

Outer flow-variables: See outer scales.

Outer region: See statistical description.

Outer scales: The free-stream velocity U_∞, the boundary layer thickness δ and the outer time scale δ/U_∞. Also known as outer flow-variables.

Perturbation: The divergence from the undisturbed state.

Phase: The time lapse since the start of an event.

Phase average: The ensemble average of a quantity at a specific phase; $< f(t) > = \sum_{i=1}^{N} f(t + t_i)$ with t the phase and N the number of realizations.

Phase jitter: The phase separation between the realizations of an ensemble.

Pocket: An area devoid of fluid markers; probably related to the ejection.

Quadrant detection-technique: The quadrant-splitting analysis-technique maps the instantaneous value of the Reynolds stress into a quadrant of the $u'v'$ plane. This defines four types of events: 1) Q1 with $u' > 0, v' > 0$, 2) Q2 with $u' < 0, v' > 0$ (generally called *ejection*), 3) Q3 with $u' < 0, v' < 0$, and Q4 with $u' > 0, v' < 0$ (generally called *sweep*). A Qi event is detected when $(u'v')_i > H\overline{u'v'}$, with $\overline{u'v'}$ the mean Reynolds stress and H the threshold parameter (generally called hole size).

Quasi-periodic: Occurring at intervals which vary from realization to realization, but with a repeatable mean value of a characteristic quantity.

Random: Occurring such that a description must be probabilistical rather than deterministical; a future value cannot be predicted.

Rayleigh's theorem: A necessary condition for instability of an inviscid flow is that the basic flow should have an inflection point.

Realization: A single observation of a quantity.

Response: The flow field due to a disturbance.

Reynolds decomposition: Decomposition of the instantaneous value f of a quantity into two components according to $f = F + f'$, with $F = \overline{f}$ the time averaged component and f' the fluctuating component. The root-mean-square or rms value of the quantity is the time-averaged square of its fluctuating component: $\overline{f'^2}$.

Reynolds (shear) stress: $u'_i u'_j$ with $i \neq j$.

Rms value: See Reynolds decomposition.

Sample: A set of one or more realizations.

Second-quadrant event: See quadrant detection-technique.

Squire's theorem: To each unstable three-dimensional perturbation there corresponds a more unstable two-dimensional perturbation.

Statistical description: The description of the turbulent boundary layer with the emphasis on time-averaged quantities. In terms of the statistical description two distinct regions exist: the *wall layer* and the *outer region*. The wall layer consists of the *viscous sublayer* ($0 < y^+ < 7...10$) with the linear velocity profile $U^+ = y^+$, and the *buffer layer* ($7...10 < y^+ < 30...40$) with the hyperbolic-tangent velocity profile $U^+ = \tanh(Cy^+)/C$. The outer region consists of the *logarithmic layer* ($30...40 < y^+ < 100...1000$) with the logarithmic velocity profile $U^+ = A \ln y^+ + B$ (with $A = 1/\kappa$ where κ is the von Karman constant), and the *wake layer* ($100...1000 < y^+ < \delta^+$).

Stream line: The line parallel to the velocity vector at each position.

Streamwise vortex: A vortex with its axis in streamwise direction.

Structure: See coherent structure.

Structural description: The description of the turbulent boundary layer with the emphasis on quasi-periodic fluid motions and flow events. The scales of these motions and events are larger than the smallest, but smaller than the largest scales of the turbulence.

Sweep: A relatively slow wallward fluid motion.

Taylor-Görtler instability: A centrifugal instability due to flow curvature. It leads to a stationary array of large-scale counter-rotating longitudinal vortices with their axes in streamwise direction.

Taylor's hypothesis: If the convection velocity U_c of a flow structure is large compared to the magnitude of its velocity trace $u(t)$, the spatial flow structure may be approximated by $u(tU_c)$.

Time line: The curve joining all particles that at an earlier instant passed a line in space.

Tollmien-Schlichting instability: An instability in the form of two-dimensional waves in a laminar boundary layer. Their driving mechanism is due to viscous effects.

Transversal vortex: A vortex with its axis in transversal direction.

Triple decomposition: Decomposition of the instantaneous value f of a quantity into three components according to $f = f_m + f_c + f_r$, with $f_m = \overline{f}$ the time averaged component, $f_c = <f> - \overline{f}$ the coherent component, and $f_r = f - <f>$ the random component; $<f>$ is the phase average of f.

Turbulent (kinetic) energy: $u'_i u'_j$ with $i = j$.

Typical eddy: A ring-like eddy structure.

U-level detection-technique: In this technique an event is detected when the low-pass filtered streamwise velocity is less than a threshold level: $u < -Lu'$, with L the threshold parameter and u' the deviation from the mean.

U-shaped vortex: A vortex with its axis in an U shape. It must have two distinct legs but does not need a plane of symmetry.

Velocity extreme: The point z_E in a velocity profile $U(z)$ where the velocity gradient vanishes: $\partial U(z_E)/\partial z = 0$. The two types of velocity extreme are the velocity minima $(\partial^2 U(z_E)/\partial z^2 > 0)$ and the velocity maxima $(\partial^2 U(z_E)/\partial z^2 < 0)$.

Velocity-profile pattern: The set of velocity profiles which are obtained from the motion of a specific time line. The profiles contain an estimate of the fluid velocity at consecutive time instants.

Viscous scales: The scales that are defined by the friction velocity u_* and the kinematic viscosity ν of the fluid: the viscous velocity u_*, the viscous length $l_* = \nu/u_*$ and the viscous time $t_* = \nu/u_*^2$. Also known as inner scales, inner flow-variables, wall units and wall scales. Parameters non-dimensionized with viscous scales are indicated with a 'sup +', e.g. $u^+ = u/u_*$.

Viscous sublayer: See statistical description.

VITA detection-technique: The Variable-Interval Time-Averaging technique detects an event when $var > ku_{rms}$, with var the variance of the velocity signal in the short time-interval T and u_{rms} the variance of the total velocity signal. Its parameters are the averaging time T and the threshold level determined by k. In the improved VITA detection-technique accelerations and decelerations in the velocity signal are separated.

Vortex: A region of flow where the projections of the streamlines onto some plane form closed paths.

Vortex line: The line parallel to the vorticity vector at each position.

Vortex sheet: A thin surface formed by parallel vortex lines.

Vortex stretching: The elongation of a vortex along its axis, with as associated effect an increase in vorticity.

Wake layer: See statistical description.

Wall layer: See statistical description.

Wall scales: See viscous scales.

Bibliography

Abernathy F.H., Bertschy J.R. and Chin R.W., 1977, *Turbulence spectra using laser-doppler anemometry and selective seeding*, In: Proc. 5th Symp. on Turbulence (ed. G.K. Patterson and J.L. Zakin), University of Missouri, Rolla

Abramowitz M. and Stegun I.A., 1970, *Handbook of mathematical functions*, 9th printing, Dover

Acarlar M.S. and Smith C.R., 1984, *An experimental study of hairpin-type vortices as a potential flow structure of turbulent boundary layers*, Report FM-5, Lehigh University

Acarlar M.S. and Smith C.R., 1987a, *A study of hairpin vortices in a laminar boundary layer. Part 1. Hairpin vortices generated by a hemisphere protuberance*, J. Fluid Mech. **175**, pp. 1-41

Acarlar M.S. and Smith C.R., 1987b, *A study of hairpin vortices in a laminar boundary layer. Part 2. Hairpin generated by fluid injection*, J. Fluid Mech. **175**, pp. 43-83

Alfredsson P.H. and Johansson A.V., 1984, *On the detection of turbulence-generating events*, J. Fluid Mech. **139**, pp. 325-345

Andreopoulos J. and Rodi W., 1984, *Experimental investigations of jets in a crossflow*, J. Fluid Mech. **138**, pp. 93-127

Antonia R.A. and Bisset D.K., 1990, *Spanwise structure in the near-wall region of a turbulent boundary layer*, J. Fluid Mech. **210**, pp. 437-458

Batchelor G.K., 1967, *An introduction to fluid dynamics*, Cambridge University Press

Beljaars A.C.M., Krishna Prasad K. and de Vries D.A., 1981, *A structural model for turbulent exchange in boundary layers*, J. Fluid Mech. **112**, pp. 33-70

Blackwelder R.F., 1978, *The bursting process in turbulent boundary layers* In: Coherent structure of turbulent boundary layers, Proc. AFOSR/Lehigh workshop, pp. 211-227, Lehigh University

Blackwelder R.F., 1983, *Analogies between transitional and turbulent boundary layers*, Phys. Fluids **26**, pp. 2807-2815

Blackwelder R.F., 1988, *Coherent structures associated with turbulent transport*, In: Transport phenomena in turbulent flows (ed. M. Hirata and N. Kasagi), pp. 69-88, Hemisphere

Blackwelder R.F. and Eckelmann H., 1979, *Streamwise vortices associated with the bursting phenomenon*, J. Fluid Mech. **94**, pp. 577-594

Blackwelder R.F. and Haritonidis J.H., 1983, *Scaling of the bursting frequency in turbulent boundary layers*, J. Fluid Mech. **132**, pp. 87-103

Blackwelder R.F. and Kaplan R.E., 1972, *The intermittent structure of the wall region of a turbulent boundary layer*, Report USCAE 1-22, University of Southern California

Blackwelder R.F. and Kaplan R.E., 1976, *On the wall structure of the turbulent boundary layer*, J. Fluid Mech. **76**, pp. 89-112

Blackwelder R.F. and Swearingen J.D., 1989, *The role of inflectional velocity profiles in wall bounded flows*, In: Near-wall turbulence (ed. S.J. Kline and N.H. Afghan), pp. 268-288, Hemisphere

Blokland R. and Krishna Prasad K., 1984, *Some visualization studies on turbulent boundary layers using multi-wire hydrogen bubble generation*, In: Proc. 8th Symp. on Turbulence (ed. G.K. Patterson and J.L. Zakin), University of Missouri, Rolla

Bogard D.G. and Tiederman W.G., 1986, *Burst detection with single point velocity measurements*, J. Fluid Mech. **162**, pp. 389-413

Bogard D.G. and Tiederman W.G., 1987, *Characteristics of ejections in turbulent channel flow*, J. Fluid Mech. **179**, pp. 1-19

Brodkey R.S., Wallace J.M. and Eckelmann H., 1974, *Some properties of truncated turbulence signals in bounded shear flows*, J. Fluid Mech. **63**, pp. 209-224

Burgers J.M., 1924, *The motion of a fluid in the boundary layer along a plane smooth surface*, In: Proc. 1st Int. Congr. for Applied Mechanics, (ed. C.B. Biezeno and J.M. Burgers), pp. 113-128, Waltman

Cantwell B.J., 1981, *Organized motion in turbulent flow*, Ann. Rev. Fluid Mech. **13**, pp. 457-515

Castleman K.R., 1979, *Digital image processing*, Prentice-Hall

Cebeci T. and Bradshaw P., 1977, *Momentum transfer in boundary layers*, McGraw-Hill

Corino E.R. and Brodkey R.S., 1969, *A visual investigation of the wall region in turbulent flow*, J. Fluid Mech. **37**, pp. 1-30

Corssin S., 1957, In: Symposium on naval hydrodynamics, Publ. 515, NAS-NRC, p. 373

Doligalski T.L. and Walker J.D.A., 1984, *The boundary layer induced by a convected two-dimensional vortex*, J. Fluid Mech. **139**, pp. 1-28

Drazin P. and Reid W., 1981, *Hydrodynamic stability*, Cambridge University Press

Einstein H.A. and Li H., 1956, *The viscous sublayer along a smooth boundary*, ASCE Proc. **82**

Falco R.E., 1977, *Coherent motions in the outer region of turbulent boundary layers*, Phys. Fluids **20**, pp. S124-S132

Falco R.E., 1978, *The role of outer flow coherent motions in the production of turbulence near a wall*, In: Coherent structure of turbulent boundary layers, Proc. AFOSR/Lehigh workshop, pp. 448-461, Lehigh University

Gad-el-Hak M. and Blackwelder R.F., 1987, *Simulation of large-eddy structures in a turbulent boundary layer*, AIAA Journal **25**, pp. 1207-1215

Gad-el-Hak M. and Hussain A.K.M.F., 1986, *Coherent structures in a turbulent boundary layer. Part 1: Generation of 'artificial' bursts*, Phys. Fluids **29**, pp. 2124-2139

Grass A.J., 1971, *Structural features of turbulent flow over smooth and rough boundaries*, J. Fluid Mech. **50**, pp. 233-255

Gupta A.K., Laufer J. and Kaplan R.E., 1971, *Spatial structure in the viscous sublayer*, J. Fluid Mech. **50**, pp. 493-512

Hanratty T.J., 1956, *Turbulent exchange of mass and momentum with a boundary*, J. Am. Inst. Chem. Eng. **2**, p. 359

Haritonides J.H., 1989, *A model for near-wall turbulence*, Phys. Fluids A **1**, pp. 302-306

Hatziavramides D.T. and Hanratty T.J., 1979, *The representation of the viscous wall region by a regular eddy pattern*, J. Fluid. Mech. **95**, pp. 655-679

Head M.R. and Bandyopadyay P., 1981, *New aspects of turbulent boundary layer structure*, J. Fluid Mech. **107**, pp. 297-338

Hinze J.O., 1975, *Turbulence, 2nd edition*, McGraw-Hill

Hussain A.K.M.F., 1983, *Coherent structures - reality and myth*, Phys. Fluids **26**, pp. 2816-2850

Jang P.S., Benney D.J. and Gran R.L., 1986, *On the origin of streamwise vortices in a turbulent boundary layer*, J. Fluid Mech. **169**, pp. 109-123

Johansson A.V. and Alfredsson P.H., 1982, *On the structure of turbulent channel flow*, J. Fluid Mech. **122**, pp. 295-314

Johansson A.V. and Alfredsson P.H., 1983, *Effects of imperfect spatial resolution on measurements of wall-bounded turbulent shear flows*, J. Fluid Mech. **137**, pp. 409-421

Johansson A.V., Alfredsson P.H. and Eckelmann H., 1987, *On the evolution of shear-layer structures in near-wall turbulence*, In: Advances in turbulence (ed. G. Comte-Bellot and J. Mathieu), pp. 383-390, Springer

Kasagi N., Hirata M. and Nishino K., 1986, *Streamwise pseudo-vortical structures and associated vorticity in the near-wall region of a wall-bounded turbulent shear flow*, Expts. Fluids **4**, pp. 309-318

Kim H.T., Kline S.J. and Reynolds W.C., 1971, *The production of turbulence near a smooth wall in a turbulent boundary layer*, J. Fluid Mech. **50**, pp. 133-160

Kline S.J., Reynolds W.C., Schraub F.A. and Runstadler P.W., 1967, *The structure of turbulent boundary layers*, J. Fluid Mech. **30**, pp. 741-773

Kline S.J. and Robinson S.K., 1989, *Quasi-coherent structures in the turbulent boundary layer: part I. Status report on a community-wide summary of the data*, In: Near-wall turbulence (ed. S.J. Kline and N.H. Afghan), pp. 200-217, Hemisphere

Kline S.J. and Runstadler P.W., 1959, *Some preliminary results of visual studies on the flow model of the wall layers of the turbulent boundary layer*, Trans. ASME: J. Appl. Mech. **26**, pp. 166-170

Kreplin H.-P. and Eckelmann H., 1979, *Propagation of perturbations in the viscous sublayer and adjacent wall region,* J. Fluid Mech. **95**, pp. 305-322

Landahl M.T., 1977, *Dynamics of boundary layer turbulence and the mechanism of drag reduction,* Phys. Fluids **20**, pp. S55-S63

Landahl M.T., 1990, *On sublayer streaks,* J. Fluid Mech. **212**, pp. 593-614

Laufer J., 1975, *New trends in experimental turbulence research,* Ann. Rev. Fluid Mech. **7**, pp. 307-326

Laufer J. and Badri Narayan M.A., 1971, *Mean period of the turbulent production mechanism in a boundary layer,* Phys. Fluids **14**, pp. 182-183

Liu Z.-C., Landreth C.C., Adrian R.J. and Hanratty T.J., 1991, *High resolution measurement of turbulent structure in a channel with particle image velocimetry,* Expts. Fluids **10**, pp. 301-312

Lu L.J. and Smith C.R., 1985, *Image processing of hydrogen bubble flow visualization for determination of turbulence statistics and bursting characteristics,* Expts. Fluids **3**, pp. 349-356

Lu S.S. and Willmarth W.W., 1973, *Measurements of the structure of the Reynolds stress in a turbulent boundary layer,* J. Fluid Mech. **60**, pp. 481-511

Luchik T.S. and Tiederman W.G., 1987, *Timescale and structure of ejections and bursts in turbulent channel flows,* J. Fluid Mech. **174**, pp. 529-552

Materon G., 1975, *Random sets and integral geometry,* Wiley

Merzkirch W., 1987, *Flow visualisation, 2nd edition,* Academic Press

Michalke A., 1965, *On spatially growing disturbances in an inviscid shear layer,* J. Fluid Mech. **23**, pp. 521-344

Monin A.S. and Yaglom A.M., 1975, *Statistical fluid mechanics: mechanics of turbulence,* MIT Press

Morrison W.R.B., Bullock K.J. and Kronauer R.E., 1971, *Experimental evidence of waves in the sublayer,* J. Fluid Mech. **47**, pp. 639-656

Nakagawa H. and Nezu I., 1977, *Prediction of the contributions to the Reynolds stress from bursting events in open-channel flows,* J. Fluid Mech. **80**, pp. 99-128

Nikolaides C., Lau K.K. and Hanratty T.J., 1983, *A study of the spanwise structure of coherent eddies in the viscous wall region,* J. Fluid Mech. **130**, pp. 91-108

Offen G.R. and Kline S.J., 1973, *Experiments on the velocity characteristics of 'bursts' and on the interactions between the inner and outer regions of a turbulent boundary layer,* Report MD-31, Stanford University

Offen G.R. and Kline S.J., 1974, *Combined dye-streak and hydrogen-bubble visual observations of a turbulent boundary layer,* J. Fluid Mech. **62**, pp. 223-239

Perry A.E. and Chong M.S., 1982, *On the mechanism of wall turbulence*, J. Fluid Mech. **119**, pp. 173-217

Pulles C.J.A., 1988, *Drag reduction of turbulent boundary layers by means of grooved surfaces*, Ph.D. thesis, Eindhoven University

Rajagopalan S. and Antonia R.A., 1982, *Use of a quadrant analysis technique to identify coherent structures in a turbulent boundary layer*, Phys. Fluids **25**, pp. 949-956

Rao K.N., Narasimha R. and Badri Narayan M.A., 1971, *The 'bursting' phenomenon in a turbulent boundary layer*, J. Fluid Mech. **48**, pp. 339-352

Reynolds O., 1883, *An experimental investigation of the circumstances which determine whether the motion of water shall be direct or sinuous*, Phil. Trans. Roy. Soc. **174**, pp. 935-982

Richardson L.F., 1920, *The supply of energy from and to atmospheric eddies*, Proc. Roy. Soc. **A97**, pp. 354-373

Robinson S.K., 1991, *Coherent motions in the turbulent boundary layer*, Ann. Rev. Fluid Mech. **23**, pp. 601-639

Robinson S.K., Kline S.J. and Spalart S.J., 1989, *Quasi-coherent structures in the turbulent boundary layer: part II. Verification and new information from a numerically simulated flat-plate layer*, In: Near-wall turbulence (ed. S.J. Kline and N.H. Afghan), pp. 218-247, Hemisphere

Rosenfeld A. and Kak A.C., 1982, *Digital picture processing, 2nd edition*, Academic Press

Runstadler P.W., Kline S.J. and Reynolds W.C., 1963, *An experimental investigation of the flow structure of the turbulent boundary layer*, Report MD-8, Stanford University

Schlichting H., 1979, *Boundary layer theory, 7th edition*, McGraw-Hill

Schraub F.A. and Kline S.J., 1965, *A study of the structure of the turbulent boundary layer with and without longitudinal pressure gradients*, Report MD-12, Stanford University

Schraub F.A., Kline S.J., Henry J., Runstadler P.W. and Littel A., 1965, *Use of hydrogen bubbles for quantitative determination of time-dependent velocity fields in low-speed water flows*, J. Basic Eng. **87**, pp. 429-444

Serra J., 1981, *Image analysis and mathematical morphology*, Academic Press

Sierputowsky P., 1991, Submitted to Turbulence, accepted for publication

Smith C.R., 1984, *A synthesized model of the near-wall behavior in turbulent boundary layers*, In: Proc. 8th Symp. on Turbulence (ed. G.K. Patterson and J.L. Zakin), University of Missouri, Rolla

Smith C.R. and Metzler S.P., 1983, *The characteristics of low-speed streaks in the near-wall region of a turbulent boundary layer*, J. Fluid Mech. **129**, pp. 27-54

Smith C.R. and Schwartz S.P., 1983, *Observations of streamwise rotation in the near-wall region of a turbulent boundary layer*, Phys. Fluids **26**, pp. 641-652

Sreenivasan K.R., 1988, *A unified view of the origin and the morphology of the turbulent boundary layer structure*, In: Proc. Turbulence man. and rel. IUTAM symp. Bangalore (ed. H.W. Liepmann and R. Narasimha), Springer

Talmon A.M., Kunen J.M.G. and Ooms G., 1986, *Simultaneous flow visualization and Reynolds-stress measurement in a turbulent boundary layer*, J. Fluid Mech. **163**, pp. 459-478

Tennekes H. and Lumley J.L., 1972, *A first course in turbulence*, MIT Press

Theodorsen T., 1955, *The structure of turbulence*, In: 50 Jahre Grenzschichtforschung (ed. H. Görtler and W. Tollmien), pp. 55-62, Vieweg & Sohn

Thijssen J.H.H., 1988, *Snelheidsbepaling met behulp van de waterstofbellentechniek & burstdetectie in een turbulente grenslaag boven verschillende wandgeometrieën in het kader van het wrijvingsverminderingsonderzoek*, Report R-932-A, Afstudeerverslag, Eindhoven University

Utami T. and Ueno T., 1984, *Visualization and picture processing in turbulent flow*, Expts. Fluids **2**, pp. 25-32

Wallace J.M., Eckelmann H. and Brodkey R.S., 1972, *The wall region in turbulent shear flow*, J. Fluid Mech. **54**, pp. 39-48

Willmarth W.W., 1975, *Structure of turbulence in boundary layers*, Adv. Appl. Mech. **15**, pp. 159-254

Willmarth W.W. and Lu S.S., 1972, *Structure of the Reynolds stress near the wall*, J. Fluid Mech. **55**, pp. 65-92

Willmarth W.W. and Sharma L.K., 1984, *Study of turbulent structure with hot wires smaller than the viscous length*, J. Fluid Mech. **142**, pp. 121-149

Young I.T., Peverini R.L., Verbeek P.W. and van Otterloo P.J., 1981, *A new implementation for the binary and minkowsky operators*, Comp. Graph. Im. Proc. **17**, pp. 189-210

Zhang Z. and Lilley G.M., 1982, *A theoretical model of the coherent structure of the turbulent boundary layer in zero pressure gradient*, In: Turbulent shear flow 3 (ed. L.J.S. Bradbury e.a.), pp. 60-72, Springer

Appendix A

The use of logical and morphological operators[12]

A.1 Binary pictures

For a quantitative use of hydrogen-bubble flow-visualization, the motion of hydrogen-bubble time-lines must be analysed. Here we assume that the time-line pictures are available in digitized form.

In general, the grey values of the bubbles differ from those of the background. With the proper correction for an unhomogeneous background and the proper segmentation technique to separate time lines and background, the binary version of the original picture can be obtained. A binary picture is a picture with only two grey values: 0 (for the background) and 1 (for the bubbles).

Binary pictures allow for logical and morphological operations (see e.g. Young e.a., 1981). The set of logical operators consists of the Boolean operators *not*, *and* and *or*. The latter two are used to combine the information that is present in two source pictures. The set of morphological operators consists of the Minkowski operators *dilate* and *erode*. These operators are non-linear filters. Both the logical and the morphological operators can be used to build higher level operators such as *sub* and *xor* (from the Boolean set), and *open* and *close* (from the Minkowski set).

A.2 Logical and morphological operations on binary pictures

The Boolean functions are the 'not', 'and' and 'inclusive or" functions of mathematical logic (table 1). The 'not' function sets 1's into 0's, and 0's into 1's. The 'and' function returns 1 when both input values are 1, and returns 0 otherwise. The 'or' function, on the other hand, returns 0 only when both input values are 0, and returns 1 otherwise.

When these functions are applied on pictures on a pixel-by-pixel basis, we get the *not* operator (which is a one-picture operator), the *and* operator and the *or* operator (which are two-picture operators). The *not* operator performed on an object gives the complement of the object. The *and* of two objects corresponds to those points that are simultaneously in both objects. The *or* of two objects corresponds to those points that are in one or in the other object. For example, we get a picture with black bubble lines in a white environment when we *not* a binary picture with white bubble lines in a black environment.

The Minkowski operators are the 'dilate' and 'erode' functions of mathematical morphology (Matheron, 1975; Serra, 1981). These functions involve the hit-or-miss trans-

---

(a)   p   not(p)

         1   0
         0   1

(b)   p   q   and(p, q)   or(p, q)

         1   1   1   1
         1   0   0   1
         0   0   0   0
         0   1   0   1

Table 1: (a) The definition of the 'not' function of mathematical logic. (b) The definition of the 'and' and the 'inclusive or' functions of mathematical logic.

```
.  x  .
x  x  x
.  x  .
```

Figure 1: The structuring element for the 'dilate' and 'erode' functions of mathematical morphology in the case of a four-connected grid.

formation, which is the interaction of a structuring element (i.e. a set of points) with an object. If at least one point of the structuring element hits the object, the value of the picture point under the central point of the structuring element is transformed. Figure 1 shows the structuring element for the dilation and erosion operations in a four-connected grid. For dilation the value of the picture point under the central point of the structuring element is set to 1 if at least one of the structuring element's points hits the object; otherwise it is set to 0. For erosion this value is set to 1 if and only if all the points of the structuring element hit the object; otherwise it is set to 0. Figure 2 shows what happens to an object when these transformations are applied. We see that dilation is comparable to inflating a balloon, and that erosion is comparable to peeling away the rings of an onion. Therefore, dilation is also called expansion or propagation, and erosion also shrinking or thinning.

In the *dilate* and *erode* operators the corresponding functions are implemented as local-neighbourhood operations. Therefore, we consider a pixel and its four-connected neighbours. For *dilate* the value of the pixel is set to 1 if at least one of the five pixels

```
o  o  o  o  o  o  o  o        o  o  o  o  o  o  o  o        o  o  o  o  o  o  o  o
o  o  o  o  o  o  o  o        o  o  o  x  o  x  o  o        o  o  o  o  o  o  o  o
o  o  o  x  o  x  o  o        o  o  x  x  x  x  x  o        o  o  o  o  o  o  o  o
o  o  x  x  x  x  o  o        o  x  x  x  x  x  x  o        o  o  o  x  o  o  o  o
o  o  x  x  x  o  o  o        o  x  x  x  x  x  o  o        o  o  o  x  o  o  o  o
o  o  o  x  x  o  o  o        o  o  x  x  x  x  o  o        o  o  o  o  o  o  o  o
o  o  o  o  o  o  o  o        o  o  o  x  x  o  o  o        o  o  o  o  o  o  o  o
o  o  o  o  o  o  o  o        o  o  o  o  o  o  o  o        o  o  o  o  o  o  o  o

         (a)                          (b)                          (c)
```
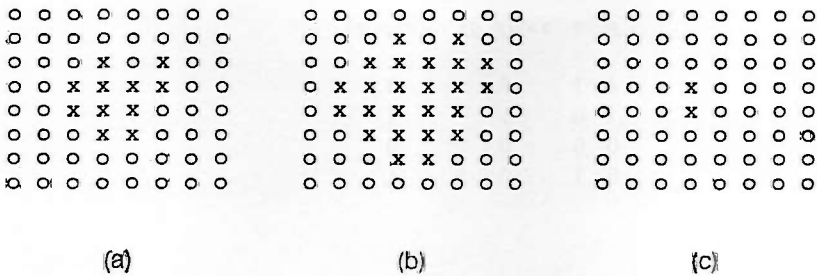
Figure 2: The dilation and the erosion of an object. (a) A binary picture with an object. (b) The dilated object. (c) The eroded object.

```
        .  o  .                    .  .  .                       .  o  .                   .  .  .
(a)     o  x  o      =>            .  x  .         and           o  o  o      =>           .  o  .
        .  o  .                    .  .  .                       .  o  .                   .  .  .


        .  o  .                    .  .  .                       .  x  .                   .  .  .
(b)     x  x  x      =>            .  o  .         and           x  x  x      =>           .  x  .
        .  o  .                    .  .  .                       .  x  .                   .  .  .
```
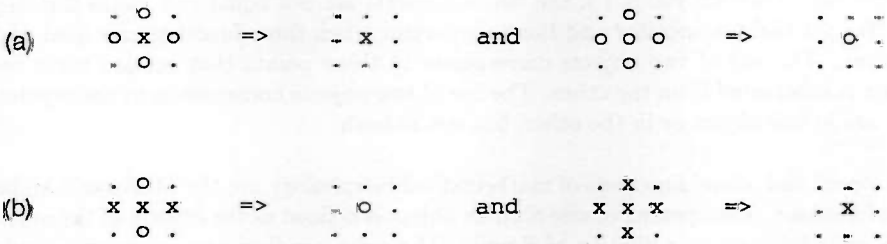
Figure 3: The implementation of (a) the 'dilate' and (b) the 'erode' function as local-neighbourhood operations.

has a value of 1; otherwise it is set to 0 (Figure 3a). This is comparable to the 'or' function, but for five input values rather than two. For *erode* the pixel value is set to 1 if and only if all five pixels have a value of 1; otherwise it is set to 0 (Figure 3b). This is comparable to an 'and' function operating on five input values.

When applied on an object, *dilate* expands it by one unit, and *erode* shrinks it by one unit. These operators may be used recursively; for example one must apply *dilate* six times in order to expand an object by six units. Note however that the 'dilate' and 'erode' functions are not inverse functions.

A.3 Higher level operations on binary pictures

The higher level operators are those that can be built from the Boolean operators and the Minkowski operators. First, we consider *sub*, *xor*, *open* and *close*.

The 'subtraction' and the 'exclusive or' functions of mathematical logic are the Boolean higher level functions. They are defined by $sub(p,q) = and(p, \neg q)$ and $xor(p,q) =$

p	q	$sub(p,q)$	$xor(p,q)$
1	1	0	0
1	0	1	1
0	0	0	0
0	1	0	1

Table 2: The definition of the 'sub' and the 'exclusive or' higher level functions of mathematical logic.

$or(and(p, \neg q), and(\neg p, q))$, with $\neg a = not(a)$ (table 2). The 'sub' function returns 1 if and only if the first argument is 1 while the second argument is 0; otherwise it returns 0. The 'xor' function yields 1 if the two arguments are not equal and yields 0 if they are. We get the *sub* operator and the *xor* operator when these functions are used with pictures. The *sub* of two objects corresponds to those points that remain when one object is subtracted from the other. The *xor* of two objects corresponds to those points that are in one object or in the other, but not in both.

The 'open' and 'close' functions of mathematical morphology are the Minkowski higher level functions. The opening of size S on an object is defined as the erosion of the object by S units followed by a dilation of S units. The corresponding *open* operator is useful for removing salt (noise in the background), and may be used to smooth the outside boundary of an object. The closing of size S on an object is defined as the dilation of the object by S units followed by an erosion of S units. The corresponding *close* operator is useful for removing pepper (noise in an object), and may be used to smooth inside boundaries of an object. Figure 4 presents an example for a four-connected grid. We see that opening is comparable to smoothing the skin of a doughnut, and that closing is comparable to removing the hole in a doughnut. Note that closing is not the inversion of opening.

Finally, we define the 'rim' function. Figure 5 shows the structuring element for the 'rim west' function. The value of the picture point under the central point of the structuring element is set to 1 if and only if the central point of the structuring element hits the object and the other point hits the background; otherwise it is set to 0 (figure 6). Similarly, we can define the 'rim north', the 'rim east' and the 'rim south' functions with the proper structuring elements. We see that the 'rim' function is comparable to the creation of a weather side due to wind blowing from a specific direction.

```
o o o o o o o o o        o o o o o o o o o        o o o o o o o o o
o o o o o o o x o        o o o o o o o o o        o o o o o o o x o
o o o x x o o o o        o o o x x o o o o        o o o x x o o o o
o o x x x x o o o        o o x x x x o o o        o o x x x x o o o
o o x x x x x o o        o o x x x x x o o        o o x x x x x o o
o x x x o x x x o        o o o x o x x x o        o x x x x x x x o
o o o x x x x x o        o o x x x x x x o        o o x x x x x x o
o o x x x x x x o        o o x x x x x x o        o o x x x x x x o
o o x x x o x x o        o o o x x o x o o        o o x x x o x x o
o o o o o o o o o        o o o o o o o o o        o o o o o o o o o
o o o o o o o o o        o o o o o o o o o        o o o o o o o o o

        (a)                      (b)                      (c)
```
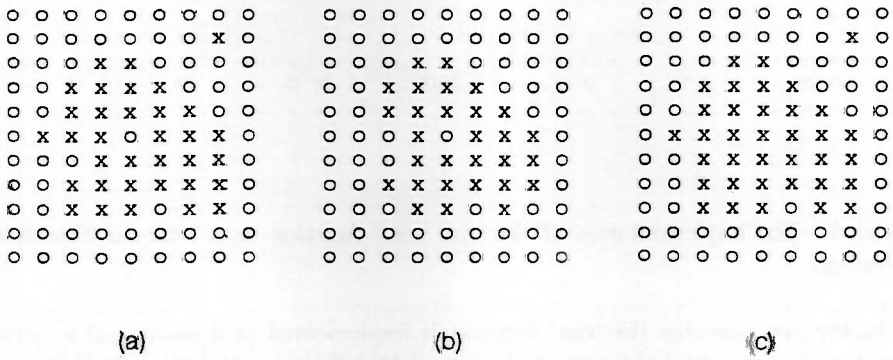
Figure 4: The opening and the closing of an object. (a) A binary picture with an object. (b) The object after an opening of size 1. (c) The object after a closing of size 1.

```
    .  .  .
    .  x  x
    .  .  .
```

Figure 5: The structuring element for the 'rim west' higher level function of mathematical morphology in the case of a four-connected grid.

```
o o o o o o o o        o o o o o o o o
o o o x o x o o        o o o x o x o o
o o x x x x o o        o o x o o o o o
o o x x x o o o        o o x o o o o o
o o o x x o o o        o o o x o o o o
o o o o o o o o        o o o o o o o o

        (a)                     (b)
```

Figure 6: (a) A binary picture with an object. (b) The object transformed by the 'rim west' function.

```
 -  .  .                 -  .                 .  .  .              .  .  .
 o  x  .     =>        .  x  .     but      x  x  .     =>       .  o  .
 .  .  .               .  .  .               .  .  .              .  .  .
```

Figure 7: The implementation of the 'rim west' function as a local-neighbourhood operation.
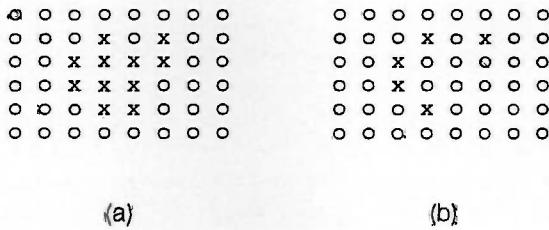
In the *rim* operator the 'rim' function is implemented as a local-neighbourhood operator. For *rim west* the central pixel is set to 1 if the central pixel itself is 1 and its western neighbour is 0 (figure 7). If the mean flow is orientated in the direction of the scan lines of a binary bubble-line picture, the *rim west* operator yields bubble lines which are reduced to a thickness of one unit and which mark the position of the bubble line at the moment the light switched on.

Appendix B

Solutions of the viscous dispersion relation for a sinusoidal basic flow

B.1 The perturbation amplitude for the sinusoidal shear layer

In a viscous fluid the amplitude $\phi(z)$ of the streamfunction which describes a two-dimensional velocity perturbation in the xz plane is governed by an equivalent of the Orr-Sommerfeld equation for a two-dimensional velocity perturbation in the xy plane:

$$i\frac{1}{R}\frac{d^4\phi}{dz^4} + \alpha\left(U(z) - c - i\frac{2\alpha}{R}\right)\frac{d^2\phi}{dz^2} - \alpha\left(\alpha^2\left(U(z) - c - i\frac{2\alpha}{R}\right) + \frac{d^2U_1}{dz^2}\right)\phi = 0 \quad (1)$$

(see section 3.3.2 and cf. Drazin and Reid, 1981, p. 156). The parameters of the perturbation are the wavenumber α and the velocity c; R denotes the non-dimensional kinematic viscosity of the fluid. In the case of the sinusoidal basic flow

$$U(z) = U_b + U_0 \sin k_z z \quad \text{for} \quad -\frac{\pi}{2k_z} \leq z \leq \frac{\pi}{2k_z} \quad (2)$$

(1) becomes

$$a_4\frac{d^4\phi}{dz^4} + (a_2 + b_2 \sin k_z z)\frac{d^2\phi}{dz^2} + (a_1 + b_1 \sin k_z z)\, \phi = 0, \quad (3)$$

with

$$
\begin{aligned}
a_4 &= i\frac{1}{R}, \\
a_2 &= \alpha\left(U_b - c - i\frac{2\alpha}{R}\right), \\
a_1 &= -\alpha^3\left(U_b - c - i\frac{\alpha}{R}\right), \\
b_2 &= \alpha\, U_0, \\
b_1 &= -\alpha\left(\alpha^2 - k_z^2\right) U_0.
\end{aligned}
\quad (4)
$$

Here the basic-flow parameters are the local mean fluid velocity U_b, the magnitude U_0 and the wavenumber k_z of the low-velocity region.

For equation (3) $z = 0$ is an ordinary point. Therefore, we look for a solution of the form

$$\phi(z) = \sum_{n=0}^{\infty} c_n\, z^n. \quad (5)$$

Differentiating (5) term by term yields

$$\frac{d^2\phi}{dz^2} = \sum_{n=0}^{\infty} (n+2)(n+1)c_{n+2}\, z^n, \quad (6)$$

and

$$\frac{d^4\phi}{dz^4} = \sum_{n=0}^{\infty} (n+4)(n+3)(n+2)(n+1)c_{n+4}\, z^n. \tag{7}$$

Using

$$\sin x = \sum_{n=0}^{\infty} \frac{(-1)^n}{(2n+1)!}\, x^{2n+1} \approx x - \frac{1}{6}x^3 + \frac{1}{120}x^5 \quad \text{for} \quad -\frac{\pi}{2} \le x \le \frac{\pi}{2}, \tag{8}$$

substituting (5), (6) and (7) in (3), and collecting coefficients of like powers of z yields

$$24a_4c_4 + 2a_2c_2 + a_1c_0 = 0, \tag{9}$$

$$120a_4c_5 + 6a_2c_3 + 2b_2k_zc_2 + a_1c_1 + b_1k_zc_0 = 0, \tag{10}$$

$$360a_4c_6 + 12a_2c_4 + 6b_2k_zc_3 + a_1c_2 + b_1k_zc_1 = 0, \tag{11}$$

$$840a_4c_7 + 20a_2c_5 + 12b_2k_zc_4 - \frac{1}{3}b_2k_z^3c_2 + a_1c_3 + b_1k_zc_2 - \frac{1}{6}b_1k_z^3c_0 = 0, \tag{12}$$

$$1680a_4c_8 + 30a_2c_6 + 20b_2k_zc_5 - b_2k_z^3c_3 + a_1c_4 + b_1k_zc_3 - \frac{1}{6}b_1k_z^3c_1 = 0, \tag{13}$$

and

$$a_4(m+4)(m+3)(m+2)(m+1)c_{m+4} + a_2(m+2)(m+1)c_{m+2} + $$
$$b_2k_z(m+1)mc_{m+1} - \frac{1}{6}b_2k_z^3(m-1)(m-2)c_{m-1} + $$
$$\frac{1}{120}b_2k_z^5(m-3)(m-4)c_{m-3} + a_1c_m + b_1k_zc_{m-1} - $$
$$\frac{1}{6}b_1k_z^3c_{m-3} + \frac{1}{120}b_1k_z^5c_{m-5} = 0. \tag{14}$$

Equations (9)...(14) are the recurrence equations which express c_m $(m \ge 4)$ in terms of lower-order coefficients. Solving for c_n (with $n \ge 4$) in terms of c_0, c_1, c_2 and c_3 gives

$$c_4 = -\frac{a_2}{12a_4}c_2 - \frac{a_1}{24a_4}c_0, \tag{15}$$

$$c_5 = -\frac{a_2}{20a_4}c_3 - \frac{b_2k_z}{60a_4}c_2 - \frac{a_1}{120a_4}c_1 - \frac{b_1k_z}{120a_4}c_0, \tag{16}$$

$$c_6 = -\frac{b_2k_z}{60a_4}c_3 + \left(\frac{a_2^2}{360a_4^2} - \frac{a_1}{360a_4}\right)c_2 - \frac{b_1k_z}{360a_4}c_1 + \frac{a_2a_1}{720a_4^2}c_0, \tag{17}$$

$$c_7 = \left(\frac{a_2^2}{840a_4^2} - \frac{a_1}{840a_4}\right)c_3 + \left(\frac{a_2b_2k_z}{630a_4^2} + \frac{b_2k_z^3}{2520a_4} - \frac{b_1k_z}{840a_4}\right)c_2 + $$
$$\frac{a_2a_1}{5040a_4^2}c_1 + \left(\frac{a_2b_1k_z}{5040a_4^2} + \frac{a_1b_2k_z}{1680a_4^2} + \frac{b_1k_z^3}{5040a_4}\right)c_0, \tag{18}$$

and so on for c_8 and higher-order coefficients. Substituting the coefficients (15), (16), (17) and (18) in (5) gives

$$\phi(z) = c_0\phi_0(z) + c_1\phi_1(z) + c_2\phi_2(z) + c_3\phi_3(z), \tag{19}$$

where $\phi_0(z)$, $\phi_1(z)$, $\phi_2(z)$ and $\phi_3(z)$ are the linearly independent solutions of (3). Substituting the coefficients (4) in (15), (16), (17) and (18) gives

$$\phi_0(z) = 1 + A_4 z^4 + A_5 z^5 + A_6 z^6 + A_7 z^7 + \dots \tag{20}$$

with

$$A_4 = -\frac{1}{24}\left(i\alpha^3 R(U_b - c) + \alpha^4\right), \tag{21}$$

$$A_5 = -\frac{1}{120}i\alpha R(\alpha^2 - k_z^2)k_z U_0, \tag{22}$$

$$A_6 = \frac{\alpha^4 R^2}{720}\left((U_b - c)^2 - i\frac{3\alpha}{R}(U_b - c) - \frac{2\alpha^2}{R^2}\right), \tag{23}$$

and

$$A_7 = \frac{k_z U_0}{5040}\left(\alpha^2 R^2(4\alpha^2 - k_z^2)(U_b - c) - i\alpha^3 R(5\alpha^2 - 2k_z^2) + i\alpha R(\alpha^2 - k_z^2)k_z^2\right). \tag{24}$$

Similarly, we find

$$\phi_1(z) = z + B_5 z^5 + B_6 z^6 + B_7 z^7 + \dots \tag{25}$$

with

$$B_5 = \frac{A_4}{5}, \quad B_6 = \frac{A_5}{3} \quad \text{and} \quad B_7 = \frac{A_6}{7}; \tag{26}$$

$$\phi_2(z) = z^2 + C_4 z^4 + C_5 z^5 + C_6 z^6 + C_7 z^7 + \dots \tag{27}$$

with

$$C_4 = \frac{1}{12}\left(i\alpha R(U_b - c) + 2\alpha^2\right), \tag{28}$$

$$C_5 = \frac{1}{60}i\alpha R k_z U_0, \tag{29}$$

$$C_6 = \frac{1}{360}\left(-\alpha^2 R^2(U_b - c)^2 + i3\alpha^3 R(U_b - c) + 3\alpha^4\right), \tag{30}$$

and

$$C_7 = \frac{k_z U_0}{2520}\left(-4\alpha^2 R^2(U_b - c) + i\alpha R(5\alpha^2 + 2k_z^2)\right); \tag{31}$$

and

$$\phi_3(z) = z^3 + D_5 z^5 + D_6 z^6 + D_7 z^7 + \dots \tag{32}$$

with

$$D_5 = \frac{3}{5}C_4, \quad D_6 = C_5 \quad \text{and} \quad D_7 = \frac{3}{7}C_6. \tag{33}$$

Thus the set of equations (19)...(33) is the general solution of the equation for the perturbation amplitude in the interval $-\pi/2k_z \leq z \leq \pi/2k_z$.

B.2 The dispersion relation for the sinusoidal shear layer

Both the spanwise and the streamwise component of the velocity perturbation must be zero at the boundaries of the shear layer. Therefore, we have for the general solution (19) two boundary conditions in $z = -\pi/2k_z$ and $z = \pi/2k_z$:

$$\phi(\pm\frac{\pi}{2k_z}) = 0 \quad \text{and} \quad D\phi(\pm\frac{\pi}{2k_z}) = 0, \tag{34}$$

with $D\phi(z)$ shorthand for $d\phi(z)/dz$. Non-trivial solutions of (34) only exist if

$$\begin{vmatrix} \phi_0(\frac{\pi}{2k_z}) & \phi_1(\frac{\pi}{2k_z}) & \phi_2(\frac{\pi}{2k_z}) & \phi_3(\frac{\pi}{2k_z}) \\ \phi_0(-\frac{\pi}{2k_z}) & \phi_1(-\frac{\pi}{2k_z}) & \phi_2(-\frac{\pi}{2k_z}) & \phi_3(-\frac{\pi}{2k_z}) \\ D\phi_0(\frac{\pi}{2k_z}) & D\phi_1(\frac{\pi}{2k_z}) & D\phi_2(\frac{\pi}{2k_z}) & D\phi_3(\frac{\pi}{2k_z}) \\ D\phi_0(-\frac{\pi}{2k_z}) & D\phi_1(-\frac{\pi}{2k_z}) & D\phi_2(-\frac{\pi}{2k_z}) & D\phi_3(-\frac{\pi}{2k_z}) \end{vmatrix} = 0. \tag{35}$$

Each element of (35) can be written as a second order equation in $U_b - c$. For example, substituting (21), (22), (23), (24) and $z = \pi/2k_z$ in (20) gives

$$\phi_0(\frac{\pi}{2k_z}) = K_{00}(U_b - c)^2 + L_{00}(U_b - c) + M_{00}, \tag{36}$$

with

$$K_{00} = \frac{\pi^6}{46080}\frac{\alpha^4 R^2}{k_z^6}, \tag{37}$$

$$\begin{aligned} L_{00} &= -\frac{\pi^4}{384}\frac{\alpha^2 R}{k_z^4}\left(i\alpha + \frac{\pi^2}{40}\frac{i\alpha^3}{k_z^2} - \frac{\pi^3}{420}\frac{\alpha^2 RU_0}{k_z^2} + \frac{\pi^3}{1680}RU_0\right) \\ &\approx -\frac{\pi^7}{645120}\frac{\alpha^2 R^2 U_0}{k_z^4}, \end{aligned} \tag{38}$$

and

$$\begin{aligned} M_{00} &= 1 - \frac{\pi^4}{384}\frac{\alpha^4}{k_z^4}\left(1 + \frac{\pi^2}{60}\frac{\alpha^2}{k_z^2}\right) + \\ &\quad \frac{\pi^5}{3840}\frac{i\alpha RU_0}{k_z^2}\left(1 - \frac{\alpha^2}{k_z^2} - \frac{5\pi^2}{168}\frac{\alpha^4}{k_z^4} + \frac{\pi^2}{84}\frac{\alpha^2}{k_z^2} + \frac{\pi^2}{168}\frac{\alpha^2}{k_z^2} - \frac{\pi^2}{168}\right) \\ &\approx 1 + \frac{\pi^5}{3840}\frac{i\alpha RU_0}{k_z^2}. \end{aligned} \tag{39}$$

The approximations hold for $|\alpha| < k_z$ and $R > |\alpha|/U_0$. (The modulus of the complex wavenumber α is denoted by $|\alpha|$.) Proceeding in a similar way, it can be shown that (35) is equivalent to

$$\begin{vmatrix} K_{00}U^2 + L_{00}U + M_{00} & K_{10}U^2 + L_{10}U + M_{10} & K_{20}U^2 + L_{20}U + M_{20} & K_{30}U^2 + L_{30}U + M_{30} \\ K_{01}U^2 + L_{01}U + M_{01} & K_{11}U^2 + L_{11}U + M_{11} & K_{21}U^2 + L_{21}U + M_{21} & K_{31}U^2 + L_{31}U + M_{31} \\ K_{02}U^2 + L_{02}U + M_{02} & K_{12}U^2 + L_{12}U + M_{12} & K_{22}U^2 + L_{22}U + M_{22} & K_{32}U^2 + L_{32}U + M_{32} \\ K_{03}U^2 + L_{03}U + M_{03} & K_{13}U^2 + L_{13}U + M_{13} & K_{23}U^2 + L_{23}U + M_{23} & K_{33}U^2 + L_{33}U + M_{33} \end{vmatrix} = 0 \tag{40}$$

with $U = U_b - c$ for ease of notation. Expressing the other determinant elements as a quadratic equation in $U_b - c$, and using the conditions as before gives

$$K_{01} = K_{00}, \quad L_{01} = -L_{00} \text{ and } M_{01} = -M_{00} + 2, \tag{41}$$

$$K_{10} = \frac{\pi^7}{645120} \frac{\alpha^4 R^2}{k_z^7}, \tag{42}$$

$$L_{10} = -\frac{\pi^5}{3840} \frac{i\alpha^3 R}{k_z^5}, \tag{43}$$

$$M_{10} = \frac{\pi}{2k_z} \left(1 + \frac{\pi^5}{11520} \frac{i\alpha R U_0}{k_z^2} \right), \tag{44}$$

$$K_{11} = -K_{10}, \quad L_{11} = -L_{10} \text{ and } M_{11} = M_{10} - \frac{\pi}{k_z}, \tag{45}$$

$$K_{20} = -\frac{\pi^6}{23040} \frac{\alpha^2 R^2}{k_z^6}, \tag{46}$$

$$L_{20} = \frac{\pi^4}{192} \frac{i\alpha R}{k_z^4} \left(1 + \frac{\pi^3}{420} \frac{i\alpha R U_0}{k_z^2} \right), \tag{47}$$

$$M_{20} = \frac{\pi^2}{4k_z^2} \left(1 + \frac{\pi^3}{480} \frac{i\alpha R U_0}{k_z^2} \right), \tag{48}$$

$$K_{21} = K_{20}, \quad L_{21} = -L_{20} + \frac{\pi^4}{96} \frac{i\alpha R}{k_z^4} \text{ and } M_{21} = -M_{20} + \frac{\pi^2}{2k_z^2}, \tag{49}$$

$$K_{30} = -\frac{\pi^7}{107520} \frac{\alpha^2 R^2}{k_z^7}, \tag{50}$$

$$L_{30} = \frac{\pi^5}{640} \frac{i\alpha R}{k_z^5}, \tag{51}$$

$$M_{30} = \frac{\pi^3}{8k_z^3} \left(1 + \frac{\pi^3}{480} \frac{i\alpha R U_0}{k_z^2} \right), \tag{52}$$

$$K_{31} = -K_{30}, \quad L_{31} = -L_{30} \text{ and } M_{31} = M_{30} - \frac{\pi^3}{4k_z^3}, \tag{53}$$

$$K_{02} = \frac{12k_z}{\pi} K_{00}, \quad L_{02} = \frac{14k_z}{\pi} L_{00} \text{ and } M_{02} = \frac{10k_z}{\pi} (M_{00} - 1), \tag{54}$$

$$K_{12} = \frac{14k_z}{\pi}K_{10}, \quad L_{12} = \frac{10k_z}{\pi}L_{10} \quad \text{and} \quad M_{12} = \frac{12k_z}{\pi}M_{10} - 5, \tag{56}$$

$$K_{13} = \frac{14k_z}{\pi}K_{10}, \quad L_{13} = \frac{10k_z}{\pi}L_{10} \quad \text{and} \quad M_{13} = -\frac{12k_z}{\pi}M_{10} + 7, \tag{57}$$

$$K_{22} = \frac{12k_z}{\pi}K_{20}, \quad L_{22} = \frac{14k_z}{\pi}L_{20} - \frac{3\pi^3}{96}\frac{i\alpha R}{k_z^3} \quad \text{and} \quad M_{22} = \frac{10k_z}{\pi}M_{20} - \frac{3\pi}{2k_z}, \tag{58}$$

$$K_{23} = -\frac{12k_z}{\pi}K_{20}, \quad L_{23} = \frac{14k_z}{\pi}L_{20} - \frac{11\pi^3}{96}\frac{i\alpha R}{k_z^3} \quad \text{and} \quad M_{23} = \frac{10k_z}{\pi}M_{20} - \frac{7\pi}{2k_z}, \tag{59}$$

$$K_{32} = \frac{14k_z}{\pi}K_{30}, \quad L_{32} = \frac{10k_z}{\pi}L_{30} \quad \text{and} \quad M_{32} = \frac{12k_z}{\pi}M_{30} - \frac{3\pi^2}{4k_z^2}, \tag{60}$$

and

$$K_{33} = \frac{14k_z}{\pi}K_{30}, \quad L_{33} = \frac{10k_z}{\pi}L_{30} \quad \text{and} \quad M_{33} = -\frac{12k_z}{\pi}M_{30} + \frac{9\pi^2}{4k_z^2}. \tag{61}$$

By reducing the fourth-order determinant (40) to a second-order determinant, it can be shown that (40) is equivalent to

$$-\frac{192k_z^2}{\pi^2}\left(K_{00}(U_b - c)^2 + 1\right)\left(-M_{10} + \frac{\pi}{2k_z}\right)\begin{vmatrix} e_{20} & e_{30} \\ e_{22} & e_{32} \end{vmatrix} = 0 \tag{62}$$

with

$$\begin{aligned}
e_{20} = \quad & \frac{\pi^4}{192}\frac{i\alpha R}{k_z^4}(U_b - c) + M_{20} + \frac{\pi^2}{4k_z^2} - \\
& \frac{\frac{\pi^4}{576}\frac{i\alpha R}{k_z^4}(U_b - c) + \frac{\pi^2}{6k_z^2}}{K_{00}(U_b - c)^2 + 1}(M_{00} + 2) + \\
& \frac{K_{20}(U_b - c)^2 + \frac{\pi^4}{288}\frac{i\alpha R}{k_z^4}(U_b - c) + \frac{\pi^2}{12k_z^2}}{-M_{10} + \frac{\pi}{2k_z}}\left(L_{10}(U_b - c) + \frac{3\pi}{2k_z}\right),
\end{aligned} \tag{63}$$

$$\begin{aligned}
e_{22} = \quad & \left(L_{20} - \frac{\pi^4}{96}\frac{i\alpha R}{k_z^4}\right)(U_b - c) - \frac{\pi^2}{2k_z^2} - \\
& \frac{\frac{\pi^4}{576}\frac{i\alpha R}{k_z^4}(U_b - c) + \frac{\pi^2}{6k_z^2}}{K_{00}(U_b - c)^2 + 1}(L_{00}(U_b - c) - 3) + \\
& \frac{K_{20}(U_b - c)^2 + \frac{\pi^4}{288}\frac{i\alpha R}{k_z^4}(U_b - c) + \frac{\pi^2}{12k_z^2}}{-M_{10} + \frac{\pi}{2k_z}}\left(K_{10}(U_b - c)^2 - \frac{\pi}{k_z}\right),
\end{aligned} \tag{64}$$

$$e_{30} = L_{30}(U_b - c) + \frac{\pi^3}{4k_z^3} - \frac{-M_{30} + \frac{\pi^3}{8k_z^3}}{-M_{10} + \frac{\pi}{2k_z}}\left(L_{10}(U_b - c) + \frac{3\pi}{2k_z}\right), \tag{65}$$

and

$$e_{32} = K_{30}(U_b - c)^2 - \frac{\pi^3}{8k_z^3} - \frac{-M_{30} + \frac{\pi^3}{8k_z^3}}{-M_{10} + \frac{\pi}{2k_z}}\left(K_{10}(U_b - c)^2 - \frac{\pi}{k_z}\right). \tag{66}$$

Equation (62), with the determinant elements (63)...(66), is the dispersion relation for the sinusoidal shear layer, provided that both the wavenumber and the spatial growth rate of the perturbation are small compared to the wavenumber of the basic flow (i.e. $\alpha_r < k_z$ and $\alpha_i < k_z$), and that the Reynolds number of the flow is large compared to the ratio of both the wavenumber and the spatial growth rate to the magnitude of the shear layer (i.e. $R > \alpha_r/U_0$ and $R > \alpha_i/U_0$).

B.3 The long-wave and high Reynolds-number approximation

The dispersion relation (62) is difficult to evaluate analytically. In the long-wave approximation ($|\alpha| \to 0$) the high-order terms in α vanish, with as a result

$$K_{00} \to 0, \quad K_{10} \to 0 \quad \text{and} \quad L_{10} \to 0. \tag{67}$$

In the high Reynolds-number approximation ($R > \frac{23040}{\pi^5}\frac{k_z^2}{|\alpha|U_0}$) only the highest-order terms in R need to be maintained. Consequently, the dispersion relation (62) reduces to

$$\begin{vmatrix} -\frac{3\pi}{2k_z}\frac{K_{20}}{M_{10}}(U_b - c)^2 - \frac{\pi^4}{576}\frac{i\alpha R}{k_z^4}M_{00}(U_b - c) + M_{20} & L_{30}(U_b - c) - \frac{3\pi}{2k_z}\frac{M_{30}}{M_{10}} \\ -\frac{\pi^4}{576}\frac{i\alpha R}{k_z^4}L_{00}(U_b - c)^2 + L_{20}(U_b - c) & K_{30}(U_b - c)^2 + \frac{\pi}{k_z}\frac{M_{30}}{M_{10}} \end{vmatrix} = 0, \tag{68}$$

which is equivalent to

$$(U_b - c)^4 + \frac{\pi^4}{360}U_0^2(U_b - c)^2 - 8\left(\frac{7\pi^2}{288} - 1\right)\frac{ik_z^2U_0^2}{\alpha R}(U_b - c) + \frac{224}{\pi^2}\frac{k_z^4U_0^2}{\alpha^2 R^2} = 0. \tag{69}$$

Equation (69) is the reduced dispersion relation, which is valid for small wavenumbers and large Reynolds-numbers.

B.4 The roots of the reduced dispersion relation

B.4.1 The general solution of a fourth-order equation

To solve the reduced dispersion relation (69), first we consider the analytical solution of a fourth-order equation (see e.g. Abramowitz and Stegun, 1970, p. 17). In general, the roots of

$$x^4 + bx^3 + cx^2 + dx + e = 0 \tag{70}$$

coincide with the roots of the second-order equations

$$x^2 + \frac{b + A}{2}x + y + \frac{by - d}{A} = 0, \tag{71}$$

where
$$A = \pm\sqrt{8y + b^2 - 4c} \tag{72}$$

and y is an arbitrary real root of the cubical equation

$$8y^3 - 4cy^2 + (2bd - 8e)y + e(4c - b^2) - d^2 = 0. \tag{73}$$

The cubical equation (73) is equivalent to

$$z^3 + 3pz + 2q = 0, \tag{74}$$

with

$$z = y - \frac{c}{6}, \tag{75}$$

$$3p = \frac{3(bd - 4e) - c^2}{12}, \tag{76}$$

and

$$2q = -\frac{c^3}{108} + \frac{c(bd - 4e)}{24} + \frac{e(4c - b^2) - d^2}{8}. \tag{77}$$

The three roots of (74) are

$$z_1 = u + v, \quad z_2 = -\frac{1}{2}(u + v) + i\frac{\sqrt{3}}{2}(u - v) \quad \text{and} \quad z_3 = -\frac{1}{2}(u + v) - i\frac{\sqrt{3}}{2}(u - v), \tag{78}$$

where u and v are determined from

$$u^3 = -q + \sqrt{D} \quad \text{and} \quad v^3 = -q - \sqrt{D}; \tag{79}$$

where the discriminant

$$D = p^3 + q^2. \tag{80}$$

B.4.2 The solution of the reduced dispersion relation

The reduced dispersion relation for the sinusoidal shear layer in the case of long waves and large Reynolds-numbers is the fourth order equation

$$(U_b - c)^4 + \frac{\pi^4}{360}U_0^2(U_b - c)^2 - 8\left(\frac{7\pi^2}{288} - 1\right)\frac{ik_z^2U_0^2}{\alpha R}(U_b - c) + \frac{224}{\pi^2}\frac{k_z^4U_0^2}{\alpha^2 R^2} = 0 \tag{81}$$

(see appendix B.3). In the terminology of the scheme described in appendix B.4.1 we have

$$b = 0, \quad c = \frac{\pi^4}{360}U_0^2, \quad d = -8\left(\frac{7\pi^2}{288} - 1\right)\frac{ik_z^2U_0^2}{\alpha R}, \quad \text{and} \quad e = \frac{224}{\pi^2}\frac{k_z^4U_0^2}{\alpha^2 R^2}. \tag{82}$$

The parameters p and q then follow by inserting the coefficients (82) in (76) and (77), with as a result

$$p = -\frac{\pi^8}{2160^2}U_0^4 - \frac{224}{3\pi^2}\frac{k_z^4U_0^2}{\alpha^2 R^2} \tag{83}$$

and

$$q = -\frac{\pi^{12}}{2160^3}U_0^6 - \frac{X}{2}\frac{k_z^4 U_0^4}{\alpha^2 R^2}, \tag{84}$$

where

$$X = \frac{28\pi^2}{135} + 8\left(\frac{7\pi^2}{288} - 1\right)^2. \tag{85}$$

The discriminant D is found by inserting (83) and (84) in (80), which gives

$$D \approx -\left(\frac{224\pi^{14}}{2160^4} + \frac{\pi^{12}X}{2160^3}\right)\frac{k_z^4 U_0^{10}}{\alpha^2 R^2}; \tag{86}$$

the approximation holding for large Reynolds numbers $(R > k_z^2 U_0^2/|\alpha^2|)$. Using (84) and (86) together with (79), we find

$$u \approx \frac{\pi^4}{2160}U_0^2\left(1 + \frac{2160^3}{3\pi^{12}}X'\frac{ik_z^2}{\alpha RU_0}\right) \tag{87}$$

and

$$v \approx \frac{\pi^4}{2160}U_0^2\left(1 - \frac{2160^3}{3\pi^{12}}X'\frac{ik_z^2}{\alpha RU_0}\right), \tag{88}$$

where

$$X' = \sqrt{\frac{224\pi^{14}}{2160^4} + \frac{\pi^{12}X}{2160^3}}. \tag{89}$$

Inserting (87) and (88) in (78b), and subsequently inserting the result in (75) gives

$$y_2 = -X''\frac{k_z^2 U_0}{\alpha R} \tag{90}$$

with

$$X'' = \frac{360^2 12\sqrt{3}}{\pi^8}X'. \tag{91}$$

Inserting (90) in (72) gives

$$\mathcal{A}_2 = \pm\frac{\pi^2}{3\sqrt{10}}iU_0\left(1 + Y\frac{k_z^2}{\alpha RU_0}\right) \tag{92}$$

with

$$Y = \frac{360^2 4320\sqrt{3}}{\pi^{12}}X'. \tag{93}$$

(Note that (78a) yields $\mathcal{A}_1 = 0$, which would produce a singularity in the equivalent second-order equation.) The second-order equations whose roots are equivalent to those of (81) then follow by inserting (90) and (92) in (71), with as a result

$$(U_b - c)^2 \pm \frac{\pi^2}{6\sqrt{10}}iU_0\left(1 + Y\frac{k_z^2}{\alpha RU_0}\right)(U_b - c) - X''\frac{k_z^2 U_0}{\alpha R} \pm \frac{24\sqrt{10}}{\pi^2}\left(\frac{7\pi^2}{288} - 1\right)\frac{k_z^2 U_0}{\alpha R} = 0, \tag{94}$$

provided that the Reynolds number is large. Solving the equations (94) gives the four roots of (81)

$$U_b - c = \mp \frac{\pi^2}{12\sqrt{10}} i U_0 \left(1 + Y \frac{k_z^2}{\alpha R U_0} \right) \pm \frac{\pi^2}{12\sqrt{10}} i U_0 \left(1 + Z_\pm \frac{k_z^2}{\alpha R U_0} \right) \qquad (95)$$

with

$$Z_\pm = Y - \frac{720}{\pi^4} X'' \pm \frac{17280\sqrt{10}}{\pi^6} \left(\frac{7\pi^2}{288} - 1 \right). \qquad (96)$$

The $\mp$ and the second $\pm$ signs are ordered as those in equation (94); the first $\pm$ sign is independent.

Acknowledgements

The turbulent boundary layer: spanwise structure, evolution of low-velocity regions and response to artificial disturbances

Abstract

In the classic view, turbulent boundary layer flow is random, and can only be characterized by moments of flow quantities. However, experiments have shown that this flow has a quasi-periodic character. In the modern view, near-wall turbulence is coherent on specific scales, and is characterized by flow events and fluid motions such as 'bursts' and low-speed streaks.

Even so, an evaluation of the knowledge on near-wall turbulence structure shows that data might not be correct, inferences might not be appropriate and opposite views may exist. It is therefore too early to decide on the significance of the concept of coherent near-wall flow, and necessary to assume that this knowledge is reliable and significant.

To this situation have contributed: 1) the inability to detect the joint temporal-spatial characteristics of the coherent motions, 2) the lack of a deterministic model for (elements of) near-wall turbulent flow, and 3) the quasi-periodic occurrence of the coherent motions. Therefore, this study has as objectives to: 1) 'measure' spanwise velocity profiles, and evaluate their structure, 2) determine the time evolution of the low-velocity regions, and develop a simple model for this kind of flow, and 3) develop a method by which non-random fluid motion can be generated artificially.

The hydrogen-bubble time-line technique is a useful method to measure mean fluid-velocities in regions not too close to (i.e. more than, say, 15 wall units above) the wall of a turbulent boundary layer. However, it fails when it is used to measure mean fluid velocities close to the wall, and velocity variances in the entire boundary layer. Moreover, its reliability is poor because of the intrinsic errors; especially those due to the presence of the bubble-generating wire and the velocity gradient in the flow.

The structure of near-wall turbulence is expressed in length scales based on the positions of the velocity extremes and inflection points in spanwise profiles of the streamwise fluid velocity. It appears that near-wall turbulence is spatially quasi-periodical with the mean values representing a range of values. The numerical values of these length scales are different from the generally accepted ones: e.g. the mean distance between low-velocity regions is 70 rather than 100 wall units, and on average the low-velocity regions are as wide as the high-velocity regions.

The time evolution of the fluid velocity in the low-velocity regions of near-wall turbulence is found by connecting the velocity extremes in the consecutive velocity profiles determined from the motion of a hydrogen-bubble time-line. It appears that the flow in a low-velocity region can be treated as an almost parallel and time-independent vis-

cous basic flow, and that a sinusoidal profile may model its shear layer. A stability analysis of this basic flow shows that always one unstable mode exists. The behaviour of the growth rate of this mode, as a function of the parameters of its basic flow, is in agreement with the one found experimentally, and suggests that in practise this mode is a temporal one. Furthermore, it is found experimentally that the distance between two low-velocity regions seems to depend on the 'age' of the time line from which the velocity profile is determined.

With periodic fluid-injection through small slots, a turbulent boundary layer is artificially disturbed on scales that are of the order of those of the natural quasi-periodic events. The periodic phase-average of the streamwise fluid velocity is determined from hot-film measurements, and used to find the coherent velocity component as defined by the triple decomposition. It appears that, when a disturbance is active, the generated flow pattern is very similar to the one caused by the interaction of a crossflow and a jet. However, when it is terminated, the turbulent boundary layer returns to its undisturbed state. In particular, there occurs no large increase in the fluid velocity which cannot be attributed to the disturbance itself; which increase one might expect if the disturbance initiates an artificial 'burst'.

From the response experiments it follows that care should be taken in interpreting the response to a disturbance in terms of a specific flow event which is not related to the disturbance itself. On the other hand, from the time-evolution experiments it follows that it might be possible to prove that near-wall turbulence contains regions which are highly deterministical, when a model is available which expresses the stability of the flow in a low-velocity region in terms of the parameters of an almost parallel and time-independent viscous basic flow.

De turbulente grenslaag: structuur in dwarsrichting, ontwikkeling van lage-snelheidsgebieden, en responsie op kunstmatige verstoringen

Uittreksel

De klassieke visie is dat een turbulente grenslaagstroming willekeurig is en alleen gekarakteriseerd kan worden door momenten van stromingsgroootheden. Experimenten hebben echter laten zien dat dit stromingstype een quasi-periodiek karakter heeft. De moderne visie is dat wandturbulentie coherent is op specifieke schalen, en gekarakteriseerd wordt door stromingsgebeurtenissen en vloeistofbewegingen zoals 'bursts' en 'low-speed streaks'.

Een evaluatie van de kennis over de structuur van wandturbulentie laat echter zien dat meetresultaten niet correct hoeven te zijn, gevolgtrekkingen niet passend hoeven te zijn, en tegenovergestelde visies kunnen bestaan. Het is daarom te vroeg om te beslissen over de betekenis van het concept van coherente wandturbulentie, en noodzakelijk om aan te nemen dat deze kennis betrouwbaar en zinvol is.

Aan deze situatie hebben bijgedragen: 1) het onvermogen om de gezamenlijke tijd-ruimte karakteristieken van de coherente vloeistofbewegingen te detecteren, 2) het ontbreken van een deterministisch model voor (elementen van) wandturbulentie, en 3) het quasi-periodiek optreden van de coherente vloeistofbewegingen. Deze studie heeft daarom als doelstellingen: 1) het 'meten' van snelheidsprofielen in dwarsrichting en het evalueren van hun structuur, 2) het bepalen van de ontwikkeling in de tijd van de lage-snelheidsgebieden en het opstellen van een eenvoudig model voor dit type stroming, en 3) het opstellen van een methode waarmee niet-willekeurige vloeistofbewegingen kunstmatig opgewekt kunnen worden.

De waterstofbelletjes-tijdlijn techniek is een bruikbare methode om gemiddelde vloeistofsnelheden te bepalen in gebieden die niet te dicht bij (dat is: meer dan ongeveer 15 visceuze eenheden boven) de wand van een turbulente grenslaag liggen. Deze methode faalt echter bij het bepalen van gemiddelde vloeistofsnelheden dicht bij de wand, en snelheidsvarianties in de gehele grenslaag. Bovendien is haar betrouwbaarheid gering door intrinsieke fouten; in het bijzonder die ten gevolge van de aanwezigheid van de draad waaraan de belletjes opgewekt worden en de snelheidsgradient in de stroming.

De structuur van wandturbulentie wordt uitgedrukt in lengteschalen die gebaseerd zijn op de posities van snelheidsextremen en -buigpunten in dwarsprofielen van de vloeistofsnelheid. Het blijkt dat wandturbulentie ruimtelijk quasi-periodiek is, met gemiddelden die een reeks van waarden vertegenwoordigen. De numerieke waarden van deze lengteschalen verschillen van de algemeen erkende waarden: bijvoorbeeld de gemiddelde afstand tussen lage-snelheidsgebieden bedraagt 70 in plaats van 100 visceuze

eenheden, en gemiddeld zijn de lage en de hoge-snelheidsgebieden even breed.

De ontwikkeling in de tijd van de vloeistofsnelheid in de lage-snelheidsgebieden van wandturbulentie wordt gevonden door de snelheidsextremen in opeenvolgende snelheidsprofielen, bepaald uit de beweging van een waterstofbelletjes-tijdlijn, te verbinden. Het blijkt dat de stroming in een lage-snelheidsgebied beschreven kan worden als een bijna parallelle en tijdonafhankelijke visceuze basisstroming, en dat een sinusvormig profiel gebruikt kan worden om zijn afschuiflaag te modelleren. Een stabiliteitsanalyse van deze basisstroming laat zien dat er altijd een onstabiele modus bestaat. Het gedrag van de groeifactor van deze modus als een functie van de parameters van zijn basisstroming komt overeen met het experimenteel gevonden gedrag, en suggereert dat deze modus een temporele is. Verder blijkt uit de experimenten dat de afstand tussen twee lage-snelheidsgebieden af lijkt te hangen van de 'leeftijd' van de tijdlijn waaruit het snelheidsprofiel bepaald is.

Met periodieke vloeistofinjectie door kleine sleuven is een turbulente grenslaag verstoord op schalen van de orde van de schalen van de natuurlijke quasi-periodieke gebeurtenissen. Het periodieke fase-gemiddelde van de vloeistofsnelheid in stromingsrichting is bepaald uit hete-film metingen, en gebruikt om de coherente snelheidscomponent volgens de drie-voudige decompositie te vinden. Het blijkt dat, wanneer een verstoring aktief is, het opgewekte stromingspatroon erg veel lijkt op het patroon dat veroorzaakt wordt door de wisselwerking tussen een dwarsstroming en een straal. De turbulente grenslaag keert echter terug in zijn ongestoorde toestand wanneer de verstoring is beëindigd. In het bijzonder treedt er geen grote toename op in de vloeistofsnelheid die niet toegeschreven kan worden aan de verstoring zelf; deze toename zou men verwachten als de verstoring een kunstmatige 'burst' initieert.

Uit de responsie experimenten volgt dat men voorzichtig moet zijn met het interpreteren van de responsie op een verstoring in termen van een stromingsgebeurtenis die niet in verband staat met de verstoring zelf. Daarentegen volgt uit de tijd-evolutie experimenten dat het wellicht mogelijk is om te bewijzen dat wandturbulentie gebieden bevat die in hoge mate deterministisch zijn, wanneer een model beschikbaar is dat de stabiliteit van de stroming in een lage-snelheidsgebied uitdrukt in termen van de parameters van een bijna parallelle en tijd-onafhankelijke visceuze basisstroming.

Curriculum vitae

Arnold Joost Brand werd geboren op 18 september 1961 in Sliedrecht. Hij bezocht als middelbare school de Chr. Scholengemeenschap 'De Lage Waard' in Papendrecht, en behaalde daar in juni 1979 het diploma Atheneum-B. Vervolgens ging hij Technische Natuurkunde studeren aan de Technische Universiteit Delft, en studeerde in mei 1987 bij de Vakgroep Stromingsleer van de Faculteit der Werktuigbouwkunde en Maritieme Techniek af als natuurkundig ingenieur (oude stijl). Hierna trad hij in dienst van de T.U.-Delft om als assistent-in-opleiding te gaan werken in de Vakgroep Stromingsleer. In deze periode werd dit promotie-onderzoek uitgevoerd. Tevens werd in de zomer van 1989 een bezoek aan het Fourier Optics and Optical Diagnostics Lab van Stanford University gebracht. Op 2 maart 1990 trad hij in het huwelijk met Janny Dijkstra. Sinds juli 1991 is hij werkzaam als junior wetenschappelijk medewerker aërodynamica bij de Business Unit Duurzame Energie van het Energieonderzoek Centrum Nederland in Petten.